High Resolution Scanning Ion Microscopy

Vincenzo Castaldo

PhD Thesis
June 15, 2011

Cover: Yojana Hernández Valdivia

HIGH RESOLUTION SCANNING ION MICROSCOPY

PROEFSCHRIFT

ter verkrijging van de graad van doctor
aan de Technische Universiteit Delft,
op gezag van de Rector Magnificus Prof. ir. K.C.A.M. Luyben,
voorzitter van het College voor Promoties,
in het openbaar te verdedigen op

woensdag 6 juli 2011 om 15:00 uur

door

Vincenzo CASTALDO

Ingegnere dei Materiali
Università degli Studi di Napoli Federico II
geboren te Napoli, Italië

Dit proefschrift is goedgekeurd door de promotor:
Prof. dr. ir. P. Kruit

Samenstelling promotiecommisie:

Rector Magnificus,	voorzitter
Prof. dr. ir. P. Kruit,	Technische Universiteit Delft, promotor
Prof. dr. B. Poelsema,	Universiteit Twente
Prof. dr. C. Pappas,	Technische Universiteit Delft
Prof. dr. H.W.M. Salemink,	Technische Universiteit Delft
Dr. ir. W.M.M. Kessels,	Technische Universiteit Eindhoven
Dr. C.W. Hagen,	Technische Universiteit Delft
Dr. J.J.L. Mulders,	FEI Company
Prof. dr. H.W. Zandbergen,	Technische Universiteit Delft, reservelid

ISBN 978-94-91211-69-0

Printed in The Netherlands

To whom is curious

Preface

This PhD project originates as part of the project *Nanometer resolution focused ion beam processing and microscopy*, in the framework of the FOM/FEI IPP program *Microscopy and modification of nano-structures with focused electron and ion beams*. The original aim of the project was "to enable nanometer resolution focused ion beam processing and microscopy by developing nm size ion probes and subsequently exploring the ion-surface interaction for various ion species at the nanoscale". Thus, a two-step project, developing of new ion sources and study of ion/matter interaction, for which the project leader, prof. Pieter Kruit, appointed two PhD students to work in his Charged Particle Optics Group at the Delft University of Technology. I am one of them, on the 'ion/matter interaction' part. Things never go exactly the way they are planned at the very beginning, but that is a rule of the game that everybody knows: due to a series of circumstances, I ended up narrowing the broad theme of ion/matter interaction to a more specific 'High Resolution Scanning Ion Microscopy', which is the title of this thesis. The motivation of the project was the idea that ions can in principle be focused into a smaller spot than electrons, because of the lower diffraction limit. However, due to requirements of current, brightness and stability, the only really usable ion sources were at the moment Liquid Metal Ion Sources, employing ions that are too heavy for high resolution microscopy. If only a reliable light ion source could be developed, then a wholly new scenario would open up to the field of scanning ion microscopy. Seen from here, almost my entire project was reshaped by two 'accidents'. The first was that Carl Zeiss managed to commercialise an ion microscope equipped with a novel helium source before the ion source developed in our group was even ready for preliminary characterisation. I guess this was quite unfortunate for the project itself, but not for me: the new device renewed the interest in scanning ion microscopy worldwide, in fact providing stage and audience for my research to come. The second accident was a real stroke of luck for me: after two years from the start of my PhD, one of the first Zeiss helium microscopes was bought by the Dutch research institution TNO, and placed in a facility right next to my building. Everything was just perfect: a microscopy community eager to learn more and more about helium microscopy, and an helium microscope available for experiments! This thesis is the result of all these factors: the vision of my promotor Pieter Kruit, his trust in assigning me on the project, the advent of the helium microscope, my capability[1] to do research and to ride the wave of luck, and, of course, the kindness of the several people that helped me at

---

[1] No judgment of merit: if it is good or bad capability is for the reader to evaluate.

any level.

In order to give the reader a ‘feeling’ for what the next (approximately) 200 pages are going to be, figures 1 and 2 provide some chapter-based statistics, while an artistic representation of the relative weight of the most recurrent words in the whole thesis is shown in fig. 3.

Vincenzo Castaldo
Delft, April 2011

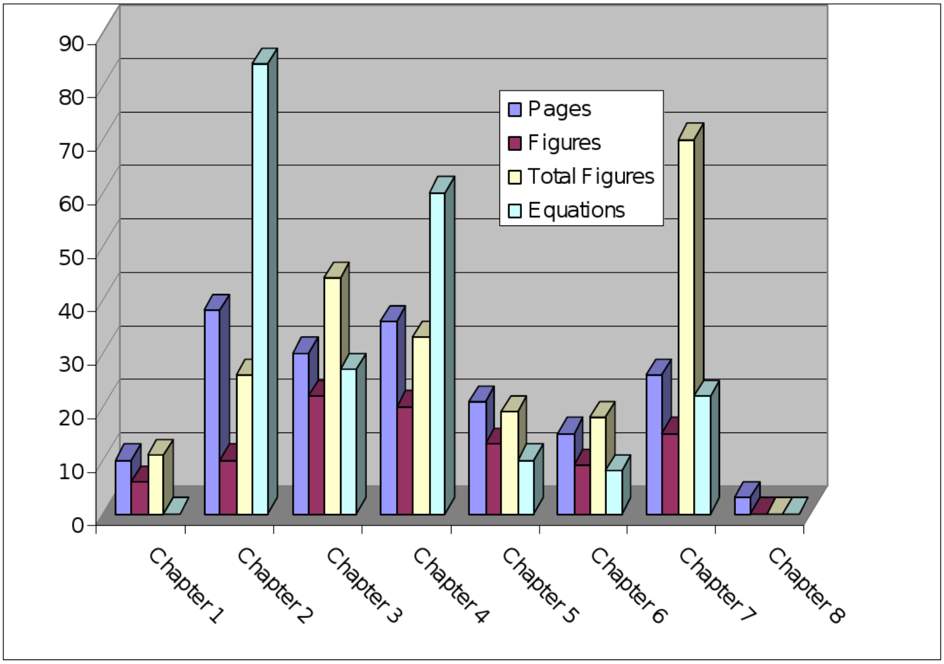

Figure 1: Some chapter-based statistics: number of pages, figures, total figures and equations for each chapter of this thesis.

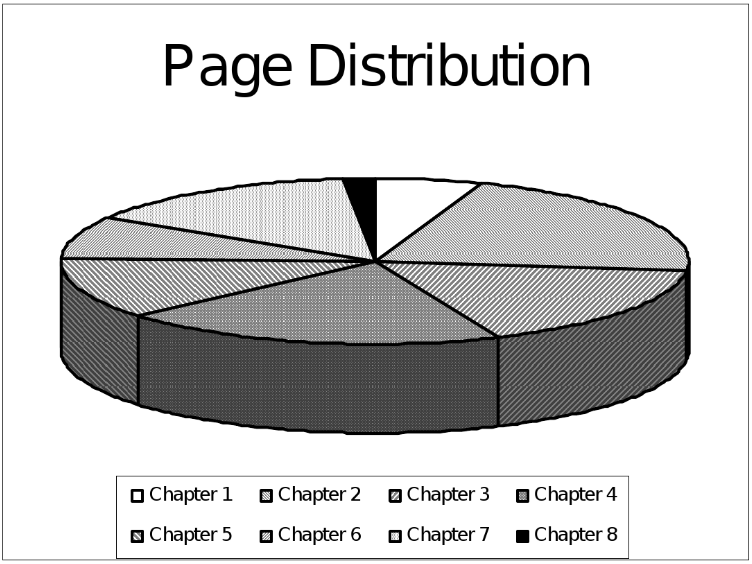

(a)

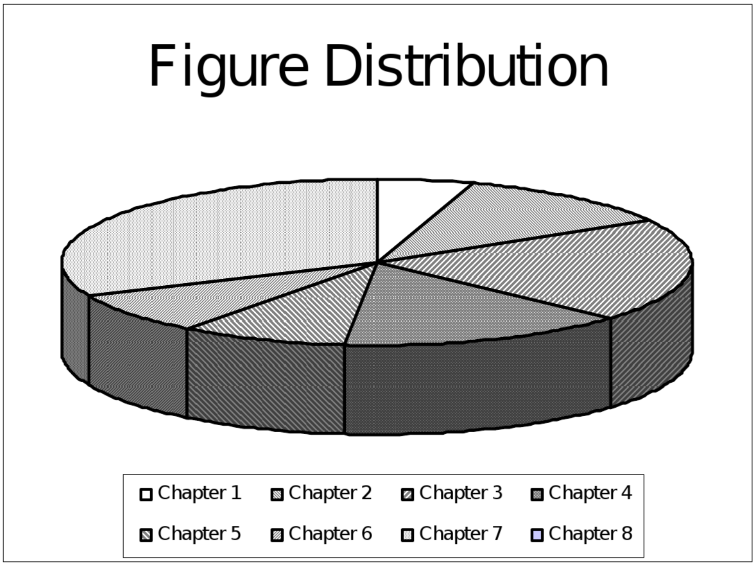

(b)

Figure 2: Distributions of pages (fig. 2(a)) and figures (fig. 2(b)) in the 8 chapters of this thesis.

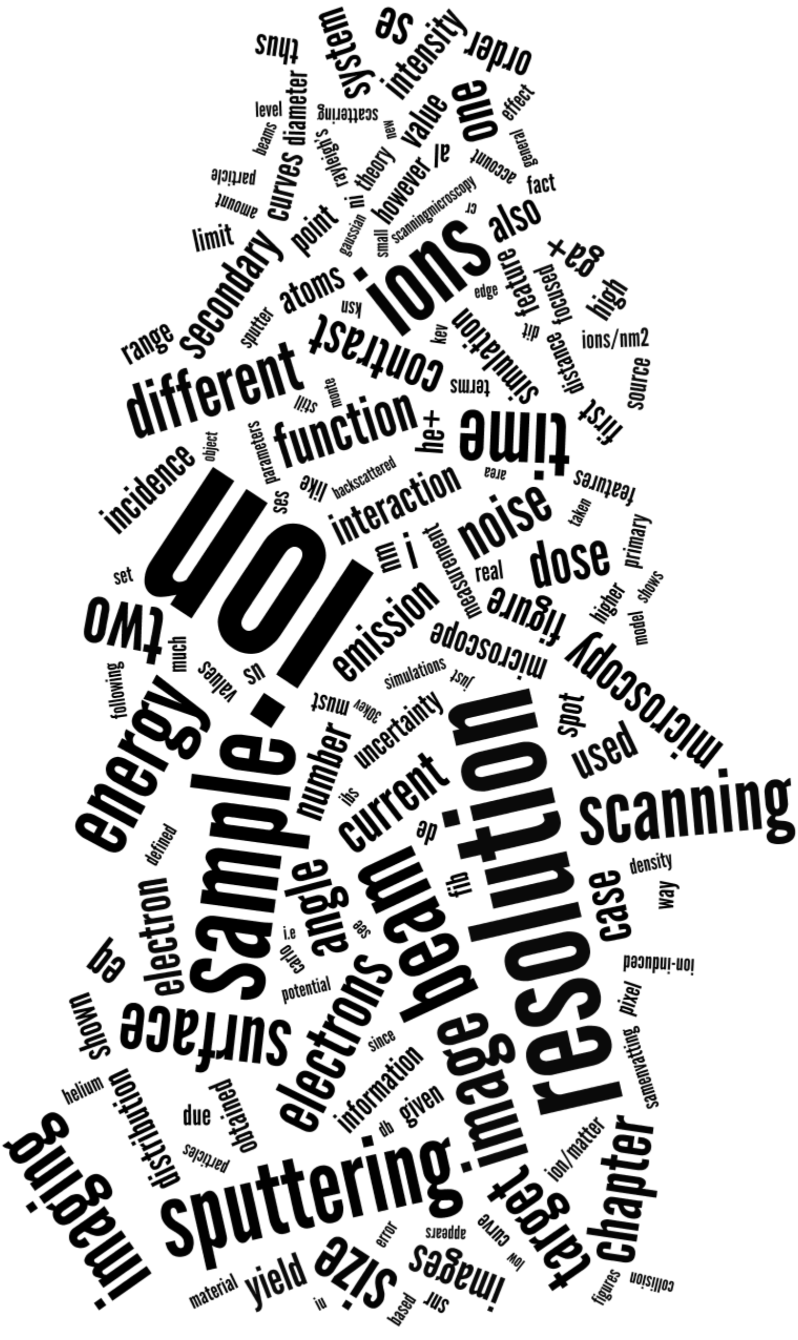

Figure 3: An artistic representation of the relative weight of the most recurrent words in the this thesis (obtained with Wordle™ on http://www.wordle.net).

Summary

High Resolution Scanning Ion Microscopy

Vincenzo Castaldo

The structure of the thesis is the following. The first chapter is an introduction to scanning microscopy, where the path that led to the Focused Ion Beam (FIB) is described and the main differences between electrons and ion beams are highlighted. Chapter 2 is what is normally referred to (which I do not really like) as ‘the theory chapter’. The theory of ion/matter interaction is presented in the first part of the chapter. The treatment is the standard one that can be found in the literature, but of course mine is the choice of the topics and the way in which they are presented. The second part of the chapter is a short introduction to Monte Carlo codes, and in particular to the two pieces of software that I have used for my basic simulations, SRIM/TRIM from J. Ziegler, and IONiSE from D. Joy. The third chapter is almost entirely made up of an article published in Microscopy & Microanalysis in 2011, on the subject of ion-induced Secondary Electron Emission; the paper is introduced by two small sections, the first being an introduction to ion beam imaging, the second presenting a standard theory of noise in scanning microscopy. Chapter 4 introduces the main topic of this thesis work, the one that is more dear to me: resolution in scanning ion microscopy. The chapter is a hybrid, for the theory of resolution that is presented is quite standard, but interlaced with a lot of rethinking and personal points of view, and finally adapted to the specific field of scanning ion microscopy. Chapters 5 and 6 are the first two articles published during my PhD, in Journal of Vacuum Science & Technology B. They both tackle the problem of resolution evaluation in scanning ion microscopy, the first for the Ga-FIB, the second for the He-FIB. The two papers have been published in 2008 and 2009, respectively, a time when the uniformity of the formalism was not yet mature, reason for which symbolic inconsistencies can be found in relation to the rest of the thesis, and to the list of symbols in appendix B. Choice was made to leave the papers in their published version, but this should not represent a problem, because each quantity is clearly defined. The last journal paper published within my project makes chapter 7. The scope of the paper is broad, for it proposes a method to simulate ion imaging that does not employ any Monte Carlo calculation. It can be regarded as a kind of summary of all the studies performed in the course of the project, and is followed by an appendix that explains the details of the noise analysis whose results are presented in the article. Conclusions and recommendations find their place in chapter 8. With referiment to the original main motivation, i.e. exploring the possibility of achieving atomic resolution with a Scanning Ion Microscope, it is shown that this is not possible, at least in the general case, because the sputtering of the sample limits the ultimate obtainable resolution to the nanometer range, even using very light ions. Also, it is pointed out that, in imaging systems causing strong sample modification, the concept of resolution itself can not be thought of as *static*; it must be regarded as *dynamic* instead. On the subject of Ion-Induced Secondary Electron Emission, a procedure to obtain curves of Secondary Electron yield versus incident angle of the beam is presented; the behaviour of those curves contributes to explain the much sharper contrast achievable with a He-FIB, as opposite to the more traditional Ga-FIB. Finally, it is shown that simulation of ion imaging based on the 'yield vs. incidence angle' curves is feasible, overcoming the computational problems that affect any Monte Carlo based approach.

Samenvatting

Hoog Resolutie Raster Ionen Microscopie

Vincenzo Castaldo

Dit proefschrift is als volgt opgebouwd: het eerste hoofdstuk geeft een introductie in de raster microscopie, met een beschrijving van de ontwikkeling van Focused Ion Beam (FIB) en een toelichting van de verschillen en overeenkomsten met electronenbundels. Het onderwerp van hoofdstuk 2 wordt meestal aangeduid met de door mij verfoeide term 'theorie' en in de eerste helft wordt de interactie tussen ionen en materie beschreven. Hoewel de standaard beschrijving bekend uit de literatuur wordt gevolgd heb ik een duidelijke keuze gemaakt in de te behandelde onderwerpen en de wijze van beschrijven. Het tweede deel van dit hoofdstuk is gewijd aan Monte Carlo codes en hier worden de twee door mij gebruikte pakketten beschreven, te weten SRIM/TRIM van J. Ziegler en IONiSE van D. Joy. Het derde hoofdstuk bestaat vrijwel geheel uit een artikel gepubliceerd in Microscopy & Microanalysis in 2011 over ion-induced secondary electron emission. Het artikel wordt voorafgegaan door twee korte paragrafen, de eerste geeft een inleiding in ion beam imaging, de tweede beschrijft de standaard theorie van ruis bij raster microscopie. In hoofdstuk 4 komen we aan bij mijn geliefde- en centrale onderwerp van dit proefschrift: resolutie bij raster ionen microscopie. In dit ietwat hybride hoofdstuk wordt een alleszins standaard behandeling van de theorie van resolutie doorspekt met persoonlijke reflecties en uiteindelijk wordt de theorie toegepast op het specifieke onderwerp raster ionen microscopie. In hoofdstuk 5 en 6 staan de eerste twee artikelen die tijdens mijn promotieonderzoek zijn gepubliceerd in Journal of Vacuum Science & Technology B. Beiden gaan over het probleem van resolutie evaluatie bij raster ionen microscopie, het eerste artikel gaat specifiek over Ga-FIB, het tweede over He-FIB. Deze artikelen zijn gepubliceerd in 2008 en 2009, een tijd dat de conventies en notaties nog niet helemaal waren uitgekristaliseerd waardoor de gebruikte symbolen enige inconsistentie vertonen met de rest van dit proefschrift en de symbolenlijst in appendix B. Er is gekozen voor het integraal overnemen van de tekst van de publicaties wat gezien de duidelijke uitleg van de begrippen geen probleem zou moeten opleveren. De laatste publicatie behorende bij mijn project vormt hoofdstuk 7 en heeft een brede opzet aangezien er een methode wordt voorgesteld om ion imaging te simuleren waarbij op geen enkele wijze gebruik wordt gemaakt van Monte Carlo calculaties. Het is te beschouwen als een integratie van alle onderzoeken uitgevoerd in het kader van dit project en is opgevolgd door een appendix met een gedetaileerde uitleg van de ruis analyse waarvan de resultaten in dit artikel is genoemd. Conclusies en aanbevelingen zijn te vinden in hoofdstuk 8. Onder verwijzing naar het oorspronkelijke onderzoeksdoel, zijnde onderzoek naar de mogelijkheid om atomaire resolutie te bereiken bij raster ionen microscopie, wordt aangetoond dat dit niet mogelijk is, in ieder geval in zijn algemeenheid, omdat het sputteren van het sample de resolutie beperkt tot de nanometerschaal, zelfs bij gebruikmaking van zeer lichte ionen. Ook wordt opgemerkt dat bij imaging systemen die het sample sterk benvloeden het concept resolutie niet als *statisch* gezien kan worden: het zal beschouwd moeten worden als *dynamisch*. Verder wordt een procedure gegeven om bij *ion-induced secondary electron emission* de *secondary electron yield* als functie van de invalshoek te bepalen. Hiermee valt te verklaren waarom bij He-FIB een veel hoger contrast valt te bereiken dan bij het traditionelere Ga-FIB. Als laatste wordt aangetoond dat simulatie van ion imaging gebaseerd op deze ‘yield-invalshoek-functie’ mogelijk is zodat de rekenkundige problemen die zo kenmerkend zijn voor Monte Carlo gebaseerde methodes vermeden kunnen worden.

Contents

1 CHAPTER

Introduction: the Focused Ion Beam

> *"I used to wonder how it comes about that the electron is negative. Negative/positive - these are perfectly symmetric in physics. There is no reason whatever to prefer one to the other. Then why is the electron negative? I thought about this for a long time and at last all I could think was 'It won the fight!'."*
>
> Albert Einstein

This is where it all starts. Beginning with analysing the motivations that led to the design of the Scanning Electron Microscope first, and of the Focused Ion Beam then, the Scanning Ion Microscope is introduced. The main differences between electrons and ions are pointed out, in terms of velocity, momentum and wavelength as function of energy, and in terms of interaction with matter. The chapter ends with a 'problem statement', i.e. the motivations at the basis of this PhD project.

The core of this thesis is a collection of four published scientific papers:

V. Castaldo, C. W. Hagen, B. Rieger, and P. Kruit.
Sputtering limits versus signal-to-noise limits in the observation of Sn-balls in a Ga^+ microscope.
Journal of Vacuum Science & Technology B, 26(6):2107–2115, 2008.

V. Castaldo, C. W. Hagen, P. Kruit, E. van Veldhoven, and D. Maas.
On the influence of the sputtering in determining the resolution of a scanning ion microscope.
Journal of Vacuum Science & Technology B, 27(6):3196–3202, 2009.

V. Castaldo, J.M. Withagen, C.W. Hagen, E. van Veldhoven, and P. Kruit.
Angular Dependence of the Ion-Induced Secondary Electron Emission for He^+ and Ga^+ Beams.
Microscopy & Microanalysis, 17(4):1–13, 2011.

V. Castaldo, C.W. Hagen, and P. Kruit.
Simulation of Ion Imaging: Sputtering, Contrast, Noise.
Ultramicroscopy, 2011; doi:10.1016/j.ultramic.2011.03.019

These four articles will be found in chapters 5, 6, 3 and 7, respectively, and are of course written in 'standard scientific style'. For the unpublished sections, however, I favoured a rather colloquial format, in the hope to make more enjoyable a reading, that, for its own subject, could otherwise result a bit too cold and tiring.

1.1 In the Beginning there was Light. Then, Electrons. Finally, Ions

In the beginning there was light. Light Microscopy. The basic idea was rather simple: take a beam of light, shine it on a tiny sample, collect the light that is transmitted through, or reflected from, the sample, send it through a series of lenses to magnify it, and plot on a plane any characteristic of the light beam that is somehow modified by the sample and that, still somehow, correlates with the topography of the sample surface. This is, in a nutshell, a way to obtain an image of a very small surface. This worked very well for quite a long time. When microscope designers started moving towards higher and higher magnifications however, it became clear that the process could not be pushed down to the infinitely small, because of a very fundamental problem: diffraction. Any beam of light that passes through a slit is diffracted by its walls, thus dispersing its energy over a broader area. As a result, the spatial information that is carried by the light beam going through the optical column is limited to a resolution that is, in first approximation, of the order of magnitude of the wavelength of light itself. Thus, in the order of few hundreds of nanometers. However (and luckily), there are quite a lot of interesting things going on in the sub-100nm world. Quantum mechanics has been able to explain many details of the basic working principles of matter and energy in our universe. And it was from a very basic principle of quantum mechanics that the solution to the diffraction problem came: the particle/wave dualism. Luis-Victor-Pierre-Raymond, 7th duc de Broglie (15 August 1892 – 19 March 1987) showed that any quantum system, like an atom or any subatomic particle, can be regarded not only as a particle. Nobody maybe really understands how this exactly works, but that this description works is a fact. The proof is simple: quantum systems, like electrons, diffract, just like a light beam. Once it was found out that the wavelength associated with a quantum particle decreases with increasing kinetic energy and particle mass, it was easy to calculate that electrons at few keV exhibit a wavelength way shorter than that of visible light (some numbers will be given in the following section). In other words, using a beam of electrons instead of a beam of light to form an image pushes the diffraction limit down to a point that, for many purposes, can be considered safe. For many purposes, but not for all of them. Point is, the ultimate target of microscopy is being able to see very small things: pushing down the resolution limit is the natural thing to do. But at this point, things are clear: particles with even smaller wavelength than electrons can be used. And here we come to Ion Microscopy; ions are thousands of times heavier than electrons (the mass of one electron is approximately 1/1836 that of one proton), which translates in a wavelength, at the same energy, hundreds of times shorter. Moreover, an ion beam can be focused with the same technology used to focus electron beams, and the interaction of ions with matter is, up to a certain point, similar to the electron/matter interaction[1].

This is a very schematic storyline. It can be imagined, however, that in reality things are much more complicated than that. For example, techniques exist to push the resolution limit in optical microscopy below the diffraction limit. Also, for each big family (optical microscopy, charged particle microscopy, probe microscopy, etc.), there are usually several different technological solutions, each defining a different microscopy technique (like x-ray microscopy, scanning tunneling microscopy, atomic force microscopy, field ion microscopy). The scope of this thesis is solely on a very specific kind of microscope: the Scanning Ion Microscope. A Scanning Ion Microscope (SIM) works exactly like the more famous Scanning Electron Microscope (SEM), just, with ions instead of electrons. Actually, SIMs are usually referred to as Focused Ion Beams (FIBs), for the reason that a FIB machine is not necessarily a microscope, but, more likely, a micro- nano- fabrication tool. The acronym SIM should be used for a FIB when, and only when, it is designed (or used) to be a microscope. The working principle of Scanning Microscopy (SM) is very straightforward: a beam of charged particles is focused into a very small spot on the sample surface, then it is scanned across an area just like in a cathode ray tube TV screen, taking care that it rests at each spot for a minimum amount of time (dwell time). At each spot a certain amount of secondary particles (secondary electrons, or backscattered ions/electrons) is emitted and collected by a detector, and, if the amount of secondary emission is a local function of the sample surface, then an image is simply formed, pixel by pixel, counting the emission at each spot and assigning a grey value to it (more on this topic in chapter 3). In principle thus, because of the lower diffraction limit, a SIM can produce smaller probe sizes than a SEM. However, the imaging resolution is often severely limited by the sputtering damage, i.e. the removal of sample material due to the ion impact. This will be one of the central topics of this entire work, and this is the reason why for long time FIBs have been used as ‘sputtering tools’, for fabrication/modification of materials at the nanoscale, but not as microscopes. FIBs became first ‘credible’, and then slowly indispensable, as nanofabrication tools thanks to the use of Liquid Metal Ion Sources (LMISs) by Seliger et al. in 1978 [1]. Due to the high brightness, high current and good reliability of the LMIS, and in particular of Ga^+ LMIS, FIBs became widely used in the semiconductor industry, in fields of application such as IC review and modification (assisted etch/deposition, cross-section cut, implantation), TEM/STEM sample preparation, thin film head manufacturing, and even mass spectrometry [2, 3]. The Ga^+ FIB used for this PhD project, a Quanta™ 3D FEG from FEI, is shown in fig. 1.1; this machine is a so-called ‘Dual Beam’, because

---

[1] By the same token, you could think of ‘Stone Microscopy’ as of something really smart, for stones have a wavelength much much smaller even than ions; careful thinking, however, suggests not to put much hope in it, for the two main reasons that stones are difficult to focus (especially in a small spot), and that their interactions with the specimen are not of the same kind as of ion/-electron/matter interactions.

Figure 1.1: The Ga-FIB Quanta™ 3D FEG from FEI; this 'dual beam' machine is in the laboratories of the Charged Particle Group at Delft University of Technology.

it integrates a Scanning Electron Microscope and a Focused Ion Beam, and both beams can be used on the same sample without breaking the vacuum in the chamber. In the last decade, however, considerable effort has been devoted to the design and development of novel Gas Field Ion Sources (GFIS) employing light ion species, which gave renewed attention to FIBs as microscopes. In particular, Alis

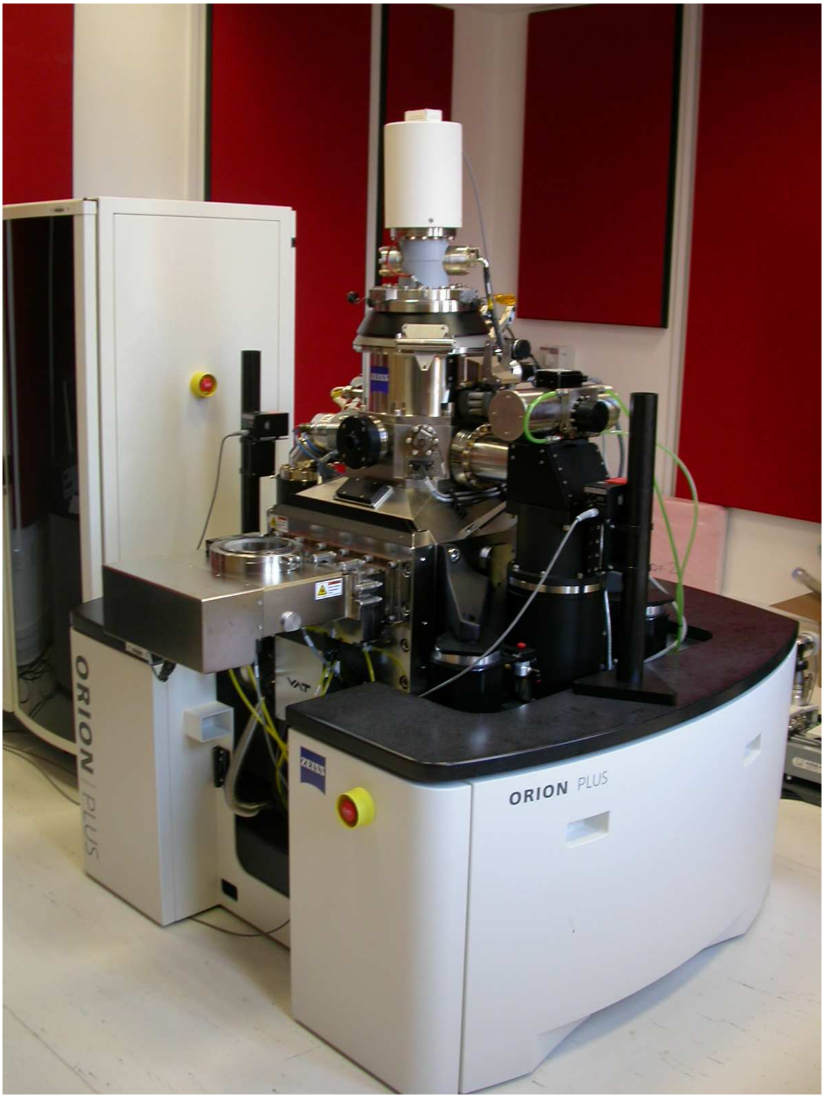

Figure 1.2: The helium microscope ORION® PLUS, from Carl Zeiss; this is the machine in the TNO facility in Delft, with which I have carried out all the helium imaging for this thesis.

Corporation has been able to develop a Helium microscope (the ORION® PLUS, in fig. 1.2, commercialised by Carl Zeiss) that provides high current with very high brightness and very low aperture angle at the sample, resulting in high depth of focus [4, 5, 6, 7]. SIMs now compete with, and complement, the traditional SEMs in terms of brightness, current, spot-size, and, ultimately, imaging resolution [8][2].

---

[2] The ORION® PLUS used during my PhD has been purchased from the NanoNed project for TNO and is operated by TNO personnel.

To be fair, electron microscopes still perform better than their ion counterparts in terms of resolution and ease of operation. Nevertheless, the use of ions instead of electrons in scanning microscopy promises several advantages: new contrast mechanisms, larger depth of focus and perhaps higher resolution, clearer contrast for heavy materials and higher sensitivity to the state of the target surface [9, 10, 11, 12].

1.2 Ions versus Electrons

In this section, I just want to give some numbers in order to get a better grasp of the different behaviour of ions when compared to electrons.

Velocity, Momentum, Wavelength Figures 1.3, 1.4 and 1.5 show plots of velocity, momentum and wavelength versus energy, for electrons and the two most common ion species in FIBs (Ga^+ and He^+). The equations that link these four quantities can be found in any physics book. The curves and the results that they present are nothing special; they are indeed what anyone with a bit of 'physics common sense' would expect. It is a good thing, however, to see these platitudes nicely plotted, and to write down the most obvious observations:

- electrons are much faster than ions at the same energy; so fast, that they require relativistic corrections also in the SM energy range (the speed of light is $\sim 3 \times 10^8 \mathrm{m/s}$, and electrons at 30keV have a velocity of $\sim 10^8 \mathrm{m/s}$);
- in the keV energy range, ions do not nearly approach the speed of light, thus requiring no relativistic corrections (ions at 30keV have a speed in the range of $10^5 - 10^6 \mathrm{m/s}$, depending on the ion);
- ions have, at the same energy, a momentum that is at least 2 orders of magnitude higher than that of electrons;
- ions have, at the same energy, a wavelength that is about 2 orders of magnitude smaller than the one of electrons;
- in order to slow electrons down to the speed of ions at 30keV, the beam energy should be no higher than a few units of eV;
- comparing He^+ and Ga^+, the first is approximately 5 times faster, has a momentum 1.5 times smaller, and a wavelength 4 times longer than the latter.

Diffraction Limit The diffraction limit for SEMs and SIMs is given by $d_a = 0.54\lambda/\alpha_i$ (eq. 4.9 in sec. 4.2.2). Plugging in numbers, assuming an energy of 30keV and a semi-aperture angle at the image side of 5×10^{-3}rad, one obtains:

- **Electrons:** $\lambda \sim 7 \times 10^{-12}\mathrm{m} \quad \Rightarrow \quad d_a \sim 7.5 \times 10^{-10}\mathrm{m}$;

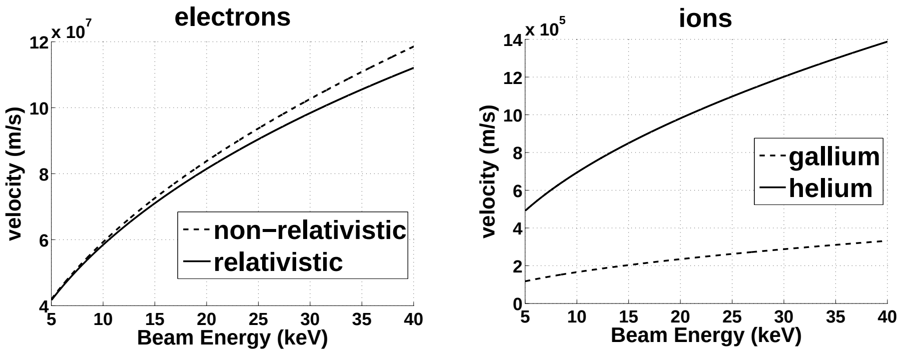

(a) (b)

Figure 1.3: Electron (fig. 1.3(a)) and ion (fig. 1.3(b)) velocity versus energy.

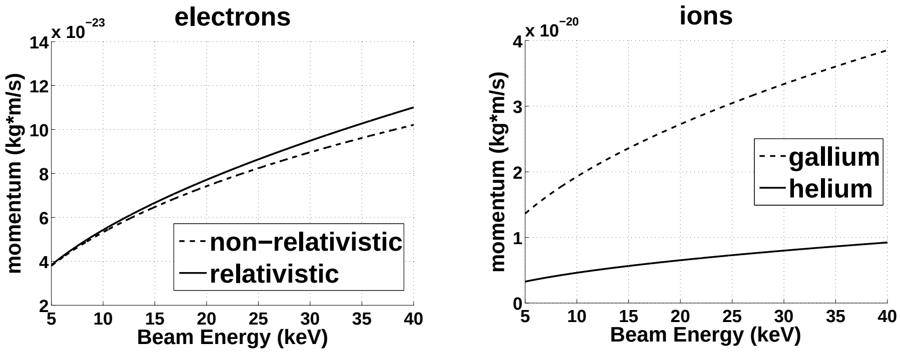

(a) (b)

Figure 1.4: Electron (fig. 1.3(a)) and ion (fig. 1.3(b)) momentum versus energy.

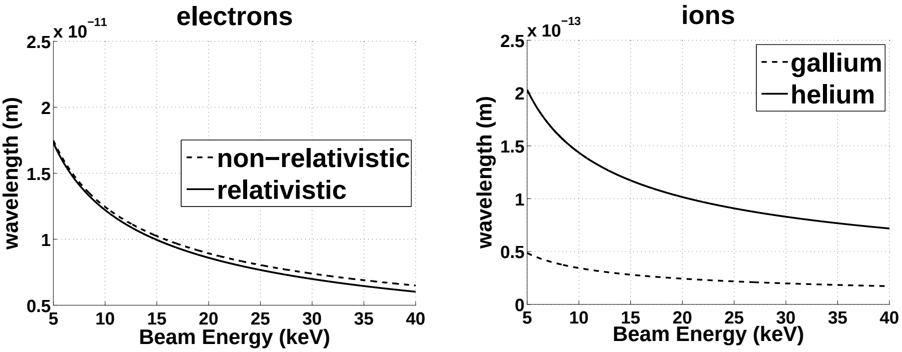

(a) (b)

Figure 1.5: Electron (fig. 1.3(a)) and ion (fig. 1.3(b)) wavelength versus energy.

- **Ga$^+$:** $\lambda \sim 2 \times 10^{-14}\text{m} \quad \Rightarrow \quad d_a \sim 2 \times 10^{-12}\text{m};$
- **He$^+$:** $\lambda \sim 8 \times 10^{-14}\text{m} \quad \Rightarrow \quad d_a \sim 8.5 \times 10^{-12}\text{m}.$

Interaction with the Sample The differences in interaction with matter between electrons and ions ultimately stem from their mass difference, and thus from their differences in velocity, wavelength, and momentum, for the same value of kinetic energy. Apart from the obvious differences in destructive power (the sputtering effect), which is negligible for electrons in most applications but never for ions, what makes the difference in microscopy are the contrast and the resolution that can be obtained with one or the other kind of charged particle. About the contrast, differences have been observed in material contrast, with one machine often (but not always!) showing a reversed contrast when compared with the other one [13], and in sensitivity to the sample surface state, which appears to be higher for SIM than for SEM [9]; also, Ohya *et al.* concluded that the topographic contrast for heavy materials is clearer in a SIM image than in a SEM image, while for light materials the difference is negligible [12]. As a further bonus, SIMs give the possibility to use backscattered ions instead of secondary electrons, which are reported to give a better material and grain contrast (the last, thanks to channeling of the primary ions through low density directions in the sample bulk) [14, 4]. About the obtainable resolution, Ohya and Ishitani [10, 11] showed that, in the assumption of point-like probe, the lateral distribution of ion-induced SEs is much narrower, leading to a better spatial resolution for SIM than for SEM, except for targets of low Z. Another good way to appreciate the differences in interaction with matter between electron and ions is looking at the particles and recoils paths inside the bulk, as they are produced by a Monte Carlo simulation code. Fig. 1.6 shows such simulations, on a target made of a 800nm layer of chromium on silicon: electrons at 25keV in fig. 1.6(a), Ga$^+$ at 30keV in fig. 1.6(b), and He$^+$ at 25keV in fig. 1.6(c). The ion simulations have been obtained with TRIM (see sec.2.2.1), while the electron simulation has been made with the Monte Carlo code CASINO [15]. What is particularly interesting about these pictures is the great difference in interaction volume between gallium on one side, and helium and electrons on the other side. Gallium ions are confined to a very thin layer below the sample surface, while the penetration power of electrons and helium ions is much greater (which is expected, for gallium ions are bigger and bigger). The intersection between the interaction volume and the sample surface is therefore greater for Ga$^+$, because in this case everything happens very close to the surface. Primary electrons and helium ions, on the other hand, can penetrate deeper into the target, making the above-mentioned intersection pretty small around the beam impact point. Given the broad interaction volume, however, there are quite a few recoils and/or electrons of second generations that reach the target surface, and potentially cause SE emission, quite far from the impact point. The consequence of all this is that the SE distribution is broader, as a whole, for helium and electrons when compared with gallium, but also tends to have a strong narrow peak around the impact point, making the obtained information potentially more local[3] [10].

---

[3] I said here ‘potentially’, because the loss of locality caused by the broad tails of the distribution must be overcome by filtering out the signal coming from the tails themselves.

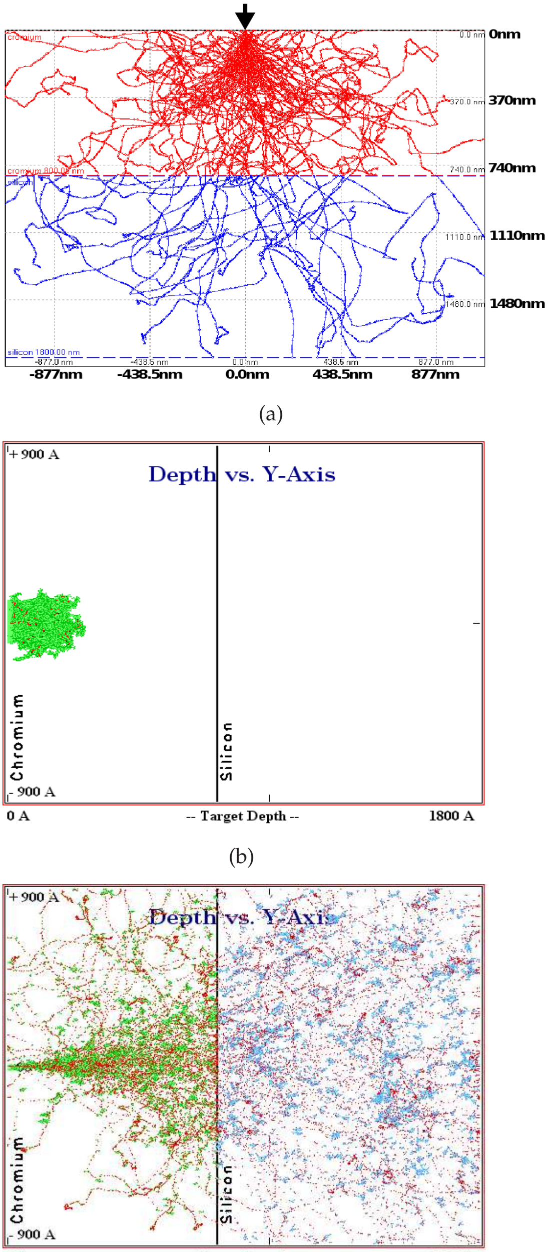

(a)

(b)

(c)

Figure 1.6: Simulations of electrons at 20keV (fig. 1.6(a)), Ga$^+$ at 30keV (fig. 1.6(b)), and He$^+$ at 25keV (fig. 1.6(c)) impacting on a 800nm chromium layer on a silicon substrate; the energies chosen are typical for imaging.

1.3 Problem Statement

Almost all focused ion beam processing, up to the moment when this PhD project was set up, had been performed with focused gallium ion beams, thanks to the high brightness, high current and good reliability of the Liquid Metal Ion Sources. FIBs are nowadays indispensable tools for the semiconductor industry, in fields of application such as IC review and modification, TEM/STEM sample preparation, thin film head manufacturing, and even mass spectrometry. The field of ion beam imaging and induced processing, however, was so young that even for this 'traditional' ion species, the limits of resolution and material purity had not been established. We had no idea what would happen when focused He beams or O beams or Xe beams would be used. Ion beam microscopy was occasionally used in order to obtain immediate visualisation of grain structures because a key difference between electron and ion microscopy is the greatly enhanced channelling contrast observable in ion images. Usually, electron microscopy was (and, to a certain extent, still is) preferred because of its higher resolution and larger signal in the available instruments. Nevertheless, the use of ions instead of electrons in scanning microscopy promised several several advantages: in addition to different new contrast mechanisms, larger depth of focus and perhaps higher resolution could be expected in a near future. Assuming a zero-sized probe, it had been already shown that, except for targets of low Z, the lateral distribution of ion-induced Secondary Electrons is much narrower, leading to a better spatial resolution for SIM than for SEM [10]; also the topographic contrast for heavy materials is clearer in a SIM image than in a SEM image, while for light materials the difference is negligible [10]. Furthemore, it had been predicted that SIM images are more sensitive to the target-surface state than SEM images [9]. The definition of resolution in scanning ion microscopy is an entire subject in its own right. The most popular definition is still the one proposed, for diffraction-limited systems, by Lord Rayleigh in 1879, based on the ability of distinguish two objects in an image. The feeling was that Rayleigh's view was not satisfactory for imaging systems causing strong sample modification: while for extended structures there are several limiting mechanisms like rearrangement and redeposition, for small particles, in the order of a few nm, the imaging resolution is probably determined by the competition between sputtering and SE production/collection. The only way to obtain higher performances in terms of resolution and collectable SNR was exploiting sources of low mass ions, such as H and He. Developing techniques for full characterisation of the ion/sample interactions, and exploring the ultimate possibilities of ion imaging, was therefore of extreme interest, especially in a time when the 'rush' towards novel light ion sources was at his peak, and was to result in the commercialisation of the first real Scanning Ion Microscope, employing a beam of positive helium ions. In particular, since this novel ion source appears to have a subnanometric spot size, the possibility of achieving atomic resolution with Focused Ion Beams had to be explored. In order to understand and optimise the contrast in ion images, moreover, the study of the processes of electron emission upon ion impact is fundamental, combined with a good understanding of all the other ion/matter nteractions that take place below the sample surface, in the so-called 'interaction volume'.

2 CHAPTER

Ion/Matter Interaction

"When it comes to atoms, language can be used only as in poetry.
The poet, too, is not nearly so concerned with describing facts as with creating images."
Niels Bohr

This is what traditionally, and reductively, is referred to as 'the theory chapter'. It is divided into two main parts. In the first part, the standard theory of ion/matter interaction is presented, within the framework of the Binary Collision Approximation. Several forms for the screened potential are introduced, in order to calculate scattering angles and the energy losses in binary collisions. The attention is then moved from the deterministic treatment of a single collision to the statistical description of an entire beam of ions interacting with matter, through the concepts of angular and energy-transfer cross sections, and range distribution. The second part is dedicated to the Monte Carlo simulation of complex systems, and the two Monte Carlo codes used in this thesis, SRIM and IONiSE, are introduced and briefly described. Of course, not all the equations presented in this chapter have actually been used in this research project, but a full analysis of the phaenomena governing the complex subject of ion/matter interaction is the necessary framework within any rethinking or advancement in ion microscoscopy must take place.

2.1 Theory of Ion/Matter Interaction

In normal operating conditions, a Focused Ion Beam, either used for imaging or for modification of materials at the nanoscale, illuminates the specimen with a beam of ions whose energy is in the range of 1keV-50keV, with a current that can be as low as 1pA up to several tens of nA. The very first step in studying this class of tools is therefore to understand what happens when fast ions impact on a specimen.

2.1.1 Introduction

At the basic level, the effects of fast ion interacting with bulk matter do not differ much from those arising when the impinging particles are electrons (see [16] and [17]). The main obvious differences are due to the (much) higher ion mass, whose most evident effect is that, at the same energy,[1] the ion range into solids is much more limited. A first gross distinction can be made according to the type of energy conservation:

- **Elastic Processes**, in which the mechanical energy (kinetic plus potential) is conserved; they are often referred to as *nuclear losses*, and typical effects are displacement of lattice atoms, surface sputtering, formation of defects;
- **Inelastic Processes**, in which the mechanical energy is not conserved, also referred to as *electronic losses*, resulting in the emission of Secondary Electrons (SE), x-rays and photons.

The possible effects due to the momentum transfer between impinging ions and target atoms are indeed a variety; a short summary of the most exploited ones can be useful, while a visual overview is shown in fig. 2.1.

Emission mechanisms Different entities can be emitted by the target under ion bombardment:

- *Secondary Electrons*, i. e. emitted low energy electrons; they represent the main information carriers for image formation;
- *Secondary Ions*, i. e. sputtered atoms that are ionised; they can be used to form an image, or collected and mass-separated to perform SIMS;
- *Photons*;
- *X-rays*.

Ion deflection by target atoms in a backscattering process This mechanism, in (poly-)crystalline materials, can give rise to *channeling*, i. e. dependence of the penetration depth on the beam angle with respect to lattice, which result in a *crystallographic contrast*, with the grains favourably oriented appearing darker. Backscattered ions, when enough, can be used to form images that contain a high level of *material contrast*, in the so-called *Rutherford Backscattering Imaging* (RBI).

---

[1] Given a mass difference of 4-6 orders of magnitude between ions and electrons, at the same energy ions are 2-3 orders of magnitude slower.

Increased disorder in the target In particular:

- production of dislocations, both at the surface and in the bulk,
- production of point lattice defects (rearrangement and amorphisation),
- physical sputtering of surface target atoms;

While the first two effects are often unwanted, for they just increase the disorder of the target, the sputtering of target atoms, while it is devastating from the microscopist point of view, is the effect that gave the FIB the status of essential tool for micro/nanomodification of materials.

Ion implantation Once its energy drops below the level required for further penetration, the impinging ion comes to rest inside the target bulk; this effect can be exploited for material modification (doping), but it is undesired in most cases for it can modify the properties of the target material (the case of Ga^+ beams, by far the most widely used in FIBs, is particularly nasty, for it can affect the magnetic properties).

Chemical sputtering This effect occurs when new volatile compounds are formed in chemical reactions between ions and surface atoms.

Ion Beam Induced Deposition (IBID) By introducing appropriate precursor gasses into the chamber, structures of selected composition can be deposited on the target surface: the energetic beam dissociates the gas molecules in a volatile part and in a heavy part (typically metallic), which deposits in a narrow area around the impact point of the beam.

Auger neutralisation When an electron is removed from a core level of an atom, leaving a vacancy, an electron from a higher energy level may fill it up, resulting in a release of energy; normally this energy is released in the form of an emitted photon, but it can also be transferred to another electron, which is ejected from the atom (Auger electron) and can neutralise a backscattering ion.

Some of these effects will be analysed in deeper details in following sections, for they represent the main mechanisms of image formation (Secondary Electron Emission) and the main drawback in ion microscopy (Sputtering).

2.1.2 Interatomic Potentials

A very great share of physical phenomena derives, more or less directly, from the exchange of electromagnetic forces between atoms. In the case of ion beams impinging on materials, all what can happen is of course a direct consequence of the

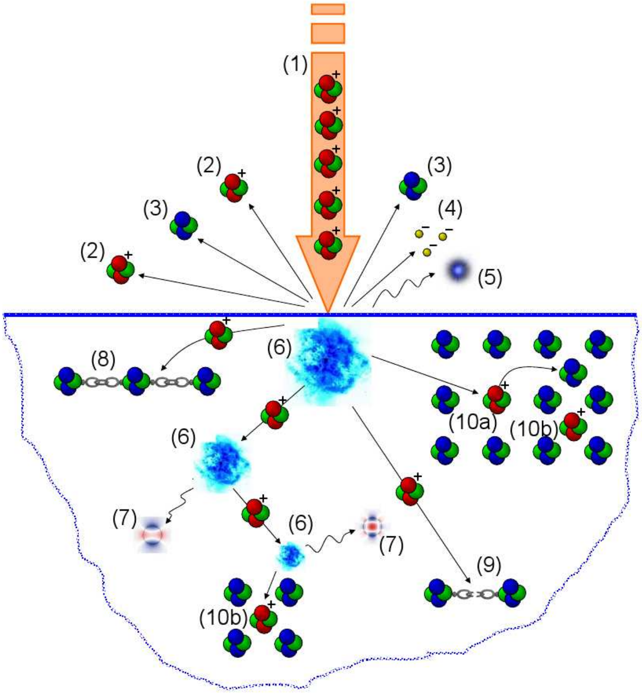

Figure 2.1: A simplified overview of the possible Ion-Matter interactions: (1) incident beam; (2) backscatter ions; (3) sputtered atoms; (4) emitted electrons; (5) emitted photons; (6) impact and energy loss; (7) generated phonon; (8) bond making (polymerisation); (9) bond breaking; (10) creation of defects: vacancy (10.a) and interstitial (10.b). It must be pointed out that these processes do not occur with equal probability.

way energy is exchanged between impinging ions and target atoms. In principle, these collision should be treated as a many-body problem, because various are the entities that constitute atoms, but normally the interactions between ion and nucleus (elastic collisions) and the ones between ions and electrons (inelastic collisions) can be kept separated, due to the large mass difference between nuclei and electrons. At the levels of energies normally encountered in FIBs, the ion sees the nucleus charges screened by the inner electrons. Many screened potentials have been proposed, the most classic approach being the use of the Coulomb potential between two charged particles multiplied by a screening function, which can be applied to all atomic species and does not take into account the atomic shell structure, nor its changes due to the collision. Typically, the screening function, Φ, is based on the Thomas-Fermi atomic model (hence Φ_{TF}):

$$V(r) = \frac{Z_1 Z_2 e^2}{r} \Phi_{TF}(x) \ , \tag{2.1}$$

where e is the elementary charge, r is the distance between the particles and $x = r/a_{TF}$, a_{TF} being the Thomas-Fermi screening length:

$$a_{TF} = \left(\frac{3\pi}{4}\right)^{2/3} \frac{\hbar^2}{2m_e e^2 Z_{eff}^{1/3}} \approx \frac{0.8853 a_0}{Z_{eff}^{1/3}} , \tag{2.2}$$

where a_0 is the Bohr radius (0.0529nm). Slightly different expressions have been suggested for the TF screening length a_{TF}. Here some.

Bohr [18]:

$$a_B = \frac{a_0}{\left(Z_1^{2/3} + Z_2^{2/3}\right)^{1/2}} ; \tag{2.3}$$

Firsov [19]:

$$a_F = \frac{0.8853 a_0}{\left(Z_1^{1/2} + Z_2^{1/2}\right)^{2/3}} ; \tag{2.4}$$

Lindhard [20]:

$$a_L = \frac{0.8853 a_0}{\left(Z_1^{2/3} + Z_2^{2/3}\right)^{1/2}} ; \tag{2.5}$$

Ziegler [21]:

$$a_U = \frac{0.8853 a_0}{(Z_1^{0.23} + Z_2^{0.23})} . \tag{2.6}$$

these expressions differ mainly for the way Z_{eff} is calculated.

The Thomas-Fermi screening function Φ_{TF} is calculated from the following differential equation:

$$\frac{d^2 \Phi_{TF}(x)}{dx^2} = \frac{\Phi_{TF}^{3/2}(x)}{x^{1/2}} , \tag{2.7}$$

whose solutions usually appear in the form of series expansions

$$\Phi_{TF} = \sum_{j=1}^{n} C_i e^{-b_i x} \quad \text{with} \quad \sum_{j=1}^{n} C_i = 1 . \tag{2.8}$$

The coefficients C_i and b_i can be determined from a least-square fit to the calculated free-electron potentials and, in principle, are different for different pairs ion/atom; nevertheless, several approximations of the Thomas-Fermi screening function, have been proposed, whose general validity is partially preserved by the screening length, which depends on the nuclear charge of the involved atomic species. Here some.

Sommerfeld [22]:

$$\Phi_S(x) = \left[1 + \left(\frac{x}{12^{2/3}}\right)^{0.8034}\right]^{-3/0.8034} , \tag{2.9}$$

where $x = r/a_F$ or $x = r/a_L$;

Moliere [23]:

$$\Phi_M(x) = 0.35e^{-0.3x} + 0.55e^{-1.2x} + 0.10e^{-6.0x} , \tag{2.10}$$

valid for $(0 < x < 6)$ and $x = r/a_F$;

Lindhard [20]:

$$\Phi_L(x) = \frac{\xi_\nu}{n} x^{n-1}, \quad 0 \leq n \leq \infty , \tag{2.11}$$

where $\xi_\nu = 2/2.7183 \times 0.8853$ and $x = r/a_L$;

Lenz-Jensen (LJ)[24, 25]:

$$\Phi_{LJ}(x) = e^{-t} \left[1 + t + 0.0344t^2 + 0.0485t^3 + 2.647 \times 10^{-3}t^4\right] , \tag{2.12}$$

where $t = 3.11126\sqrt{x}$ and $x = r/a_F$ or $x = r/a_L$;

Wilson-Haggmark-Biersack (WHB)[26]:

$$\Phi_{WHB}(x) = 0.1909e^{-0.2785x} + 0.4737e^{-0.6371x} + 0.3354e^{-1.9192x} , \tag{2.13}$$

where $x = r/a_F$ or $x = r/a_L$;

Ziegler-Biersack-Littmark (ZBL)[21]:

$$\Phi_U(x) = 0.1818e^{-3.2x} + 0.5099e^{-0.9423x} + 0.2802e^{-0.4029x} + 0.0282e^{-0.2016x} , \tag{2.14}$$

where $x = r/a_U$.

More detailed discussions about the interatomic potentials can be found in literature [26, 27, 28, 29]. Evaluations of the different equations can be made through direct comparison of the calculated potentials with experimental ones [27] or via other derived quantities, such as sputtering yields, penetration depths and reflection coefficients [29]. Eq. (2.14) is known in literature as *Universal Screening Function*, and was calculated assuming each atom has a spherically symmetric charge distribution, with a total interaction potential energy given by:

$$V = V_{nm} + V_{en} + V_{ee} + V_k + V_a , \tag{2.15}$$

where V_{nm} is the electrostatic potential between the nuclei, V_{ee} is the electrostatic potential between the electron distributions, V_{en} is the interaction potential between the nucleus of one atom and the electron distribution of the other atom, V_k is the increase in kinetic energy of the electrons due to Pauli excitation, and V_a is the increase in exchange energy. Accordingly, eq. (2.6) represents the *Universal Screening Length*.

It appears that the WHB and the Universal potentials, being mean potential determined on individual atoms in their ground state, exhibit different accuracies for different ion/atom pairs, while the Moliere potential often requires a correction factor to the screening leg in order to obtain a better agreement with experimental data [30]. It has also been pointed out that all the most used potentials, like the ones showed here, are purely repulsive and do not take into account the fact the atoms in the ground state usually attract each other above some distance; this is certainly a good approximations at large energies, but could not be as good for the modeling of phenomena, like sputtering, for which low energies and larger internuclear separations become important [29]. The Universal potential is generally considered to be the best performing one[2].

2.1.3 The Binary Collision Approximation

The way in which an impinging ion transfers energy to target atoms is usually modeled with two different approaches, both based on classical dynamics [30]:

- **Binary Collision Approximation (BCA)**, in which the ion is assumed to undergo a series of independent binary scattering events with target atoms;
- **Molecular Dynamics (MD)**, in which the multiple interaction of each moving ion with all the atoms in some surrounding is taken into account.

While the MD approach is based on the solution of Newton's equations of motion, in the BCA the interatomic collisions are assumed to be elastic binary collision described by any of the interatomic potential presented in section 2.1.2, leading to elastic (nuclear) energy loss; the energy loss to electrons is treated separately as inelastic.

Summarizing, BCA scattering calculations are based on the following assumptions:

1. *all the collisions take place between two atoms;* this is quite reasonable in the keV energy range, where the colliding particles have enough energy to come very close, and the probability for many-particles collision processes is low;
2. *classical dynamics is applied;*

---

[2] It is also the potential used in the most popular freeware simulation code for ion/matter interaction, the TRIM, distributed, not surprisingly, by Ziegler at `http://www.srim.org/`.

3. *electronic collisions are a source of energy loss, but do not influence the collision dynamics;* this is allowed if the electronic collisions involve much smaller energies than the ones involved in nuclear collisions or do not result in appreciable deflection;

4. *one of the two colliding particles is initially at rest;* this assumption cannot be considered valid for very dense collision cascades, where most of the colliding atoms are already in motion.

2.1.3.1 Binary Scattering

When a particle of mass M_1 and velocity $\boldsymbol{v_0}$ gets close enough to a particle of mass M_2 at rest, an exchange of energy will take place; that is what is called 'collision': the moving particle is deflected by an angle θ and the stationary particle recoils with an angle φ with respect to the direction of $\boldsymbol{v_0}$; after the collision the particles emerge with velocities v_1 and v_2 (see fig. 2.2(a)). The scatter and the recoil angles, and the final velocities, can be calculated applying the conservation laws for energy and momentum:

Energy:

$$E_0 = \frac{1}{2} M_1 v_0^2 = \frac{1}{2} M_1 v_1^2 + \frac{1}{2} M_2 v_2^2 \ . \tag{2.16}$$

Longitudinal Momentum:

$$M_1 v_0 = M_1 v_1 \cos\theta + M_2 v_2 \cos\varphi \ . \tag{2.17}$$

Lateral Momentum:

$$0 = M_1 v_1 \sin\theta + M_2 v_2 \sin\varphi \ . \tag{2.18}$$

Since the mutual forces are purely radial, the relative motion of the two particles can be reduced to the motion of a single particle moving in the interatomic potential centred at the center of mass of the system; this is the reason why the collision problem is usually stated in the so called Center-of-Mass coordinate system, whose velocity v_c is defined in such a way to keep the net momentum at zero:

$$M_1 v_0 = (M_1 + M_2)\, v_c \ . \tag{2.19}$$

The parameters involved in the description of the collision in the CM system are defined in fig. 2.2(b). The velocities of the two particles become:

$$v_{ion} = v_0 - v_c = v_0 M_c / M_1 \ , \tag{2.20}$$

$$v_{atom} = v_c = v_0 M_c / M_2 \ , \tag{2.21}$$

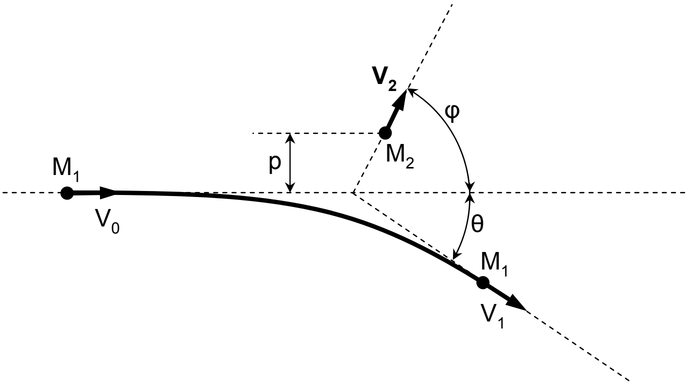

(a)

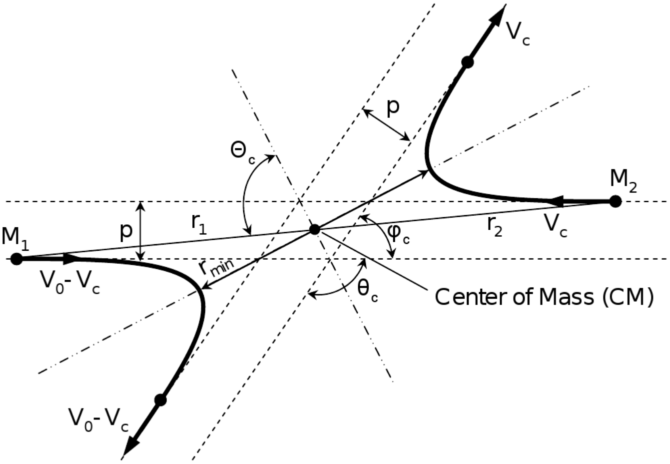

(b)

Figure 2.2: Laboratory (fig. 2.2(a)) and Center-of-Mass systems of coordinates (fig. 2.2(b)); M_1 and M_2 are the mass of, respectively, the ion and the atom, p is the impact parameter; θ and φ are the scatter and the recoil angle in the laboratory system, θ_c and φ_c are the same angles in the center-of-mass system.

where $M_c = M_1 M_2/(M_1 + M_2)$ is the reduced mass. The total energy E_c is equal to the initial kinetic energy:

$$E_c = \frac{1}{2} M_c v_0^2 \ , \tag{2.22}$$

while the angular momentum J_c is the same in both systems and can be expressed in terms of the impact parameter p, defined in fig. 2.2:

$$J_c = M_c v_0 p \ , \tag{2.23}$$

Formulas for the conversion of the quantities from the laboratory system to the CM system (and vice versa) can be found in [31].

In the CM system, the scattering angle can be obtained from the following integral equation (known in literature as *classical scattering integral*) [31]:

$$\theta_c = \pi - 2p \int_{r_{min}}^{\infty} \frac{\mathrm{d}r}{r^2 \sqrt{1 - \frac{V(r)}{E_c} - \left(\frac{p}{r}\right)^2}} \ . \tag{2.24}$$

If the scattering angle is known, the energy of the scattered (E_1) and recoiled (E_2) particles can be calculated as [32]:

$$E_1 = \frac{(M_1 - M_2)^2 + 4 M_1 M_2 \cos^2(\theta_c/2)}{(M_1 + M_2)^2} E_0 \ , \tag{2.25}$$

and

$$E_2 = E_0 \frac{4 M_1 M_2}{(M_1 + M_2)^2} \sin^2\left(\frac{\theta_c}{2}\right) \ . \tag{2.26}$$

The recoil energy E_2 is also called *transferred energy*, and is often indicated with T; eq. 2.26 can be rewritten as [31]:

$$T = T_M \sin^2\left(\frac{\theta_c}{2}\right) \ . \tag{2.27}$$

Eq. 2.27 shows that:

- the transferred energy is highest when the collision is ‘head-on’, i.e. when $\theta_c = 0$;
- $T_M = [(4M_1M_2)/(M_1 + M_2)^2]E_0$ is the energy transferred in a head-on collision;
- when $M_1 = M_2$ the whole ion energy can be transferred to the recoil, while only a fraction can be transferred when $M_1 \neq M_2$.

2.1.3.2 Cross-Section

Equations 2.25 and 2.26 can be used to calculate the energy transferred in the collision when the scattering angle is known, or vice versa, to calculate the scattering angle when the transferred energy is known. The more general scattering integral equation (eq.2.24), on the other hand, expresses the scattering angle as a function of the impact parameter p, the system energy E_c, and the interatomic potential $V(r)$ describing the electromagnetic interaction between the two colliding particles. In any real system employing ion beams, however, there are billions of charged particles impacting the sample surface every second[3]. Calculating the energy transferred to the target, and determining the evolution of the ion beam as a whole in and out the target bulk, requires therefore a statistical approach. Central to this statistical approach is the concept of 'cross-section', and its differential counterpart, the 'differential cross-section'. The cross-section is a general concept, that expresses the probability of a certain event to happen; in the context of ion/matter interaction, differential cross-sections are usually defined to express the probability of scattering, or the probability of energy transfer.

- **Angular Differential Scattering Cross-Section** ($\mathrm{d}\sigma(\theta_c)$): relates to the probability for the projectile ion to scatter between the angle θ_c and the angle $\theta_c + \mathrm{d}\theta_c$.
- **Energy-Transfer Differential Scattering Cross-Section** ($\mathrm{d}\sigma(E)$): relates to the probability for the projectile ion to transfer an amount of energy between T and $T + \mathrm{d}T$.

In other words, the scattering cross-section is the effective target area for each scattering center, i.e. target atoms, as seen by an incident ion; it is a function of the impact parameter.

Angular Scattering Cross-Section The angular total and differential scattering cross-section are schematised in figures 2.3(a) and 2.3(b), respectively. The scattering angle is a function of the impact parameter: any ion travelling towards a target with impact parameter p, or lower, will be deflected by an angle θ_c, or higher. The total cross-section is thus the area defined by the impact parameter:

$$\sigma\left(\theta_c\right) = \pi p^2 \ . \tag{2.28}$$

The differential scattering cross-section is obtained differentiating eq. 2.28:

$$\mathrm{d}\sigma\left(\theta_c\right) = 2\pi p\, \mathrm{d}p \quad \Rightarrow \quad \frac{\mathrm{d}\sigma\left(\theta_c\right)}{\mathrm{d}\theta_c} = 2\pi p\left(\theta_c\right)\left|\frac{\mathrm{d}p\left(\theta_c\right)}{\mathrm{d}\theta_c}\right| \ , \tag{2.29}$$

where the absolute value is needed to keep $\mathrm{d}\sigma$ positive[4]. Eq. 2.29 expresses the differential cross-section per unit scattering angle. Since in practice the scattered particles are usually counted on the solid angle, expressing $\mathrm{d}\sigma$ per unit solid angle is preferable. This can be done noting that the differential solid angle $\mathrm{d}\Omega$ subtended between θ_c and $\theta_c + \mathrm{d}\theta_c$ is the gray area in fig. 2.3(b) divided by R^2, so

---

[3] For example, a current of just 10pA of single-charged ions means a flow rate of 160 billion particles per second.

[4] The term $\mathrm{d}p/\mathrm{d}\theta_c$ is always negative, being p and θ_c in an inverse relation.

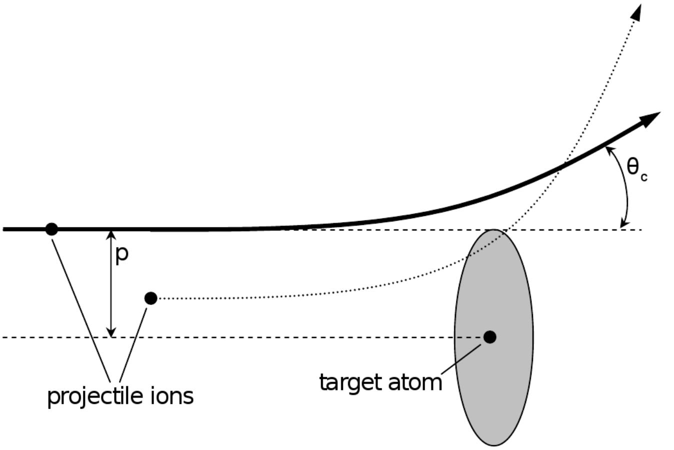

(a)

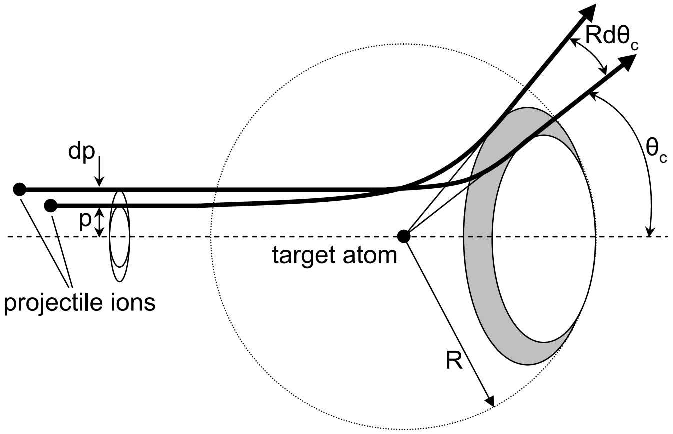

(b)

Figure 2.3: Scattering of energetic ions by a target atom. The total cross-section, given by πp^2, is shown in fig. 2.3(a), while fig. 2.3(b) schematises the quantities involved in the definition of the differential cross-section.

that:

$$\mathrm{d}\Omega = 2\pi \sin\theta_c \mathrm{d}\theta_c \ . \tag{2.30}$$

Combining equations 2.29 and 2.30 one obtains:

$$\frac{\mathrm{d}\sigma\left(\theta_c\right)}{\mathrm{d}\Omega} = \frac{p}{\sin\theta_c}\left|\frac{\mathrm{d}p\left(\theta_c\right)}{\mathrm{d}\theta_c}\right| \ . \tag{2.31}$$

In equations 2.29 and 2.31, the cross-section is expressed as a function of θ_c and p. These two parameters are univocally related by eq. 2.24 once the shape of the interaction potential is assigned, so that $\mathrm{d}\sigma$ can be rewritten as function of the scattering angle only. Here two examples [32]:

$$V\left(r\right) = \frac{Z_1 Z_2 e^2}{r} \quad \Rightarrow \quad \frac{\mathrm{d}\sigma\left(\theta_c\right)}{\mathrm{d}\theta_c} = \left(\frac{Z_1 Z_2 e^2}{4E_c}\right)^2 \frac{1}{\sin^4\left(\theta_c/2\right)} \tag{2.32}$$

$$V\left(r\right) = \frac{Z_1 Z_2 e^2}{r^2} \quad \Rightarrow \quad \frac{\mathrm{d}\sigma\left(\theta_c\right)}{\mathrm{d}\theta_c} = \frac{\pi^2 Z_1 Z_2 e^2}{E_c} \frac{\pi - \theta_c}{\theta_c^2\left(2\pi - \theta_c\right)^2 \sin\theta_c} \tag{2.33}$$

Eq. 2.32, based on the pure Coulomb potential, is known in literature as *Rutherford differential cross-section*.

Energy-Transfer Scattering-Cross Section It can be shown that the energy-transfer differential cross-section per unit of transferred energy T can be expressed as [31]:

$$\frac{\mathrm{d}\sigma\left(E\right)}{\mathrm{d}T} = 2\pi \sin\theta_c \left|\frac{\mathrm{d}\theta_c}{\mathrm{d}T}\right| \frac{\mathrm{d}\sigma\left(\theta_c\right)}{\mathrm{d}\Omega} \ . \tag{2.34}$$

Combining equations 2.27, 2.31 and 2.34, the energy-transferred differential cross-section can be rewritten as function of scattering angle and impact parameter, just like the angular differential cross-section in equations 2.29 and 2.31:

$$\frac{\mathrm{d}\sigma\left(E\right)}{\mathrm{d}T} = \frac{4\pi}{T_M}\left|\frac{\mathrm{d}p\left(\theta_c\right)}{\mathrm{d}\theta_c}\right| \ . \tag{2.35}$$

Total cross-sections can be obtained integrating equations 2.29 and 2.34 between the limits $[0, p_{max}]$ and $[T_{min}, T_M]$, respectively. The results of these two operations will be the same, i.e. $\sigma\left(\theta_c\right) = \sigma\left(E\right)$, because the two different cross-sections become equivalent once integration on the whole range of events is performed.

Summarising, the two parameters on which the differential cross-section depends, p and θ, can be reduced to just one, once the potential $V(r)$ is assigned; the complexity of the calculation depends, of course, on the form of the potential that is chosen to describe the interaction. However, it has been shown that $\mathrm{d}\sigma$ not only depends on the pair $p - \theta_c$, but also on 5 other quantities: Z_1, Z_2, E, M_1 and M_2 (the latter two via the total kinetic energy E_c, see eq. 2.22). In order to simplify the matter, J. Lindhard *et al.* [20] proposed a universal one-parameter scattering cross-section using the Thomas-Fermi potential (eq. 2.2):

$$\frac{\mathrm{d}\sigma(t)}{\mathrm{d}t} = \frac{-\pi a_{TF}^2}{2} \frac{f\left(t^{1/2}\right)}{t^{3/2}} , \tag{2.36}$$

with:

$$t = \left(\frac{a_{TF} E_c}{Z_1 Z_2 e^2}\right)^2 \sin\left(\frac{\theta_c}{2}\right) . \tag{2.37}$$

The universal parameter t is inversely related to distance between the two interaction particles. The function $f\left(t^{1/2}\right)$ can be tabulated, or analytically approximated [33].

2.1.3.3 Energy Losses

Ions passing through matter lose their energy due to collisions with constituent atoms. It is common practice to divide this energy loss, also called *stopping power*, into two categories:

- **electronic**, or **inelastic**, when the energy is transferred to electrons and produces excitation and/or ionisation (high velocity range);
- **nuclear**, or **elastic**, when kinetic energy is transferred from the scattering particle to the particle in the bulk, that may then recoil (low velocity range).

Nuclear Stopping Nuclear Stopping is the average energy loss during elastic collisions between the nuclear charge of the ion and the target atoms. In order to calculate it, the interaction potential between the two impacting particles must be known. Typically, different interaction potentials should be used in different energy ranges:

- **Low energies** → very complex interaction.
- **Medium energies** → screened Coulomb scattering.
- **High energies** → Rutherford scattering.

Nuclear energy losses tend to dominate when $E_1 < M_M$keV, M_M being the ion molecular mass. Typical beam energies in FIBs are too low for the nuclei to get so close to give rise to Rutherford scattering, so that a screened Coulomb potential can be used for the calculation, like the Thomas-Fermi screened potential of eq. 2.1. A good approximation of eq. 2.1 over small distances, not listed in sec. 2.1.2, is the following [31]:

$$V(r) = \frac{Z_1 Z_2 e^2}{r} \frac{k_s}{s} \left(\frac{a_{TF}}{r}\right)^{s-1} , \tag{2.38}$$

where k_s is a constant and s is a fitting parameter (integer); as a rule of thumb:

- $(a_{TF}/r) << 1 \Rightarrow s \approx k_s \approx 1$;
- $(a_{TF}/r) >> 1 \Rightarrow s \approx 2 - 3$.

Contrary enough to common sense, things become easier if two dimensionless parameters are introduced. A reduced energy:

$$\epsilon = \frac{a_{TF} M_2 E_1}{Z_1 Z_2 e^2 \left(M_1 + M_2\right)} \; ; \tag{2.39}$$

and a reduced path length:

$$\rho = R N_a \pi a_{TF}^2 \gamma \; , \tag{2.40}$$

where N_a is the atomic density (in atoms/cm^3), R the path length (see fig. 2.4) and $\gamma = 4M_1M_2/\left(M_1 + M_2\right)^2$. For the TF screening length a_{TF} any of the proposed expressions listed in sec. 2.1.2 can be used. Using, for example, the form proposed by Lindhard (eq. 2.5), equations 2.39 and 2.40 become, respectively [3]:

$$\epsilon = \frac{32.53 M_2 E_1}{\left(M_1 + M_2\right) Z_1 Z_2 \left(Z_1^{2/3} + Z_2^{2/3}\right)^{1/2}} \; , \tag{2.41}$$

and

$$\rho = \frac{166.8 M_1}{\left(M_1 + M_2\right) \left(Z_1^{2/3} + Z_2^{2/3}\right)} z \; . \tag{2.42}$$

The stopping power $-\mathrm{d}E/\mathrm{d}R$ is the average energy lost per unit path length into the material[5] [6]; therefore, it is expressed by the integral of the energy transferred over the energy transfer cross-section $\mathrm{d}\sigma$, multiplied by the target atomic density N_a:

$$-\left(\frac{\mathrm{d}E}{\mathrm{d}R}\right)_n = N_a \int_{\sigma(E=0)}^{\sigma(E=E_{max})} E \, \mathrm{d}\sigma = -N_a S_n\left(E\right) \; , \tag{2.43}$$

where $S_n(E)$ is the *nuclear stopping cross-section*, the subscript n standing for 'nuclear', as opposed to 'electronic', that will be indicated with the subscript e. In dimensionless units eq. 2.43 becomes:

$$-\left(\frac{\mathrm{d}\epsilon}{\mathrm{d}\rho}\right)_n = s_n\left(\epsilon\right) \; , \tag{2.44}$$

with the following relationship between the nuclear stopping cross-section $S_n\left(E\right)$ and its dimensionless version $s_n\left(\epsilon\right)$ [31]:

$$s_n\left(\epsilon\right) = \frac{\epsilon}{\pi a_{TF}^2 \gamma E} S_n\left(E\right) \; . \tag{2.45}$$

---

[5] From now on, for ease of comparison with the related literature, the projectile energy E_1 will be simply indicated with E, while the energy E_2 transferred to the target will be always indicated with T.

[6] $\mathrm{d}E/\mathrm{d}R$ is a negative quantity, for the energy of the projectile decreases while advancing into the target bulk; the negative sign is used to keep it positive.

For $s_n(\epsilon)$ the following approximation has been proposed [3]:

$$s_n(\epsilon) = \frac{0.5 \ln(1+\epsilon)}{\epsilon + 0.14\epsilon^{0.42}} \ . \tag{2.46}$$

In order to calculate the stopping power and the scattering cross-section, a better approximation over a broader energy range is obtained using the ZBL universal screening function (eq. 2.14) [21]; in this case eq. 2.45 must be rewritten as:

$$s_n(\epsilon) = \frac{\epsilon}{\pi a_U^2 \gamma E} S_n(E) \ , \tag{2.47}$$

and the reduced nuclear stopping cross-section is expressed as:

$$s_n(\epsilon) = \frac{\epsilon}{a_U^2} \int_0^\infty \sin^2\left(\frac{\theta_c}{2}\right) \mathrm{d}\left(p^2\right) \ . \tag{2.48}$$

Eq. 2.48 can be fit with the following formula for $\epsilon \leq 30$:

$$s_n(\epsilon) = \frac{0.5 \ln(1+1.1383\epsilon)}{\epsilon + 0.01321\epsilon^{0.21226} + 0.19593\epsilon^{0.5}} \ , \tag{2.49}$$

while for the high energy regime (not normally used in FIBs) a good fit is:

$$s_n(\epsilon) = \frac{\ln(\epsilon)}{2\epsilon} \ . \tag{2.50}$$

Warning: If the ZBL universal potential is used, a_{TF} must be substituted by a_U in eq. 2.39, so that eq. 2.41 becomes:

$$\epsilon = \frac{32.53 M_2 E_1}{(M_1+M_2) Z_1 Z_2 \left(Z_1^{0.23} + Z_2^{0.23}\right)} \ . \tag{2.51}$$

Electronic Stopping Looking at any of the proposed expressions for $s_n(\epsilon)$ (equations 2.46, 2.49 and 2.50), it appears that the nuclear stopping power decreases with increasing ion energy/velocity[7]. Moreover, the more the ion velocity v_1 approaches the Bohr velocity $v_B (= 2.2 \times 10^6 \mathrm{m/s})$ multiplied by $Z_1^{2/3}$, the more it can be regarded as a positive point-charge Z_1, whose impact on an atom results in a sudden energy transfer to the atom's electrons. The 'continuous slowdown approximation', which has been widely used, recognises two different energy regimes: the electronic stopping power increases from zero, passes through a maximum when the incident velocity v_1 is of the order of the orbital velocities of lattice electrons ($\approx Z_2^{2/3} v_B$), and then falls off inversely as the first power of energy. While in FIB microscopy ion velocities greater than $v_B Z_2^{2/3}$ are not usually reached[8], electronic losses should not be neglected already for $v_1 \approx 0.1 v_B$. For

---

[7] Remember that the ion velocity is proportional to the square root of its energy.

[8] Incidentally, this is the reason why Ga^+ ions with an incident energy of tens of keV have too low a velocity to excite X-rays, which is not true for electrons in the same energy range: X-rays excitation requires the incident velocity to be in the same order as that of the target atom shell electrons.

this lower velocity regime, Lindhard *et al.* derived an expression for the electronic stopping power that is proportional to v_1 [34]:

$$-\left(\frac{\mathrm{d}E}{\mathrm{d}R}\right)_e = K_L\sqrt{E} = N_a S_e\left(E\right) \ , \tag{2.52}$$

which, in dimensionless units, is written as:

$$-\left(\frac{\mathrm{d}\epsilon}{\mathrm{d}\rho}\right)_e = s_e\left(\epsilon\right) = k_L\sqrt{\epsilon} \ , \tag{2.53}$$

where

$$k_L = Z_1^{1/6}\frac{0.0793Z_1^{1/2}\left(M_1+M_2\right)^{3/2}}{\left(Z_1^{2/3}+Z_2^{2/3}\right)^{3/4}M_1^{3/2}M_2^{1/2}} \tag{2.54}$$

and

$$K_L = k_L\sqrt{\frac{E}{\epsilon}}\left(\frac{\rho}{R}\right) \ . \tag{2.55}$$

S_e (s_e) is the *(reduced) electronic stopping cross-section.*

Total Stopping Power When calculating the total stopping power of an energetic ion impacting the target, the assumption that is usually made is that nuclear and electronic losses are completely independent from each other. In this case, the total stopping power is just the sum of the two nuclear and electronic components. In dimensionless units:

$$-\frac{d\epsilon}{d\rho} = \left[s_n\left(\epsilon\right)+s_e\left(\epsilon\right)\right] \ ; \tag{2.56}$$

and in practical units:

$$-\frac{\mathrm{d}E}{\mathrm{d}R} = -\left(\frac{\mathrm{d}E}{\mathrm{d}R}\right)_n - \left(\frac{\mathrm{d}E}{\mathrm{d}R}\right)_e = N_a\left[S_n\left(E\right)+S_e\left(E\right)\right] \ . \tag{2.57}$$

The stopping power, therefore, can be seen as the cumulative effect of statistically independent scattering events between incident ion and target atoms, and each event can be written as:

$$-\left(\frac{\mathrm{d}E}{\mathrm{d}R}\right)_i = -\left(\frac{\mathrm{d}\epsilon}{\mathrm{d}\rho}\right)_i\left(\frac{\rho/R}{\epsilon/E}\right) \ , \tag{2.58}$$

where the subscript i can either stand for n, or for e.

2.1.3.4 Ion Range and Range Distributions

So far, the general theory of ion/matter interaction has been presented, together with the main equations that have been used, in the literature, to calculate stopping powers and distributions of ions into the target bulk. The knowledge of the ions' distribution inside the target, as well as the estimation of the fraction of them that leave the target either as transmitted or backscattered ions, is important not only in FIB semiconductor fabrication by ion implantation, but also in FIB microscopy. The 'interaction volume' of the ions into the target determines, on the one hand, the area on the sample surface from which secondary emission occurs (see chapter 3, and, on the other hand, the amount of subsurface damage that is an unwanted effect always present in FIB imaging. Moreover, the stopping power plays a role in the amount of sputtering of surface target atoms. In following chapters it will be shown that the resolution obtainable with a FIB microscope derives from a compromise between secondary electron signal and sputtering of the target surface. Therefore, the way the energetic ions interact with the target atoms ultimately determines the resolution of any ion microscope. While the electronic stopping power can be seen as a kind of viscous friction that slows down the ion in a continuous fashion, the nuclear stopping power, which is largely dominant for the usual energies of few tens of keV, is intrinsically discrete. From each collision event the ion emerges with, in general, a different absolute velocity and a different direction of motion, so that its path into the target bulk appears, at the atomic scale, as a broken line (just like in fig. 2.4). The actual distance covered by the ion is the 'range' R, which can be estimated, as a function of the stopping

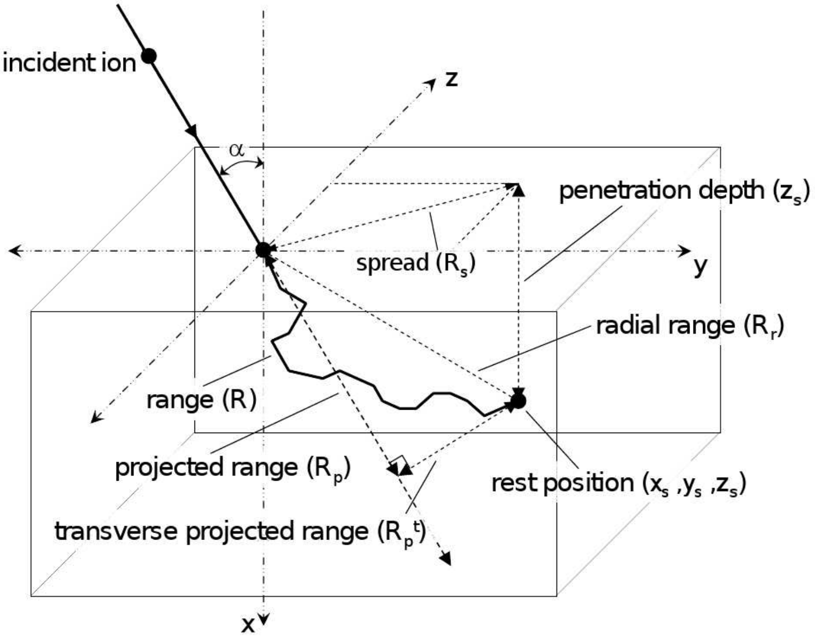

Figure 2.4: Coordinate system and range definitions for an ion impinging onto the target.

power, with the following formula [3]:

$$R\left(E\right) = \int_E^0 \frac{\mathrm{d}E}{\mathrm{d}E/\mathrm{d}R} = \int_0^E \frac{\mathrm{d}E}{N_a\left[S_n\left(E\right)+S_e\left(E\right)\right]} \ . \tag{2.59}$$

Better equations can be found in literature, but the best way for estimating ion ranges (and range distributions, that will be shortly introduced) is through Monte Carlo simulations. Two codes employing Monte Carlo methods will be presented at the end of this chapter. It is important, however, to precisely define the quantities that describe the range and the distributions of the implanted ions into the target bulk, in order to avoid confusion. Fig. 2.4 shows an ion entering into the target at the position $(0, 0, 0)$ and coming to rest inside the bulk at the position (x_s, y_s, z_s), with an incident angle α, defined as the angle between the ion beam direction and the direction normal to the sample surface. With referiment to the single ion in the picture, the following quantities are defined:

- **Range** - R: actual distance traveled by the ion;
- **Radial Range** - R_r: Cartesian distance between the entrance point $(0, 0, 0)$ and the rest point (x_s, y_s, z_s)

$$R_r = \left(x_s^2 + y_s^2 + z_s^2\right)^{1/2} \ ; \tag{2.60}$$

- **Spreading Range** - R_s: projection of R_r onto the surface plane $x = 0$

$$R_s = \left(y_s^2 + z_s^2\right)^{1/2} \ ; \tag{2.61}$$

- **Transverse Projected Range** - R_p^t: projection of R_r onto the direction normal to the beam direction

$$R_p^t = \left[\left(x_s \sin\alpha - y_s \cos\alpha\right)^2 + z_s^2\right] \ ; \tag{2.62}$$

- **Projected Range** - R_p: projection of R_r onto the beam direction;

$$R_p = \left[\left(\left(R_r\right)^2 - \left(R_p^t\right)^2\right)^2\right]^{1/2} \ . \tag{2.63}$$

Note that, for normal-incident ions ($\alpha = 0$), $R_s = R_p^t$ and $R_p = x_s$. Of course, each implanted ion, even when characterised by the same values of α and E, will have a different range, ultimately dependent on a series of random events (the elastic and/or inelastic collisions). All the quantities defined in equations 2.59-2.63, therefore, must be regarded as stochastic, and for each of them a statistical distribution is in fact observed. For each of these distributions the moments up to the fourth order are usually employed to characterise the interaction volume within the target. Once again, in order to avoid confusion, it is a good idea to expressly define the most used of these moments in terms of the Cartesian coordinate system of fig. 2.4. The following definitions are the ones used in the simulation program SRIM/TRIM (sec. 2.2.1) [35], and are given, for simplicity of notation, in the case of normal incidence. For the first moments it is customary to use the same symbols of the stochastic variable itself, without expressly indicating that they are mean values; the subscript i refers to the i^{th} ion, N_i being the total number of ions. Attention must be paid to the fact that, also because all the distributions obtained with TRIM are rotationally symmetric around the beam direction (which is coincident with the x-axis when $\alpha = 0$), the terms 'radial' and 'lateral' appearing below have not the same meaning of the terms 'radial' and 'transverse' used above, and in fig. 2.4. Their meaning however, should be clear.

- **First Moments**
  - mean projected range:

$$R_p = \frac{1}{N_i} \sum_i x_{s,i} \quad = \quad < x_s > ; \tag{2.64}$$

  - lateral projected range:

$$R_y = \frac{1}{N_i} \sum_i |y_{s,i}| \quad = \quad < |y_s| > ; \tag{2.65}$$

  - radial range:

$$R_r = \frac{1}{N_i} \sum_i \left(y_{s,i}^2 + z_{s,i}^2\right)^{1/2} \quad = \quad < r_s > \ . \tag{2.66}$$

- **Second Moments**
  - straggling:

$$\sigma_p = \left(\frac{1}{N_i} \sum_i x_{s,i}^2 - R_p^2 \right)^{1/2} \quad = \quad < (x_s - R_p)^2 >^{1/2} ; \tag{2.67}$$

  - lateral straggling:

$$\sigma_y = \left[\sum_i \left(\frac{|y_{s,i}| + |z_{s,i}|}{2} \right)^2 \right]^{1/2} \quad \approx \quad < y_s^2 >^{1/2} ; \tag{2.68}$$

  - radial straggling:

$$\sigma = \left(\frac{1}{N_i} \sum_i x_{s,i}^2 - R_r^2 \right)^{1/2} \quad = \quad < (r_s - R_r)^2 >^{1/2} \ . \tag{2.69}$$

- **Third Moment**
  - skewness:

$$\gamma_p = \sum_i \frac{(x_{s,i} - R_p)^3}{N_i \sigma_p^3} \ . \tag{2.70}$$

- **Fourth Moment**
  - kurtosis:

$$\beta_p = \sum_i \frac{(x_{s,i} - R_p)^4}{N_i \sigma_p^4} \ . \tag{2.71}$$

The skewness defines the relationship between mean and mode in the range distribution: if the skewness is negative then the mode is higher than the mean (i.e. most ions are at rest deeper into the target then the mean depth of the distribution), and vice versa.
The kurtosis relates to the extent of the tails of the distribution; a Gaussian distribution has a kurtosis of 3; as a rule of thumb, a kurtosis between 0 to 3 indicates short tails, while a kurtosis greater than 3 indicates broad tails.

2.1.4 Ion-Induced Secondary Electron Emissions

Of all the secondary species emitted by a sample under ion irradiation (see fig. 2.1), the most abundant ones are, generally, the Secondary Electrons (SE): SE contrast is the most common contrast mechanism used to build images with FIB microscopes. The topic of SE emission is therefore a central one in ion microscopy, because any attempt to interpret a scanning ion image would fail without proper qualitative and quantitative knowledge of the contrast response of the system sample/beam. The subject will be widely covered in chapter 3, with special focus on the dependence of the ion-induced SE yield δ_i (number of SEs per incident ion) on the beam incidence angle, which is at the basis of what I call ‘first order SE contrast’. Before entering into the realm of experimental measurement of SE yields, I shall outline here the basic theory of Ion-Induced Secondary Electron Emission, mainly following the exposition of K. Ohya and T. Ishitani in [13].

Emission of Secondary Electron induced by ion bombardment may proceed via two independent effects, which differ for the mechanism of energy transfer from the incident to the electrons of the solid.

2.1.4.1 Potential Emission

If the potential energy of the ion is twice or more the work function of the solid, SE emission may proceed via resonance neutralisation and subsequent Auger deexcitation or Auger neutralisation. This process, called *Potential Emission*, takes place in front of the solid surface, at low energies (several keV), and, as long as only single charged ions are involved, an empirical formula for the SE yield has been proposed by Baragiola *et al.* [36]:

$$\delta_{i,p} = 0.032\,(0.78E_i - 2\phi)\ , \tag{2.72}$$

where E_i is the ionisation potential of the projectile and ϕ is the work function of the solid surface, both in units of eV. Since Potential Emission requires $E_i \geq 2\phi$, it does not play a role in the case of Ga^+ bombardment, since the ionisation potential for Gallium is ~ 6eV, and for normal metals $\phi \sim 4-5$eV (see sec. 3.3.2)

2.1.4.2 Kinetic Emission

In addition to the mechanism described above, SEs can also be excited within the solid for direct transfer of kinetic energy, and the SEs excited near the surface may be emitted if their energy is higher than the Surface Binding Energy (SBE). This mechanism, called *Kinetic Emission*, is the major (if not only) source of SEs at medium and high energies, and can be described by a three-stage process:

1. production of SEs within the solid;
2. migration of some of these SEs to the surface;
3. escape of some of these migrated SEs through the surface.

The mechanism of ion-induced kinetic emission is very similar to the one of electron-induced SE emission, the main difference being in SEs production stage, while the other important parameters (energy-loss rate, mean free path, magnitude and shape of the surface barrier) are of course common for both processes. In particular, since at a given primary energy the velocity of ions is two or three order of magnitude lower than the one of electrons, the electron-induced SE yield δ_e has a maximum for energies below 1 keV, while the maximum of the ion-induced SE yield δ_i is at energies of hundreds of keV. As a result, at the normal operative energies (few tens of keV), δ_e decreases for increasing primary energy, while the opposite happens for δ_i. In general, the energy dependence of δ_i closely resembles that of the electronic stopping power for fast light ions, but no simple relation holds for slow heavy ions.

Excitation of Secondary Electrons The excitation of SEs can occur with three different collision processes, and each can be characterised by a partial SE yield:

- collisions between projectile ion and target electrons ($\rightarrow \delta_{i,i}$);
- collisions between recoiled target atoms and target electrons ($\rightarrow \delta_{i,r}$);
- collisions between excited SEs and other target electrons ($\rightarrow \delta_{i,e}$).

And each of these collision processes can give rise to different excitation mechanisms:

- direct impact excitation of single conduction electrons (electrons from the ‘Fermi sea’);
- creation of plasmons in real metals (for energies above an ion/target dependent threshold energy), whose decay leads to excitation of conduction electrons;
- direct impact excitation of core electrons, whose vacancies are immediately filled by outer electrons.

For heavy ions with velocity smaller than the Bohr velocity v_B, electron promotion is the dominant mechanism: temporary molecules can be formed, lifting up electrons to higher energy levels, thus producing inner-shell vacancies that may lead to electron emission via Auger transitions. In this case, the inverse Mean Free Path (MFP) of a primary ion or of a recoiled atom is calculated as [13]:

$$\begin{aligned}\frac{1}{\lambda} &= \frac{3\pi n v}{4\sqrt{2}v_F^2}\sum_{l=0}^{\infty}\sum_{m=0}^{\infty}(2l+1)\times\\ &\quad\times\left\{1-\cos 2\delta_l\left(E_F\right)-\cos 2\delta_m\left(E_F\right)+\cos\left[2\left(\delta_l\left(E_F\right)-\delta_m\left(E_F\right)\right)\right]\right\}\times\\ &\quad\times\int_{-1}^{1}\sqrt{1-x}P_l(x)P_m(x)\mathrm{d}x\ ,\end{aligned} \tag{2.73}$$

where $\delta_{l,m}$ are the phase shifts for the scattering of a conduction electron at the Fermi energy E_F by the potential of the ion/atom at rest, n is the density of conduction electrons and $P_{l,m}$ are the Legendre polynomials.

Transport of Secondary Electrons Excited electrons traveling in a material may lose their energy due to different mechanisms.

- Inelastic collision with other electrons, which may also cause other electron excitations. This mechanism is very efficient in metals, where the stopping power for electrons has a maximum between 100eV and 1keV, and depends on the density of conduction electrons.
- Collisions with atoms through their density fluctuations (phonons). This is the dominant (and rather inefficient) mechanism in insulators, where electrons which posses less energy than the energy gap E_g cannot lose energy by electronic excitation.
- Elastic scattering, caused mainly by atoms (but also, occasionally, by electron-electron collisions), which leads to directional changes. This mechanism is responsible for a completely isotropic distribution of SEs in the solid.

Escape of Secondary Electrons In order to be emitted from the target surface into the vacuum, SEs have to overcome the SBE E_{surf}, which has different expressions for metals and insulators.

Atomic Species	E_{th} [keV]
Al	10.7
Cu	18.8
Au	26.6

Table 2.1: Threshold energies E_{th} for kinetic secondary emission for Ga^+ on Al, Cu and Au [13].

- **Metals**
  For metallic targets, $E_{surf} = \phi + E_F$. The kinetic emission occurs if the projectile ion gives a conduction electron sufficient velocity in the direction normal to the surface plane to overcome the SBE barrier. Doing the maths, one finds that the minimum beam energy that give rise to electron emission is:
  $$E_{th} = \frac{1}{8} M_1 v_F^2 \left(\sqrt{1 + \phi E_F} - 1 \right)^2 , \tag{2.74}$$
  v_F being the Fermi velocity. The values of E_{th} for gallium ions on three common metals are listed in table 2.1; these values are quite funny, because SE emission is normally observed also at only a few keV! This problem can be 'numerically' solved with newly developed electron-promotion mechanisms [37], or simply[9] modeled with a reduction of the surface barrier energy [38]. It remains, however, quite a puzzle at the moment of writing.

- **Insulators**
  In this case, the surface barrier E_{surf} is determined by the electron affinity, whose value usually lies between 0 and 1eV. The average electronic stopping power is similar for metals and insulators with similar atomic numbers, but the energy lost by slow electrons migrating towards the surface and the magnitude of the SBE are much smaller, with the result that δ_i for insulator is normally much larger than δ_i for metals of similar atomic numbers [13].

In general, δ_i is quite a strong function of the target atomic number ($\delta_i = f(Z_2)$) and of the beam incidence angle ($\delta_i = f(\alpha)$). This is fundamental in ion microscopy, for the first dependence is what produces material contrast, while the second dependence is responsible for the topographical contrast. The way δ_i varies with Z_2 has not been tackled in this PhD project, but several discussions can be found in literature, for example in [39] and in [40]. The function $\delta_i = f(\alpha)$, on the other hand, will be the subject of the entire chapter 3, as anticipated already.

Other parameters that are important to describe the SE emission, other than the SE yield, are the energy and the angular distribution of the emitted electrons. A formula that is often used to estimate the number of electrons per unit energy is [40]:

$$\frac{\mathrm{d}N_e(E)}{\mathrm{d}E} = k \frac{E - E_F - \phi}{(E - E_F)^4} , \tag{2.75}$$

---

[9] Here, 'simply' means 'with little physical meaning'.

where N_e is the number of electrons and k is a material dependent constant. The angular distribution, on the other hand, is normally approximated with a cosine distribution:

$$N_e(\theta) = N_{e,0} \cos\psi \ , \tag{2.76}$$

where ψ is measured normal to the target surface, so that $N_{e,0}$ is the number of electrons emitted perpendicularly from the target.

2.1.5 Sputtering from Ion Impact

In the previous section it has been pointed out that, at the typical energies of few tens of keV used in FIB microscopy, elastic collisions are dominant over inelastic ones. When a target atom is displaced due to the impact with the projectile ion, it will in turn start moving inside the bulk, very likely colliding with other atoms, that are in turn displaced from their position: an avalanche starts inside the target, what is usually called a 'collision cascade'. While the majority of these recoiled atoms will eventually get at rest somewhere inside the bulk (contributing to its disorder increasing the number of punctual defects like vacancies and interstitials), a fraction of those that are set in movement close enough to the sample surface, namely the ones that have enough velocity in the direction of the surface, might eventually leave the target, as neutral or charged particles. The removal of atoms from the target surface due to the energy transfer from the impinging ions is called 'sputtering'[10]. This ability to modify the sample surface almost at the atomic level is indeed what gave the FIB the status of indispensable nanofabrication/nanomodification tool. This same ability is, however, a real problem when it comes to FIB imaging, and it is indeed the very reason why FIBs have been used for microscopy only marginally, at least up to the arrival of light ion sources, in which the sputtering power is strongly reduced when compared with the classical Liquid Metal Ion Sources (LMIS). In the course of this PhD project, the quantitative knowledge of the sputtering for given imaging conditions has been of primary importance for the characterisation of ion microscopes. Even thought this knowledge has been always obtained either experimentally or via Monte Carlo simulations, I believe that it is useful to give at this point a very short overview of the theoretical work that has been done on the subject. Be it only for the satisfaction of having an idea of how the simulation program pull out the numbers we need! Like most of the material in this 'background' chapter, I am not going to say here much more than what is already in books, and in particular in [32] and [3]; a good qualitative discussion can also be found in [39]. Modelling the sputtering is a rather complex matter, for the amount of ejected target atoms depends on a great number of factors, related to the primary ions, to the sample materials and structure, and to the qualities of ejected atoms. To name the main ones:

- **Factors related to the incident beam:**
    - ion mass;

---

[10] 'Physical sputtering', to be precise, as opposed to chemical sputtering; since the topic of chemical sputtering does not belong to this work, I will just refer to it as sputtering.

  - ion energy;
  - angle of incidence of the beam;
  - beam broadening;
  - ion dose rate;
  - clustering;

- **Factors related to the target structure and materials:**
  - masses of atoms;
  - fractions of atoms;
  - Surface Binding Energy;
  - conductivity;
  - surface curvature;
  - degree of crystallinity;
  - crystal orientation.

- **Factors related to ejected atoms:**
  - energy distribution;
  - angular distribution;
  - chemical affinity with the target surface;
  - clustering.

A model successfully used to describe the phenomenon of sputtering is the so-called 'Linear Collision Cascade' (LCC) model, developed by Sigmund in the late 60's [41]. According to the LCC model, energy and momentum are transferred to the target via a cascade of binary collisions between primary ions and target atoms and between recoiled atoms and stationary atoms. Sputtering happens when an atom near the surface is given enough energy to overcome the SBE of the solid. Aim of the LCC model is giving quantitative predictions of sputtering yields γ (defined, analogously to the SE yields, as the average number of sputtered atoms per incident ion) as a function of primary energy, angle of incidence, mass and atomic number of ions and target atoms. Assuming a smooth and amorphous target, and using Boltzmann's equation and general transport theory, Sigmund derived a formula for the number of recoiling atoms ($\mathrm{d}N_a$) per unit of energy of the primary ions (E) arriving to the surface at an angle ψ (the same angle of eq. 2.76) with energy between E_a and $E_a + \mathrm{d}E_a$ and within the solid angle $\mathrm{d}\Omega$:

$$\frac{\mathrm{d}^3 N_a}{\mathrm{d}\Omega \mathrm{d}E_a} = \frac{3}{2\pi^2} \frac{\beta\left(\frac{M_1}{M_2}\right) S_n\left(E\right)}{C_0} \frac{\cos\psi}{E_a^2} , \tag{2.77}$$

where β is a dimensionless factor dependent on M_1/M_2 and $C_0 = 1.81\text{Å}$. For normal incidence, in the range of keV, β can be approximated by:

$$\beta = 0.15 + 0.13\frac{M_2}{M_1} . \tag{2.78}$$

According to the Sigmund theory, the sputter yield is a function of the primary energy E, the incidence angle α and the depth of sputtering surface from the ion entering point, t:

$$\gamma\left(E,\alpha,t\right)=\frac{4.2\times10^{14}F_D\left(E,\alpha,t\right)}{N_aE_{surf}}\ , \tag{2.79}$$

where N_a is the target density, E_{surf} is the SBE, and F_D is the depth distribution of the deposited energy. Integrating over α between 0 and $\pi/2$, the total sputter yield as a function of primary energy E is obtained:

$$\gamma_{tot}\left(E\right)=\frac{4.2\times10^{14}\beta\left(\frac{M_2}{M_1}\right)S_n\left(E\right)}{N_aE_{surf}}\ , \tag{2.80}$$

where $\beta\left(M_2/M_1\right)$ is given by eq. 2.78, and $S_n\left(E\right)$ is calculated as:

$$S_n\left(E\right)=8.462s_n\left(\epsilon\right)\frac{M_1}{M_1+M_2}\frac{Z_1Z_2}{\left(Z_1^{2/3}+Z_2^{2/3}\right)^{1/2}}\ . \tag{2.81}$$

For s_n expression 2.46 can be used. More accurate expression for the sputter yield than eq. 2.79 can be found in [42] and [43].

Sputter Yield Dependence on the Beam Incidence Angle In assumption of 'isotropicity' (and thus polycrystallinity) of the target, the LCC model gives for the sputter yield the following dependence on the beam incidence angle α:

$$\gamma\left(E,\alpha\right)=\gamma\left(E,0\right)\cos^{-f}\left(\alpha\right)\ , \tag{2.82}$$

f being a constant that mainly depends on M_2/M_1. As it will be shown in chapters 5 and 6, eq. 2.82 works quite well up to $\alpha=0.3-0.4\pi$, but then the real yield drops, to reach 0 at $\pi/2$[11], while γ from eq. 2.82 steeps up to infinity. In general, however, the morphology of the surface strongly influences the amount of sputtering, so that the reproducibility of measured sputter yields curves is usually quite low. Also, it must be kept in mind that in crystalline targets there can be very specific directions of reduced sputtering, due to the 'channeling'. An ion can 'channel' into the target if it strikes on it in a direction coincident with a low density crystallographic direction. In this case, the ion would reach higher-than-normal depths into the target bulk, thus not contributing to any surface emission. This phenomenon influences in exactly the same way the SE emission. Another theoretical expression for the dependence of γ on the incidence angle has been proposed by Yamamura [43]:

$$\gamma\left(E,\alpha\right)=\gamma\left(E,0\right)\cos^{-f}\left(\alpha\right)\mathrm{e}^{-S\left(1/cos\alpha-1\right)}\ , \tag{2.83}$$

where S and f are adjustable parameters. Of course, eq. 2.83 is more accurate than eq. 2.82 over a wider angle range, but one additional parameter is the price to pay

---

[11] Mainly because at high angles many ions are just bounced off the surface without even penetrating it.

for it.

Angular Distribution of Sputtered Atoms The angular distribution of the sputtered atoms is usually assumed to be of the Sigmund-Thompson type [41]:

$$\frac{\mathrm{d}^3\gamma}{\mathrm{d}E_a\mathrm{d}\Omega} \propto \frac{E_a}{(E_a + E_{surf})^{3-2m}} \cos\psi \ , \tag{2.84}$$

where m is an adjustable parameter (close to 0).

2.2 Monte Carlo Simulations

As I have already mentioned a few times in this chapter, the high number of ions that reach the target each second, in typical FIB imaging conditions, requires that a statistical approach must be used in order to calculate the range and the range distribution of the ions into the sample, the sputtering of target atoms, and the emission of secondary species. The very nature of the ion/matter interaction, i.e. many ions undergoing a series of elastic and/or inelastic collisions, each ion entering the collision and emerging from it with its own velocity, each collision characterised by a different impact parameter, etc., seems crying for a so-called Monte Carlo approach. Since Monte Carlo algorithms are not my field of expertise, I shall quote the Wikipedia entry at the time of writing (22 March 2011):

> "*Monte Carlo methods* (or *Monte Carlo experiments*) are a class of computational algorithms that rely on repeated random sampling to compute their results. Monte Carlo methods are often used in simulating physical and mathematical systems. These methods are most suited to calculation by a computer and tend to be used when it is infeasible to compute an exact result with a deterministic algorithm."

In other words, using a Monte Carlo approach means estimating the behaviour of a physical system, characterised by a very high number of elements of a kind, variously coupled with each other, by simulating the behaviour of a sample of these elements, each starting its evolution with slightly different initial conditions. Should this not be clear enough, here a quote from one of the few books tackling the problem of Monte Carlo modeling for electron microscopy, from D.C. Joy [16], which in turns quotes one of the early papers published on the subject [44]:

> "By applying random sampling techniques to the problem [of interest] deductions about the behaviour of a large number of [electrons] are made from the study of comparatively few. The technique is quite analogous to public opinion polling of a small sample to obtain information concerning the population of the entire country."

Imagine, thus, that you want to know what is the mean depth at which a certain species of ions with a certain energy gets implanted into a given target; or that you want to estimate the average volume inside the target where the incoming ions move and interact; or still, that you want to know how many ions/atoms are transmitted/reflected per incident ion. What would you do? You could use a deterministic approach: you could build up your space of phases for the problem at hand, solve the interaction equations for each set of input values, and perform the statistic on all the possible outputs. This would work, but would also take a very long time, because the space of phases for an ion/matter interaction problem can be huge. But you could also do something smarter: you could define the set of possible interaction events, input the equations governing each event in the BCA framework (or in the MD framework, a subject that has not been covered into this thesis), define the probability of occurrence of each event, and shot an ion at time, deciding on the type of collision event on the basis of a random choice weighted on the occurrence probability of each event. And then you could shot one more ion, and then one more, up to a statistically meaningful number, and finally plot the outcome. This is more or less what Monte Carlo algorithms for ion/matter interaction do.
Several codes are available that implement Monte Carlo algorithms for ion/matter calculations using the LCC approximation. A rough distinction can be made according to the following classification:

- codes that *do not take* the dynamic compositional change into account;
    - amorphous targets;
    - crystalline targets;
- codes that *do take* dynamic compositional change into account;
    - amorphous targets;
    - crystalline targets.

In my opinion, the choice between a dynamic and a not-dynamic code is one of method. Dynamic algorithms should be used when the purpose of the simulation is miming the behaviour of a real system, thus for solving problems like ion dose-optimisation and imaging simulation. But if the purpose is estimating first-principle parameters, then the choice should fall on a non-dynamic code; for example: if i want to know what is the sputter yield for 30keV Ga^+ ions on amorphous carbon, I don't want my target to change into something different (i.e. a mix of carbon and gallium) after, let's say, 10,000 ions have been shot; I want my target to be carbon all the time, till the end of my simulation!
About the possibility of defining crystalline targets, that is a matter of complexity. Amorphous targets are completely homogeneous and isotropic, thus relatively simple to treat. Crystalline targets, on the other hand, can still be homogeneous, but certainly are not isotropic; ions impinging onto a crystalline target can channel, whereas this is not possible in an amorphous target. Also, the possible dynamic changes become more complex when the target is crystalline: the only effect of ions accumulating into an amorphous target is to change the relative abundance

of the elements involved (thus, something that can be modeled with a single parameter), while ions accumulating into a crystalline target do not only change is composition, but also the amount of amorphisation, because each implanted atom is a defect into the crystal. A short review of the main BCA and MD codes can be found in [32]. Here, I will limit myself to a brief introduction to the two codes which I have enjoyed during my PhD project.
The first one is SRIM, by J. Ziegler [35, 21], which falls into the first group of the above classification (non-dynamic, amorphous targets). I have used it mainly for obtaining sputter yields.
The second one is IONiSE, developed by the group of D.C. Joy [45]. IONiSE can be seen as an extension of SRIM, on which it is based for the stopping calculation; on top of SRIM, it implements the SE emission calculation, but only for helium primary ions.

2.2.1 SRIM/TRIM

SRIM, whose meaning is 'Stopping and Range of Ions in Matter', is a collection of softwares which calculate the energy losses and the range distributions of ions into matter, in the energy range 10eV/emu-2GeV/emu. The program is freely distributed by J. Ziegler on his website [35], and its main component is TRIM, an acronym that stands for 'Transport of Ions in Matter'. The two names are quite self-explicative: the main purpose of SRIM/TRIM is simulating the elastic/inelastic collisions between energetic ions and target atoms, and calculate for each collision the scattering angle θ, the recoil angle φ and the transferred energy T. To simplify it at the best of my 'summarising' capabilities, this is the way it works:

1. An ion begins its 'adventure' at the target surface plane with a certain energy E and a certain direction;

2. the ion travels into the target on a straight line for a length that is randomly chosen from a given distribution centered on the mean free path λ for the chosen ion/atom pair;

3. another random choice, weighted according to the ratio of occurrence probability between elastic and inelastic collisions, determines the kind of collision;

4. the new energy $E - T$ and the new ion direction are calculated; the scattering angle is obtained from the scattering integral (eq. 2.24) with a randomly chosen impact parameter, while the azimuth angle is completely random;

5. the ion begins its path towards the next collision, with a new energy, a new velocity and a new initial position, thus starting again from point 1;

6. if the collision is elastic, and if the transferred energy is greater than Lattice Binding Energy (LBE)[12], then the hit atom is displaced, and begins its

---

[12] In symbols: if $T > E_{lat}$.

own collision path, being treated just like an ion, thus starting from point 1, with initial energy T, initial direction determined by the recoil angle φ and random azimuth angle.

Thus, each impinging ion can, during its collision path, displace target atoms that in turn will begin their own collision path, possibly displacing even more atoms. A 'collision cascade' is generated into the target bulk. Each ion/atom is followed along its path till one of the following conditions is verified.

1. The ion's (atom's) energy becomes lower than E_{lat} $\rightarrow$
   $\rightarrow$ the ion (atom) sits at rest into the target bulk, and it is *discharged*[13];
2. the ion (atom) reaches the target *bottom* with a normal velocity component sufficient to overcome the SBE E_{surf} $\rightarrow$
   $\rightarrow$ the ion (atom) is counted as a *transmitted* ion (atom);
3. the ion (atom) reaches the target *surface* with a normal velocity component sufficient to overcome the SBE E_{surf} $\rightarrow$
   $\rightarrow$ the ion (atom) is counted as a *backscattered ion* (*sputtered atom*).

Of course things are more complicated than that; from the SRIM website, for example, you can discover that:

- statistical algorithms are implemented, which allow ions to make jumps between calculated collisions and then averaging the collision results;
- screened Coulomb potentials are implemented, together with exchange and correlation interactions between the overlapping electron shells;
- ions have long range interactions which enable creation of electron excitations and plasmons within the target;
- the targets'models include descriptions of the target's collective electronic structure and interatomic bond structure;
- the charge state of the ion within the target includes a velocity dependent charge state and long range screening due to the collective electron sea of the target.

Since SRIM is (luckily) often upgraded and improved, for a complete description of the model used for the calculations I refer to the website [35] and to the tutorial book *The Stopping and Range of Ions in Solids*, from J.F. Ziegler, J.P. Biersack and U. Littmark, in its 2003 edition [21]. In the book (which is also updated quite often, last edition in 2009), a complete description of the physical model is found, together with the SIM source code. The main basic features of SRIM/TRIM, or at least the ones that have been more useful for me during this work, are best

---

[13] If the target were crystalline and/or dynamic, than a displaced atom and/or an implanted ion could be a lattice punctual defect; neither a displaced atom nor a implanted ion has any effect in a static amorphous target.

explained through the pictures in this section. Maintaining the opinion that the code is indeed extremely useful and well written, I want to emphasise here the main two limitations that I would like to see overcome in the future:

- while TRIM accepts complex targets made of compound materials with up to eight layers, the layers always extend infinitely in the xy plane; I find this very limiting, for it makes it impossible to define lateral walls and/or vertical interfaces between different materials/compounds;
- TRIM does calculate target damage, sputtering, ionization, and phonon production, but *does not* implement SE emission mechanisms; thus it can not be used to simulate SE contrast nor to calculate SE yields.

To be fair, however, I must add here that the fact that the SRIM code is freely available makes it possible for developers to implement additional modules and routines that interface with and extend the capabilities of the main SRIM program. Available extra modules include, for example, a package for the statistical analysis of the range distributions, and a package that enables to define a finite ion spot on the target (the beam size in SRIM is always point-like). Also IONiSE, the code that partially solved the second one of the above mentioned limitations, is based on the TRIM code for the range calculation.

I shall conclude this section with a small SRIM/TRIM photo gallery. Fig. 2.5 shows the SRIM front page and input windows, while the TRIM input and output windows are in fig. 2.6. Figures 2.7 and 2.8 present some of the ion/matter interaction and distribution plots that are directly available in the TRIM output windows. Many other plots can be manually created from the several output files that are obtainable with TRIM.

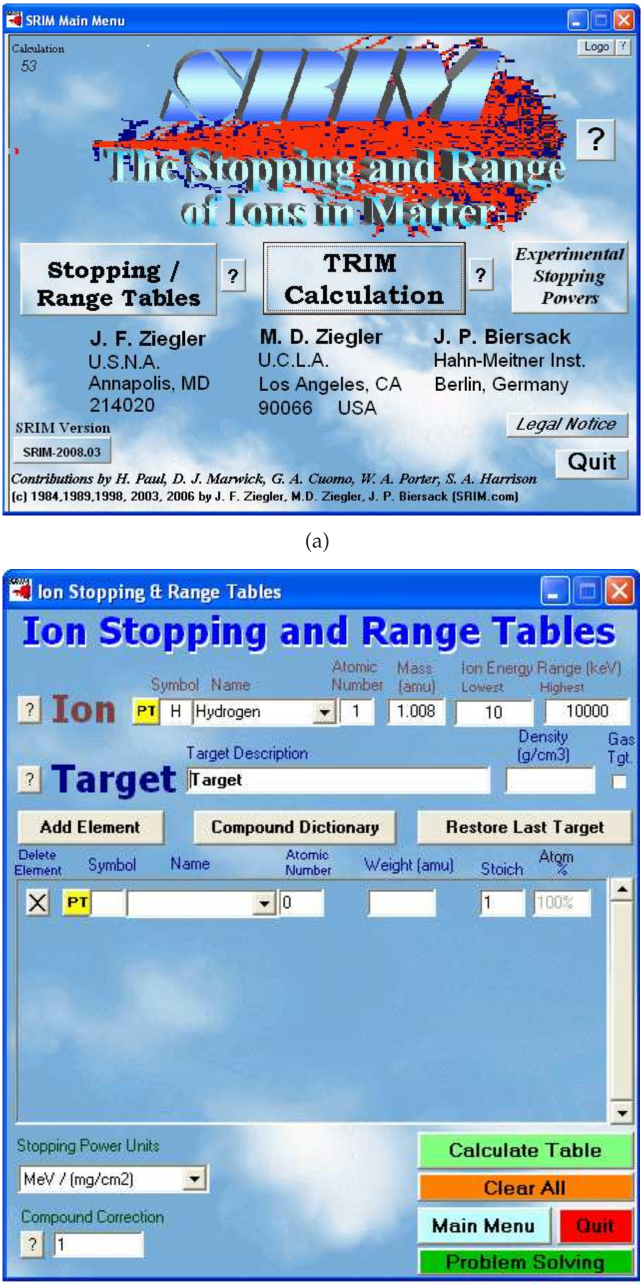

Calculation
53

J. F. Ziegler
U.S.N.A.
Annapolis, MD
214020

M. D. Ziegler
U.C.L.A.
Los Angeles, CA
90066 USA

J. P. Biersack
Hahn-Meitner Inst.
Berlin, Germany

SRIM Version
SRIM-2008.03

Contributions by H. Paul, D. J. Marwick, G. A. Cuomo, W. A. Porter, S. A. Harrison
(c) 1984,1989,1998, 2003, 2006 by J. F. Ziegler, M.D. Ziegler, J. P. Biersack (SRIM.com)

(a)

Ion: Symbol H, Name Hydrogen, Atomic Number 1, Mass (amu) 1.008, Ion Energy Range (keV) Lowest 10, Highest 10000

Target: Target Description Target, Density (g/cm3), Gas Tgt ☐

Delete Element	Symbol	Name	Atomic Number	Weight (amu)	Stoich	Atom %
☒	PT		0		1	100%

Stopping Power Units: MeV / (mg/cm2)

Compound Correction: 1

(b)

Figure 2.5: SRIM package front page (fig. 2.5(a)) and input interface of the SRIM module for the calculation of ion ranges and energy losses (fig. 2.5(b)), with fields for the ion and the target definition.

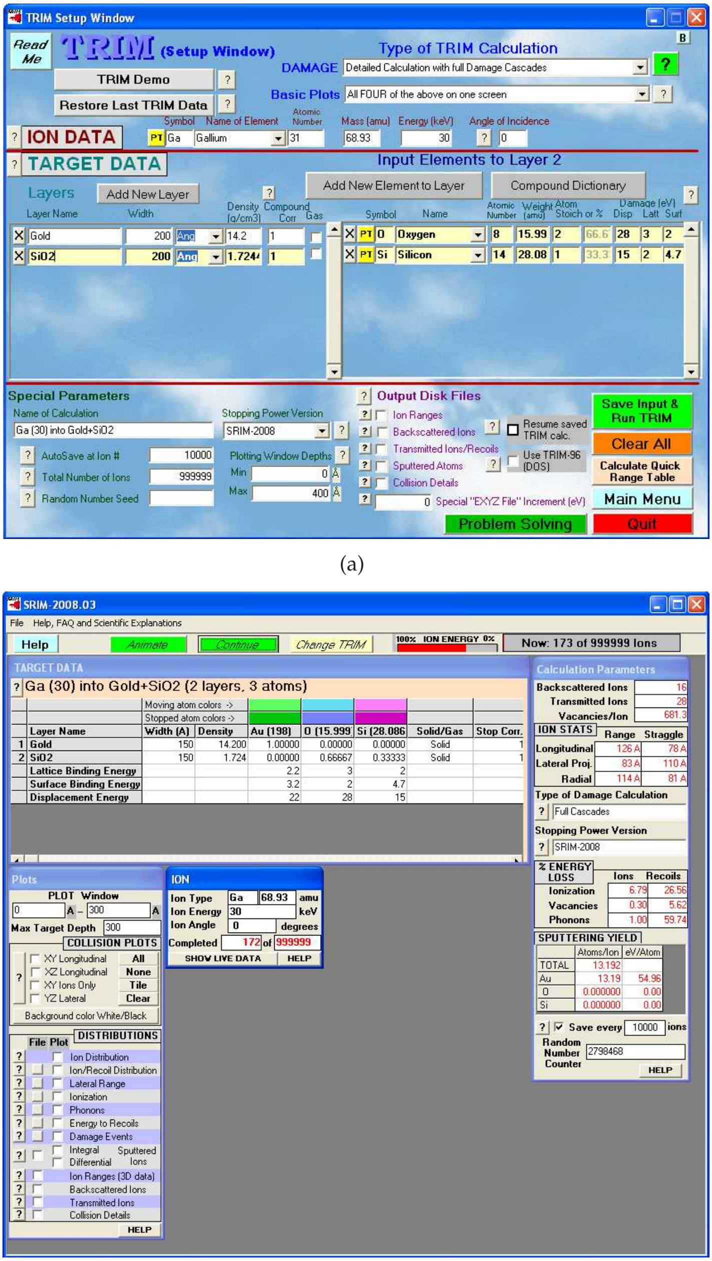

Type of TRIM Calculation
DAMAGE: Detailed Calculation with full Damage Cascades
Basic Plots: All FOUR of the above on one screen

ION DATA

Symbol	Name of Element	Atomic Number	Mass (amu)	Energy (keV)	Angle of Incidence
Ga	Gallium	31	68.93	30	0

TARGET DATA

Layers

Layer Name	Width		Density (g/cm3)	Compound Corr	Gas
Gold	200	Ang	14.2	1	☐
SiO2	200	Ang	1.724	1	☐

Input Elements to Layer 2

Symbol	Name	Atomic Number	Weight (amu)	Atom Stoich	or %	Damage (eV) Disp	Latt	Surf
O	Oxygen	8	15.99	2	66.6	28	3	2
Si	Silicon	14	28.08	1	33.3	15	2	4.7

Special Parameters
Name of Calculation: Ga (30) into Gold+SiO2
Stopping Power Version: SRIM-2008
AutoSave at Ion #: 10000
Total Number of Ions: 999999
Random Number Seed:
Plotting Window Depths: Min 0 Å, Max 400 Å

Output Disk Files
☐ Ion Ranges
☐ Backscattered Ions
☐ Transmitted Ions/Recoils
☐ Sputtered Atoms
☐ Collision Details
0 Special "EXYZ File" Increment (eV)
☐ Resume saved TRIM calc.
☐ Use TRIM-96 (DOS)

(a)

Now: 173 of 999999 Ions

TARGET DATA

Ga (30) into Gold+SiO2 (2 layers, 3 atoms)

	Layer Name	Width (A)	Density	Au (198)	O (15.999	Si (28.086	Solid/Gas	Stop Corr.
		Moving atom colors ->		🟩	🟦	🟪		
		Stopped atom colors ->		🟩	🟦	🟪		
1	Gold	150	14.200	1.00000	0.00000	0.00000	Solid	1
2	SiO2	150	1.724	0.00000	0.66667	0.33333	Solid	1
	Lattice Binding Energy			2.2	3	2		
	Surface Binding Energy			3.2	2	4.7		
	Displacement Energy			22	28	15		

Plots

PLOT Window: 0 A – 300 A
Max Target Depth: 300

COLLISION PLOTS
☐ XY Longitudinal
☐ XZ Longitudinal
☐ XY Ions Only
☐ YZ Lateral

DISTRIBUTIONS

File	Plot	
	☐	Ion Distribution
☐	☐	Ion/Recoil Distribution
☐	☐	Lateral Range
☐	☐	Ionization
☐	☐	Phonons
☐	☐	Energy to Recoils
☐	☐	Damage Events
☐	☐ Integral ☐ Differential	Sputtered Ions
☐		Ion Ranges (3D data)
☐		Backscattered Ions
☐		Transmitted Ions
☐		Collision Details

ION

Ion Type	Ga	68.93	amu
Ion Energy	30		keV
Ion Angle	0		degrees
Completed	172	of 999999	

Calculation Parameters

Backscattered Ions	16
Transmitted Ions	28
Vacancies/Ion	681.3

ION STATS	Range	Straggle
Longitudinal	126 A	78 A
Lateral Proj.	83 A	110 A
Radial	114 A	81 A

Type of Damage Calculation: Full Cascades
Stopping Power Version: SRIM-2008

% ENERGY LOSS	Ions	Recoils
Ionization	6.79	26.56
Vacancies	0.30	5.62
Phonons	1.00	59.74

SPUTTERING YIELD

	Atoms/Ion	eV/Atom
TOTAL	13.192	
Au	13.19	54.96
O	0.000000	0.00
Si	0.000000	0.00

☑ Save every 10000 ions
Random Number Counter: 2798468

(b)

Figure 2.6: TRIM input (fig. 2.6(a)) and output (fig. 2.6(b)) windows; the output window contains sub-windows showing the target parameters (up-left), the ion parameters (small window in the center), the possible output files/plots (down-left), and some calculation outputs (right).

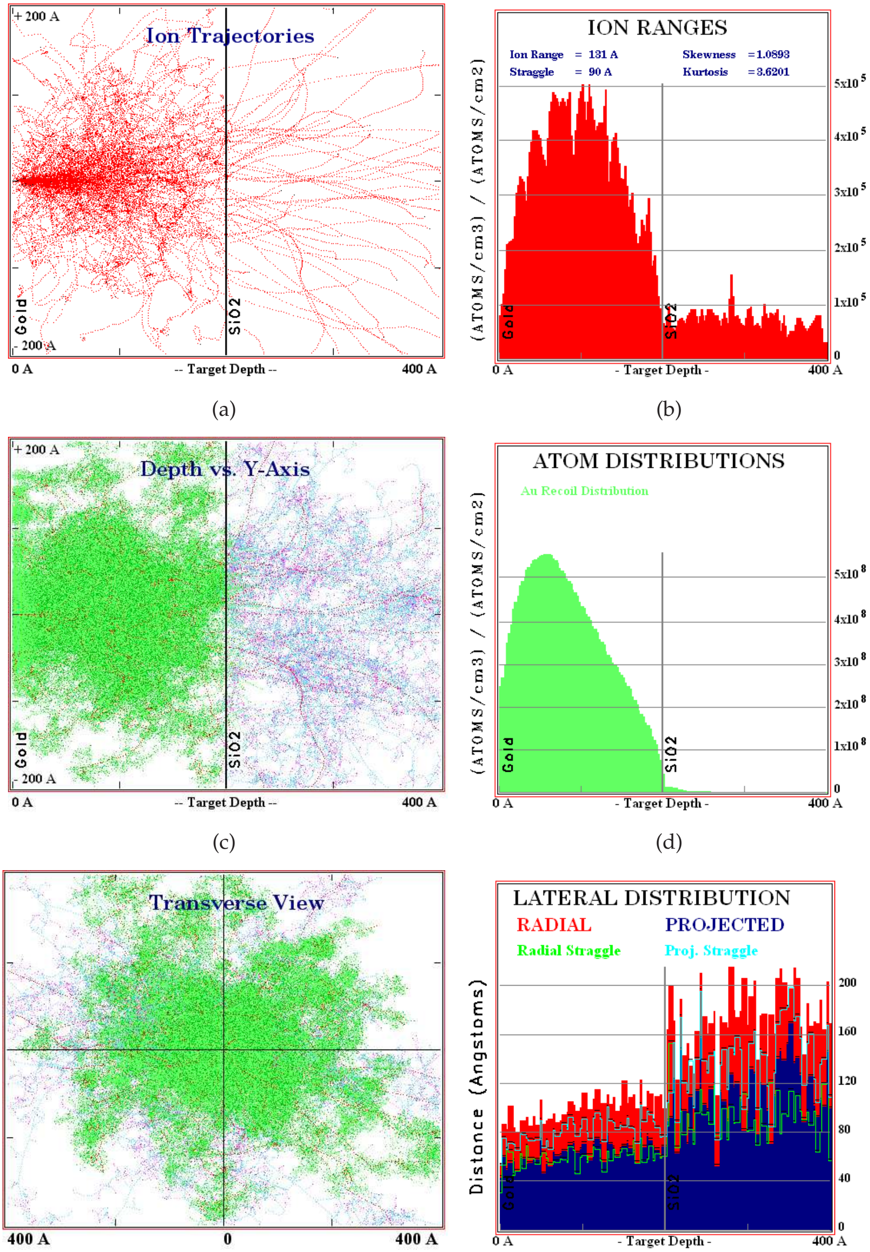

(a) (b) (c) (d) (e) (f)

Figure 2.7: TRIM's main plots and distributions: ions in the xy plane and ion range distribution (figures 2.7(a) and 2.7(b)); ions and recoils in the xy plane and recoil distribution (figures 2.7(c) and 2.7(d)); ions and recoils in the yz plane and ion lateral distribution (figures 2.7(e) and 2.7(f)).

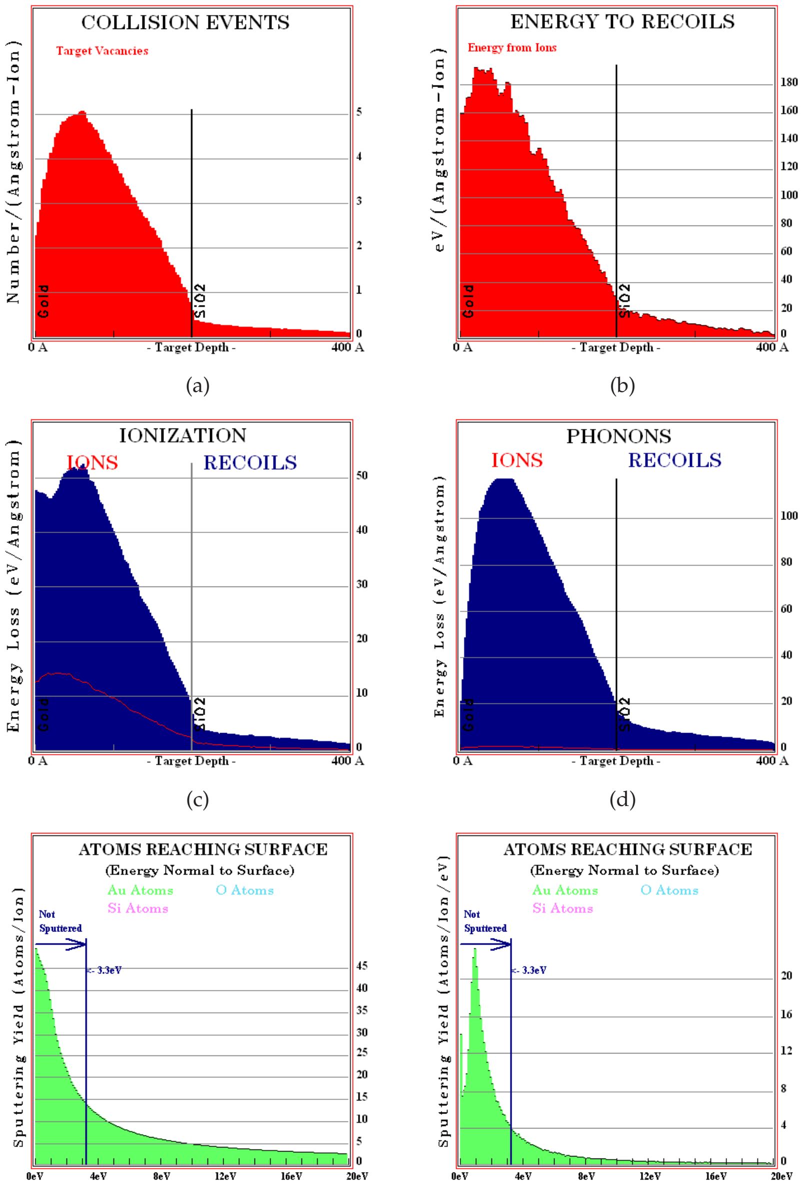

(a)

(b)

(c)

(d)

(e)

(f)

Figure 2.8: Other distributions that are directly obtainable in the TRIM output window: vacancies created into the target per incident ion (fig. 2.8(a)); energy transferred from ions to recoils per incident ion (fig. 2.8(b)); energy lost into ionisation and atomic vibrations (figures 2.8(c) and 2.8(d)); integral and differential energy distributions of atoms reaching the surface (figures 2.8(e) and 2.8(e)).

2.2.2 IONiSE

IONiSE is a small piece of software, developed by R. Ramachandra, B. Griffin and D. Joy [45], that saved my day when I needed SE emission yields data and I had no time and/or possibility to obtain them experimentally[14]. It is freely available on request to the authors as an executive file ready to run on Windows systems. The calculation of energy loss, range and sample damage in IONiSE is entirely based on TRIM, so there is nothing new to say about that. What makes IONiSE very valuable (at least for me), is the fact that it implements a model for ion-induced SE emission, although only for He ions in the keV energy range, on a variety of targets. Referring to [45] for the physical and the mathematical details of the model, what is important to know is that the iSE emission calculation is based on two principles developed in the '40s, and generally valid for electrons as well as for ions:

1. in [46], H.A. Bethe proposed that the rate of production of SEs is proportional to the stopping power of the incident ions according to a scaling factor $1/\epsilon$, ϵ being the 'Bethe parameter';
2. in [47], H. Salow suggested that SEs escape from the target via a diffusion process, characterised by an effective electron diffusion length λ, also referred to as 'Salow parameter'.

Before moving, for a taste of the code's potential, to the little IONiSE photo gallery that concludes this section (figures 2.9(a)–2.10(b)), there is one more feature of IONiSE that is worth mentioning. The target definition in IONiSE is even more basic that in TRIM. In the version of the code that I have used (1.8 Beta 08-20-2008) there is no compound data base, nor there is the possibility to define multilayers. It is known, however, that the SE emission is strongly dependent on the local surface morphology, and IONiSE gives the possibility to define rectangular bumps or cavities at the point of impact of the beam, which is not possible with SRIM/TRIM.

---

[14] SE yield measurements are very time consuming, as it will clearly appear from chapter 3, almost entirely dedicated to this subject.

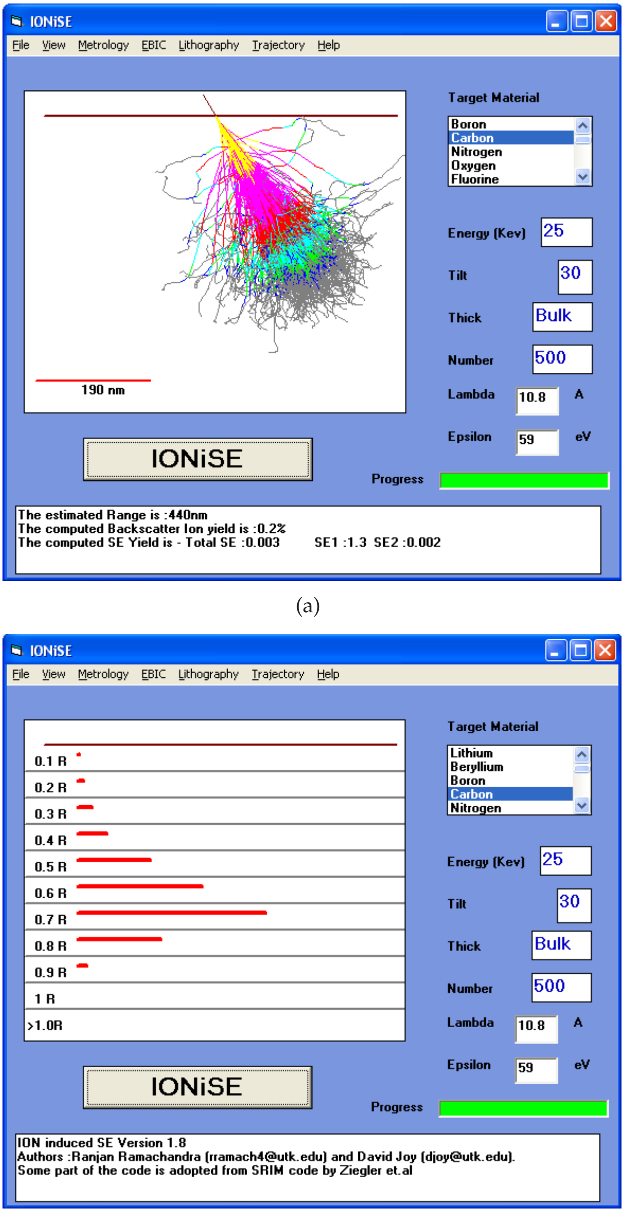

Target Material: Boron, Carbon, Nitrogen, Oxygen, Fluorine (Carbon selected)
Energy (Kev) 25
Tilt 30
Thick Bulk
Number 500
Lambda 10.8 A
Epsilon 59 eV

The estimated Range is :440nm
The computed Backscatter Ion yield is :0.2%
The computed SE Yield is - Total SE :0.003 SE1 :1.3 SE2 :0.002

(a)

Target Material: Lithium, Beryllium, Boron, Carbon, Nitrogen (Carbon selected)
Energy (Kev) 25
Tilt 30
Thick Bulk
Number 500
Lambda 10.8 A
Epsilon 59 eV

ION induced SE Version 1.8
Authors :Ranjan Ramachandra (rramach4@utk.edu) and David Joy (djoy@utk.edu).
Some part of the code is adopted from SRIM code by Ziegler et.al

(b)

Figure 2.9: IONiSE front-end, with the input parameters on the right and a plot window on the left; the plot window shows the ion paths in fig. 2.9(a), and the implantation profile in fig. 2.9(a).

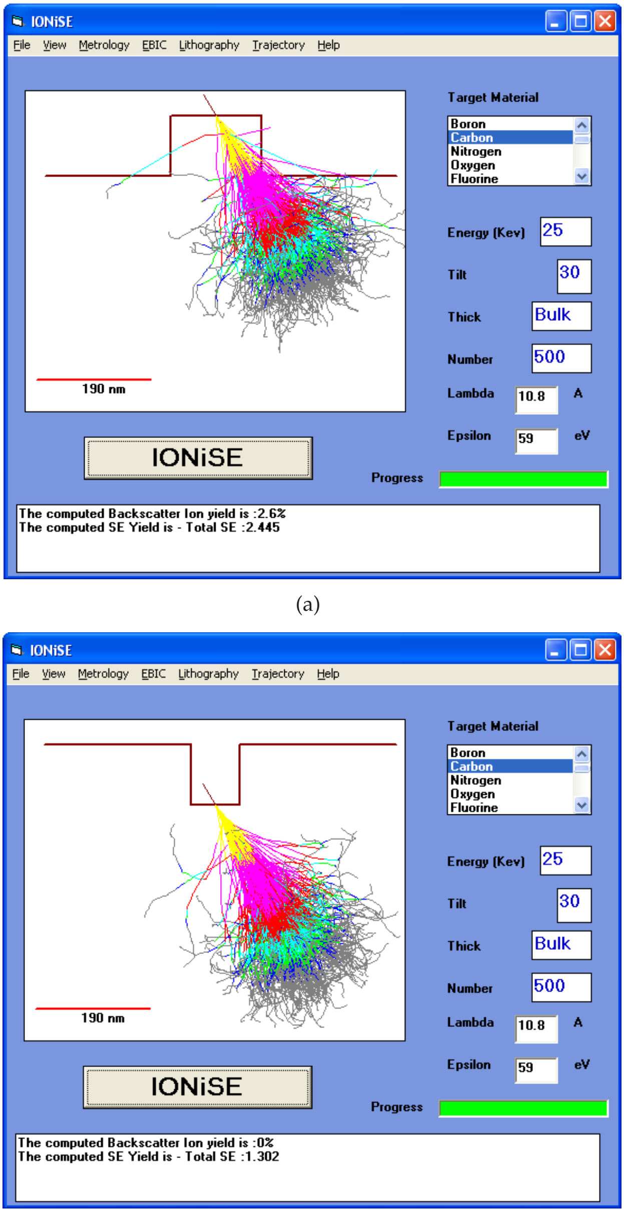

Target Material: Boron, **Carbon**, Nitrogen, Oxygen, Fluorine

Energy (Kev) 25

Tilt 30

Thick Bulk

Number 500

Lambda 10.8 A

Epsilon 59 eV

```
The computed Backscatter Ion yield is :2.6%
The computed SE Yield is - Total SE :2.445
```

(a)

Target Material: Boron, **Carbon**, Nitrogen, Oxygen, Fluorine

Energy (Kev) 25

Tilt 30

Thick Bulk

Number 500

Lambda 10.8 A

Epsilon 59 eV

```
The computed Backscatter Ion yield is :0%
The computed SE Yield is - Total SE :1.302
```

(b)

Figure 2.10: IONiSE plots showing a target with a rectangular bump (fig. 2.10(a)) and a rectangular cavity (fig. 2.10(b)).

3 Chapter

Contrast and Image Formation in Scanning Ion Microscopy

> *"All that glisters may not be gold, but at least it contains free electrons."*
> John Desmond Bernal

In this chapter the main FIB imaging mode, involving Secondary Electrons, is investigated. First the Focused Ion Beam and its mechanisms of image formation are described, with focus on the two machines used in this PhD project: the Dual Beam Quanta™ 3D FEG from FEI, employing a traditional gallium Liquid Metal Ion Source, and the ORION® PLUS from Carl Zeiss, which instead uses a novel helium Gas Field Ion Source. A brief presentation of a theory of noise in Scanning Microscopy introduces then the main part of the chapter, an experimental study on ion-induced Secondary Electron Emission, to be published this year (2011) in *Microscopy & Microanalysis*.

3.1 Imaging with Focused Ion Beams

The design and the functioning of a FIB microscope, or SIM, resemble very much the design and the functioning of a SEM, its more famous close relative. The principles of imaging formation in SEMs and SIMs, already outlined in chapter 1, are strikingly simple. Ions (electrons) are extracted from a source thanks to an electric field, they are then accelerated through a 'ion column up' to few tens of keV and finally they are focused into a tiny spot[1] on the sample surface. The ion beam is then scanned over an area on the sample (thanks to scanning plates, or deflectors, placed into the column), standing at each scanning spot for a certain amount of time, the dwell time t_d. The energetic beam penetrating into the sample bulk causes emission of secondary species, typically electrons, whose amount

---

[1] Here 'tiny' stands for 'as tiny as possible while still maintaining a decent amount of current.

is a function of the topography of the sample surface (and close subsurface) and of the sample composition[2]. The secondaries that are emitted at each position of the beam are collected by a detector (in its simplest description, a positively biased metallic grid followed by some circuitry), which then sends a proportional signal to an acquisition board (Analog-to-Digital converter, or ADC) where this signal is converted in a grey level and stored, or represented on a screen as a pixel in the final image. The total number of grey levels depends on the number of bits that are used to store each level: 256 in 8-bit images, 65,536 in 16-bit images), while the total number of pixel is usually set by the FIB operator. Without entering in the details, for which I refer to the dedicated literature [3], important requirements are for the dwell time to be long enough to cause a 'sufficient' amount of secondary emission, but not too long in order to keep the sample modification low, and for the size of the image (i.e. the number of pixels) to be big enough not to degrade the spatial resolution of the beam, but also not too big in order to avoid over-sampling[4]. These general considerations will be made more quantitative in the following chapters.

Fig. 3.1 shows a schematic of a FIB microscope. The schematic is taken from the website of Carl Zeiss, and refers to an ORION® microscope. It is however quite general, and it well describes any kind of FIB microscope, including the other protagonist of this research project, the Quanta™ 3D FEG. It comes handy to (virtually) break down the machine into 3 main parts: the ion source, the ion column, and the sample chamber; each of these parts is characterised, in principle, by a different value of pressure[5]. A good chamber vacuum would be around $10^{-5} - 10^{-6}$mbar (High Vacuum, HV), while for the column and the source Ultra High Vacuum (UHV) is required, thus at least 10^{-7}mbar. In the Quanta™ 3D FEG source and column share the same vacuum, but that is not the case for the ORION® PLUS, which has a gaseous source with flowing helium, in which the gas pressure determines the amount of extracted current.

The Ion Source The source module is the part that makes the real difference amongst FIBs (and also between FIBs and SEMs). The extraction of the charged particles is always carried out with a strong electric field, produced by a potential difference between the source itself and the extractor plate, which defines the border between the source and the column. The method used to produce the ions, however, can vary greatly. Traditional FIBs, like the Quanta, use Liquid Metals Ions Sources, of which the best known is the so called 'low-drag blunt-needle' LMIS [48]. This source is made of a refractory metal needle (tungsten in most

---

[2] Different secondary species can provide different contrast; for example, if the secondaries are backscattered ions grain contrast can be obtained, thanks to channeling, see sections 2.1.1 and 2.1.5.

[3] Like the monographes referred in [2], [39] and [32], the only recent books entirely dedicated to FIBs of which I am aware of, or the more general 'Handbook of Charged Particle Optics', edited by J. Orloff for CRC Press (2$^{\mathrm{nd}}$ edition in 2009).

[4] Ideally, the pixel size should be not too far from the beam size, a bit bigger in order to cover the whole sample surface with a bit of overlap between neighbouring positions, see sec. 4.5.

[5] Something that I have not mentioned so far is that SEMs and SIMs require more-or-less high levels of vacuum in order to keep the primary beam together; this is because the charged particles, ions or electrons, have to be free to travel, without being scattered in all directions by gas molecules.

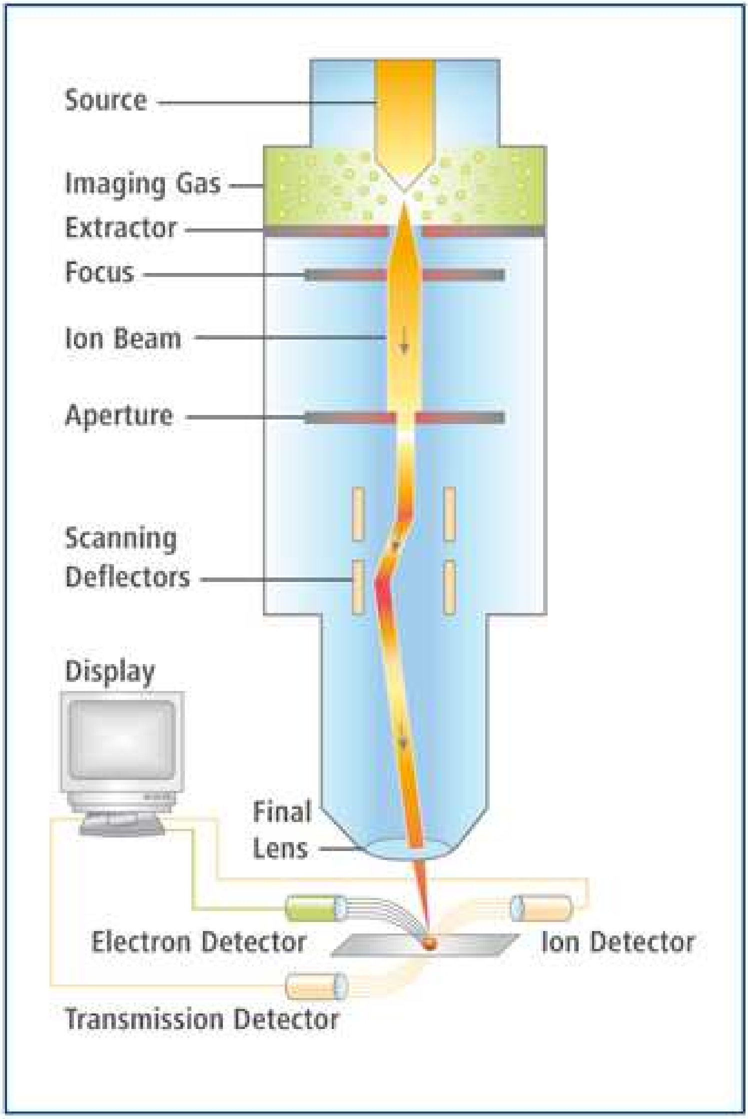

Figure 3.1: Schematic of a FIB. This drawing refers to a ZEISS ORION® (from Carl Zeiss website: `www.zeiss.com`), but, apart for the special gas field source, can be regarded as a general FIB scheme.

cases), electrically heated up in order to get covered by a thin layer of liquid metal (gallium, most commonly). The competition between the electric force and the surface tension shapes the liquid film in the form of a cone, the 'Taylor-Gilbert

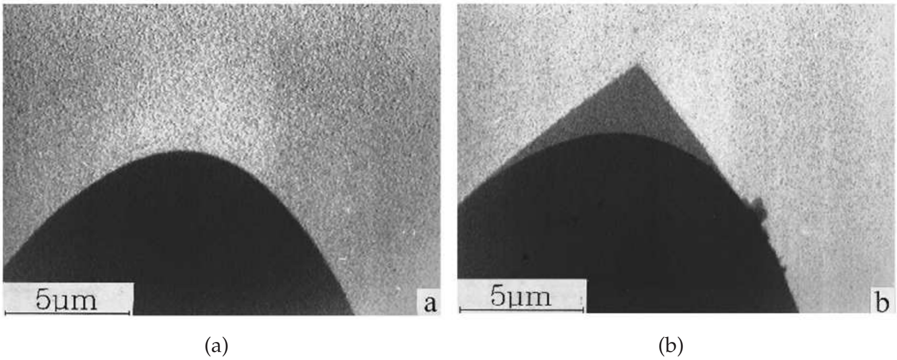

(a) (b)

Figure 3.2: The metallic tip (fig. 3.2(a)) and the Taylor-Gilbert cone (fig. 3.2(b)) of an AuGe LAIS (both pictures are taken from [49]).

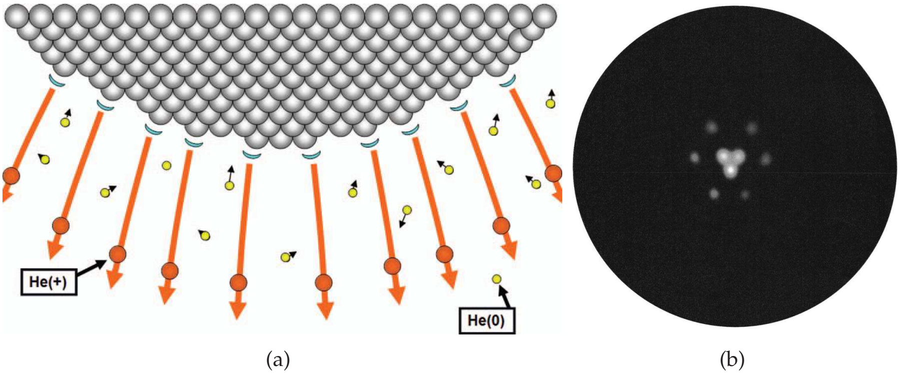

(a) (b)

Figure 3.3: Schematic of the Zeiss helium GFIS (fig. 3.3(a)), and the 'footprint' of the trimer (fig. 3.3(b)) (both pictures are taken from [4]).

cone. While the radius of the tungsten tip at his apex is in the order of micrometers, the tip of a Taylor-Gilbert cone can be as small as 1-2nm, so that the electric field becomes there so high to ionise the liquid metal. Fig. 3.2 shows TEM images of an AuGe LMIS (thus, to be more precise, not a Liquid Metal Ion Source, but a Liquid Alloy Ion Source, or LAIS), the uncovered metallic tip in fig. 3.2(a), and the Taylor-Gilbert cone in fig. 3.2(b) (both taken from [49]). The ORION® is in this respect a non-traditional FIB, for it has a Gas Field Ion Source, and it is designed specifically for imaging. The helium source of this machine is shown in fig. 3.3(a). The metallic needle, kept at cryogenic temperatures is here exposed to a flow of neutral helium atoms. The atoms are polarised by the strong electric field at the apex of the needle and attracted towards it; once they get close enough to the tip, the field becomes so strong that electrons begin tunneling, quantum mechanically, into the tip itself, leaving behind positively charged helium ions that are immediately accelerated away from the tip into the column [4]. What makes the Zeiss source very special is the metallic tip. Using a proprietary technology, they can make it so sharp (in situ!) that the top is actually formed by only 3 atoms, what they call 'trimer'. This give the ORION® an atomic-sized source, thus not in the order of nanometers, but in the order of Angstroms, or fractions. Should the reader be skeptical, fig. 3.3(b) shows the pattern produced by the ions extracted at the trimer on screen. It can be noted that partial emissions occurs also from outer atoms (in figure, the six atoms constituting the next atomic ring), but for imaging purposes usually only one of the three main ion beams is selected.

The Ion Column An ion column is really nothing else than a SEM column, with due technical differences arising from the fact that the particles to be focused are here positively charged. Electrostatic lenses are used to collimate and/or focus the beam, deflector plates are used for the scanning, multipoles can be present for aberration correction, several apertures can be placed to control the beam and the amount of current in it, and a final probe forming lens focuses the beam on the sample's surface.

The Sample Chamber The sample chamber, usually at the bottom end of the ion column, is where the interaction between the beam and the sample takes place, and where one or more detectors can be found. Of the three modules, this is the one to which the attention of this thesis is mainly devoted; as a matter of fact, the title name of my project was, at the beginning, a quite general 'Ion/Matter Interaction', to be narrowed down to 'High Resolution Scanning Microscopy' only later. Since all the remaining chapters will deal with this aspect, backed up by the theory presented in chapter 2, I will limit myself here to point out the only thing that can differentiate a FIB from a SEM: the ion detector that appears at the bottom right in fig. 3.1. SIMs allow backscattered ion imaging mode, which gives some interesting contrast mechanisms (see sec. 1.2), with possibility of material and/or structural characterisation. Such an imaging mode is of course lacking in a SEM, where ions are nowhere to be found! Secondary Electron imaging mode, however, remains to most commonly used one, for the sheer abundance of SEs, compared to any other secondary species. Breaking down the Scanning Ion Microscope into the three modules just described also comes handy with respect to the main topic of my research: optimisation of resolution in Scanning Ion Microscopy. This is because each of these parts, or better, each of its sub-components, can, independently and dramatically, degrade the imaging power of a FIB: each of them can be the bottleneck that limits the obtainable resolution. With the purpose of high imaging resolution, great effort must thus be devoted in equal measure to the good design of each module: to the source, in terms of (virtual) source size, beam current, and beam broadening due to Coulomb interactions; to the column, in terms of magnification and aberrations; and to the ion/sample interaction and the detection, in terms of contrast, sputtering, SNR, and locality of the SE information. Fig. 3.4 is an attempt to render the chaos of the many, variously interconnected, parameters that ultimately define the quality of a FIB microscope.

The rest of this chapter is made up of an experimental study of ion-induced Secondary Emission, published in *Microscopy & Microanalysis*, preceded by a brief examination of the theory of Signal-to-Noise Ratio in Scanning Microscopy.

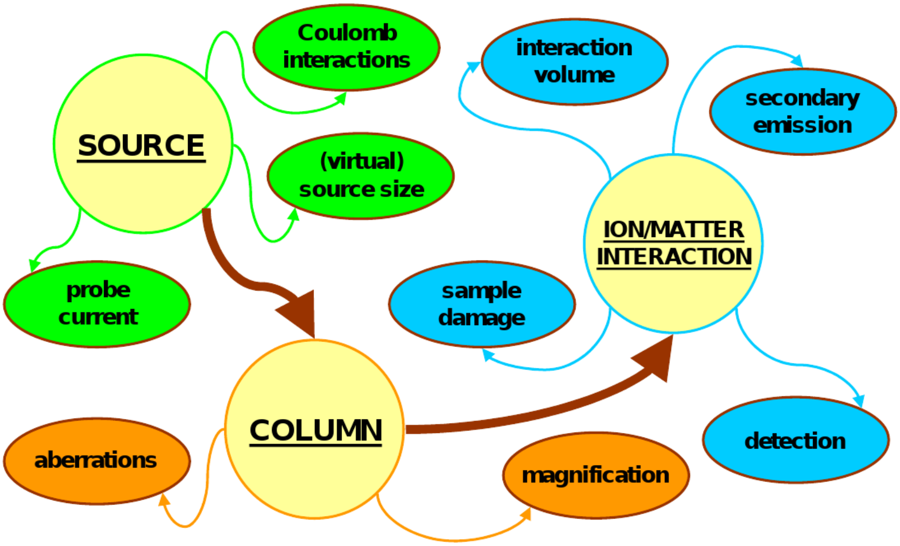

Figure 3.4: The chaos of the many, variously interconnected, parameters that ultimately define the quality of a FIB microscope.

3.2 Detection and Signal-to-Noise Ratio

The Signal-to-Noise Ratio is defined by the Root Mean Square (RMS) of signal and noise:

$$\mathrm{SNR} = \mathrm{RMS}_{\mathrm{signal}}/\mathrm{RMS}_{\mathrm{noise}} \ . \tag{3.1}$$

Following the approach used by O.C. Wells in [50], when evaluating the SNR in a micrograph, it is useful to think of a scanning ion microscope as a series of different processes of information transfer, leading from the sample surface to the image on the screen:

- sample excitation through the primary ion beam;
- sample response through secondary emission (electrons or ions);
- detection of secondaries;
- amplification (multiplication of the secondary counts);
- recording system and/or visualisation.

Each of these processes has its own sources of noise. For each pixel, let n_i be the signal quanta at the i^{th} stage and $k_{sn,i}$ the corresponding SNR. Since the first stage is the sample excitation through the ion beam, n_1 is the number of incident ions, while the value of the other n_i depends on the conversion efficiency at the given stage. The rms fluctuation in the ion beam is $\sqrt{\overline{n_1}}$, from which it follows that the SNR at the stage 1 is given by:

$$k_{sn,1} = \frac{\overline{n_1}}{\sqrt{\overline{n_1}}} \ . \tag{3.2}$$

The signal quanta at any following stage i is expressed as product of the signal and a conversion factor ϵ at the previous stage:

$$\overline{n_i} = \overline{\epsilon_{i-1}}\ \overline{n_{i-1}} \ . \tag{3.3}$$

The noise at the stage i depends on the fluctuations in the conversion factor ϵ_{i-1} and in the quanta signal from the previous stage, n_{i-1}. The total fluctuation in n_i is given by [51]:

$$\overline{(n_i - \overline{n_i})^2} = \overline{\epsilon_{i-1}}^2\ \overline{(n_{i-1} - \overline{n_{i-1}})^2} + \overline{n_{i-1}}\ \overline{(\epsilon_{i-1} - \overline{\epsilon_{i-1}})^2} \ . \tag{3.4}$$

In the usual assumption of Poisson statistics, for which the mean coincides with the variance ($\overline{(\epsilon - \overline{\epsilon})^2} = \overline{\epsilon}$), eq. 3.4 becomes:

$$\overline{(n_i - \overline{n_i})^2} = \overline{\epsilon_{i-1}}^2\ \overline{(n_{i-1} - \overline{n_{i-1}})^2} + \overline{\epsilon_{i-1}}\ \overline{n_{i-1}} \ , \tag{3.5}$$

which, dividing all the terms by $\overline{n_i}^2$ and using eq. 3.3, can be rewritten as:

$$\frac{\overline{(n_i - \overline{n_i})^2}}{\overline{n_i}^2} = \frac{\overline{(n_{i-1} - \overline{n_{i-1}})^2}}{\overline{n_{i-1}}^2} + \frac{1}{\overline{n_i}} \ , \tag{3.6}$$

or as:

$$\frac{1}{k_{sn,i}^2} = \frac{1}{k_{sn,i-1}^2} + \frac{1}{\overline{n_i}} = \frac{1}{\overline{n_1}} + \frac{1}{\overline{n_2}} + \cdots + \frac{1}{\overline{n_i}} \ . \tag{3.7}$$

Eq. 3.7 has been obtained in the assumption that the noise in all the conversion processes is Poisson-distributed. If this is not the case[6], and the noise is instead greater than that, eq. 3.7 can be corrected multiplying at each stage for the factor $b_{i-1}\overline{\epsilon_{i-1}}$, being $b_i = \overline{(\epsilon_i - \overline{\epsilon_i})^2}/\overline{\epsilon_i}^2$:

$$\frac{1}{k_{sn,i}^2} = \frac{1}{\overline{n_1}} + \frac{b_1\overline{\epsilon_1}}{\overline{n_2}} + \cdots + \frac{b_{i-1}\overline{\epsilon_{i-1}}}{\overline{n_i}} \ . \tag{3.8}$$

Taking into account only the first two stages (primary beam excitation and secondary emission), the SNR is easily obtained from eq. 3.7:

$$\frac{1}{k_{sn,2}^2} = \frac{1}{\overline{n_1}} + \frac{b_1\overline{\epsilon_1}}{\overline{n_2}} \ , \tag{3.9}$$

---

[6] It seems that the beam noise is more accurately described by the Neyman distribution, in which the variance is greater than the mean.

and, applying eq. 3.3:

$$\frac{1}{k_{sn,2^2}} = \frac{1+b_1}{\overline{n_1}} \Rightarrow k_{sn,2} = \sqrt{\frac{\overline{n_1}}{1+b_1}} \ . \tag{3.10}$$

For the Poisson distribution, $b_i\overline{\epsilon_i} = 1$ and eq. 3.10 becomes:

$$k_{sn,2} = \sqrt{\frac{\overline{\epsilon_1}\ \overline{n_1}}{1+\overline{\epsilon_1}}} \ . \tag{3.11}$$

The conversion factor from the first to the second stage, $\overline{\epsilon_1}$, is the ion-induced SE yield δ_i, and n_i is the number of primary ions N_i, so that the SNR, in the case of Poisson-distributed noise in the primary beam and in the secondary emission and perfect detection, is:

$$k_{sn,2} = \sqrt{\frac{\delta_i\overline{N_i}}{1+\delta_i}} \ . \tag{3.12}$$

The SNR is in principle different for each pixel, for each pixel is characterised by a different value of δ_i; for this reason, an effective SNR, k_{sn}^{eff} can be obtained for the whole image, from the darkest parts to the brightest parts:

$$k_{sn}^{eff} = \frac{2}{N_g}\left(\sqrt{n_{white}} - \sqrt{n_{black}}\right) \ , \tag{3.13}$$

where N_g is the number of gray levels in the image[7]. Eq. 3.13 shows a counterintuitive effect: in order to maximise the effective SNR in a micrograph, the number of grey levels should be minimised.

If also the detection is taken into account, the static SNR can be calculated with the following formula:

$$k_{sn,3}|_{\nu=0} = \sqrt{6\eta_e t_d \delta_i \frac{I_b}{e}} \ , \tag{3.14}$$

where η_e is Detector Quantum Efficiency (DQE) of the SE detector, t_d is the dwell time in microseconds, δ_i is the ion-induced SE yield, and I_b is the beam current in picoAmpére. The effective SNR for a detail in the image at the given spatial frequency ν is obtained multiplying $k_{sn,3}|_{\nu=0}$ with the Modulation Transfer Function $\|\tau(\nu)\|$ of the system (see sec. 4.1):

$$k_{sn,3}\left(\nu\right) = k_{sn,3}|_{\nu=0}\left\|\tau\left(\nu\right)\right\| \ . \tag{3.15}$$

---

[7] Eq. 3.13 has been written under the assumption that in the imaging chain there is one stage for which the signal quanta is minimum, and the noise fluctuation is calculated as if it were coming only from this bottleneck; in SE imaging mode, the noise bottleneck is between the specimen and the collector.

3.3 Angular Dependence of the Ion-Induced Secondary Electron Emission for He$^+$ and Ga$^+$ Beams

V. Castaldo, J.M. Withagen, C.W. Hagen, E. van Veldhoven, and P. Kruit.
Microscopy & Microanalysis, 17(4):1–13, 2011.

Abstract: *In recent years, novel ion sources have been designed and developed that have enabled focused ion beam machines to go beyond their use as nano-fabrication tools. Secondary electrons are usually taken to form images, for their yield is high and strongly dependent on the surface characteristics, in terms of chemical composition and topography. In particular, the Secondary Electron Yield varies characteristically with the angle formed by the beam and the direction normal to the sample surface in the point of impact. Knowledge of this dependence, for different ion/atom pairs, is thus the first step towards a complete understanding of the contrast mechanism in scanning ion microscopy. In this article, experimentally obtained ion-induced secondary electron yields as a function of the incidence angle of the beam on flat surfaces of Al and Cr are reported, for usual conditions in Ga$^+$ and He$^+$ microscopes. The curves have been compared with models and simulations, showing a good agreement for most of the angle range; deviations from the expected behaviour are addressed and explanations are suggested. It appears that the maximum value of the ion-induced secondary electron yield is very similar in all the studied cases; the yield range, however, is consistently larger for helium than for gallium, which partially explains the enhanced topographical contrast of helium microscopes over the gallium focused ion beams.*

3.3.1 Introduction

For years, the only ion sources used in Focused Ion Beams (FIBs) have been the Liquid Metal Ion Sources (LMIS) [1], especially the ones employing gallium ions. Since gallium (and in general, metallic) ions are heavy, the amount of energy and momentum that they transfer to the sample is destructive for the sample itself; this effect (sputtering) has prevented the FIBs from being used as microscopes, and limited them to employment as nano-fabrication tools [2, 3]. Ga-induced secondary electron images were only used to find the sputtering and/or the redeposition target and inspect the results. In the last decade, however, considerable effort has been devoted to the design and development of novel ion sources, employing gaseous light ion species, such as helium, which gave renewed attention to FIBs as microscopes (Scanning Ion Microscopes, SIMs). They now compete with, and complement, the traditional Scanning Electron Microscopes (SEMs) in terms of brightness, current, spot-size, and, ultimately, imaging resolution [8].

The use of ions instead of electrons in scanning microscopy has some undiscussed advantages, like different contrast mechanisms, smaller spot size, and perhaps higher resolution, also due to the much smaller wavelength [10, 11]. The Gas Field Ion Sources (GFIS), in particular, provide high current in a sub-nanometer spot (i.e. high brightness) and very low aperture angle at the sample, resulting in high depth of focus [4, 5]. The contrast mechanism most frequently used is the collection of Secondary Electrons (SEs), for they are produced in a much larger amount than other species (like backscattered ions, that can also be used to form images) [52, 53]. It is common practice, in literature, to refer to ion-induced secondary electrons and electron-induced secondary electrons with iSE and eSE, respectively. A good way to estimate the imaging capability of an ion imaging machine is thus to measure, and/or simulate, the iSE Yield (δ_i, the number of secondary electrons per incident ion) as a function of the angle α formed between the incident beam and the surface. These curves are responsible for the 'first order contrast', while other effects, like edge enhancement and transparencies, can only be explained in terms of ion/atom interaction at the atomic level in a finite volume inside the sample (interaction volume). However, ions are always much more massive than electrons, and the sputtering, with consequent sample modification, is an ever-present unwanted effect, even with He ions. It has been shown that the removal of sample atoms is in fact the mechanism that ultimately limits the resolution of SIMs [54, 55, 56].

The objective of this study is the measurement of δ_i as a function of the angle α. Curves for 25keV He^+ beams and 30keV Ga^+ beams incident on Al and Cr samples are presented and discussed.

3.3.2 Angular Dependence of Ion-Induced Secondary Electron Emission

When energetic ions impact on a solid surface, they slow down in a pseudo-continuous process of energy loss. Eventually, they can find their way out from the top surface of the sample (backscattered ions), or from its bottom, if the sample is thin enough (transmitted ions), but most of the time their energy drops to a level that does not allow any further movement and the ions end up in a rest position in the target. In any case, due to the energy transfer from the beam, many secondary processes take place in the target: emission of photons, emission of electrons (SEs), emission of ions, displacement of target atoms (with consequent creation of point defects in crystals), sputtering of target atoms, nuclear reactions, chemical reactions (creation and breaking of molecular bonds). Secondary emission is the process that is mostly used in image formation. It can be further divided into *Secondary Ion Emission*, occurring when surface atoms are ionised and expelled, and *Secondary Electron Emission*, occurring when shell electrons receive enough energy to reach the surface and overcome the Surface Energy Barrier (SEB). Since in most cases SEs are the species produced in the largest amount, they are most commonly used to create an image. Secondary Electron emission is the process that will be addressed here. Furthermore, the amount of secondary emission is very surface sensitive, thus providing good topographical (and, in some cases, material) contrast.

Ion-induced electron emission is in general due to two different processes, one of which can be dominant, depending on the ion species and energy.

Potential emission This might occur when the potential energy of the ion is twice or more the work function of the solid, and takes place in front of the solid

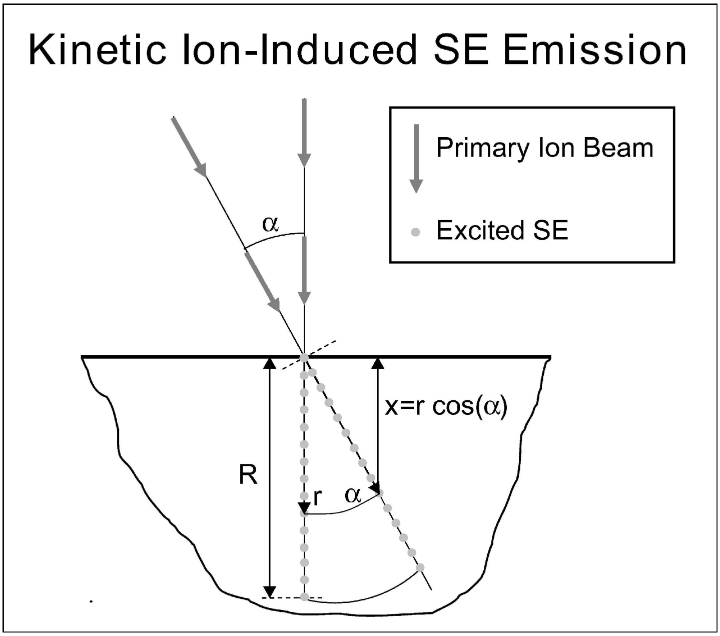

Figure 3.5: The simple origin of the secant law for ion- electron- induced Secondary Electron emission: the higher the incidence angle, the closer the energised electrons are to the sample surface.

surface: SE emission proceeds via resonance neutralisation and subsequent Auger de-excitation or Auger neutralisation [57, 58]. It does not play a role in the case of Ga^+ bombardment, since the ionisation potential for Gallium is ~ 6eV, and for normal metals $\Phi \sim 4 - 5$eV, while for helium, whose first ionisation potential is ~ 24.6eV, potential emission could be present. This process, however, becomes important only for slow ions and/or at grazing incidence, but it is usually negligible under standard Scanning Ion Imaging conditions, where primary energies are in the order of tens of keV [45].

Kinetic emission This occurs for direct transfer of kinetic energy, and it is the major (if not the only) source of SEs at medium and high energies; it is normally described as a three-stage process:

1. production of SEs within the sample;
2. migration to the sample surface;
3. escape through the Surface Energy Barrier.

The mechanism of ion-induced kinetic emission is very similar to the electron-induced SE emission; the main difference is in the production stage, while the other parameters (energy-loss rate, mean free path, magnitude and shape of the surface barrier) are common for both cases. In particular, since at a given primary energy the velocity of ions is two or three orders of magnitude lower than for electrons, the electron-induced SE yield (δ_e) exhibits a maximum for energies below 1keV, while the maximum of the iSE yield δ_i is at hundreds of keV. As a result, at the normal operating energies (tens of keV), δ_e decreases with increasing primary energy, while the opposite happens for δ_i.

The theory of iSE emission is quite well established, and several studies can be found in literature accounting for the variation of δ_i with the primary energy and molecular weights of primary ions and target atoms, and for the differences with electron-induced SE (eSE) [59, 60]. The object of the present study, however, is the dependence of δ_i on the angle α formed by the ion beam and the normal to the sample surface, which is at the basis of contrast in scanning ion images. This dependence is less well studied, but a good treatment for $\delta_i = f(\alpha)$, can be found in [61] or in [62]. The traditional fitting function for $\delta_i = f(\alpha)$ is the simple 'inverse cosine law' [63]:

$$\delta_i(\theta) = \delta_i(0)\cos^{-1}\theta \; . \tag{3.16}$$

This law accounts only for the second step of the kinetic emission mechanism, and can be easily explained with reference to fig. 3.5; for the incidence angle α, δ_i can be written as:

$$\delta_i(\alpha) = K\frac{1}{\int_0^R r\cos(\alpha)\,\mathrm{d}r} \; , \tag{3.17}$$

where R is the distance inside the bulk material at which ions stop producing electrons and K is a constant; for $\alpha = 0$ equation 3.17 becomes:

$$\delta_i(0) = K\frac{1}{\int_0^R r\,\mathrm{d}r} \; ; \tag{3.18}$$

equation 3.16 follows directly. A more general expression for δ_i can be found in [62]:

$$\delta_i(x) = C\int_0^R N(r)\exp(-x/L)\,\mathrm{d}r \; , \tag{3.19}$$

where x is the coordinate normal to the sample surface, r is the linear coordinate along the ion path, $N(r)$ is the number of electrons produced at r, L is the mean electron attenuation length, C is a target/dependent constant; equation 3.16 is obtained for N constant over distances much larger then L and a straight ion path (in which case $x = r\cos(\alpha)$, as in fig. 3.5).

The inverse cosine law is of course quite a gross simplification, even when only considering the migration of electrons to the surface, for they are not produced along a straight line into the sample, but in an interaction volume whose shape can be complex (see fig. 3.6). In addition, electrons are not only produced by primary ions, but also by recoils, i.e. target atoms that have been displaced. In fact, some qualitative predictions can be made on the basis of the interaction volume alone. Comparing figures 3.6(a) and 3.6(c), it appears that the He ions have higher penetration power, resulting in lower SE emission at normal incidence; when the incidence angle increases, the intersection between the interaction volume and

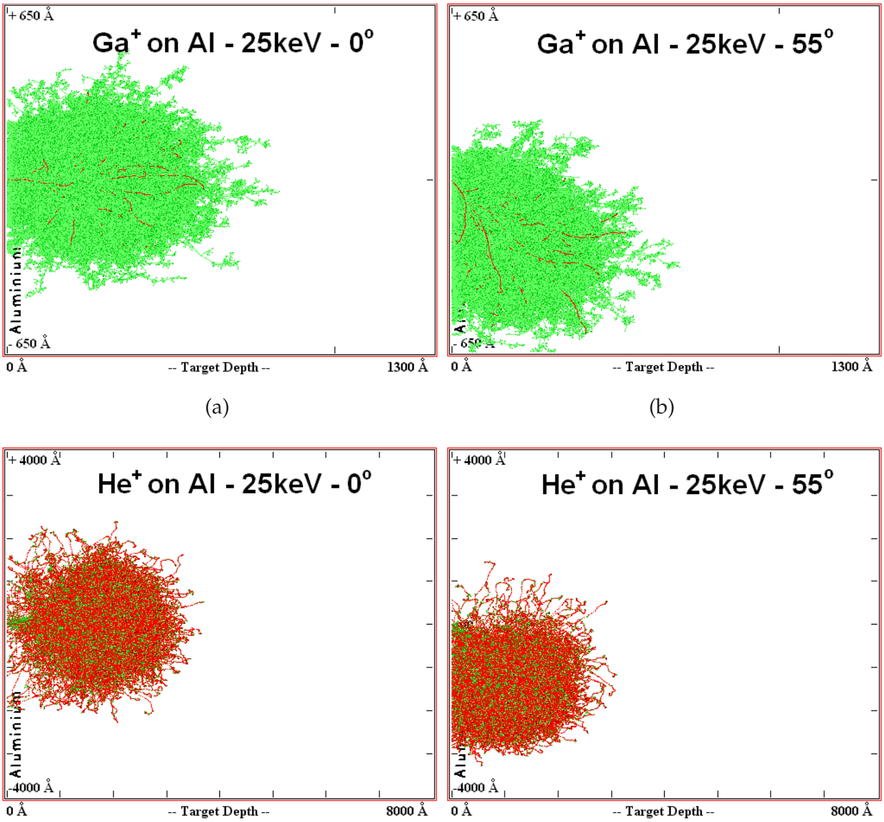

(a) (b) (c) (d)

Figure 3.6: Interaction Volume: the position inside the sample occupied by primary ions and recoiled atoms for different ions and different incidence angles; the ion beam enters the sample from the left, the impact point being at the center of the vertical axis; 3.6(a) Ga^+ on Al, 30keV and 55°, x-axis: 130nm; 3.6(b) Ga^+ on Al, 30keV and 55°, x-axis: 130nm; 3.6(c) He^+ on Al, 25keV and 0°, x-axis: 800nm; 3.6(d) He^+ on Al, 25keV and 55°, x-axis: 800nm. The darker points are primary ions; the lighter points are recoiled target atoms.

the sample surface increases substantially; in the case of Ga ions, on the other hands, the extent of such intersection is less dependent on the angle of the beam. Therefore, a higher SE yield range is expected in the case of He; this prediction will be confirmed in the following sections. However, the fact that, as it will be shown, in most cases the secant law is quite a good approximation for $\delta_i = f(\alpha)$ is a pleasant obscure surprise on one hand, and on the other hand proves that the kinetic emission is indeed the dominant emission mechanism, and that the process is usually limited by the second stage, i.e. the distance from the surface where SEs are generated.

At low energies (<10keV) the behavior of $\delta_i(\alpha)$ strongly deviates from the one predicted by equation 3.16, because the potential emission becomes more and more important, but also because more and more primary ions are backscattered and/or reflected. Even at energies of tens of keV, deviations have been observed and, based on Monte Carlo simulations in the energy range 100eV-1MeV, a modified version of equation 3.16 has been proposed and is widely used [64]:

$$\delta_i\left(\alpha\right) = \delta_i\left(0\right)\cos^{-f}\left(\alpha\right) \ , \tag{3.20}$$

where the corrector factor f can assume values smaller or greater than 1:

- at intermediate energies, the backscattered ions penetrate below the surface before exiting again, thus enhancing excitation of SEs near the surface $\Rightarrow f > 1$;
- at low energies, ions can just be reflected from the surface, without contributing to the SE formation $\Rightarrow f < 1$.

A similar argument can be made for the incidence angle, for any value of the primary energy: SE production is enhanced at intermediate angles, and strongly suppressed at high incidence angles, which once again results in a deviation from the secant law; this effect can be modeled with a correction factor f that is a function of α.
A more general fitting function for $\delta_i = f(\alpha)$ is found in [65]:

$$\delta_i\left(\alpha\right) = \delta_i\left(0\right)\frac{1}{\cos^{-f}\left(\alpha\right)}\exp\left[-g\left(\frac{1}{\cos\left(\alpha\right)}\right)\right] \ , \tag{3.21}$$

where f and g are the adjustable parameters.

3.3.3 The Experimental Setup

Secondary Emission measurements are notoriously difficult because of several reasons[66].

- **Backscattered Particles** A fraction of the incident ions find their way out of the sample surface as backscattered ions; these ions are partially responsible for the deviation of the SE yield from the secant law, for they can contribute to the SE emission in different ways: they can be reflected by the sample, especially at very high angles, thus contributing almost nothing to the SE production, or they can travel for a while inside the sample, close to the surface, thus producing a higher-than-normal number of SEs. In any case, for reasons that will be clear soon, the backscatter yield must be known, or at least estimated, in order to correctly quantify the SE yield.
- **Different Types of SEs** SEs can be produced directly by incident ions, or by recoiled atoms cascading into the interaction volume; these secondaries of different origin are usually referred to as $\mathrm{SE_I}$ and $\mathrm{SE_{II}}$, respectively, and

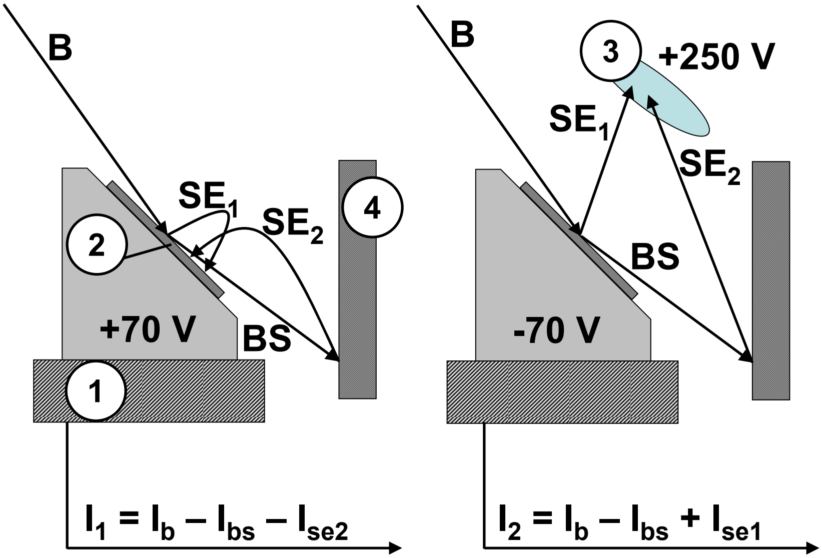

Figure 3.7: A schematic of the setup for the measurement of the iSE Yield δ_i: in the first measurement the sample is positively biased and the SE detector is off; in the second measurement the sample is negatively biased and the SE detector is on; 1. sample holder; 2. sample; 3. detector; 4. chamber wall. B are the ions in the primary beam, SE_1 and SE_2 are the SEs emitted respectively from the sample and the chamber walls, BS are the backscattered ions.

treated separately, because they are characterised by different spatial and energy distributions[11]. In the present study a third class of SEs must be taken into account, i. e. those secondaries that are not produced in the sample, but by the chamber/holder walls, and still reach the detector. Since SE_I and SE_II are equivalent with respect to the SE yield, their current is not differentiated, and is indicated as I_{se1}. The current coming from electrons produced somewhere else is called I_{se2}.

- **Surface Status** The SE yield is strongly dependent on the work function of the sample material, and thus on the surface conditions. In general, the control on the surface status of a sample is scarce, which generates strong uncertainties in the measurement of SE yields. In the case of iSE emission, however, the surface status is much less wild, because of the cleaning effect of the ion beam.

The iSE yield is defined as the number of SEs emitted per incident ion:

$$\delta_i = \frac{\text{SE}}{\text{ion}} = \frac{I_{se}}{I_b} , \tag{3.22}$$

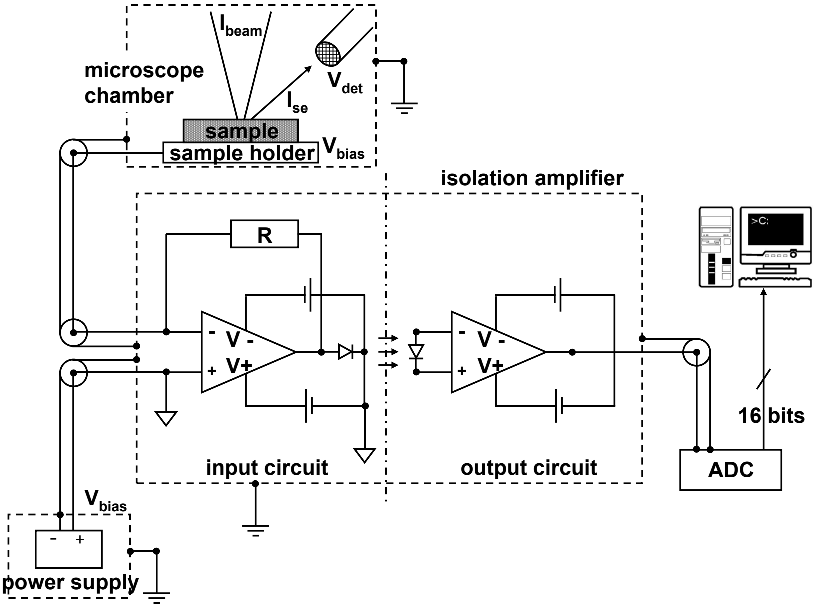

Figure 3.8: The electronic circuit used for the bias of the sample and the reading and recording of the sample current.

where I_{se} and I_b are the SE current and the primary ion current, respectively. These two currents will be measured on a flat sample at different incidence angles in order to build curves of $\delta_i(\alpha)$. In fact, they can not be measured directly, but they can be estimated measuring the sample current in two conditions, at different values of α; with reference to fig. 3.7, and assuming ionic currents flowing from the column to the sample as positive:

- **measurement 1:** the sample is positively biased, and the detector is switched off, so that all the produced SEs are pulled back towards the sample: the measured current is $I_1 = I_b - I_{bs} - I_{se2}$, where I_{bs} is the current of the backscattered ions leaving the sample, and I_{se2} is the (negative) current of SEs produced by backscattered ions anywhere in the chamber and hitting the sample;

- **measurement 2:** the sample is negatively biased, and the SE detector is on at the maximum voltage, so that all (or most of) the SEs are collected, and the current measured at the sample is: $I_2 = I_b - I_{bs} + I_{se1}$, with I_{se1} being the current of SEs from the sample.

If there were no backscattered ions, then $I_{bs} = I_{se2} = 0$; in this case $I_{se1} = (I_2 - I_1)$, and $\delta_i = (I_2 - I_1)/I_1$. The presence of a non-negligible backscattered ion current requires a correction, as will be shown later.

The sample bias voltage is set at +70V in the first measurement, a value that is slightly higher than the highest energy conventionally assumed for the SEs (50eV), to be sure to pull back all the electrons. In the second measurement the sample bias is set at -70V, to assist the electrons in leaving the surface, without affecting the primary ions, incident at 25-30keV. It should be noted that the best way to measure the primary current I_b would be with a Faraday cup, which assures that none of the SEs are lost. The cup, however, should be removed to measure I_2; the chamber should be opened at each value of α, making the whole measurement extremely cumbersome. In fig. 3.8 the electric circuit employed for the measurement is shown; since the sample has to be biased and the current has to be measured at the same time, a floating amplifier, with an optical connection between the input and the output circuit, is used; the impedance of the amplifier is 1GΩ, so one volt in output corresponds to a sample current of 1nA. The output is measured and recorded via an Analog-to-Digital Card.

Because no stage can be tilted up to $\pi/2$, in order to span the whole range of incident angles, two different holders had to be used for each experiment, one flat, tilted up to $\pi/4$, and one on which the sample is already at $\pi/4$, to allow incident angles up to $\pi/2$ (see fig. 3.7). In machines in which only one sample at time can be placed, the chamber had to be open and the sample mounted on the tilted stage for measurement at angles higher than $\pi/4$.

Considering that the absolute values of the recorded currents always contain an offset (i.e. a non-zero current also when $I_b = 0$), I_1 and I_2 are written as:

$$I_1 = I_{off1} + I_b - I_{bs} - I_{se2} \; ; \tag{3.23}$$

$$I_2 = I_{off2} + I_b - I_{bs} + I_{se1} \; . \tag{3.24}$$

The current I_{se2} only appears in I_1 because in the second measurement these SEs hit the detector, not the sample. Problem is that now the SE current can not be simply calculated as $I_{se1} = (I_2 - I_1)$; in fact, there is no way to measure the current I_{se2}, nor to cancel it combining equations 3.23 and 3.24. The backscatter yield I_{bs}/I_b is itself a function of α, in general monotonically increasing. The minimum value of I_{bs}, at $\alpha = 0$, is usually very close to 0 (see figures 3.11 and 3.14(a)). Assuming that at normal incidence $I_{bs}/I_b \approx 0$, then $(I_1 - I_{off1})\,|_{\alpha=0} \approx I_b$, and I_{se1} can be approximated in different ways, each characterised by a different error:

a $I_{se1} \approx (I_2 - I_{off2}) = I_{se1} + (I_b - I_{bs}) \;\; ;$

b $I_{se1} \approx (I_2 - I_{off2}) - (I_1 - I_{off1}) = I_{se1} + I_{se2} \;\; ;$

c $I_{se1} \approx (I_2 - I_{off2}) - I_b = I_{se1} - I_{bs} \;\; .$

Method b has been dismissed as the most risky, for there is no way to make any assumption about I_{se2}, which can vary in an unpredictable way, also as a function of the chamber conditions. Methods a and b are roughly equivalent, the first resulting in a slight overestimation, the second in a similarly slight underestimation. For this study, method c is chosen, because usually $I_{bs} < I_b/2$ in most of the angle range $[0, \pi/2)$.

3.3.4 Results I: Secondary Electrons from Ga$^+$ bombardment

For the experiments on the Ga$^+$-induced Secondary Emission, a Dual Beam Quanta 3d FEG from FEI is used. With a beam current of about 500 pA, the sample is probed in spot mode (i.e. the beam is stationary in a certain position, without scanning) with a focused beam. There are several reasons behind this choice. As expected and observed, the chemical and physical surface changes caused by the ion beam affect the SE production, making I_2 vary in time. In scanning mode, this variation is slow, and I_2 appears to drift in time, so that deciding about its value is rather difficult; in addition, when in the field of view there is a 'bad spot', like an impurity or a dust particle, the different amount of SEs is mediated over the whole image, getting by totally undetected. The same happens in spot mode with a defocused beam. When working in spot mode with a focused beam, on the other hand, the measured current can be referred to a precise location on the sample, and the spot can be moved several times on the sample, with a fixed step chosen in order not to overlap with the previous position. As can be seen in fig. 3.9, a graph of I_2 in time appears as a sequence of spikes followed by fast decay (more on this in section 3.3.6.3). The maximum of each spike, corresponding to time zero for each new area of illumination, has been taken as the current of interest, for it is the current produced by a 'virgin' area of the sample; in this way, given the availability of many measurement points for each measurement, a statistical analysis is possible, allowing the estimation of the error band for each measurement angle. Illumination points in which topological or compositional anomalies are present can be recognised easily and dismissed: they give a signal whose magnitude is far off from the magnitude of other spikes in the graph.

Figures 3.9(a) and 3.9(c) show that also I_1 is a function of time, stronger for higher angles. Also this effect will be discussed in section 3.3.6.3. Finally, fig. 3.9(a) proves that I_{se2} is actually present and can not be neglected at grazing angles (when I_{bs} is high): it is this term that makes $(I_1 - I_{off1}) < 0$. In fig. 3.10, the curves showing $\delta_i = f(\alpha)$ for Al and Cr under 30keV Ga$^+$ bombardment, together with the statistical error at each measurement angle. As has been pointed out already, the value of δ_i calculated as $[(I_2 - I_{off2}) - I_b]/I_b$ is an underestimation, for it is actually $\delta_i - I_{bs}/I_b$. These curves should therefore be corrected for the backscatter current I_{bs}. This can be estimated from I_1, once the relationship between I_{bs} and I_{se2} is assumed; choosing a simple relationship such as $I_{se2} = nI_{bs}$, eq. 3.23 becomes:

$$I_1 - I_{off1} = I_b - I_{bs} - nI_{bs} = I_b - (n+1)\,I_{bs}\ , \tag{3.25}$$

where n is a fraction of the δ_i of the chamber walls (not all the backscattered ions hit the chamber, and not all the SE2 are pulled towards the sample). Thus, it is reasonable to assume for n values of at most few units; the backscatter current can be expressed as:

$$I_{bs} = \frac{I_b - (I_1 - I_{off1})}{n+1}\ . \tag{3.26}$$

Another way to estimate I_{bs} is via Monte Carlo simulation, with softwares like TRIM [35]. Fig. 3.11 shows the curves of I_{bs}/I_b vs. α obtained for different values

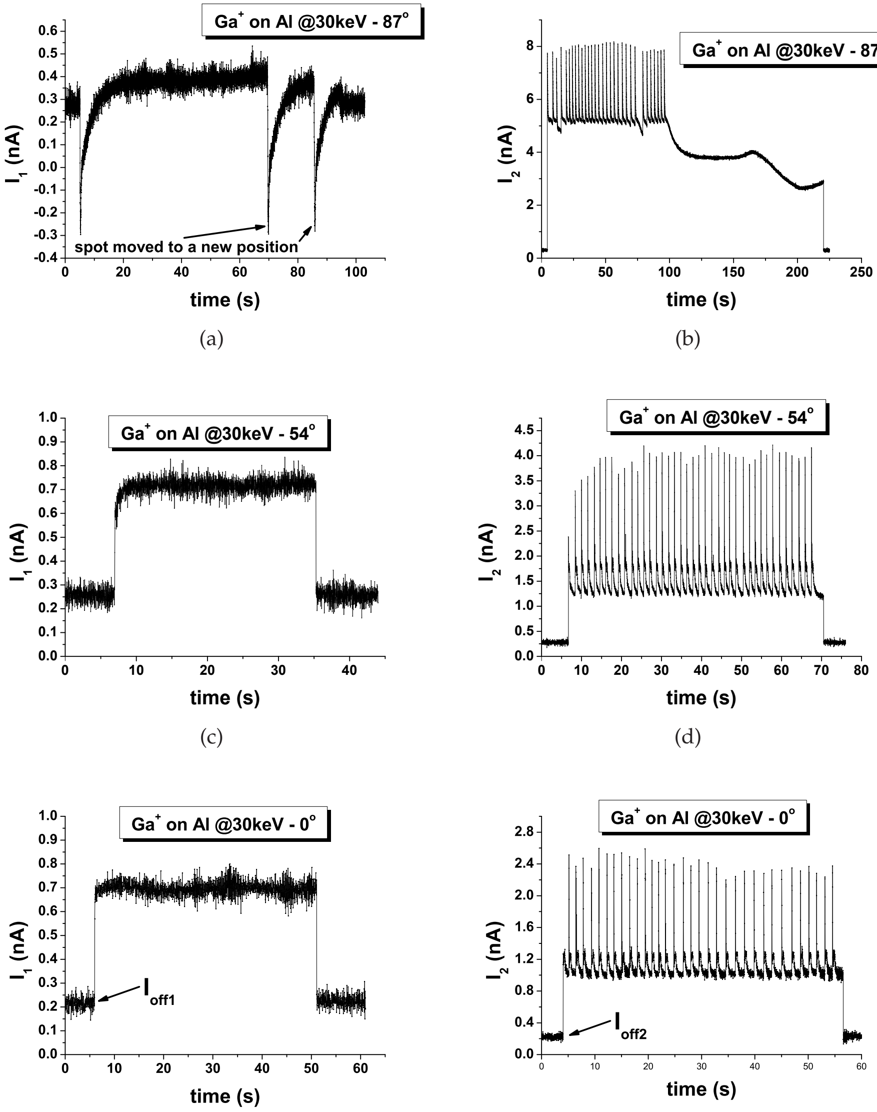

(a) (b)

(c) (d)

(e) (f)

Figure 3.9: Graphs of the recorded currents I_1 and I_2 for Ga$^+$ at 30keV on Al, for three different incidence angles.

of the factor n in eq. 3.26, and as obtained by TRIM simulation, for Al (fig. 3.11(a)) and for Cr (fig. 3.11(b)). Some considerations; first of all, the curves that show values higher than 1 have no physical meaning, for I_{bs} can not be greater then I_b, so that certain values for n can be dismissed; the values obtained by simulation match in the case of Cr (for $n = 1$) reasonably well up to $\alpha \sim 0.45\pi$), but substantially differ in the case of Al (simulations have been also performed covering the

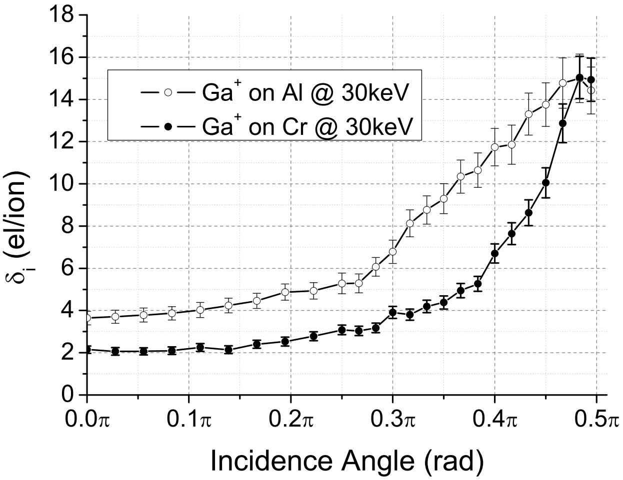

Figure 3.10: The experimental curves showing δ_i vs. α for Al and Cr under bombardment of Ga$^+$ at 30keV.

Al sample with a 3-5nm layer of Al_2O_3, for no appreciable difference). With an estimation of I_{bs} at hand, the curves of fig. 3.10 can be corrected, simply adding the term I_{bs}/I_b:

$$\delta_i^{corr} = \delta_i + I_{bs}/I_b \ . \tag{3.27}$$

The result is shown in fig. 3.12, for Al (fig. 3.12(a)) and Cr (fig. 3.12(b)), together with the secant law normalised at $\delta_i\,(\alpha = 0)$. Good news: not even in the worst allowed case (lowest value of the factor n that keeps $I_{bs}/I_b < 1$) the correction moves the curve outside the error band.

3.3.5 Results II: Secondary Electrons from He$^+$ bombardment

For the experiments on the He$^+$-induced Secondary Emission, a He-microscope ORION from Zeiss has been used. In this case biasing the target has not been possible, because it is not well insulated: any voltage applied on it results in a current measured at the sample. While measurement 2 should not be affected much, also because the detector can be biased up to 500V, the absence of a positive bias in measurement 1 could lead to an overestimate of the beam current I_b, due to the fact that some SEs might not to be readsorbed into the target, thus subtracting a negative current from I_1. For this reason measurement 1 has not been performed, and I_b has been taken as the blanker current, as given by the instrument reading. In this case, however, there can still be an overestimation, for all the ions that reach the blanker might not reach the sample. However, a correction can be performed also in this case, thanks to simulations obtained with the Monte Carlo based code IONiSE, developed by D. Joy [45]. While there is no commercially/publicly available code that can simulate electron emission induced by any ionic species (at least

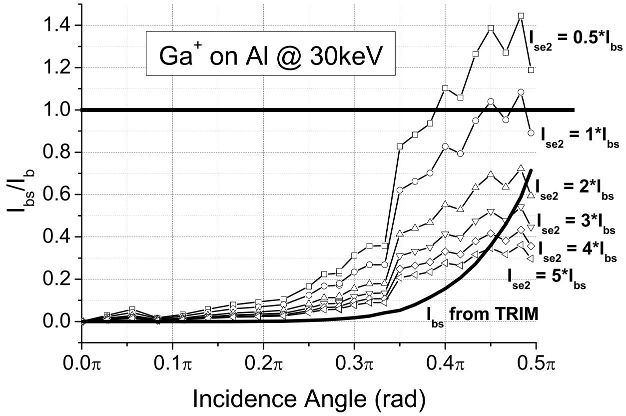

(a)

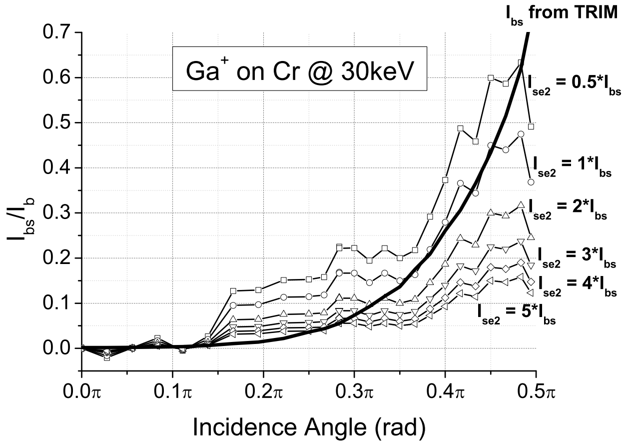

(b)

Figure 3.11: Estimation of the backscattered current, as obtained by TRIM simulation and as calculated for different values of the parameter n in equation 3.26; the curves showing values greater than 1 have no physical meaning.

none known to the authors), IONiSE is able to produce He-induced SE yields at varying beam energy, incident angle, and target material, once the correct values for the two parameters (Bethe-Salow parameters, see [63]) λ and ϵ are selected. In the present study the focus is on Al and Cr targets, whose Bethe-Salow parameters are shown in table 3.1. To take into account the likely overestimation of I_b, the experimental curves can be corrected under the assumption that the real I_b is only a fraction of the measured one: $I_b^{real} = xI_b^{meas}$ with $x \in [0, 1]$; the coefficient x is then regarded as a fitting parameter, its value being obtained matching

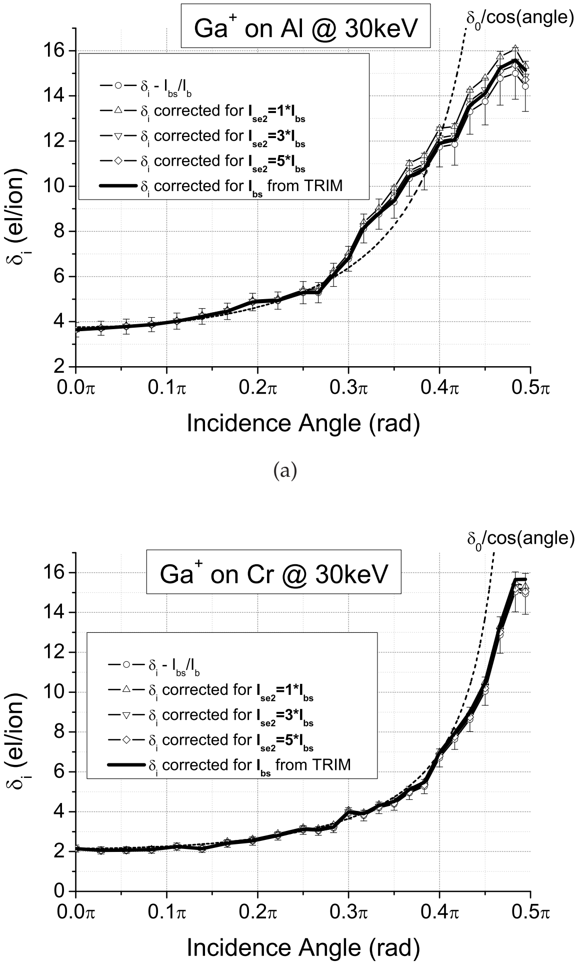

(a)

(b)

Figure 3.12: Curves of fig. 3.10 with different corrections for the backscattered current; in all cases the correction lies within the error band of the original curve. In the graphs, also the secant curve is plotted, for comparison.

	λ (Å)	ϵ (eV)
Al	12	40
Cr	7.5	70

Table 3.1: Bethe-Salow parameters for iSE emission in Al and Cr.

experimental and simulated curves. The experimentally obtained δ_i curves, both ‘raw’ and corrected, are shown together with the ones obtained via simulations in

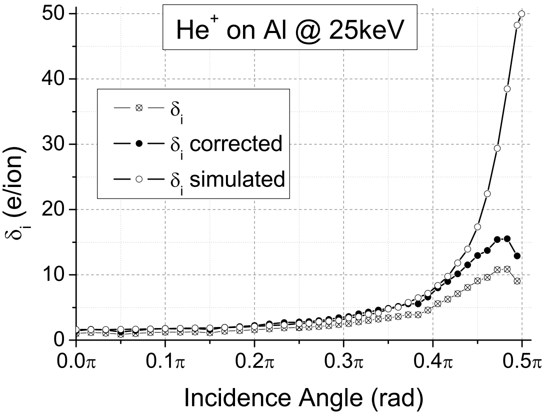

(a)

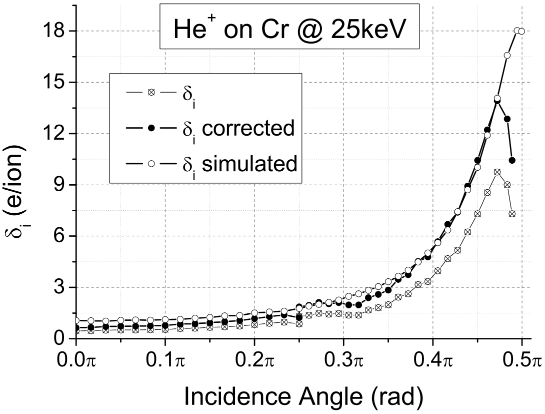

(b)

Figure 3.13: Curves of δ_i vs. α, for He$^+$ on Al and Cr at 25keV; in each graph: the curve as directly obtained by experiment; the curve as obtained by IONiSE simulation; the experimental curve normalised to the simulated values for the first part of the angle range. The discontinuity at 0.25π is due to the change of specimen.

fig. 3.13. The coefficient x appears to be 0.7 for both target materials, i.e. only 70% of the blanker ion current reaches the sample.

As for the Ga-FIB, also in this case the curves of fig. 3.13 do not take into account the current lost at the target due to the backscattered ions; also in this case, the fraction of ions that are backscattered can be simulated via TRIM, and δ_i can be corrected at each angle with equation 3.27. I_{bs}/I_b and δ_i^{corr} are shown in fig. 3.14. It is comforting that even taking into account the backscattered current, the curves

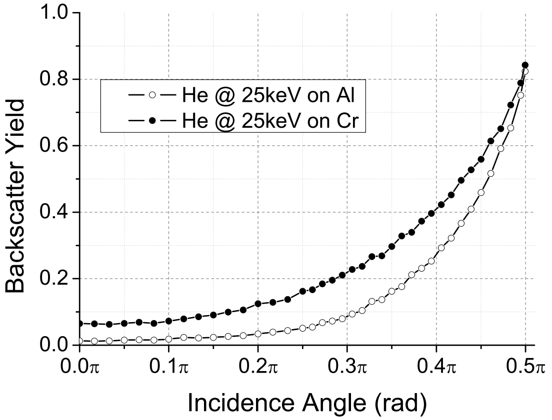

(a)

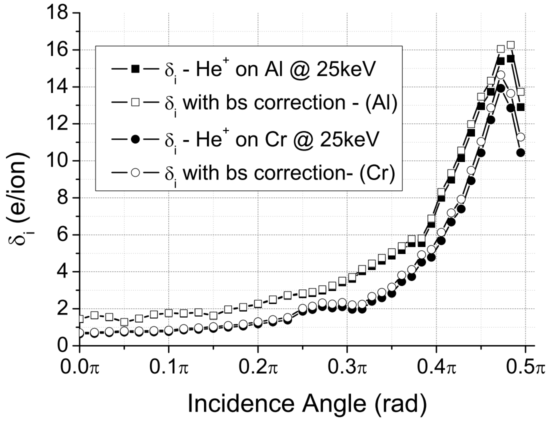

(b)

Figure 3.14: Backscatter yields for 25keV He^+ on Al and Cr (fig. 3.14(a)), and SE yields corrected for the backscattered ion current (fig. 3.14(b)).

do not change drastically.

3.3.6 Discussion

3.3.6.1 Experiments and Simulations

In fig. 3.13, experimental He-induced SE yield curves together with simulations are shown, for Al and Cr target. In the case of Cr, the two curves match almost in the whole range of incidence angles, differing only above 0.48π, while for Al they substantially differ already for angles above 0.4π. The most likely explanation for

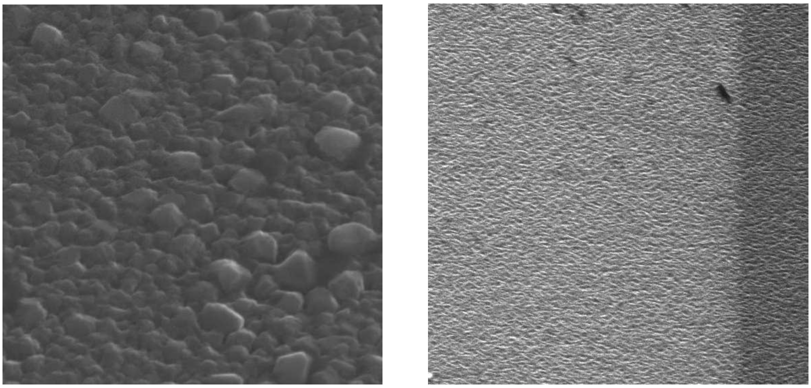

(a) (b)

Figure 3.15: SEM image of the Al sample (fig. 3.15(a)), and He image of the Cr sample (fig. 3.15(b)); both images are taken with the sample tilted at 45°, with a field of view of $2\mu\mathrm{m}$.

this discrepancy lies in the characteristics of the surface of the samples used for the measurement. Both samples have been made via sputter deposition. As it can be clearly seen in fig. 3.15(a), the Al sample looks very rough at the nanoscale, making it practically impossible for the ion beam to hit the surface at grazing angles: when α approaches $\pi/2$ macroscopically, the ion beam hits the surface structures on their side, so that the real incidence angle is always much lower than the apparent one. As a result, the measured value of δ_i at high angles is lower than the value coming from simulations. This effect is much reduced in the case of Cr (but still present) because the surface of the Cr appears to be more regular, as can be seen in fig. 3.15(b). Moreover, it is known that δ_i depends as strongly on the surface topology as on the surface composition, and any piece of Al exposed to air becomes swiftly covered with a 3-5nm thick layer of Al_2O_3. Further investigation is required in order to quantify how much the oxide layer influences the SE emission (simulations show, however, that the backscattered yield is not affected by the presence of the oxide layer). For the Ga-induced emission, simulations are not available, but the curves can still be compared with the ideal secant law (see fig. 3.12). Once again, Cr behaves 'better' than Al: while for the former the curve follows surprisingly well the secant law up to values of α higher then 0.4π, for the latter the curve appears to deviate from the secant law already for $\alpha \sim 0.25\pi$. The explanation for this anomaly is beyond the purpose of this study, but it is clear that the secant law is not always a good approximation for δ_i also at medium/high energies.

One more thing to point out is that both the Al and Cr samples used in this study are polycrystalline at the nanometric scale, i.e. the target material is assumed to be homogeneous and the length of the ion path in the bulk depends only the ion energy (for a given ion/target pair) but not on the incidence angle. If this is not the case, and the sample is monocrystalline (or coarsely polycrystalline), there will be some incidence angles that coincide with low index directions inside the lattice. Ions impinging the target under those angles will encounter a reduced resistance and will be able to travel much longer distances into the sample. This results in depressed secondary emission for certain specific incidence angles, depending on the crystal structure of the sample. A discussion on the channeling effect, including its consequences on nanofabrication, can be found in [67].

3.3.6.2 SE Yield and Image Contrast

The curves $\delta_i = f(\alpha)$ can be regarded as the first order term for the contrast mechanism in Scanning Microscopy, while higher orders come from less local effects that might enhance or suppress the escape of electrons from the sample surface. Figures 3.16(c) and 3.16(d) show the contrast obtained applying the experimental yield curves to the sample in figures 3.16(a) and 3.16(b). Figures 3.16(e) and 3.16(f) show line intensity profiles through diameters of the features, and it appears that He ions produce, for both materials, thinner edges when compared with Ga imaging. Also, the features are brighter in the He images, when related to the background level, while the material contrast is, in this case, higher in the Ga images than in the He images. In terms of the yield curves, the reason is that, although the maximum values are impressively close in all cases (~15 electrons per ion at grazing angles), the range is higher for He: $\delta_{i-max}/\delta_{i-min} \sim 16$, while the values for Ga$^+$ are between 5 and 8 (see table 3.2). This can be easily explained in terms of interaction volume, as shown in fig. 3.6. For Ga$^+$ the interaction volume is much more isotropic, with the consequence that the area of its intersection with the sample surface changes less with the incidence angle; for He$^+$, on the other hand, a normal incident beam produces many fewer electrons that are close enough to the sample surface to be emitted as SEs. Incidentally, this also means that the information carried by each pixel in a Ga image refers to a similar area around the impact point at every point of the image, while in a He image the information coming from a steep point is, so to say, less local.

3.3.6.3 Surface Modification

Fig. 3.17 shows details of the graphs I_2 vs. $time$ in fig. 3.9, recorded for ~600pA of Ga$^+$ current in a focused spot on Al. Two things strike here; firstly, the SE signal drops very fast to just a fraction of its maximum at the time zero of each new beam position; secondly, the shape of the peaks seems very repeatable at each α. The

	δ_i^0	δ_i^{max}	$\delta_i^{max}/\delta_i^0$
Ga/Al	3.6	16	4.45
Ga/Cr	2	15.5	7.75
He/Al	1.4	16.3	11.65
He/Cr	0.7	14.7	21

Table 3.2: δ_i^0, δ_i^{max} and their ratio for the different pairs ion/atom analysed in this study.

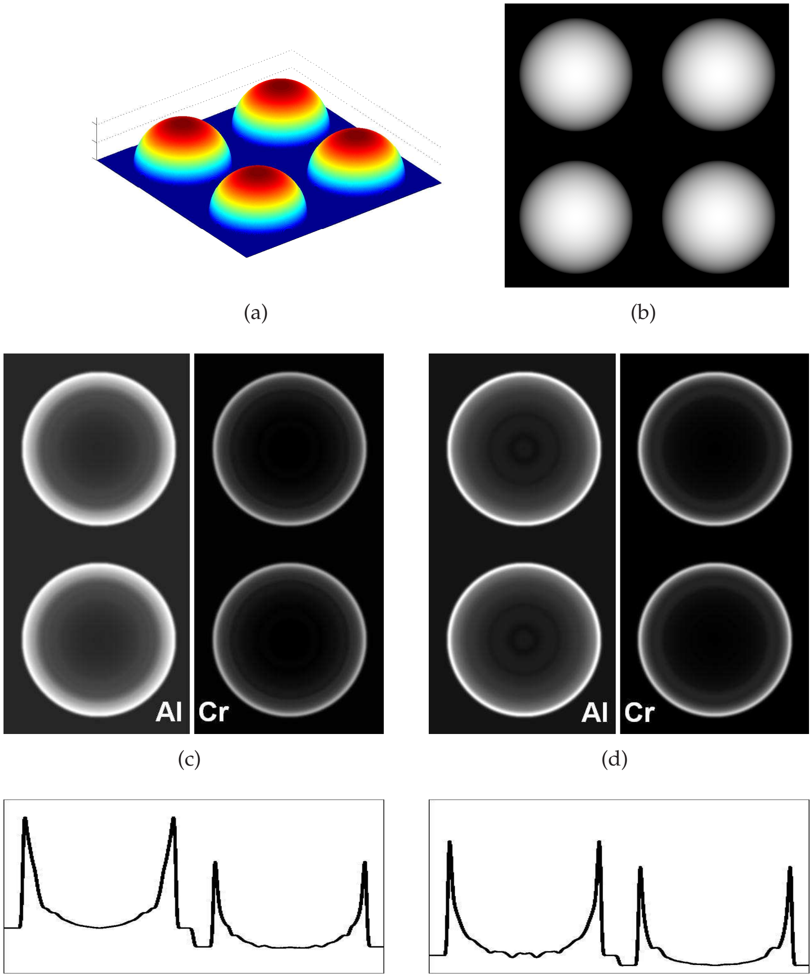

(a) (b)

(c) (d)

(e) (f)

Figure 3.16: First order material and topological contrast: sample, visualised as a 3d plot of the surface (fig. 3.16(a)) and as height map (fig. 3.16(b)); contrast from 30keV Ga^+ (fig. 3.16(c)); contrast from 25keV He^+ (fig. 3.16(d)); figures 3.16(e) and 3.16(f) show line intensity profiles through diameters of the features in the pictures above; the zero of the intensity axis is at the bottom line, the units are arbitrary.

reason of the signal drop must be connected with the surface modification that the sample surface undergoes under ion bombardment. In particular, it could be either due to sample contamination/charging (it is known in Scanning Microscopy that an area becomes darker when imaged over and over again) or to surface sputtering/redeposition: if a hole is dug, fewer electrons make it out of the sample, and the deeper the hole, the fewer electrons escape. A full understanding of this phenomenon certainly requires further investigation, but the fact that the signal

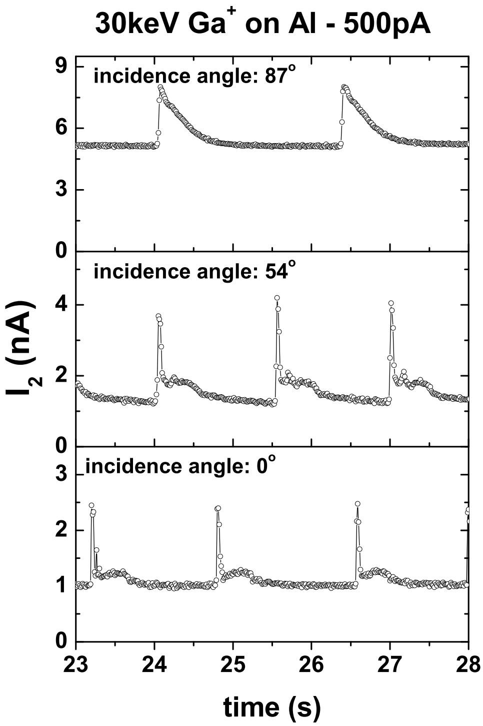

Figure 3.17: Details of the graphs I_2 vs. $time$ in fig. 3.9, showing that the current dynamics of the sample after ion bombardment to a new spot are repeatable for each incidence angle.

dynamics appears to be exactly the same at each incidence angle gives the latter explanation more credibility, for if it was due to charging/contamination, the variation would have been much less regular. Holes are indeed dug during the measurement, as it can be seen from a SEM image of an area of the Al sample subjected to ion beam irradiation during the measurement shown in fig. 3.18. Similar arguments can be made to explain the time-dependence of the current I_1 at high angles, evident from figures 3.9(e), 3.9(c) and 3.9(a). At low angles $I_1 \approx I_{se1} \approx 0$, so that $I_1 \approx I_b$, constant in time; when the angle increases, more ions are backscattered, and more SEs are produced by these ions hitting the chamber walls, thus reducing I_1; with a beam standing still on the sample, however, and a hole is dug on the sample surface, backscattered ions can enter again into the sample, so that the deeper the hole, the fewer backscattered are lost, and the fewer SE2 are produced: in time, I_1 tends to approach the value of I_b. Comparing figures 3.9(a) and 3.9(b), it appears that the variation of I_1 and I_2 is characterised by a different time constant, I_2 varying much faster. The reason for this could be the fact that, on average, backscattered ions have higher energy than SEs: they can escape from deeper holes.

The connection between time-dynamics of I_{se1} and sputtering of the sample is also

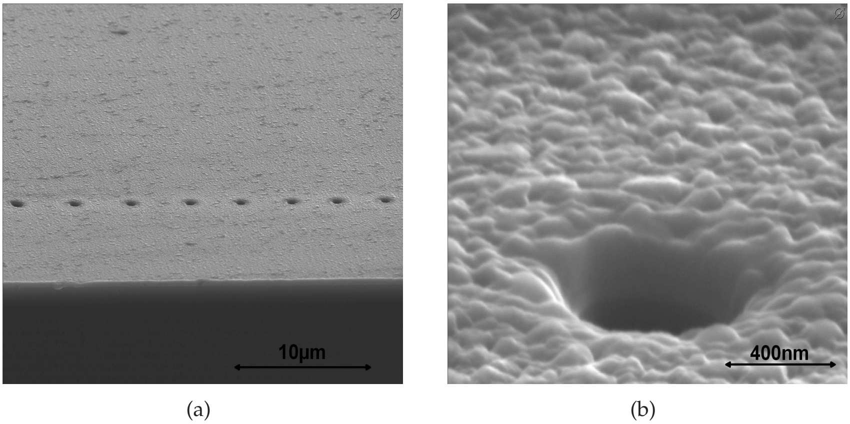

(a) (b)

Figure 3.18: SEM micrographs showing the surface modification on the Al sample due to Ga ions; each spot results from few seconds of irradiation with ~500pA in a focused beam; the field of view is 30μm in fig. 3.18(a) and 1.5μm in fig. 3.18(b).

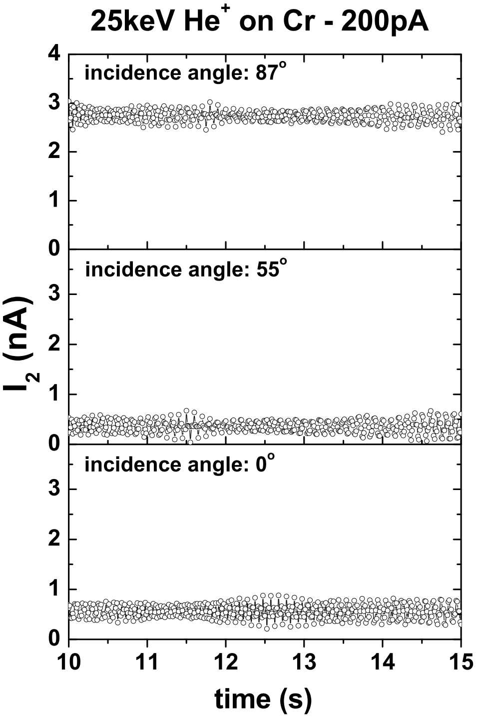

Figure 3.19: Current I_2 vs. time for 25keV He$^+$, with a focused spot of ≈200pA; the current is constant at all values of the angle α.

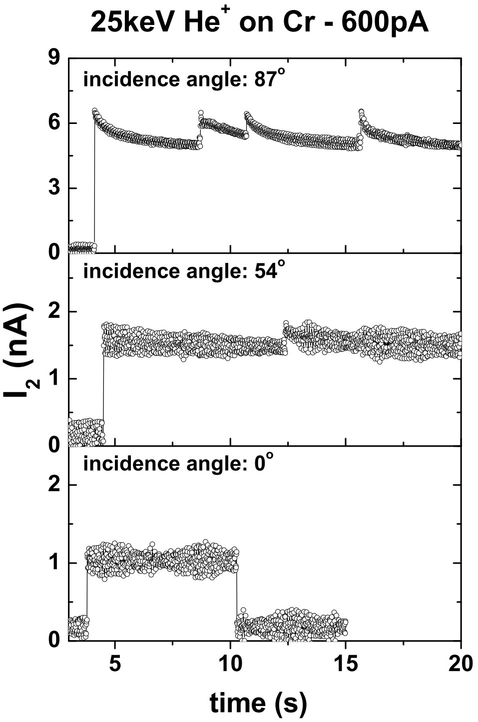

Figure 3.20: Current I_2 vs. time for 25keV He$^+$, with a focused spot of ~600pA; the current shows similar dynamics as in fig. 3.17, but smaller in magnitude and only for high α.

suggested by the plots in figures 3.19 and 3.20. Fig. 3.19 is taken for a He$^+$ current of ~200pA, and shows a constant current over the whole angle range. Fig. 3.20 is taken for a higher current, ~600pA: in this case the current signals begins decaying in time for high values of α, showing that surface modification is taking place. Fig. 3.21 compares the current signals at high incidence angle generated from a focused He$^+$ beam and from a slightly defocused one; in the first case, after the same exposure time, the ion dose received by the sample is much higher, resulting in a more profound surface modification; this is in turn reflected in a higher variation of the current signal in time. Fig. 3.22 shows the footprints of the He$^+$ beam on the Cr sample; in fig. 3.22(a) different sets of marks, showing that δ_i has dropped, are visible, the more elliptic ones coming from higher incidence angles; fig. 3.22(b) shows a spot in which a dust particle is present, on which Cr atoms appear to have been redeposited.

The fact that the signal dynamics at each new spot is repeatable for each incidence angle has a two-fold implication; on the one hand, it is a proof that each spot actually represents the sample surface, for a different one (like a particle of dust) would give a clearly different signal; on the other hand, it shows that the electronic dynamics are uniquely correlated with the topology of the surface, and

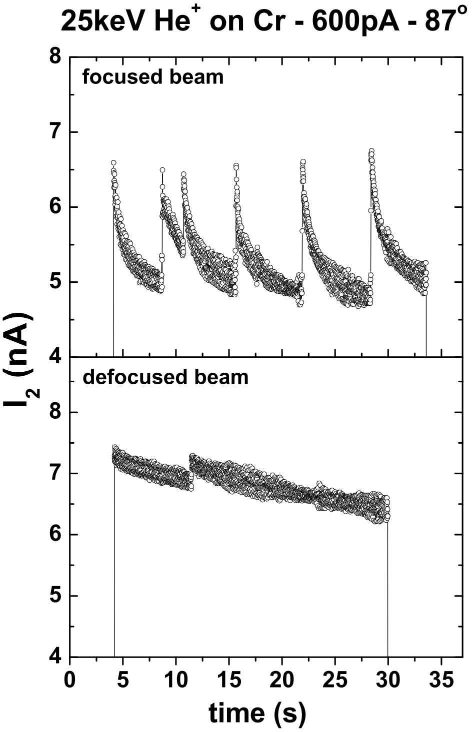

Figure 3.21: Different dynamics recorded for I_2 when probing the sample with a focused and a slightly defocused ion beam.

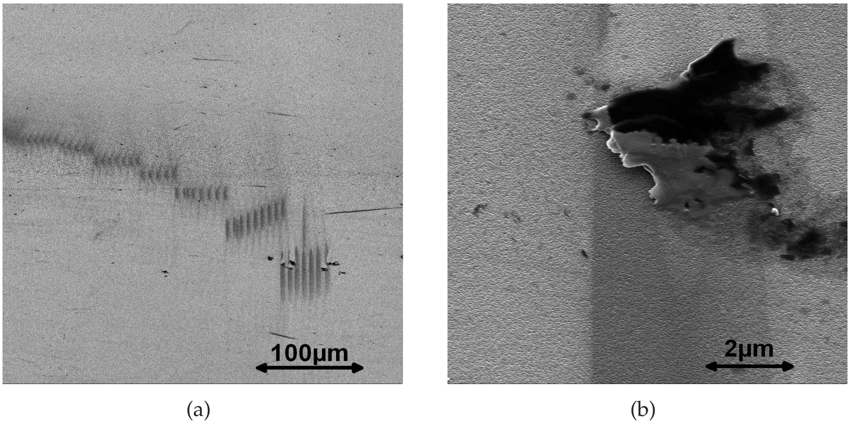

(a)

(b)

Figure 3.22: He micrographs showing the surface modification on the Cr sample due to He ions; each spot results from a few seconds of irradiation with ~600pA in a focused beam; the field of view is 400μm in fig. 3.22(a) and 10μm in fig. 3.22(b).

a further analysis of these current recordings could result in a better understanding of the sample modification under ion bombardment.

3.3.7 Conclusions

In this article, measurements of the ion-induced Secondary Electron yield as a function of the ion beam incident angle have been performed for different pairs ion/atom.

Several factors that influence the results have been analysed: modification of the sample surface under ion bombardment, backscattered ions, production of SEs from places other than the sample; the influence of each of these factors has been discussed and, in the case of the backscattered ions, quantified.

The resulting curves have been compared with the secant law (Ga-induced emission) or with simulations (He-induced emission); in both cases the Cr appears tamer than Al: the match is good up to 0.4π for Ga/Cr, and up to 0.48π for He/Cr; but only up to 0.25π for Ga/Al, and up to 0.4π for Ga/Cr.

The maximum value of δ_i is very similar in all cases ($\sim 14 - 16$ el/ion), but the SE yield range for He is higher than for Ga, due to the lower He-induced SE emission at low angles. This translates in a better topographic contrast for the He microscope.

Acknowledgments: *This work is part of the research programme "Microscopy and Modification of Nano-structures with focused electron and ion beams" (MMN) of the "Stichting voor Fundamenteel Onderzoek der Materie" (FOM), which is financially supported by the "Nederlandse Organisatie voor Wetenschappelijk Onderzoek" (NWO). The MMN programme is co-financed by FEI Company. Also, the authors wish to thank David Joy, for the kind support with the code IONiSE, and for providing the values of the Bathe-Salow parameters.*

4 CHAPTER

Resolution in Scanning (Ion) Microscopy

> *"Examples [...] show how difficult it often is for an experimenter to interpret his results without the aid of mathematics."*
>
> John William Strutt, 3$^{\text{rd}}$ Baron Rayleigh

This chapter is devoted to the analysis of the concept of resolution in scanning microscopy in general, and in ion scanning microscopy in particular. First, some of the functions involved in the image formation are presented, like the Point Spread Function and its electron-optical counterpart, the Current Density Distribution. The Rayleigh criterion for resolution is then introduced, and translated from its original optical statement to nearly equivalent electron-optical formulations. The very meaning of the Rayleigh limit is explored, both in ideal systems and in real systems as affected by noise and aberrations, and it is shown that *smallest detectable size*, *smallest resolvable distance* and *measurement accuracy* represent three interconnected aspects of the same matter. Practical methods to determine the resolution of a scanning microscope are introduced and discussed, from the simplest ones, like the 'point-to-point' method, to the most sophisticated algorithm employing the 'density of Information Passing Capacity'. Finally, it is shown that contrast response and SNR do not suffice to determine the ultimate resolution achievable with a FIB microscope, and the uncertainty stemming from the sputtering of the sample surface must be taken into account.

4.1 Prologue: PSF and Transfer Functions

Traditionally, any discussion about resolution in microscopy must stem from the Rayleigh criterion [68]. It is important to bear in mind that Lord Rayleigh was more concerned with optical tools (like the human eye) than with scanning microscopes (not yet around at his times), thus the idea of resolution á la Rayleigh must be adapted to the more familiar (for me) realm of scanning microscopy. This will be indeed the object of the next section; before that, a few definitions are needed.

An ideal imaging system would image a point-like object into a point-like image, which would give an infinite resolution (vaguely defined, at the moment, as 'resolving capability'). In reality, however, the intensity of a point-like object is not point-like in the image, but it is spread over a finite area. This is due to aberrations in the optical column, and in particular to the diffraction, which makes the intensity spread not just a technical problem, but a fundamental fact. In electron-optics the problem is worsened by the fact that some aberrations are intrinsically more difficult to correct than in the optical case.

This effect is modeled with the so-called Point Spread Function and its electron-optical counterpart, the Current Density Distribution:

- **Point Spread Function (PSF)** → response of an imaging system to a point source (object); it will be indicated in the following sections as $w_a(\mathbf{r_i}) = w_a(x_i, y_i)$, x_i and y_i being the space coordinates in the image plane;
- **Current Density Distribution (CDD)** → analogue of PSF in electron/ion-optical imaging systems; it will be indicated in the following sections as $J_{b,p}(\mathbf{r_i}) = J_{b,p}(x_i, y_i)$.

In imaging analysis it is customary to switch back and forth between spacial domain and frequency domain, depending on what is more convenient. The Fourier transform of the PSF/CDD is the Optical Transfer Function:

- **Optical Transfer Function (OTF)** → Fourier Transform of PSF (or CDD); it will be indicated in the following sections as $\tau(\boldsymbol{\nu}_i) = \tau(u_i, v_i)$, u_i and v_i being the frequency coordinates in the image plane.
  In optics:

$$\tau\left(u, v\right) = \int_{-\infty}^{+\infty} \int_{-\infty}^{+\infty} w_a\left(x, y\right) \mathrm{e}^{-j2\pi(ux+vy)}\, \mathrm{d}x\mathrm{d}y\ . \tag{4.1}$$

  In electron-(ion-)optics:

$$\tau\left(u, v\right) = \int_{-\infty}^{+\infty} \int_{-\infty}^{+\infty} J_{b,p}\left(x, y\right) \mathrm{e}^{-j2\pi(ux+vy)}\, \mathrm{d}x\mathrm{d}y\ . \tag{4.2}$$

- **Modulation Transfer Function (MTF)** → modulus of the OTF.
- **Phase Transfer Function (PTF)** → phase of the OTF.

Most microscopes are not equipped with phase detectors[1], which makes the MTF the important parameter. In this case, a perfect imaging system would have a

---

[1] Phase of light in optics, phase of electrons in electron-optics.

MTF equal to 1 and a PTF equal to 0 in the whole range of spatial frequencies. When a phase detector is available however, and the PTF is function of the spatial frequency and/or of the sample materials, phase contrast images can be formed.

4.2 Resolution in Absence of Noise

4.2.1 The Rayleigh Criterion

In Rayleigh's view, the resolution is etymologically defined as the ability of 're-solving' two details in an image.

Rayleigh's Resolution: *The resolution can be defined as the minimum distance between separate point-like objects that can be distinguished in the image.*

Let's consider a point-like object in an imaging system whose only aberration is diffraction[2]. In the case of a circular aperture and for unitary intensity, the PSF (i.e. the image), given the symmetry, has the following form [69]:

$$w_a\left(R_i\right)=\left(\frac{2J_1\left(R_i\right)}{R_i}\right)^2 \quad , \quad \text{with} \quad R_i=2\pi r_i\frac{\lambda}{\alpha_i}=2\pi\sqrt{x_i^2+y_i^2}\,\frac{\lambda}{\alpha_i}\ , \tag{4.3}$$

where $J_1(R_i)$ is the first-order Bessel function, λ is the wavelength of the light used, and α_i is the aperture semi-angle at the image plane. When the PSF has the form given by eq. 4.3, it is called *Airy pattern*. A graphical representation of eq. 4.3 is shown in fig. 4.1 When imaging two close point-like objects, their Airy patterns will overlap to some extent; in a diffraction-limited incoherent system, the intensity of the image for two neighboring point-like objects is the sum of the PSFs of each object, as shown in fig. 4.2. Rayleigh criterion, in its original formulation, simply defines how close the Airy patterns can be before the two imaged points become indistinguishable.

Rayleigh Criterion: *Two monochromatic spectra should be regarded as being just resolved when the maximum of one spectrum coincides with the minimum of the other.*

The criterion is graphically represented in fig. 4.3. The first zero of w_a, as defined by eq. 4.3, is at $r_i = 0.61\lambda/\alpha_i$; the disk of radius $r_i = 0.61\lambda/\alpha_i$ is called *Airy disk*. According to the Rayleigh criterion, therefore, the numerical value of the resolution in a diffraction-limited system coincides with the radius of the Airy disk:

$$R_{es,RC}=r_{i,RC}=0.61\frac{\lambda}{\alpha_i}\ . \tag{4.4}$$

At the local minimum between the two global maxima, the sum of the two PSFs assumes a value that is approximately equal to 73.5% of the intensity value at the peaks. Requiring that the intensity at the image plane between two points must be equal or smaller than 73.5% of its peak value (*Rayleigh limit*), in order to be able to resolve the two points, is an alternative way of stating the Rayleigh criterion. In

---

[2] For some authors diffraction is not an aberration because it is a fundamental limit; I count it as an aberration.

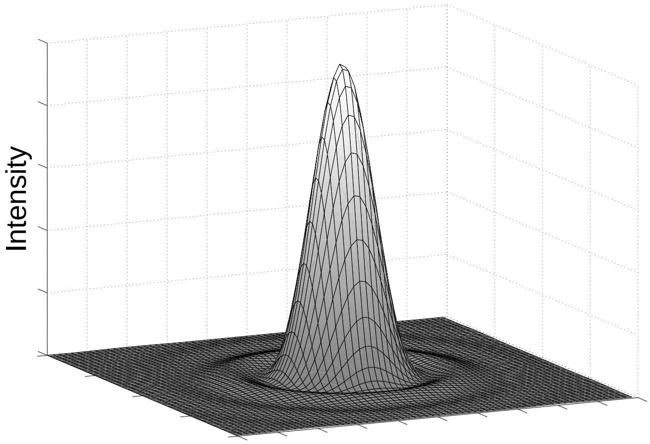

Figure 4.1: Graphical representation of the Airy pattern (eq. 4.3).

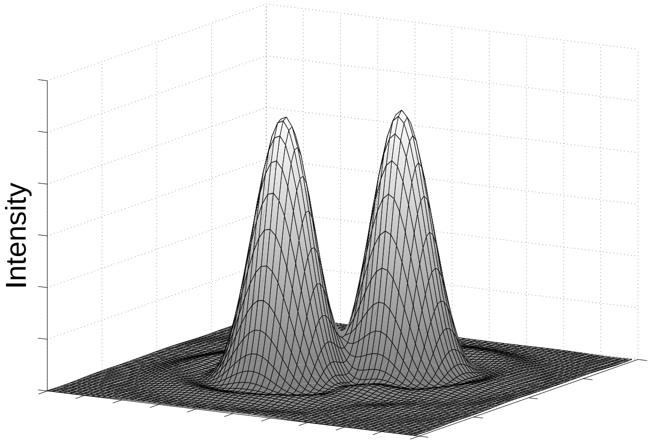

Figure 4.2: Image of two close point-like objects in a diffraction-limited incoherent imaging system: the intensity is given by the sum of the two PSFs.

this way, it can be easily exported to any image-forming system, without requiring anything on the PSF, but just declaring two imaging point 'resolved' when the minimum intensity between them is equal, or smaller, than the peak intensity.

Leaving a more detailed discussion on the meaning and limitations of the criterion to the end of this section, it should be noted here that the choice of the value of the minimum intensity drop for which two image points can be distinguished

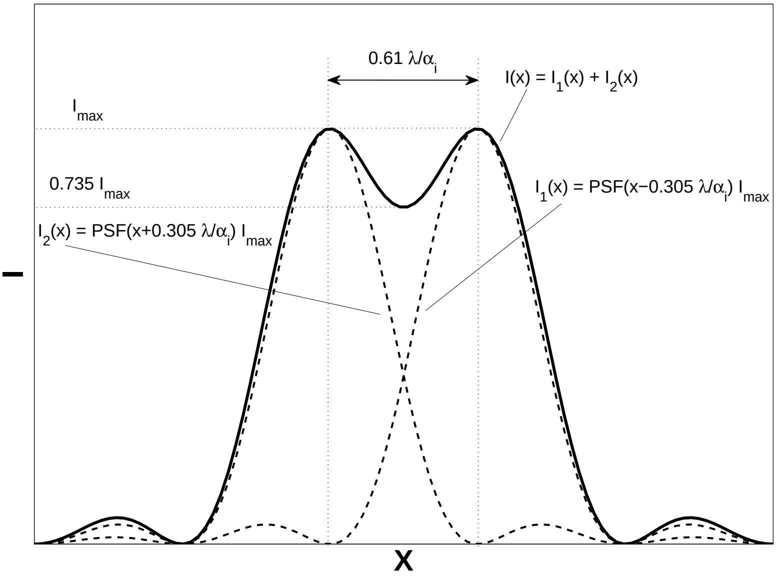

Figure 4.3: Monodimensional representation of the Rayleigh criterion: two points can be distinguished if the maximum of one PSF coincides with the first minimum of the other; in this case the two Airy patterns I_1 and I_2 are separated by a distance $0.61\lambda/\alpha_i$.

stems from considerations regarding the human eye resolving power (or, at least, what it was supposed to be at Rayleigh's times). Thus it is, somehow, arbitrary. Once the value is chosen, however, it uniquely defines the resolution of a given imaging machine, assigning a number to it that does not depend on anything else but the machine itself.

4.2.2 Rayleigh in Scanning Microscopy: Resolution as Beam Size

The Rayleigh criterion, though stated for optical imaging systems, can be easily exported to scanning microscopy. Also in this case, its formulation is based on a strong assumption about the CDD, but can then be applied in situations where nothing is actually known about the beam current distribution.

In an ideal aberration-free electron-optical system, the CDD can be assumed to be Gaussian:

$$J_{b,p}\left(r\right) = \exp\left[-\left(\frac{r}{c}\right)^2\right] , \tag{4.5}$$

c being the value of r at which the intensity has fallen to 1/e of the maximum (assumed unitary in eq. 4.5), and can be defined as the beam radius r_b[3]. The sum of two overlapping Gaussian CDDs, shown in fig. 4.4, looks pretty similar to the sum of two overlapping Airy patterns of fig. 4.3; in this case, the Rayleigh limit is reached when the two Gaussians are separated by a distance $\sim 2r_b$ Thus, according to the Rayleigh criterion, the resolution of an electron-optical system with a Gaussian CDD corresponds to the beam diameter $2r_b = d_b$, better referred to as *beam size*.

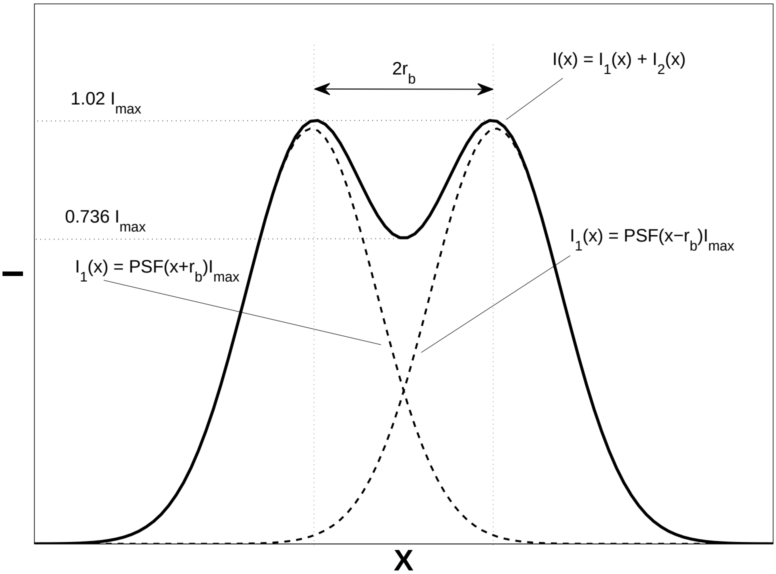

Figure 4.4: Monodimensional representation of two overlapping Gaussian distributions I_1 and I_2, separated by a distance $2r_b$; these curves look very similar to the curves in fig. 4.3.

Defining the resolution of a scanning microscope as the beam size is a choice. Leaving for later the discussion about the decency of this choice, in this view quantifying the resolution means quantifying the beam size. Which is a problem in its own right. It is common practice to calculate the size of the beam on the basis of following contributions (the subscript i refers, as usually, to quantities calculated on the image plane) [70].

- image of the virtual source:

$$d_g = M d_v \ , \tag{4.6}$$

where M is the magnification of the system and d_v is the diameter from which the rays appear to originate (which is not necessarily coincident with

---

[3] The definition of the beam radius is in fact arbitrary, since the current distribution is never a block function.

the diameter of the area from which the electrons are actually emitted, hence the distinction between 'real source' and 'virtual source');

- spherical aberration contribution, arising from the fact that electrons travelling at different distances from the optical axis are not exactly focused in the same point:

  $$d_s = K_s C_{s,i} \alpha_i^3 \ , \tag{4.7}$$

  where $C_{s,i}$ is the spherical aberration coefficient and α_i is the aperture semi-angle;

- chromatic aberration contribution, arising whenever the beam is not strictly monochromatic, but is instead characterised by an energy distribution:

  $$d_c = K_c C_{c,i} \frac{\Delta E_b}{E_b} \alpha_i \ , \tag{4.8}$$

  where $C_{c,i}$ is the chromatic aberration coefficient, E_b is the energy of the primary beam and ΔE_b is its variation in the electron (ion) population;

- diffraction contribution, always present, defined as the diameter of the Airy disk:

  $$d_a = K_d \frac{\lambda}{\alpha_i} \ , \tag{4.9}$$

The values of the constants K_s, K_c and K_a are still object of discussion, depending on the definition of the size of a distribution. For example, the size could be the width of distribution that accounts for a certain share of the current, or the width of the distribution corresponding to a certain fraction of its maximum. If the CCD were known, they could be mathematically calculated, and the relations between the values according to different definitions would also be known. Since this is not the case, they must be estimated fitting experimental data. For this reason, the Full Width that comprises 50% of the current (FW50) should be preferred to the Full Width at Half Maximum (FWHM), especially for distributions that deviate much from Gaussian (see fig. 4.5). Estimated values of the constants in Scanning Electron Microscopy for the two choices are given in [70], and summarised in tab. 4.1.

	FWHM	FW50
K_s	0.50	0.18
K_c	0.34	0.60
K_a	0.61	0.54

Table 4.1: Values of the constant appearing in equations 4.7, 4.8 and 4.9, for the two different choices as size of a distribution.

Other arguments arise when it comes to sum all these contributions to build up the actual probe size. In this case the choice depends on the shape of the current

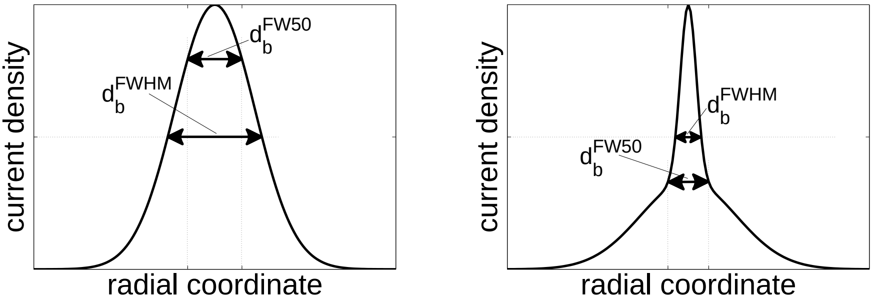

(a) (b)

Figure 4.5: Sizes at FWHM and at FW50, for a Gaussian distribution (fig. 4.5(a)) and for a distribution with a narrow peak and wide tails (fig. 4.5(b)); in the first case the size at FWHM is bigger; in the second case the opposite is true.

distribution (or rather, on the assumption, since the shape is usually unknown). Gaussians must be added quadratically:

$$d_b = \sqrt{d_g^2 + d_s^2 + d_c^2 + d_a^2}\ . \tag{4.10}$$

However, since real beams are hardly Gaussian, a quadratic sum is not justified. In fact, it appears that the best way of calculating the final beam size, at least for electron microscopes, is the following [70, 71]:

$$d_b = \sqrt{\left[d_g^{1.3} + (d_s^4 + d_a^4)^{1.3/4}\right]^{2/1.3} + d_c^2}\ , \tag{4.11}$$

where all the size contributions are FW50.

At this point, there could be some confusion about the very meaning of resolution. It has been shown that in Rayleigh's view resolution is the smallest distance between two points on the image plane that can still be distinguished. Therefore, it relates to a pair of features on a background, imaged by an optical diffraction-limited microscope. It has been also shown that the concept can be translated almost directly into the realm of scanning microscopy, exploiting the similarity between two overlapping Airy patterns and and two overlapping Gaussian distributions[4]. However, if the resolution is nothing else than the spot size (or the Rayleigh limit), a number can be assigned to it always, independently of the number of features in the image. In order to reconcile these two apparently different concepts, it is worthwhile to investigate what the Rayleigh limit really is in scanning microscopy. The normal imaging mode in Scanning Electron and Ion Microscopy is with SE contrast, as it has been discussed in chapter 3. It has also been

---

[4] The requirement that the CDD is Gaussian is not necessary; a different model could be chosen, as long as the relation between the distribution and its 'size' is known.

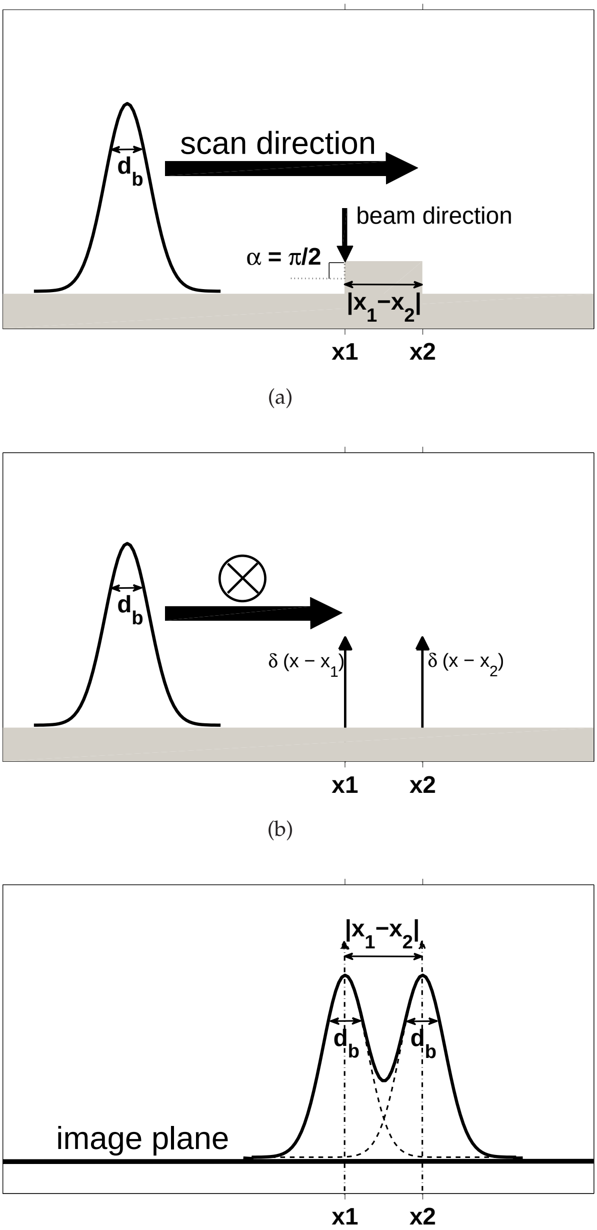

(a)

(b)

(c)

Figure 4.6: Schematic of imaging formation in scanning microscopy; 4.6(a): scanning of the sample; 4.6(b): convolution of the CDD with the transform of the sample surface into the the incidence angle domain; 4.6(c): image.

shown that the SE signal is not (pseudo-)proportional to the height of the object, but to the angle formed by the beam and the direction normal to the object surface. This means that SEM/SIM images do not relate to the object surface, but to its first derivative. Fig. 4.6 shows, very schematically, the process of image formation, in the ideal case of a flat surface with one rectangular feature on it, with flat surface and vertical walls. Scanning the beam along the surface (fig. 4.6(a)) means convolving the CDD with the transform of the sample surface into the incidence angle domain, which is the linear combination of two delta functions centered at each edge of the feature, $\delta(x - x_1)$ and $\delta(x - x_2)$ (fig. 4.6(b)). The convolution of the CDD with a delta function is of course the function itself; the resulting image, therefore, will be the sum of two CDDs, centered at the position of the two edges (fig. 4.6(c)). A situation very similar to what Lord Rayleigh had in mind with his two-component system!

We can go a bit further. Following [72], in the evaluation of resolution there can be two kinds of errors, systematic and statistical. Systematic errors arise from the choice of the model: in this case we are assuming a three-parameter model, in which the parameters are the two locations where the CDD is sampled, and its variance (or size). We are also assuming that it is the correct model, so there is no need to worry about systematic errors. About the statistical errors, one might think that there aren't any, because we are still neglecting the noise. And this would indeed be the case, if a perfect knowledge of the CDD were available. If the Gaussian curves shown in these pages were the exact current distribution functions, then the knowledge of the system would be complete, and the resolution would be infinite (i.e. the smallest resolvable distance would be 0). However they are not, for they are an estimate of the image point based on the chosen model. The CDD should thus be regarded as the probability density function for the current density, and not as a deterministic current function. Looking again at fig. 4.6(c), which represents the image of the object in fig. 4.6(a), we can estimate the dimension of the object as $|x_1 - x_2| \pm 2r_b = |x_1 - x_2| \pm d_b = |x_1 - x_2| \pm R_{es,RC}$. It can be concluded that:

> *in scanning electron and ion microscopy, when there is no knowledge of the current density distribution, the Rayleigh resolution $R_{es,RC}$ can be regarded as the uncertainty with which a dimension can be estimated from a micrograph.*

The confidence level that is associated with a measurement error depends, of course, on the model chosen. In this case, being d_b the Gaussian size of a two-parameter model (the model has three parameters when considering the Gaussian pair, a single Gaussian has two parameters), the statement above means that we can claim that the size of the imaged feature falls somewhere in the interval $[|x_1 - x_2| - d_b, |x_1 - x_2| + d_b]$ with a confidence of 68.3%. When the estimated size of the feature becomes smaller, the relative measurement error increases, up to 100% when the separation distance between the two edges is exactly d_b. When the distance becomes even shorter, that is, when the Rayleigh limit is exceeded, nothing anymore can be said about the size of the feature, because there is a non-zero probability that its size is negative, i.e. there is no feature. The numerical value of this probability can be calculated from the sum of the two overlapping distributions; when they are perfectly superimposed, for example, in the Gaussian model that has been discussed so far the probability of existence of the feature is 68.3%.

4.2.3 A Quick Tour into the Frequency Domain

It has been pointed out already that the Rayleigh criterion can be expressed (and generalised) in terms of contrast difference between the intensity of two peaks in the image and the 'valley' separating them. An alternative way to formulate the Rayleigh criterion of resolution is in the spatial frequency domain, through Fourier transformation. One of the main advantages of this approach is that any operation of convolution in the real space becomes a simple multiplication in the Fourier domain. Following [73], if the object is defined by the scalar field $s_o(x_o, y_o)$, the image s_i is given by s_o convolved with the current density J_b[5]:

$$s_i\left(x_i, y_i\right) = s_o\left(x_o, y_o\right) \otimes J_b\left(x, y\right) \ . \tag{4.12}$$

The Fourier transform of the image is therefore given by:

$$F\left[s_i\left(x_i, y_i\right); u, v\right] = F\left[s_o\left(x_o, y_o\right); u, v\right] \cdot F\left[J_b\left(x, y\right); u, v\right] \ . \tag{4.13}$$

The Fourier transform of the J_b is the frequency response of an imaging system as degraded by a finite CDD, and it is indicated with τ_b; in a rotationally symmetric system it can be written as:

$$\tau_b\left(\nu\right) = \frac{F\left[J_b\left(r\right); \nu\right]}{F\left[J_b\left(r\right); \nu\right]_{\nu=0}} \ , \tag{4.14}$$

where $r = \sqrt{x^2 + y^2}$ and $\nu = \sqrt{u^2 + v^2}$ and F is the Fourier operator defined as:

$$F\left[f\left(r\right); \nu\right] = \int_0^\infty f\left(r\right) J_0\left(2\pi\nu r\right) r \, \mathrm{d}r \ , \tag{4.15}$$

J_0 being the 0th-order Bessel function. If the object is point-like, J_b becomes $J_{b,p}$, its Fourier transform is the OTF $\tau(\nu)$, and its amplitude $|\tau|$ is the MTF. The degraded OTF τ_b can be then expressed in terms of the MTF:

$$\tau_b\left(\nu\right) = \tau_s\left(\nu\right) \left\|\tau\left(\nu\right)\right\| \quad \text{with} \quad \tau_s\left(\nu\right) = \frac{F\left[J_s\left(r\right); \nu\right]}{F\left[J_s\left(r\right); \nu\right]_{\nu=0}} \ , \tag{4.16}$$

where $J_s(r)$ is the CDD at the image plane. In an ideal (i.e. aberration free) optical system, the one for which the criterion was originally formulated, $J_{b,p}(r)$ is the Airy pattern, and the MTF is:

$$\left\|\tau^{id}\left(\bar{\nu}\right)\right\| = \frac{1}{\pi}\left(\theta - \sin 2\theta\right) \ , \tag{4.17}$$

---

[5] J_b differs from $J_{b,p}$ for it is the current density distribution coming from a finite size source, thus not necessarily from a point-like object.

where $\bar{\nu} = (\lambda/\alpha_i)\nu$ is a dimensionless spatial frequency and $\theta = \cos^{-1}(\bar{\nu}/2)$, with $\bar{\nu} \leq 2$. The Rayleigh criterion, formalised by eq. 4.4, can be combined with eq. 4.17:

$$r_{i,RC} = 0,61\frac{\lambda}{\alpha_i} = \nu_{RC}^{-1} \quad \Rightarrow \quad \bar{\nu}_{RC}^{-1} = \frac{1}{0.61} \quad \Rightarrow \quad \left\|\tau_{RC}^{id}\right\| \cong 0.1\ . \tag{4.18}$$

Eq. 4.18 shows that, in an ideal system, the reciprocal of the spatial frequency ν for which the MTF assumes the value of 0.1 is resolution limit corresponding to the Rayleigh criterion. This result can be extended to real systems, in what is actually an approximation of the Rayleigh criterion stated in the frequency domain:

$$r_{i,RC} = \nu_{RC}^{-1} : \quad \tau_b\left(\nu_{RC}^{-1}\right) = 0.1\ . \tag{4.19}$$

Eq. 4.19 is 'visualised' in fig. 4.7.

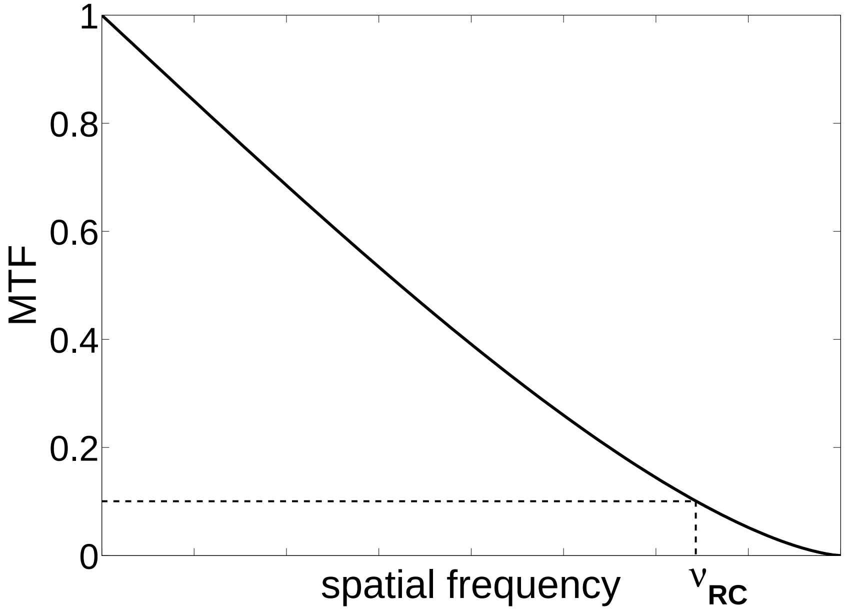

Figure 4.7: MTF of an aberration-free optical system, showing the analogue of the Rayleigh criterion in the frequency domain.

4.3 Resolution in Presence of Noise

The entire discussion so far has been carried out in the assumption of a deterministic relation between the current density and the contrast response of the object. In reality, however, both the current density and the contrast response must be regarded as stochastic quantities. In fact, the stochastic nature of the CDD has been considered already, otherwise the resolution would blow up to infinity. The amount of secondary particles emitted, however, used to build up the image and described by the yield curves that are the object of chapter 3, is certainly not deterministic: it fluctuates around the expected value.

4.3.1 Noise into the Rayleigh Criterion

Fig. 4.8(a) shows the image of two point-like objects, for a Gaussian beam, in the presence of random noise proportional to the pixel density[6]. This time, distinguishing the two points in the image is not immediate, even though 4.8(a) has been obtained adding noise to two Gaussians profiles separated by the distance d_b, thus exactly at the Rayleigh limit, as shown in fig. 4.8(b). It seems that, in presence of noise, the resolution cannot be quantified by $R_{es,RC}$ anymore. However, according to my way of thinking, the Rayleigh-based analysis is still perfectly valid. In sec. 4.2.2 it has been shown that one interpretation of the Rayleigh limit in scanning microscopy is in terms of uncertainty of a given measurement on the image plane: in a Gaussian model, d_b is the uncertainty of the measurement with a level of confidence equal to 68.3%. When the response of the object is not deterministic, but affected by noise, there is a certain confidence level also associated with the estimated value of the Gaussian model, namely, the position and the width of the peaks. The confidence level associated with the uncertainty d_b is therefore degraded by the lower-than-100% confidence level affecting the contrast function itself. If the Rayleigh's resolution is defined as the measurement uncertainty with a 68.3% confidence level, and I believe this is the right way to define it, in presence of noise this quantity will be bigger than the spotsize! Another way to see it is exemplified in fig. 4.8(c). The image of the point-like objects is not a singled-valued function anymore, but a thick band associated to a confidence level representing the probability that the intensity value at a certain point falls somewhere in it. Even in the ideal case of a finite band thickness for a 100% confidence level, when the center of the bands draw Gaussians that are separated by the distance d_b (curves 1 and 2), the bands as a whole are separated by a distance that is lower than the Rayleigh limit. All the curves in fig. 4.8(c) have the same Gaussian radius, so it could seem that d_b is still the minimum distance that allows the two objects to be resolved in the image. However, looking, for example, just at the curves 1.a and 2.b, one can notice that while they are still separated by the distance d_b, the intensity drop between them is lower than the Rayleigh limit of 73.5%. The two image points cannot be separated according to Rayleigh's rule.

Summarising, the Rayleigh's approach is still valid also in presence of non-negligible noise. Just, the resolution is degraded by finite confidence levels for the system's response, and the measurement uncertainty, or, equivalently, the smallest detectable size, will be greater than $R_{es,RC}$.

Without entering into the mathematics of noise, which is discussed in chapter 3, let's just say here that the main consequence of the stochastic nature of the

---

[6] An underlying assumption of the whole chapter is that the sample is correctly sampled; in case of undersampling, of course, a degradation of resolution, when compared to ideal case, is expected.

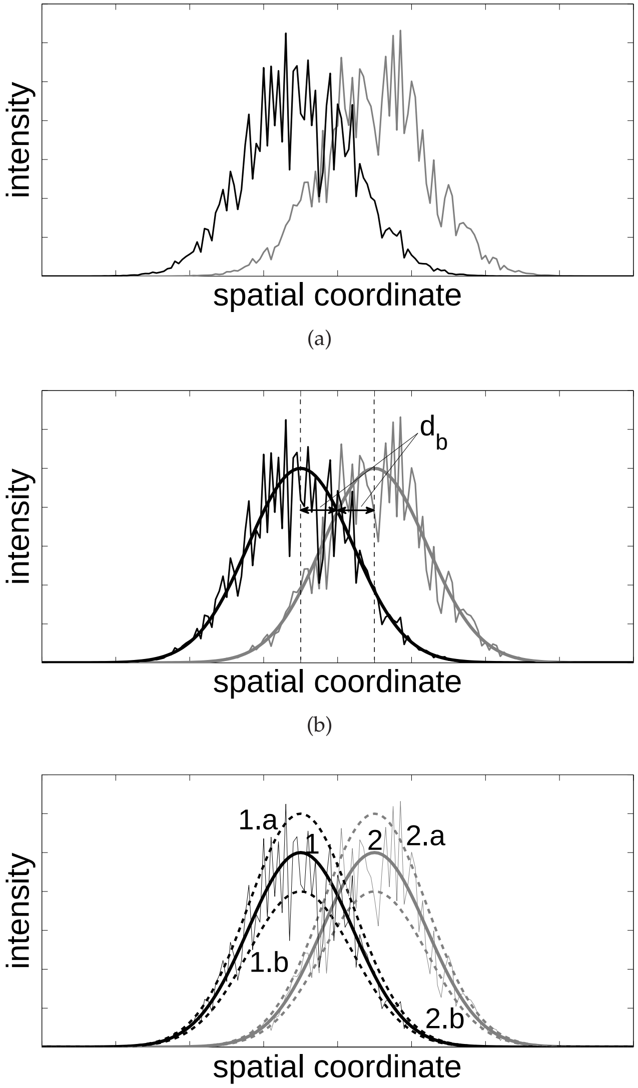

(a)

(b)

(c)

Figure 4.8: Two noisy Gaussians separated by the distance d_b are not resolvable because the Rayleigh limit for the contrast drop between them is not reached.

system response is not in the degradation of the resolution limit, but in the introduction of a time-dependence for this limit itself. The reason is that, while both signal and noise increase with the electron/ion dose (or dwell time), the noise increases more slowly than the signal. Since the degradation of the resolution is not dependent on the absolute noise, but on the SNR (the discussion before was implicitly assuming a normalised intensity), the result is that the resolution limit decreases with increasing the ion/electron dose (see fig. 4.9). Fig. 4.10 provides a graphic visualisation of the difference between an approach that takes noise into account, and one that does not. In the latter case, the Rayleigh limit is constant with dose and coincident with the spot size d_b; when noise is included in the model, the Rayleigh limit is generally bigger than the spot size, decreases with

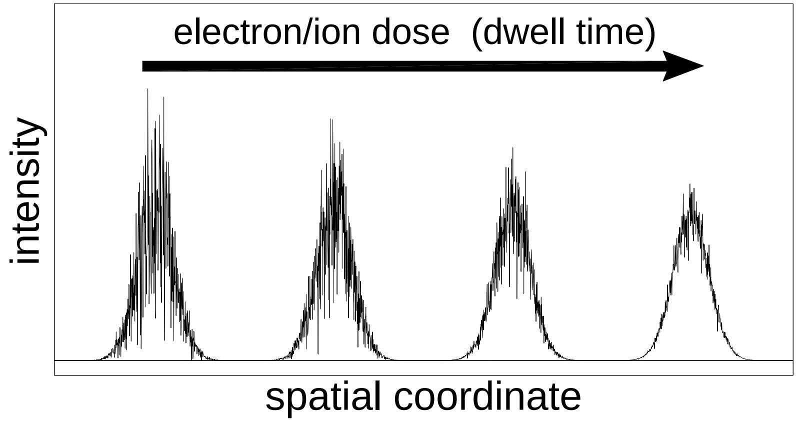

Figure 4.9: The Signal-to-Noise Ratio in a scanning microscope image increases with the dose, so that the resolution degradation decreases.

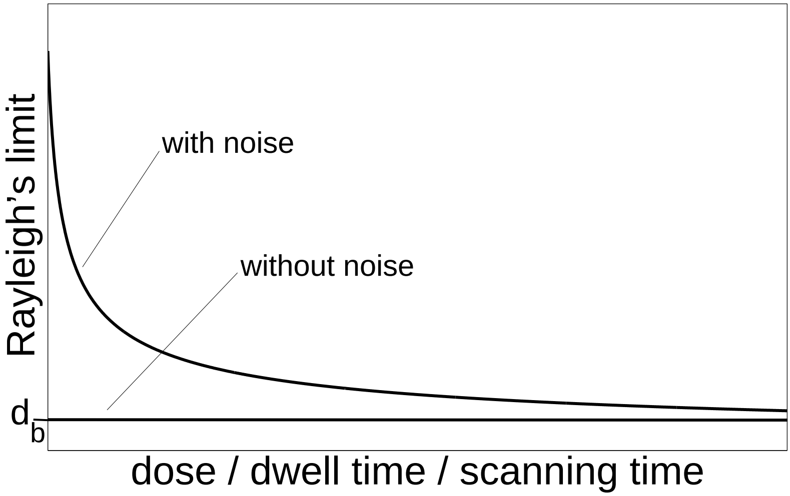

Figure 4.10: When noise is not taken into account, the Rayleigh limit is constant; in presence of noise, it decreases with increasing dose.

increasing dose/dwell time, and reaches the numerical value d_b at infinity. In this theoretical framework it is always possible to push the resolution down to the spot size limit: all what is needed is imaging the sample for a very long time in order to reach very high values of SNR. In reality this is not possible, for there are limitations to the amount of time that can be used to build up the image, and thus to the obtainable SNR level. It is always true that the collected signal can never be infinite. In ion microscopy, in particular, the main limitation is represented by the sputtering of sample material due to the high-energy impinging ion. An extensive discussion about the sputtering effect and the way it limits the resolution in ion microscopy will be the subject of the next chapter. Before that, a different concept of resolution based on information theory will be presented, and some practical methods of resolution assessment will be considered and discussed.

4.3.2 Resolution Based on Image Quality

In this section, a theory of resolution based on information theory, developed by M. Sato and J. Orloff in the early 90's [74], is presented.

The basic idea is the evaluation of the resolution in terms of the quality of the image produced by an (electron-)optical system, together with the consideration that any suitable figure of merit of an image, q_{im} must depend on the resolution (defined as the ability of distinguish two point-like objects next to each other) and the Signal-to-Noise Ratio (SNR) k_{sn}:

$$q_{im} = q_{im}\left(R_{es}, k_{sn}\right) \ . \tag{4.20}$$

If two images from a point-like object, one produced by an ideal system, and the other produced by a real system (where aberrations are present and the source is not infinitely small), have the same quality and the same SNR, then:

$$q_{im}\left(R_{es}^{id}, k_{sn}\right) = q_{im}\left(R_{es}, k_{sn}\right) \quad \Rightarrow \quad R_{es} = R_{es}^{id} = 0.61\frac{\lambda}{\alpha} \ . \tag{4.21}$$

Eq. 4.21 means that the resolution of an image from a point-like object produced by an imperfect imaging system is the same as the one produced by an ideal system, if the image quality and the SNR are the same.

If an image is regarded as a received message, then each image produced by a given imaging system is a *message state*. In a digital imaging system, the total number of possible images, and thus the total number of message states, is $N_g^{N_{px}}$, with:

- $N_g \rightarrow$ number of intensity levels;
- $N_{px} \rightarrow$ total number of pixels in the image.

Assuming that every state has the same prior probability, the information content of a single image is given by:

$$H = N_{px} \ln N_g \ . \tag{4.22}$$

It is worthy to note that eq. 4.22 can also be written for optical imaging systems, once the produced images are discretised, in terms both of space and intensity; doing this operation, the smallest detectable change in intensity will be a function of the SNR in the image, while the number of pixels, intended as portions of the image in which the intensity variation is negligible (isoplanatic patch), will depend on the image resolution:

- $N_g = N_g(k_{sn})$;
- $N_{px} = N_{px}(R_{es})$.

The parameters determining the information content are the same as those determining the quality of an image (see eq. 4.20).

What is needed now is a suitable figure of merit for the quality of an image; a good one could be the *mean information content* H_A [75], that, applying the theory of charged particle optics developed by E.H. Linfoot in the 50's [76] can be written as:

$$H_A = \frac{A}{2\ln 2} \int\int \ln\left[1 + \left|\frac{S(u,v)}{S(0,0)}\right|^2 k_{sn}\right] \mathrm{d}u\mathrm{d}v \ , \tag{4.23}$$

where S is the 2D Fourier transform of the image intensity field, A is the pixel area (or the area of an isoplanatic patch), and k_{sn} is the SNR in A[7]. The information content H_A can be divided by A to obtain the more general *density of information content* ρ_H:

$$\rho_H = \frac{H_A}{A} = \frac{1}{2\ln 2} \int\int \ln\left[1 + \left|\frac{S(u,v)}{S(0,0)}\right|^2 k_{sn}\right] \mathrm{d}u\mathrm{d}v \ . \tag{4.24}$$

In a real system, the image of a point-like object is not just the PSF/CDD but its further convolution with the raster size of the screen used for display; assuming a cylindrical symmetry, and a Gaussian raster intensity distribution with radius r_{rast}, this blurred PSF can be written as:

$$w_{ar} = \mathrm{e}^{-(r_i/r_r)} \quad \text{with} \quad r_r = \frac{r_{rast}}{M_{scr}} \ , \tag{4.25}$$

M_{scr} being the magnification of the screen. The 2D Fourier transform of w_{ar} is called *acceptance factor*, and it is indicated with $\tau_{ar}(\nu)$; in the Fourier space, the final image of a point-like object is then given by the product of τ_{ar} with the frequency response of the system τ_b:

$$\frac{S(u,v)}{S(0,0)} = \tau_{ar}(\nu)\, \tau_b(\nu) \ , \tag{4.26}$$

and τ_{ar} can be obtained from eq. 4.25:

$$\tau_{ar} = \mathrm{e}^{-(\pi r_r \nu)^2} \ . \tag{4.27}$$

---

[7] k_{sn} is here defined as the mean divided by the standard deviation of the intensity distribution in A; this definition is acceptable as long as there is no offset in the imaging system, see sec. 7.2.

Combining equations 4.24 and 4.26, the density of information content ρ_H can be rewritten under the assumptions of cylindrical symmetry and Gaussian intensity distribution of the screen:

$$\rho_H = \frac{\pi}{\ln 2} \int_0^{+\infty} \ln \left[1 + \left|\tau_{ar}\left(\nu\right) \tau_b\left(\nu\right)\right|^2 k_{sn}\right] \, \nu \mathrm{d}\nu \; . \tag{4.28}$$

In diffraction-limited systems an useful expression of ρ_H is in terms of the dimensionless spatial frequency $\bar{\nu} = (\lambda/\alpha_i)\nu$:

$$\rho_H = \frac{\pi}{(\lambda\alpha_i)^2 \ln 2} \int_0^{2} \ln \left[1 + \left|\tau_{ar}\left(\bar{\nu}\right) \tau_b\left(\bar{\nu}\right)\right|^2 k_{sn}\right] \, \bar{\nu} \mathrm{d}\bar{\nu} \; . \tag{4.29}$$

In the view of image as received message, the problem of estimating the quality of an image becomes a problem of communication theory. A point-like object can be regarded as an infinite information source, and ρ_H represents the *density of Information Passing Capacity* (IPC); ρ_H is therefore a measure of the quality of an image.

The Rayleigh criterion for resolution can be restated in this communication theory frame. The mean information content H in a circle of radius λ/α_i for the image of a point-like object in an ideal, aberration-free, system, can be easily obtained replacing the product $\tau_{ar}\tau_b$ with the OTF τ^{id}, which is the Fourier transform of the Airy pattern:

$$H_A^{id} = \pi \left(\frac{\lambda}{\alpha_i}\right) \rho_H^{id} = \frac{\pi^2}{\ln 2} \int_0^{2} \ln \left[1 + \left|\tau^{id}\left(\bar{\nu}\right)\right|^2 k_{sn}\right] \, \bar{\nu} \mathrm{d}\bar{\nu} \; . \tag{4.30}$$

Comparing equations 4.4 and 4.30, it appears that the Rayleigh resolution $r_{i,RC}$ is proportional to the inverse of the square root of ρ_H^{id}. If the resolution of a real imaging system, R_{es}^{id}, is defined in such a way to coincide with $r_{i,RC}$ when $\rho_H = \rho_H^{id}$, then it follows that:

$$R_{es} = 0.61 \frac{\lambda}{\alpha_i} \sqrt{\frac{\rho_H^{id}}{\rho_H}} = 0.61 \sqrt{\frac{H_A^{id}\left(k_{sn}\right)}{\pi \rho_H}} \; . \tag{4.31}$$

In eq. 4.31 it as been expressively pointed out that H_A^{id} is only a function of the SNR k_{sn}.

4.3.3 On the Contributions to the Final Image

In sections 4.2.3 and 4.3.2 it has been shown that several density distributions must be convolved (or, in the Fourier domain, multiplied) in order to obtain the final image in an (electron-/ion-)optical imaging system. It can be useful, at this point, to summarise the terms that have been taken into account so far. For sake of notational simplicity, all the functions are here expressed for rotationally symmetric systems, so to use one coordinate instead of two, in the real domain ($r = (x^2 + y^2)^{1/2}$) and in the Fourier domain ($\nu = (u^2 + v^2)^{1/2}$).

Optical Transfer Function: $\tau(\nu)$ (sec. 4.1) It is the 2D Fourier Transform of the PSF (or CDD), which is in turn the response of an imaging system to a point-like object:

$$\tau\left(\nu\right)=\int_{-\infty}^{+\infty}w_a\left(r\right)\mathrm{e}^{-j2\pi\nu r}\,\mathrm{d}r\ , \tag{4.32}$$

or

$$\tau\left(\nu\right)=\int_{-\infty}^{+\infty}J_{b,p}\left(r\right)\mathrm{e}^{-j2\pi\nu r}\,\mathrm{d}r\ . \tag{4.33}$$

Acceptance Factor: $\tau_{ar}(\nu)$ (sec. 4.3.2) It is the 2D Fourier Transform of the PSF after it has been blurred by (convolved with) the raster size of the screen where the image is displayed (w_{ar}):

$$\tau_{ar}\left(\nu\right)=\int_{-\infty}^{+\infty}w_{ar}\left(r\right)\mathrm{e}^{-j2\pi\nu r}\,\mathrm{d}r\ . \tag{4.34}$$

FT of Source Intensity Distribution: $\tau_s(\nu)$ (sec. 4.2.3) It is the 2D Fourier Transform of the Source Intensity Distribution at the image plane, $J_s(r)$:

$$\tau_s\left(\nu\right)=\int_{-\infty}^{+\infty}J_s\left(r\right)\mathrm{e}^{-j2\pi\nu r}\,\mathrm{d}r\ . \tag{4.35}$$

$\tau_s(\nu)$ appears normalised in eq. 4.16. In most applications the Source Intensity at the object plane, $B_s(r)$ can be assumed as a Gaussian of size $r_{o,s}$:

$$B_s\left(r\right)=B_s\left(0\right)\mathrm{e}^{-\left(r/r_{o,s}\right)^2}\ , \tag{4.36}$$

so that $J_s(r)$ becomes:

$$J_s\left(r\right)=J_s\left(0\right)\mathrm{e}^{-\left(r/r_{i,s}\right)^2}\ ,\quad \text{with}\quad r_{i,s}=Mr_{o,s}\ , \tag{4.37}$$

and the normalised $\tau_s(\nu)$ is written as:

$$\tau_s\left(\nu\right)=\mathrm{e}^{-\left(\pi r_{i,s}\nu\right)^2}\ . \tag{4.38}$$

Spatial Frequency Response: $\tau_b(\nu)$ (sec. 4.2.3) It is the 2D Fourier Transform of the current density distribution $J_b(r)$:

$$\tau_b\left(\nu\right)=\int_{-\infty}^{+\infty}J_b\left(r\right)\mathrm{e}^{-j2\pi\nu r}\,\mathrm{d}r\ . \tag{4.39}$$

If the source is point-like, eq. 4.39 coincides with eq. 4.33, and $\tau_b(\nu)$ becomes the CDD. In the general case of finite-sized source, $\tau_b(\nu)$ (normalised) is the product of $\tau_s(\nu)$ and $\tau(\nu)$ (eq. 4.16).

4.3.4 Resolution in Practice

In this section, four methods used to evaluate the resolution of a given micrograph in the daily practice are presented. They are nothing more that 'gross' implementations of the Rayleigh criterion, thus affected by all its limitations, plus others that are peculiar of each method. The first three methods are applied in the real space; in particular, the first two are based on a very 'Rayleighian' definition of resolution (i.e. resolution as the ability of distinguishing two features in an image), while in the third method the resolution is related to the sharpness of the contours of one single feature. The fourth applies in the Fourier domain, and is an adaptation of the method presented in sec. 4.2.3 in order to take the noise into account.

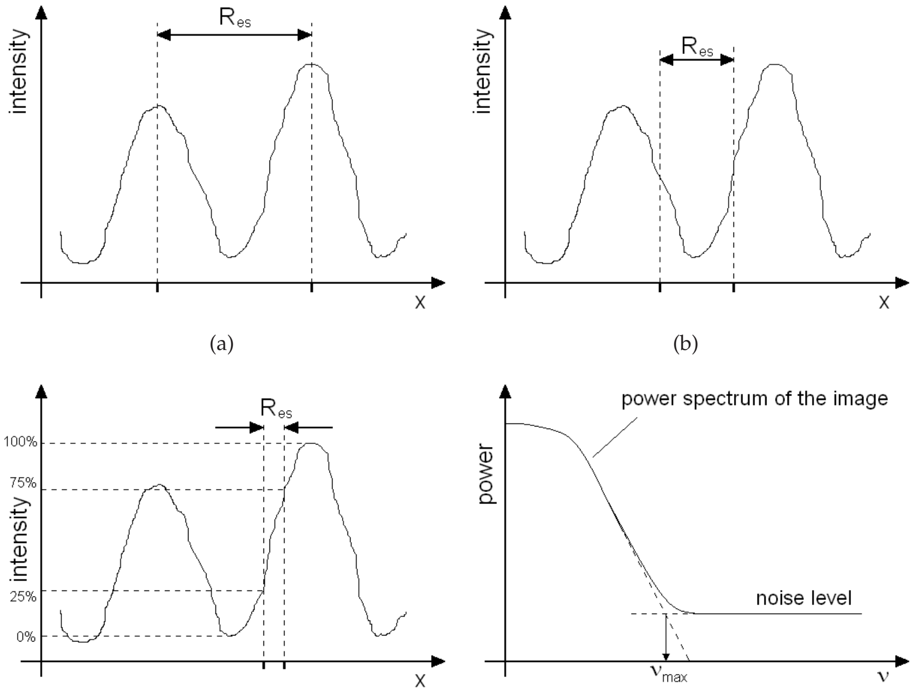

(a) (b)

(c) (d)

Figure 4.11: Four common ways of assessing the resolution in the daily practice. 4.11(a): Point-to-Point Resolution; 4.11(b): Gap Resolution; 4.11(c): Edge Resolution; 4.11(d): Resolution as the inverse of the maximum spatial frequency.

Point-to-Point Resolution In this case, the distance between two features in the image is calculated as the distance between the two intensity peaks; the resolution is assumed to be numerically coincidence with this distance, when determined between the two closest but still distinguishable features (fig. 4.11(a)).

Gap Resolution This is just a variation of the previous method, the only difference being the definition of distance between two features; not peak to peak, but from the middle of one contour to the middle of the other (fig. 4.11(b)).

Edge Resolution This method differs from the previous two for it defines the resolution based on a single feature, and not on the distance between two of them. In this case, the resolution is taken as the width of the intensity profile across the feature's edge between the points whose intensity is 25% and 75% of the intensity peak, respectively (fig. 4.11(c)).

Resolution as the Inverse of the Maximum Spatial Frequency According to this method, the resolution is evaluated as the inverse of the maximum frequency, in the power spectrum (i.e. the MTF) of the image, that is not embedded in the noise:

$$R_{es} = \frac{1}{\nu_{max}} \ , \tag{4.40}$$

where ν_{max} is the maximum value of spatial frequency that still carries a discernible signal (fig. 4.11(d)).

4.4 Reality Check

Before taking the sputtering effect into account in evaluating the resolution of an ion microscope (which will be the subject of the following chapter), it is appropriate at this point to think through what has been discussed so far.

On the Rayleigh criterion The entire subject of resolution, as I have presented it, revolves around the Rayleigh criterion. The criterion itself is a mathematical definition. Of course, it could be argued that the closest distance at which two images of two point-like objects can still be resolved is not given by the Rayleigh limit (distance for which the intensity in the middle is 73.5% of the intensity at the peaks), but by an intensity ratio that is bigger or smaller. This does not affect the validity of the criterion, it merely moves the threshold. What must be discussed is the way the criterion is applied. As mentioned in sec. 4.2.2, two errors must be considered when quantifying the resolution: statistical errors, and systematical errors. The first kind has been analysed already, and the conclusion was that resolution *is* a statistical error, associated to a certain confidence level, in the measurement of a certain dimension on the micrograph. The second kind is more subtle, for it stems from a wrong choice of the model. In a Gaussian model, the size of the Gaussian is coincident with half the distance at which the curves must be from each other in order to be at the Rayleigh limit for the intensity. However, this coincidence exists only if the PSF is Gaussian indeed; if that is not the case, then the size of the PSF, however it is defined, will not necessarily be half the distance that guarantees the Rayleigh limit: that distance could be shorter or longer, according to the shape of the distribution and to the definition of its size.

About the Resolution Based on the Beam Size As it has been shown, the custom of using the spot size as numerical value for the resolution of a microscope originates from the similarity between an Airy pattern for which the distance between the central peak and the first minimum is d_b and a Gaussian distribution of the same size. There are three major problems with this definition.

- **Wrong choice of the model for the CDD:** if the CDD looks very different from a Gaussian distribution, then it will not resemble an Airy pattern, and the transformation 'optics → electron-optics' based on the assumption 'size of the Airy pattern ≈ size of the beam' ceases to be valid; using the spot size as value for the resolution will result in a systematic error that will be bigger the less the actual CDD looks like a Gaussian.
- **Wrong choice of the size for the CDD:** even if the real nature of the current distribution were known, attention should be devoted to the definition of its size. For example, fig. 4.12(a) shows that, in a purely Gaussian CDD, the size at FWHM is a good approximation of the Rayleigh's resolution $R_{es,RC}$, while choosing the size at FW50 would result in an overestimation of the microscope's resolving power. On the other hand, if the CDD exhibits a narrow peak and wide tails, like in fig. 4.12(b), the size at FWHM would still be a good approximation of $R_{es,RC}$, while choosing the size at FW50 would lead to a nearly four-fold underestimation of the resolving power.
- **Underestimation of the emission area:** in electron (ion) scanning microscopy the image is formed merely counting the amount of secondary emission at each beam position (i.e. at each pixel in the image). Due to the scattering of the charged particles in the sample bulk, the area of the sample surface from which secondaries are emitted is in general bigger than the spot size on the sample plane, making the actual resolution generally worse than suggested by the spot size.

About the Resolution Based on the Contrast Performance A real imaging system can have a frequency response (MTF) very different from the ideal one shown in fig. 4.7, and still, the value of ν_{RC} can be exactly the same as the one of an aberration-free system. The fact that two different system responses intersect exactly at the point ν_{RC} does not mean, however, that the resolution provided by the two systems is the same. In a system with strong spherical aberration, for example, in which the current distribution has long tails, the amplitude of the response would drop quite soon, to be very low and slowly degrading over a wide range of frequencies, while in the ideal case the response would be much steeper around ν_{RC} (see fig. 4.13). In the aberrated system the contrast response is low over a wide frequency range, and the quality of the image, in terms of resolution, would depend ultimately om the SNR. If the SNR is high, a slowly degrading MTF would be an advantage, because it would go to zero for much higher values of the spatial frequency, and details at $\nu > \nu_{RC}$ could still be resolved; but if the SNR is low, in the aberrated system the response would be insufficient the resolve details for which $\nu < \nu_{RC}$.

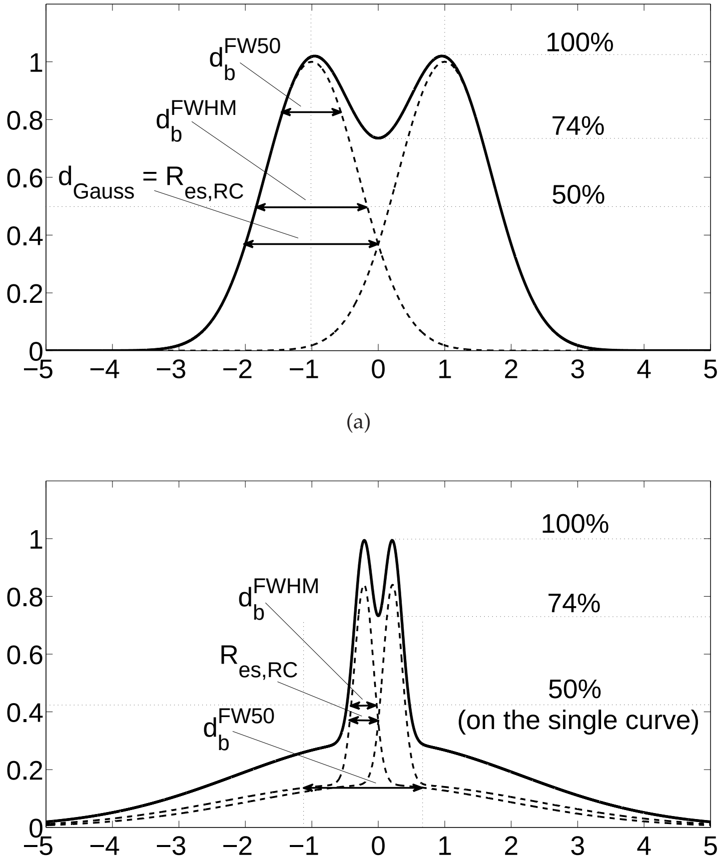

(a)

(b)

Figure 4.12: Relationship between size at FW50, size at FWHM, and distance corresponding to the Rayleigh limit for two different distributions: Gaussian, in fig. 4.12(a); and a distribution with narrow peak and wide tails, in fig. 4.12(b).

About the Resolution Based on the Density of IPC Amongst the methods presented in this section, the one based on the density of IPC is certainly the more sophisticated. The density of information content ρ_H, expressed by equation 4.29, is calculated taking into account not only the SNR and the column aberrations, but also the broadening of the CDD due to finite size of the source (through the spatial frequency response τ_b), and the blurring deriving from the convolution with the screen raster size (through the acceptance factor τ_{ar}. When it comes to its application, however, there are two problems.

- **Computational Complexity:** calculating ρ_H requires solving the integral appearing in eq. 4.24, or its simplified form of eq. 4.29, neither of which is triv-

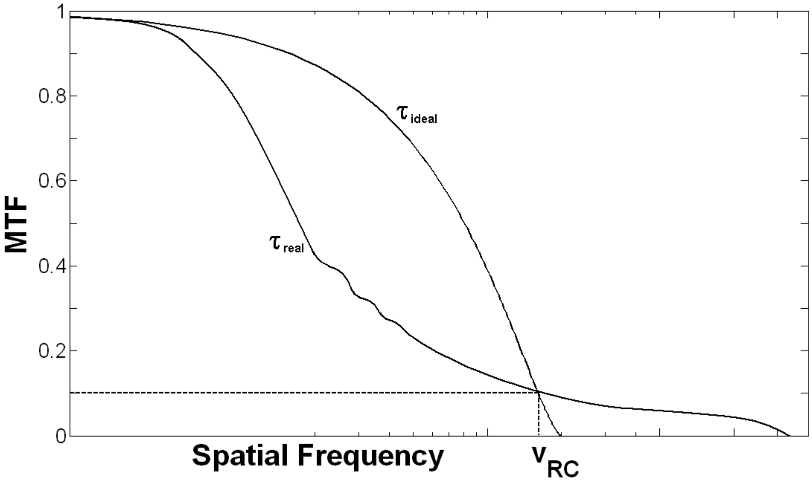

Figure 4.13: Difference between the MTF of an ideal imaging system and and the MTF of a real, aberrated system.

ial.

- **Risk for Systematical Errors:** the transfer functions τ are in general not known, and also not easily determined. In order to estimate them, strong assumptions are usually made on the shape of the current distribution (see [73], pages 406–425), which makes the risk of systematical errors due to a wrong choice of the model quite high.

About the Practical Methods for Measuring Resolution The aim of three of the four methods discussed, point-to-point, gap, and inverse of ν_{max} is measuring the distance corresponding to the Rayleigh limit directly on the final image. That distance will not therefore be coincident with the spot size, because of the effect of the noise, and of the serial blurrings deriving from the convolutions of all the transfer functions involved, but will be in any case a measure of the resolving power obtained in the image, regardless of what is the chosen figure of merit (point-to-point distance, gap distance, or inverse of ν_{max}). As long as, of course, the chosen distance is clearly defined. Numerically, the point-to-point distance and the distance calculated as inverse of ν_{max} would be very close to the spot size if the CDD were Gaussian, and there was no broadening effect (from finite-size source, screen raster size, finite-size object and source); in practice, since these blurring effects are always present, the resulting number is still a decreasing function of the dose used for imaging, like curve (a) in fig. 4.15, tending, at infinity, to an asymptotic value that is generally greater than the spot size. The gap distance would be very close to zero in the ideal case (see fig. 4.12(a)), but in reality it is once again a decreasing function of the dose because of the noise, asymptotically tending to a value that is typically smaller than the spot size (curve (b) in fig. 4.15). Measuring the resolution as width of the image of a perfect edge is different, for it aims to an estimation of the spot size, and not of the distance that still allows two close features to be resolved. In an imaging system in which the contrast response is a function of the height map of the sample surface, when a beam scans across a sharp knife-edge, infinitely extended in the y direction, the intensity profile in the x direction in the image is given by:

$$I\left(x\right)=\int_{-\infty}^{x}\mathrm{d}x\int_{-\infty}^{+\infty}J_b\left(\sqrt{x^2+y^2}\right)\,\mathrm{d}y\;. \tag{4.41}$$

If the beam intensity $J_b(r)$ is Gaussian, then also the intensity profile $I(x)$ is Gaussian cumulative density function, and the distance between the two points at 25% and 75% of I_{max} corresponds to the beam radius at which the intensity has fallen to 1/e of its maximum, which is usually taken as the half the size of the beam (see sec. 4.2.2):

$$\begin{array}{ll} x_{25}: & I\left(x_{25}\right)=0.25I_{max} \\ x_{75}: & I\left(x_{75}\right)=0.75I_{max} \end{array} \Rightarrow \Delta x|_{25}^{75}=R_{es}=r_b \tag{4.42}$$

In scanning ion and electron microscopy, however, where the contrast is, in first approximation, a function of the incidence angle, eq. 4.42 would be valid if the beam is scanned across a ramp, and not across an edge, like in fig. 4.14(a). As shown in sec. 4.2.2 the FIB/SEM image of a perfect edge would be not the integral of the CDD, but the CDD itself, as shown in fig. 4.14(b). This means that the 25%–75% width of the image of a perfect edge ($r_{25\%}^{75\%}$ in fig. 4.14(b)) is in general smaller that the spot radius[8]; the correct relation between $r_{25\%}^{75\%}$ and r_b should be at least estimated when using this method to measure the spot size. In conclusion, while the other three practical methods give a measure of resolution related to the Rayleigh limit, the edge method gives a measure of the spot size. Taking noise into account does not change the diameter of the beam, so that the 'edge resolution' is itself not a function of the dose. What is function of the dose, however, is the error connected with the edge measurement for the spot size (curve (c) in fig. 4.15). Since the error measurement is just another way of regarding the resolution, the fact that it decreases with the dose is in consistent with the analogous behaviour of the separation distance corresponding to the Rayleigh limit.

There is something very important that has been left out so far, but that can not be neglected in FIB microscopy: scanning ion microscopy is, ultimately, a destructive technique. The fact that the sample under observation is somehow degraded by the imaging process itself poses a strong limit to the amount of SNR obtainable, and this limit depends not only on the imaging system itself, but on the interaction between the ion beam and the particular sample under observation[9]. In a system that is not limited by sputtering, the resolution, intended either as the separation distance that still enables to resolve to features or as the uncertainty on a measurement in the image plane, increases monotonically with the dose, or the

---

[8] Even more when considering the edge effect in scanning microscopy, which decreases the intensity before the edge and increases it after the edge, stretching the Gaussian profile

[9] It is true that no system allows the collection of an infinite SNR; in case of ion microscopy however, the sample modification is of the same scale of the imaging resolution already for minimum accepted values of SNR; this point will be clarified in the next chapter.

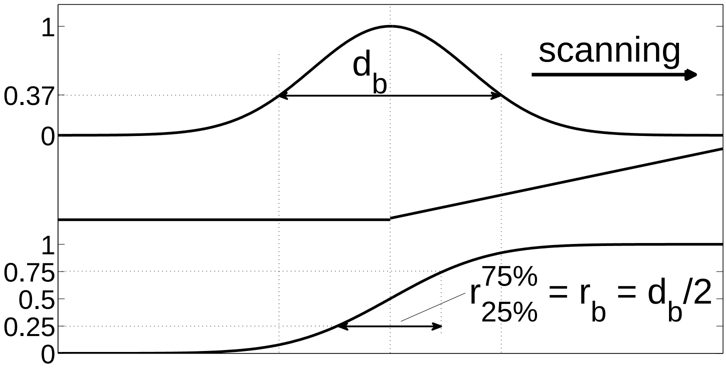

(a)

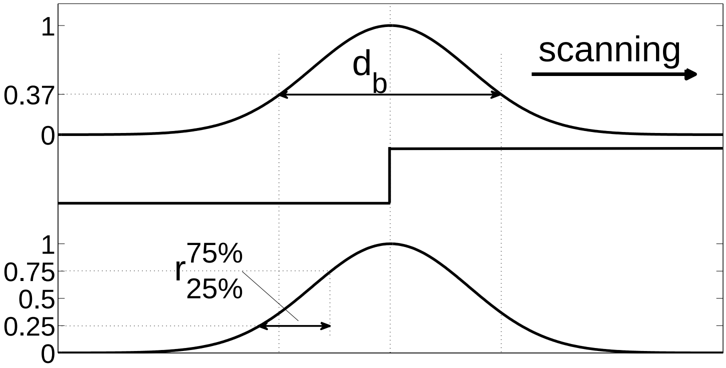

(b)

Figure 4.14: Visualisation of the meaning of $r_{25\%}^{75\%}$ in the case of a Gaussian beam scanning across a ramp (fig. 4.14(a)) and across a perfect edge (fig. 4.14(b)).

SNR[10].

When features are sputtered away during the imaging process there is another uncertainty to consider: the uncertainty deriving from the fact that the size of a given feature changes 'in line' due to the ion beam. It is easy to imagine that this 'Sputtering Uncertainty' (U_S), as it will be referred to in the rest of the thesis, increases monotonically with the dose/SNR, being 0 when the dose is 0. Let's collapse all the resolution figures shown in fig. 4.15 to just one, which can be called 'Information Uncertainty' (U_I), caring that it represents the same physi-

---

[10] There is always some confusion in saying that the resolution decreases or increases; if the resolution is the *ability* to resolve feature, then it *increases* with the dose; but if the resolution is a *distance*, or an uncertainty, it *decreases* with dose.

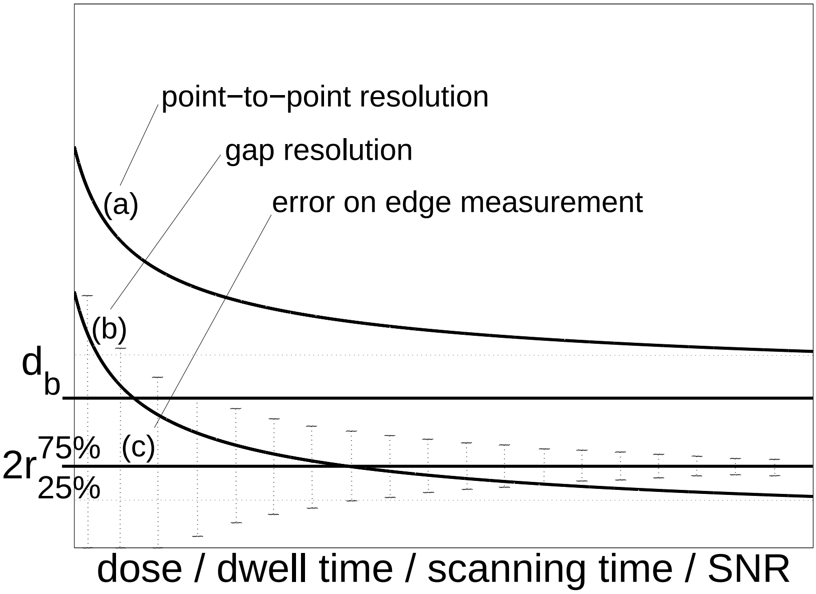

Figure 4.15: Schematic of the dependence of all the resolution figures considered in this section on the dose/SNR, and of the relationship between each other.

cal quantity represented by U_S. What we are left with are two uncertainties: U_S, which increases with dose/SNR; and U_I, which decreases with dose/SNR. If these two quantities are plotted against the dose/SNR, like it is schematically shown in fig. 4.16, it becomes clear that there is a minimum in the uncertainty that is achievable with an ion microscope: a best resolution value, corresponding to an optimum imaging time. If the imaging time is shorter than the optimum, then the image will be noise limited; if it is longer, it will be limited by sputtering. The value of ion dose/SNR for which the two curves intersect is the optimum imaging time, the one for which the best resolution will be obtainable.

Next section is devoted to the evaluation of the Sputtering Uncertainty, according to a theory of sputtering and resolution developed by J. Orloff, L.W. Swanson and M. Utlaut in the 90's [54]. This theory can be further expanded, for it does not take into account the Information Uncertainty. Putting together the 'Rayleigh's resolution' and the 'Orloff's Resolution' will be the subject of the two journal papers that make up the next chapter. In particular, a method will be proposed to calculate U_I and U_S consistently (so that the two quantity can actually be plotted on the same graph), as a function of the ion dose[11]

---

[11] In this section I have considered ion dose, dwell time, and SNR as representing the same quantity; in fact, switching between ion dose and dwell/scanning time, which are in a linear relationship with each other, does not change the behaviour of the functions that are assumed to be dependent on one of

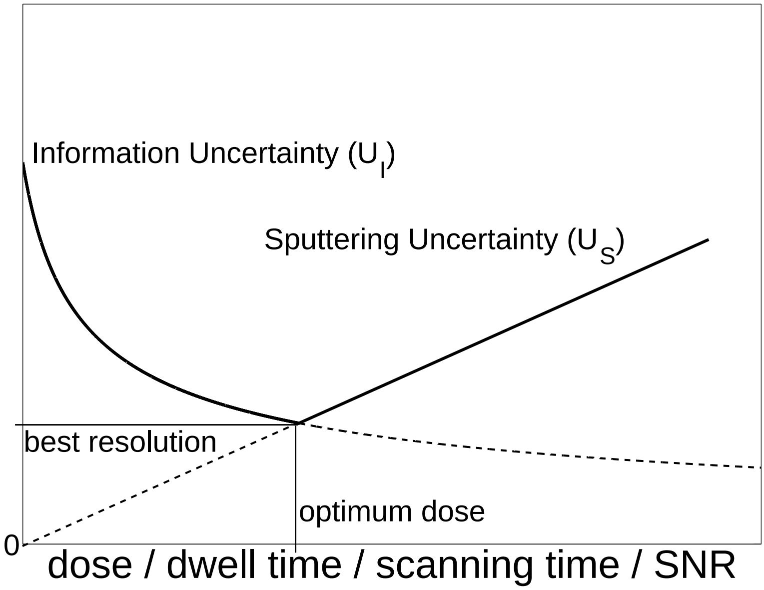

Figure 4.16: Schematic of the dependence of the Sputtering Uncertainty and the Information Uncertainty on the ion dose; their opposite trends result in a best obtainable resolution value, provided by the best ion dose.

4.5 Sputtering-Limited Resolution

When talking about resolution in FIBs, it must be kept in mind that the features under observation are in the same time canceled (sputtered) by the ion beam. Since the smaller the feature the faster it is sputtered away, the size of the smallest detail that can still be recognised in a micrograph will be the one that still gives a good amount of contrast and a decent SNR in a time not long enough for the detail to disappear.

The number of target atoms that are knocked off the sample per each incident ion is the sputter yield γ; γ is a complex function of the way impinging ions interact with the sample atoms, and therefore it depends on a multitude of factors: mass of ions and target atoms, structure of the target bulk, Surface Binding Energy (SBE), Lattice Binding Energy (LBE), and angle of incidence of the beam (α). If during a raster scan of the beam the volume V is removed from the target, the number of sputtered atoms can be expressed as:

$$N_{a,V} = \frac{V \rho N_A}{M_M} \;, \tag{4.43}$$

---

them. Switching between ion dose and SNR requires more attention, because they are in a non-linear relationship.

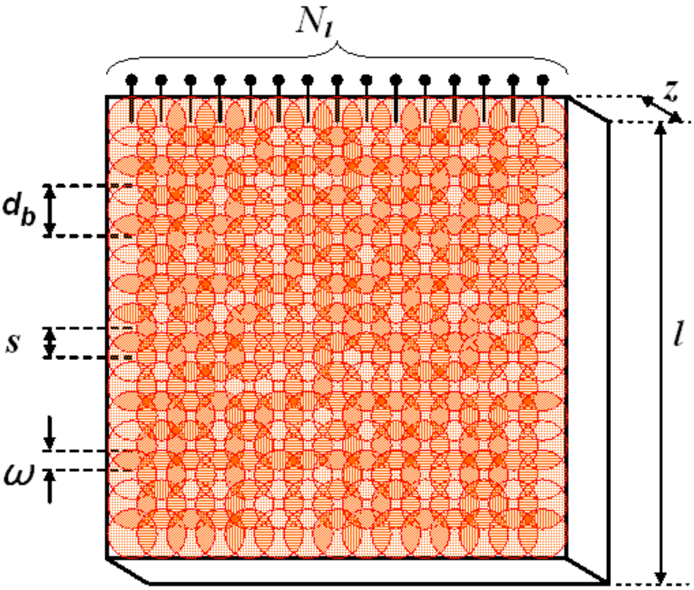

Figure 4.17: Definition of the geometrical parameters appearing in this section.

where N_A is the Avogadro's number and M_M and ρ are the molar mass and the density of the target, respectively; $N_{a,V}$ can also be expressed in terms of the sputter yield γ, as:

$$N_{a,V} = \gamma N_{i,px} N_l^2 \ , \tag{4.44}$$

where $N_{i,px}$ is the number of impinging ions per pixel, and N_l is the number of pixels per scan line (the number of pixels in the x and y directions are assumed here to be coincident). With referiment to fig. 4.17, and combining equations 4.43 and 4.44, the total removed volume (per scan) can be written as:

$$V = l^2 z = \frac{L^2}{M^2} z = \frac{\gamma N_{i,px} N_l^2 M_M}{\rho N_A} \ ; \tag{4.45}$$

here, l is the raster size on the sample and L is the raster size on the screen, and they are related to each other via the system lineal magnification M; z is the depth up (down?) to which the surface has been removed ($z = 0$ before scanning). In order to fully cover an area with a supposedly circular beam, the beam spot must overlap to a certain extent when passing to the next position on the sample. For a beam of diameter d_b scanning an area with a step s, the fraction of beam that overlaps ω is:

$$\omega = \frac{d_b - s}{d_b} = 1 - \frac{s}{d_b} = 1 - \frac{l}{N_l d_b} = 1 - \frac{L}{M N_l d_b} \ . \tag{4.46}$$

Eq. 4.45 can be rewritten in order to obtain the depth of sputtering z:

$$z = \frac{V}{l^2} = \frac{\gamma N_{i,px} N_l^2 M_M}{\rho N_A} \frac{1}{l^2} = \frac{\gamma N_{i,px} N_l^2 M_M}{\rho N_A} \frac{M^2}{L^2} \ ; \tag{4.47}$$

and then multiplied by the spot area in order to obtain the volume of target material that is removed at each position of the beam:

$$\frac{\pi}{4} z d_b^2 = \frac{V}{l^2} = \frac{\pi}{4} \frac{\gamma M_M N_{i,px}}{\rho N_A} \frac{M^2 N_l^2 d_b^2}{L^2} = \frac{\gamma M_M N_{i,px}}{\rho N_A} \frac{1}{(1-\omega)^2} \ . \tag{4.48}$$

Remember that ω in the picture is actually $\omega \cdot d_b$ At this point it is convenient to define a *sputtering sensitivity* S, which expresses the volume of removed target material per unit of ion current:

$$S = \frac{\gamma M_M}{\rho N_A \left(n \cdot e\right)} \ , \tag{4.49}$$

with $(n \cdot e)$ being the ion charge, expressed as the electron charge multiplied by the order of ionisation. In terms of sputter sensitivity, for single charged ions eq. 4.48 becomes:

$$\frac{\pi}{4} z d_b^2 = \frac{\pi}{4} \frac{S N_{i,px} e}{\bar{\omega}^2} \ , \tag{4.50}$$

where $\bar{\omega}$ is the complement to 1 of ω: $\bar{\omega} = 1 - \omega$. In the assumption of perfect collection efficiency and Poisson distribution for both the primary ions and the secondary electrons the SNR assumes a simple expression (see sec.3.2):

$$k_{sn} = \sqrt{\frac{\delta_i N_{i,px}}{1 + \delta_i}} \ , \tag{4.51}$$

from which:

$$N_{i,px} = \frac{1 + \delta_i}{\delta_i} k_{sn}^2 \ . \tag{4.52}$$

Combining equations 4.50 and 4.52, the sputtered volume at each beam position can be expressed as a function of sputter sensitivity, SNR, beam overlap and secondary electron yield:

$$\frac{\pi}{4} z d_b^2 = \frac{\pi}{4} \frac{e S k_{sn}^2 \left(1 + \delta_i\right)}{\bar{\omega}^2 \delta_i} \ . \tag{4.53}$$

Now, let's assume that the limiting factor to the reproduction of small details is the sputtered length z, and that the beam can always be made as small as z[12]:

$$\frac{\pi}{4} z^3 = \frac{\pi}{4} \frac{e S k_{sn}^2 \left(1 + \delta_i\right)}{\bar{\omega}^2 \delta_i} \ . \tag{4.54}$$

Eq. 4.54 means that every detail on the sample that is smaller than z will not appear in the image, for it has already been sputtered away; it represent, therefore,

---

[12] There is nothing to support this assumption at the moment, but it will be shown in the next sections that this is indeed the case, at least for Ga-FIBs and He-FIBs.

what could be called 'volumetric resolution'. The monodimensional counterpart is easily obtained, finally representing the linear, sputter limited, resolution:

$$R_{es} = \sqrt[3]{\frac{eSk_{sn}^2 \left(1+\delta_i\right)}{\bar{\omega}^2 \delta_i}} \ . \tag{4.55}$$

Eq. 4.55 shows that the resolution limit in a scanning ion microscope is a function of sputter sensitivity, SNR, SE yield, and beam overlap. It is worthy to show explicitly here on what parameters these four quantities depend on:

- $S = f(M_M, \rho, \gamma) = f(\rho, M_M, E_{surf}, E_{lat}, Z_i, E_b, \alpha)$;
- $k_{sn} = f(N_i, \delta_i) = f(N_i, \rho, M_M, E_{surf}, E_{lat}, Z_i, E_b, \alpha)$;
- $\delta_i = f(\rho, M_M, E_{surf}, E_{lat}, Z_i, E_b, \alpha)$;
- $\bar{\omega} = f(l, N_l, d_b)$.

The resolution limit is thus a more complex quantity than eq. 4.55 suggests:

$$R_{es} = f\left(\rho, M_M, E_{surf}, E_{lat}, Z_i, E_b, \alpha, N_i, l, N_l, d_b\right) \ , \tag{4.56}$$

where E_{surf} and E_{lat} are the SBE and the LBE of the target, respectively; Z_i is the atomic number of the primary ions; E_b is the energy of the primary beam.

Incidentally, the maximum magnification beyond which no further information is added to the image can be obtained from eq. 4.46:

$$\bar{\omega} = \frac{L}{MN_l d_b} \Rightarrow M_{max} = \frac{L}{\bar{\omega} N_l d_b^{min}} = \frac{L}{\bar{\omega} N_l R_{es}} = f\left(S, k_{sn}\right) \ , \tag{4.57}$$

In other words, M_{max} is the magnification that *should* be used for imaging, and it depends on beam overlap, screen size, and number of pixels in the image: a magnification higher than M_{max} lead to high overlap and thus oversampling, while if the magnification is too low, there is undersampling and consequent loss of information. Equations 4.55 and 4.57 shows that the resolution limit and the maximum magnification can be expressed as functions of sputter sensitivity S, SNR k_{sn}, SE yield δ_i and overlap $\bar{\omega}$. Fig. 4.18 shows the dependency of the ratio $R_{es}/\sqrt[3]{S}$ on k_{sn}, δ_i and $\bar{\omega}$; figures 4.19 and 4.20 show R_{es} and M_{max}, respectively, as a function of S and k_{sn}, once the parameters δ_i and $\bar{\omega}$ have been assigned the fixed values 2 and 0.5 respectively (which are typical in FIB practice).

One final remark. In the treatment presented here, the resolution in scanning ion machines has been expressed as a function of sputter sensitivity S and SNR k_{sn} (eq. 4.55). Sometimes it can be more practical to express R_{es} through the sputter yield γ instead of S, which can be done through eq. 4.49; k_{sn} can also be replaced by the number of ions per pixel, $N_{i,px}$, via eq. 4.51, or by any of the following parameters: ion dose D_i (number of impinging ions per surface unit), dwell time

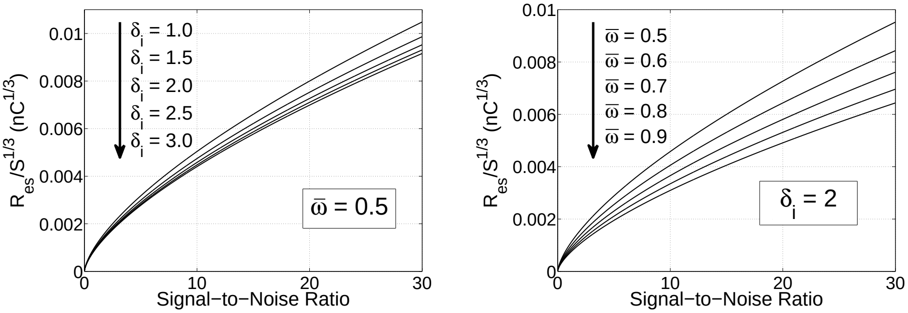

(a) (b)

Figure 4.18: Dependency of $R_{es}/\sqrt[3]{S}$ on k_{sn}, $\bar{\omega}$ and δ_i.

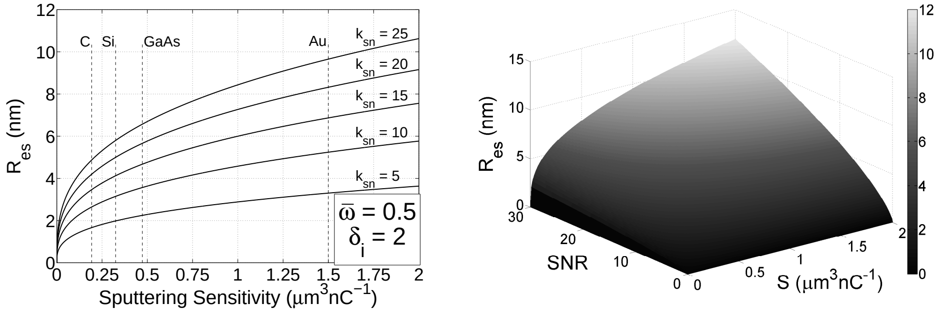

(a) (b)

Figure 4.19: Sputtered-limited resolution as a function of S and k_{sn}.

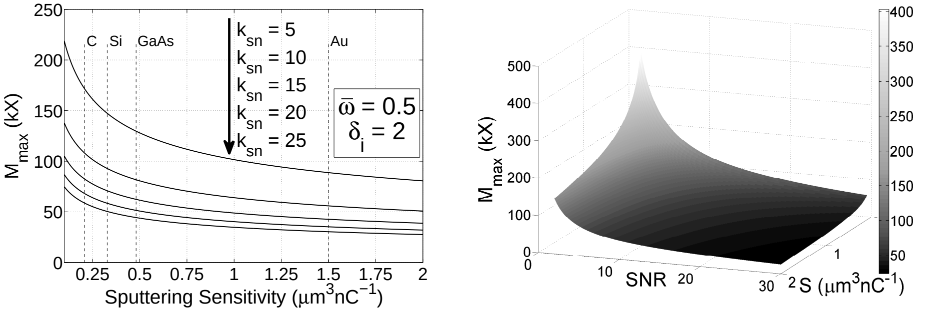

(a) (b)

Figure 4.20: Maximum magnification as a function of S and k_{sn}.

t_d (permanence time of the ion beam at each position of the sample), scanning time t_s (time it takes to form the whole image), which are univocally and linearly linked to each other:

$$D_i = \frac{1}{A_{px}} \cdot N_{i,px} \; ; \tag{4.58}$$

$$t_d = \frac{l^2 e}{I_b N_l^2} \cdot D_i \; ; \tag{4.59}$$

$$t_s = N_l^2 \cdot t_d \; . \tag{4.60}$$

where A_{px} is the pixel area.

The following two chapters consists of two published articles on the topic of resolution in scanning ion machine. The idea of sputtering-limited resolution presented in this section has been used as a starting point for an experimental study of the actual resolution in the two most used scanning ion microscopes, the Ga-FIB and the He-FIB.

4.6 Conclusions

In the next two chapters, the idea of resolution as deriving from a compromise between information collection and sample modification will be further developed. The topic that has been introduced in this chapter will be widely discussed, both from a theoretical and experimental point of view. A practical method to quantify the actual resolution of a FIB imaging system will proposed, and implemented for a Ga-FIB and for a He-FIB. At the end, it should be clear that in Scanning Ion Microscopy the resolution ceases to be a static concept, but is in fact a dynamic one. Before moving to the journal papers, here my conclusions about the topic of resolution in Ion Scanning Microscopy.

The obtainable resolution is, tautologically enough, a key feature when it comes to evaluating the performances of any imaging system. The very nature of resolution, however, is kind of woolly, especially in the field of Scanning Ion Microscopy, where the strong invasivity towards the sample poses a strong limit for the imaging time, and thus for the amount of SNR in the final image, from which the resolution certainly depends. In my view, the best way to think about the matter is starting with the Rayleigh's definition, based on the ability to 'resolve' two close features in an image. Since the Rayleigh criterion was originally stated for optical imaging systems, which are analogical and, in general, diffraction-limited, some care is required when translating it into the realm of Scanning Microscopy, in which the obtained images are intrinsically digital and are limited not by diffraction, but, in most cases, by spherical aberration. In this chapter I tried and reconciled different aspects of the topic with the 'Rayleighian' ability to resolve two close features: resolution as the ability to detect small features, and resolution as the ability to perform measurements on the image with small uncertainty. They can all be related to the concept of Rayleigh limit, i.e. the decrease in contrast that must be required in between two image points in order to distinguish them. It has been shown that the the noise that adds up in the each step of the image formation decreases the confidence associated with the measurement uncertainty, or, in terms of Rayleigh limit, increases the minimum separation distance that still enables to distinguish two objects on the image plane. Toward the end of the chapter, a qualitative analysis has been performed of the outcomes of a few methods routinely used to determine the resolution of a scanning imaging system, and of their mutual relationships. All what has been said up to that point holds indifferently for SEM and FIB microscopy. What strongly differentiates an ion microscope from a SEM is the sputtering of the sample surface, which is negligible, in most cases, when the probing particles are electrons, but that can be dramatic when heavy ions are used. When the sputtering is taken into account, the problem of evaluating the resolution becomes more subtle, because the uncertainty connected with the information gained from the sample ('Information Uncertainty'), which decreasing while increasing the scanning time, is coupled with a new kind of uncertainty, which i refer to as 'Sputtering Uncertainty', which increases with the scanning time. The main consequences of this new scenario are the following.

- Imaging becomes a problem of optimisation. There is an optimum value of resolution for a given sample/microscope system, deriving from the competition between Information Uncertainty and Sputtering Uncertainty; this value is obtained with a precise amount of ion dose, or equivalently, a precise value of scanning/dwell time.
- The resolution is not a characteristic of the imaging system only. This is actually true for any kind of scanning microscopy, for the quality of an image depends on the contrast that is typical of the combination sample/machine. The role of the sample, however, both in terms of topology of the surface and of nature/structure of the materials, is much stronger in the case of ion microscopy, where a material, or a geometry, that is less sputter-sensitive than another, will generally provide, in the same conditions, a better resolution.
- The resolution becomes a dynamic concept, in the sense that it cannot be calculated on the basis of a single image, for the dynamics of the modification of the features on the sample surface must be taken into account; an image, thus, is not enough: we need a movie.

The two journal papers that make up the following two chapters implement a procedure to determine the above-mentioned resolution optimum, and compare and discuss the results obtained from a beam of heavy ions (Ga^+ FIB) with those obtained from a beam of very light ions (He^+ FIB). In neither case a subnanometric resolution has been obtained, but I believe that, given the subnanometric spot size of the He^+ FIB, this target is achievable with the Helium microscope on well designed, low sputter-sensitive, samples. It has also been shown that the ultimate resolution can be lowered with a wise use of a priori knowledge, both on the sample and on the current distribution in the beam. This, however, belongs to the realm of image post-processing, and is beyond the scope of a discussion about the very nature of resolution, which I have attempted here.

In conclusion, I believe that the best parameter to describe, or better to 'suggest', the imaging capabilities of an ion microscope, is the spot size; it is the only number that can be univocally associated with a given microscope. This could be seen as a platitude, for the spot size is actually the number that manufacturers usually provide to advertise the qualities of their machines. Problem is that the spot size is not the resolution, and this should always be stated very clearly. The spot size can not even be seen as the limit for the resolution: the width of a perfect edge will probably be smaller than that, and in theory a better numerical value for the resolution than the spot size can be achieved in the post-processing phase, with the a priori knowledge about the sample, or with a very accurate knowledge of the current distribution. The spot size, however, still represents a limit when talking about the ability to resolve features in a raw image, or when evaluating the uncertainty of a measurement on the image plane. A microscope with a very small spot size will 'probably' provide, a better resolution that a microscope with a bigger one, but this is how far it goes. It has been shown very clearly that the factors that concur to determine the ultimate resolution are several, and in general dependent on the interaction between the ion beam and the sample, and not on the ion beam alone. The effect on the resolution of each of these factors, like the contrast given by the sample, its material and geometrical sensitivity to the sputtering, and the broadening of the beam in the sample bulk that results in an expansion of the secondary emission area, must be estimated in each case. This can actually be done, once the spot size and the ion species are known. Of course, the information about the spot size should be correctly interpreted, in order to avoid gross systematic errors. The accuracy of this interpretation increases with the accuracy of the knowledge of the current distribution in the beam.

Warning: Chapters 5 and 6 are made up of two articles published in *Journal of Vacuum Science & Technology B*, in 2008 and in 2009, respectively. I have chosen to leave the text exactly as it appears in the journal, with the exception of the original bibliography, that has been merged into the general one. As a consequence, the formalism might not be consistent with the one used throughout the rest of the thesis. All the quantities are, however, well defined in the text when they are introduced.

5 CHAPTER

Sputtering Limits vs. Signal-to-Noise Limits in the Observation of Sn-Balls in a Ga^+ Microscope

V. Castaldo, C.W. Hagen, B. Rieger, and P. Kruit.

Journal of Vacuum Science and Technology B, 26(6):2107–2115, 2008.

"Isn't life a series of images that change as they repeat themselves?"
Andy Warhol

In principle, a Scanning Ion Microscope can produce smaller probe sizes than a Scanning Electron Microscope, because the diffraction contribution is smaller. However, the imaging resolution is often severely limited by the sputtering damage. In this paper, an experimental procedure to establish the limit of a Focused Ion Beam system for imaging purposes is proposed. The procedure is based on the observation of the change in geometry (i.e. shrinking) of the features in a Sn-ball sample imaged with a Ga^+ beam. Plots of the balls' diameter versus the irradiation time give a straightforward visual evaluation of the time allowed for the observation of a single feature before the removal of material due to the ion bombardment becomes unacceptable. For each particle, the curve, together with the error band connected with the imaging process, gives the values of uncertainty/resolution due to the two competing processes, collecting of information (for example from Secondary Electrons) and damaging of the target. A plot of the uncertainty that is derived from these two processes for different sampling times allows the determination of the limiting factor of the imaging mode in use, and, ultimately, the highest possible resolution obtainable with a given machine for the observation of a certain sample. Together with simulations and theoretical studies, the described procedure will be able to confirm the effectiveness of the new ion sources that are currently being developed.

5.1 Introduction

Since the development of Liquid Metal Ion Sources (LMISs) and their application to Focused Ion Beam (FIB) systems by Seliger et al. in 1978 [1], FIBs became more and more widely used, not anymore as mere laboratory instruments, but, thanks to the high brightness, high current and good reliability of the LMIS, as indispensable tools for the semiconductor industry, in fields of application such as IC review and modification (assisted etch/deposition, cross-section cut, implantation), TEM/STEM sample preparation, thin film head manufacturing, and even mass spectrometry [2, 3].

Currently, Scanning Electron Microscopes give better results than Scanning Ion Microscopes in terms of resolution and ease of operation. Nevertheless, the use of ions instead of electrons in scanning microscopy promises several advantages: new contrast mechanisms, larger depth of focus and perhaps higher resolution. Assuming a zero-sized probe, Ohya and Ishitani [10, 11] showed that, except for targets of low Z, the lateral distribution of ion-induced Secondary Electrons (SE) is much narrower, leading to a better spatial resolution for SIM than for SEM; the same authors concluded that the topographic contrast for heavy materials is clearer in a SIM image than in a SEM image, while for light materials the difference is negligible [12]. Furthermore, Ishitani et al. [9] predicted that SIM images are more sensitive to the target-surface state than SEM images.

5.1.1 Theory of Sputtering

The main problem, when it comes to imaging with an ion beam, is the sputtering of target atoms: ions are thousands times more massive than electrons, so the damage to the imaged sample can actually be the limiting factor for the resolution. This issue has been addressed by Orloff et al. [83, 54].

Defining the resolution is not an easy task. The most popular definition is still the one proposed, for diffraction-limited systems, by Lord Rayleigh in 1879 [68], based on the ability to distinguish two objects in an image (thus, implicitly requiring a sufficient amount of contrast and Signal-to-Noise Ratio, SNR).

More quantitative definitions involve the notion of the Optical Transfer Function (OTF), defined as the Fourier Transform of the Point Spread Function (which describes the response of an imaging system to a point source or point object) or, in the case of electron-optical systems, as the Fourier Transform of the Current Density Distribution [2]. A relatively simple way to define the resolution in an electron-optical system is assuming that it is equal to the size of the focused beam, which is in turn quite difficult to determine. Following [2] or [70], this can be calculated adding the contributions from the source image, the spherical aberration and the chromatic aberration. More complete expressions for d, taking into account also the contributions of diffraction, Coulomb interaction, Boersch effect, etc., can be found in literature [77, 78].

None of these definitions is fully satisfying for a FIB, in which the beam can destroy an object before an adequate amount of signal is detected. This limit must be taken into account when defining the resolution for such a system. From geometric reasoning, considering that the beam can overlap itself during the scan of an image, and assuming that both the primary ion beam and the SE are Poisson distributed, that all the SE are collected, and that there are no other sources of noise in the system, Orloff et al. [54] proposed the following definition of resolution in a FIB:

$$D_{min} = \sqrt[3]{\frac{eSK^2(1+\delta)}{\Omega^2\delta}} \,, \tag{5.1}$$

where D is the feature size, K is the signal-to-noise ratio, δ is the SE yield, Ω (scan-step-size/beam-diameter) is a measure of the overlap and S (in μm^3/nC) is the 'sputtering sensitivity', defined as:

$$S = \frac{YA}{\rho N_0 e} \,, \tag{5.2}$$

where ρ and A are the target density and atomic weight, N_0 is Avogadro's number (6.02×10^{23} at/mol), and Y is the sputter yield (sputtered atoms/primary ion). A plot of eq. 5.1, showing D_{min} as a function of S and K, is in fig. 5.1. It can

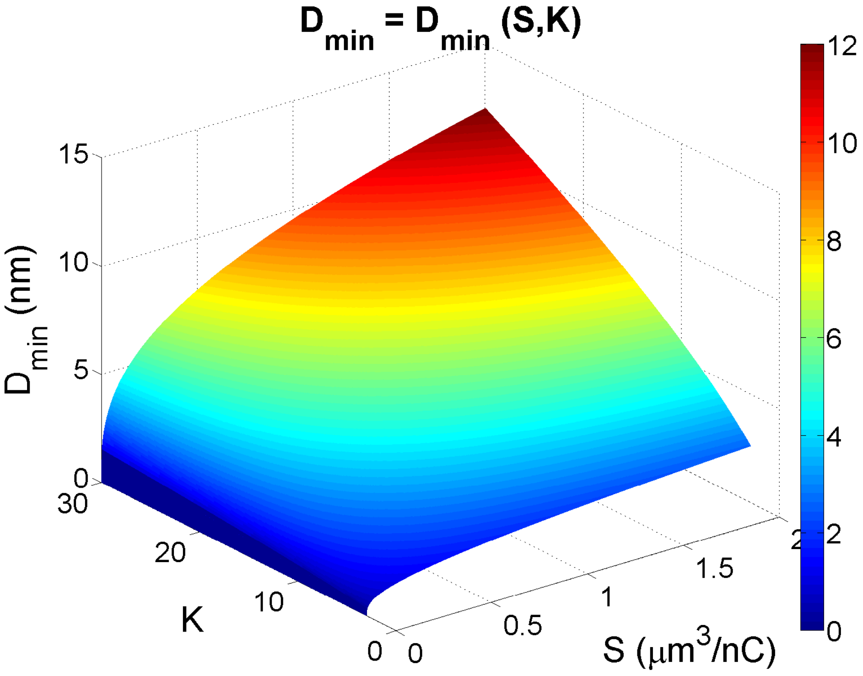

Figure 5.1: The minimum detectable feature in a FIB imaging system from eq. 5.1, as a function of sputtering sensitivity S and signal-to-noise ratio K, for $\delta = 2$ and $\Omega = 0.5$.

be useful to express D_{min} as a function of scanning-time instead of SNR. This is straightforward, under the same assumptions for which eq. 5.1 holds:

$$K = \sqrt{\frac{N_i \delta}{1+\delta}} = \sqrt{\frac{\delta}{1+\delta} \frac{I_{beam}}{e \cdot px} t_{scan}} \tag{5.3}$$

and

$$D_{min} = \sqrt[3]{\frac{eS}{\Omega^2} \frac{I_{beam}}{e \cdot px} t_{scan}} \ , \tag{5.4}$$

where N_i is the number of primary ions per pixel, I_{beam} is the ion current, and px the total number of pixels in the image. Equations 5.3 and 5.4 are written for single charged ions; should this be not the case, the electron charge e must be multiplied by the order of ionisation.

It appears that, while for extended structures there are several limiting mechanisms like rearrangement and redeposition, for small particles, in the order of a few nm, the imaging resolution is actually determined by the competition between sputtering and SE production/collection. This is indeed the case in the present FIB systems, most of which exploit beams of Ga$^+$ (Atomic Weight: 69.723), whose high sputtering power represents the fundamental limit to the resolution. The only way to obtain higher performances in terms of resolution and collectible SNR is exploiting sources of low mass ions, such as H$^+$ and He$^+$.

5.1.2 New Ion Sources

In the last few years, much effort has been directed to the design of novel ion sources, especially for imaging purposes (see [79] for a review). The 'perfect ion source' will be able to overcome the drawbacks connected with the use of LMISs (high energy spread, $\Delta E/E \sim 2 \times 10^{-4}$, leading to high chromatic aberration; strong sputtering of the sample; permanent implantation of metal ions, that can change the electrical and/or magnetic properties of the specimen under inspection) while keeping its advantages (high reduced brightness, in the order of 10^6 A/m^{2}srV; high current stability; long lifetime). Presently LMISs remain state-of-the-art ion sources, being unsurpassed in terms of robustness and reduced brightness. Recently ALIS Corporation developed a new helium microscope, which is expected to produce as small a spot size as 0.25 nm, thanks to a high predicted source brightness ($B > 10^9$ A/cm^{2}sr), low energy spread ($\Delta E/E \sim 2 \times 10^{-5}$) and small diffraction effects [4]. Whether or not this new microscope fulfills these expectations, the excitement about novel ion sources makes a procedure capable of characterising ion imaging systems and predicting their performances an urgent one.

5.2 The *Ball Size-Time* curve

As mentioned above, when imaging with a FIB system, two different 'uncertainties' must be taken into account to define the precision with which a feature can be characterised:

- **Information Uncertainty (*IU*),** which depends on the amount of information that is collected from the image ($IU \propto \sqrt{N}$, where N is the number of counts); this terms decreases for increasing scan/dwell time (i.e. increasing K);

- **Sputtering Uncertainty (*SU*),** which is due to the fact that atoms from the feature are being sputtered while imaged, changing the size of the feature during the scan; this term increases for increasing scan/dwell time.

The actual resolution of a SIM will be ultimately determined by the competition between these two factors: the first term dominates for high acquisition rates, while the second term is the limiting factor for images that are acquired with a long scan/dwell time.

Further to the theory of Orloff et al. outlined in sec. 5.1.1, in this paper a practical method of defining the resolution of a SIM is proposed, which does not depend on the implicit assumptions of the cited theory (Poisson-distributed ions and SE, perfect SE collection efficiency), and takes into account not only the uncertainty due to the sputtering, but also the one connected with the amount of collected information.

The basic idea is to follow the evolution of a sample under observation with an ion beam. In order to have isotropic features, with only one characteristic size, a Sn-ball sample has been chosen, one of those commonly used for SEM calibration. Such samples are commercially available, in particular, the one used for our experiments is a “Universal Resolution Tin on Carbon” from Agar Scientific, with particle diameters ranging from <5 nm to 30 μm. Different sets of images have been recorded, each with a different scan/dwell time ($t_{dwell} = t_{scan}/px$), because each scan-time corresponds to a different amount of collected signal (see eq. 5.3). All the images have been taken with a Ga$^+$ Dual-Beam (FEI Strata DB 235), with a nominal current of 1 pA and a beam energy of 30 keV. The image size is 1024×954 px (the largest size supported by the machine), with a magnification of 80 kX, and a pixel size of 3.7 nm/px. The six sets used for the analysis are summarised in table 5.1. Fig. 5.2 shows the time evolution of the sample under ion bombardment through six frames from set 3, from the first to the last scan; the damage is already evident in fig. 5.2(b), it becomes dramatic in fig. 5.2(f).

The image analysis was carried out with the MATLAB toolbox DIP*image* [1]. For each set of scans the *BallSize-Time* curve for different particles is obtained, which is a plot of the particle’ s diameter versus the scan/dwell time. The way such a diagram is expected to look is shown in fig. 5.3. The plot also includes the parameter *IU*, calculated for each point according to the procedure that will be outlined in the next section. In this way, both terms needed to define the resolution appear in the curve:

---

[1] DIP*image* reference website: `http://www.diplib.org/`.

Set	Scanning Time (s)	Dwell Time (μs)	# Scans	Total Time (s)
1	6.337	6.487	160	1014
2	11.77	12.048	100	1177
3	22.63	23.165	60	1358
4	45.26	46.330	40	1810
5	90.52	92.661	20	1810
6	162.9	166.753	5	814.5

Table 5.1: Scan/dwell time and total time for the sets of images used for the analysis.

- $SU = \int_{t^*-\Delta t/2}^{t^*+\Delta t/2} \frac{dy}{dt}(t)\, dt$, where t^* is a given instant, and Δt is the scan-time; the derivative is calculated along the curve $y = y(t)$, which fits the experimental data;
- $IU \propto 1/\sqrt{n}$, where n, as it will be shown in par. 5.2.2, is the number of pixel lines on which the diameter of a ball can be assumed constant, and is a function of the current size of the ball.

The main issue here is that:

- $SU = SU\left(\frac{dy}{dt}\right),\ \frac{dy}{dt} = \frac{dy}{dt}(t) \ \Rightarrow\ SU = SU(t);$
- $IU = IU(n),\ n = n(y),\ y = y(t) \ \Rightarrow\ IU = IU(t);$

i.e. none of the two terms are constant along the curve. This problem will be addressed in sec. 5.4. In order to plot the curve, the image-analysis procedure must be able to:

- measure the diameter of a chosen particle, for each frame of a set of images;
- determine the error that affects the estimation of the diameter, in terms of absolute length;

The second item has a key role in this analysis, and its definition must be set with care.

5.2.1 Determination of the Particle Diameter (*D*)

The measurement of the balls' diameter for each frame of a set of images is performed with a semi-automated algorithm based on 2^{nd} order derivative edge detection [80]. The procedure consists of the following steps:

1. **Image Preprocessing:** each set must be corrected for the image drift, that is always present in the order of few nanometers for images taken over a time of $15 - 20$ minutes.

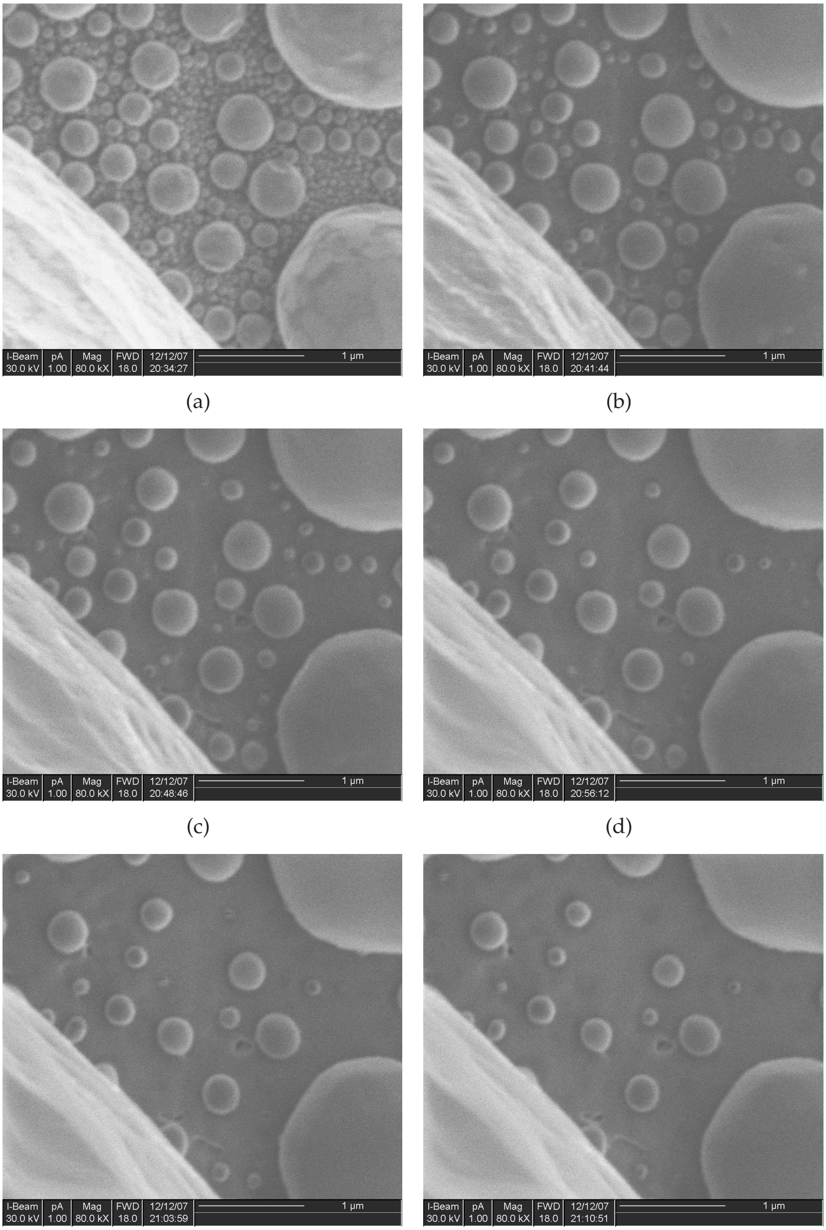

(a) (b)

(c) (d)

(e) (f)

Figure 5.2: Time evolution of the Sn-ball sample under ion bombardment shown through six time frames from set 3; the damage is already evident in fig. 5.2(b); 5.2(a): after ∼22 s of imaging; 5.2(b): after ∼294 s; 5.2(c): after ∼565 s; 5.2(d): after ∼837 s; 5.2(e): after ∼1110 s; 5.2(b): after ∼1358 s.

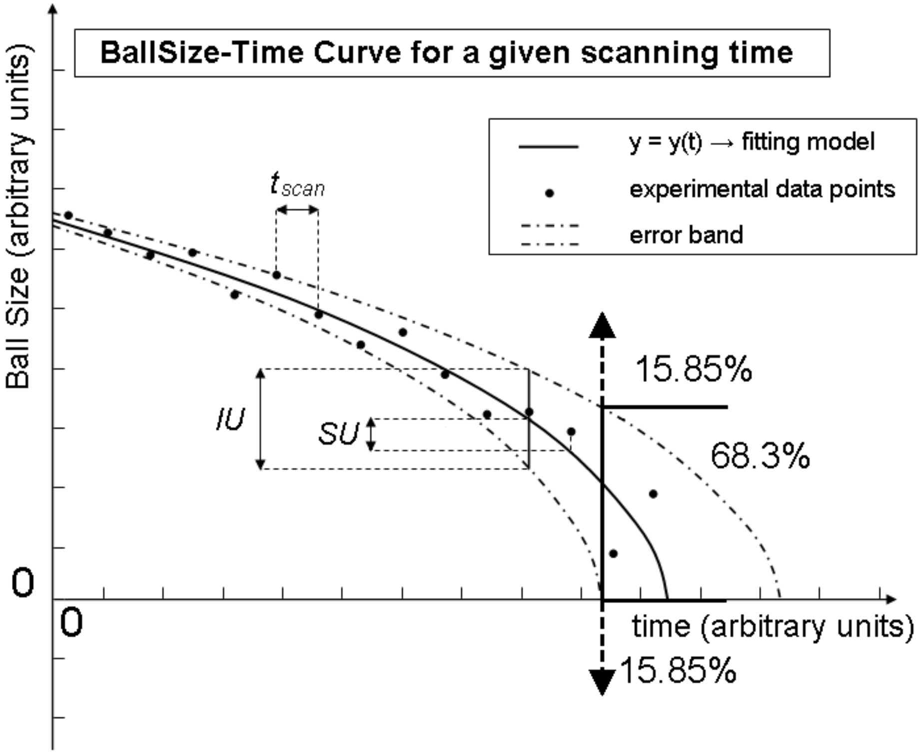

Figure 5.3: The ideal appearance of the *BallSize-Time* curve; IU is the thickness of the uncertainty band at each point, corresponding to a given confidence level of the measurement (68.3% in this picture); SU is the reduction in size between two successive scans; t_{scan} is the distance between two successive data points.

2. **Feature Selection:** in this step the balls of interest are manually selected on the first frame of the set; what is actually selected is a rectangular box comprising the ball's diameter (fig. 5.4).

3. **Averaging:** the intensity levels of each pixel in the box are averaged over the width of the box, in order to obtain a one pixel profile for the length estimation (par. 5.2.2).

4. **Edge Detection:** this is the core of the algorithm; the zeros in the second derivative are found; because with shot noise and shadow effects there can be more zeros than edges, a check on the local maxima and minima is performed in order to select the right points (fig. 5.5): only the two zeros (one per side) with highest distance between the nearest local minima and maxima are identified as edges and selected.

5. **Refining:** the subpixel positions of the zero crossing are found by interpola-

tion of the second derivative;

6. **Slope measurement:** for each edge, the slope at half maximum is calculated (see par. 5.2.2).

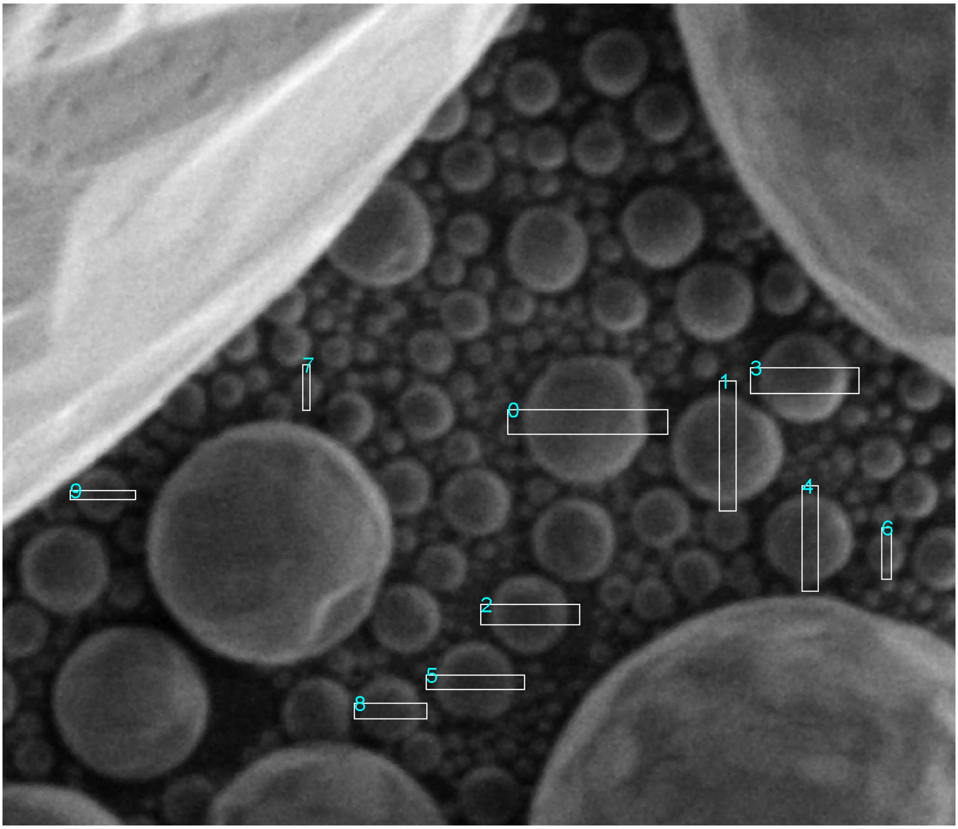

Figure 5.4: Features of interest selected on the first frame of the time series; for each ball the diameter is calculated averaging the pixel lines over the width of the selection boxes.

5.2.2 Determination of the Information Uncertainty (*IU*)

The term that we have indicated as '*IU*', i.e. the resolution connected with the image acquisition process, depends essentially on three things:

1. the shot noise, σ, decreasing while increasing the acquisition time;
2. the slope of the edge of the particle, in the diagram Intensity-Position;
3. the 'a priori' knowledge available about the feature.

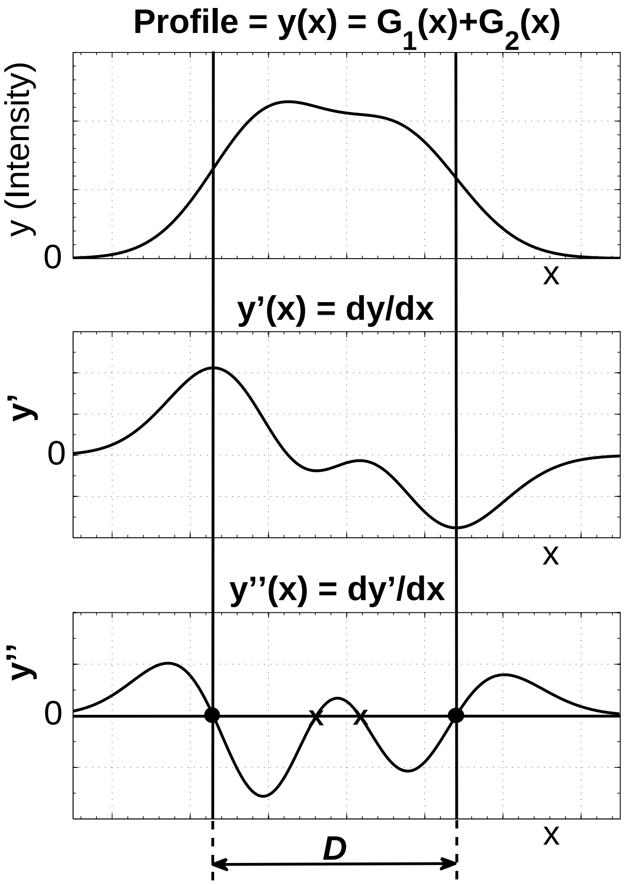

Figure 5.5: The edges of the features are found among the zero-points of the second derivative of the intensity level; here the simple case of an analytic profile (sum of Gaussians) is shown, in which only the two zeros for which the distance between the nearest local maximum and the nearest local minimum is the highest correspond to the edges of the feature.

Shot Noise (σ) The shot noise σ is intensity-dependent and is normally evaluated through different images of the same area. Being this not possible in the case of FIB imaging, an estimation of σ for a given intensity can be obtained as the variance of the grey levels in a flat surface (i.e. an area of the sample void of features); this is shown in fig. 5.6 in the monodimensional case. This value of σ must then be corrected for the intensity level of the part of the feature where the size and the slope (see par. 5.2.2) are measured. In order to do this, the variance is evaluated at different (void) positions in the image, each characterised by a different mean grey level: the value of σ corresponding to the intensity level of the feature is then estimated through interpolation.

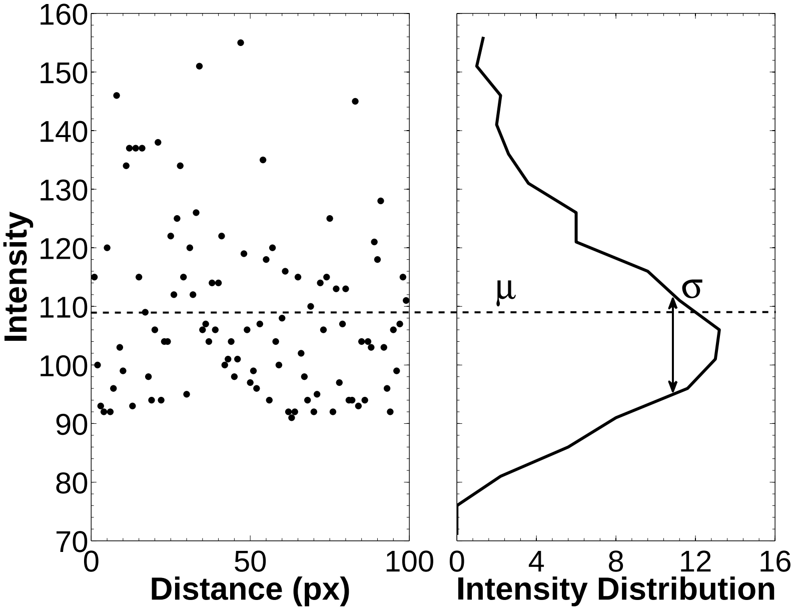

Figure 5.6: The shot noise σ is evaluated as the variance of the gray levels in a flat area. Here a monodimensional case: on the left the intensity levels along a straight line, on the right their distribution, with its mean (μ) and standard deviation (σ).

Error on theDiameter Measurement (ΔD) The shot noise σ must be converted into an estimation of the uncertainty in the determination of the particle diameter. This can be done, once again in a model-independent way, determining the slope at 50% of the step profile. In the general case of an asymmetric profile, the left and right sides must be taken separately into account. With reference to fig. 5.7, indicating with D the particle diameter, ΔD can be expressed how:

$$\Delta D = \frac{\Delta D_L + \Delta D_R}{\sqrt{2}} = \frac{\sigma/|\tan\theta_L| + \sigma/|\tan\theta_R|}{\sqrt{2}} \ . \tag{5.5}$$

Dependence of *IU* on the Feature's Size *IU* and σ are strictly related, but not exactly coincident. In every measurement process, regarding the result as a stochastic variable, the error is reduced repeating the measurement a certain number of times, and averaging the results. This is not possible in the case of ion imaging, because of the intrinsically destructive nature of the process. Moving around this obstacle is possible exploiting a priori knowledge of the system being observed. Suppose we want to estimate the thickness of an $m \times n$ pixel line, a measurement along one pixel column will be affected by an error ΔT, which cannot be reduced, since imaging the same column again for a second measurement would affect the

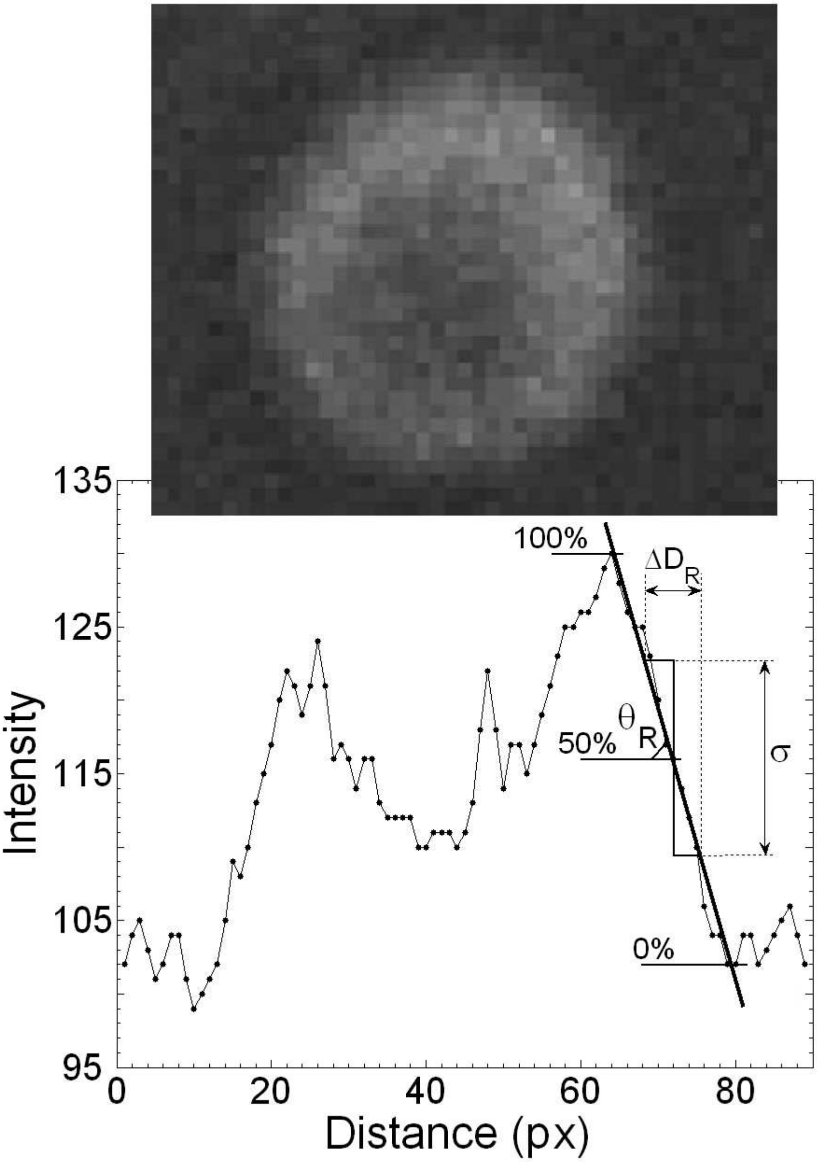

Figure 5.7: Evaluation of ΔD as projection of the error band due to the shot noise on the distance axis; for each edge, the slope of the intensity level at half maximum is considered.

thickness itself, and the value of this second measurement would not represent the same stochastic variable. Nevertheless, if the thickness of the line 'is known' to be constant along the whole length (or a part of it), measurements of the thicknesses T_i along different pixels column would represent different observations of the same random variable, the theoretical thickness T. In this way the error ΔT can be reduced by simply averaging different observations along different pixel columns, being the total number of observations (n) only limited by the length of the line along which the thickness is known to be constant.

The case of a sphere is analogous: the a priori knowledge of the feature (assumed as a perfect sphere) suggests that it is possible to average over different diameters. This is theoretically correct, but may not be the best approach in terms of implementation. An approximation is to assume that the diameter is constant for a certain number of adjacent pixel lines (centers on a geometric diameter). This solution has been chosen for different reasons:

- it is less affected by the fact that the particle might not be a perfect sphere, or might change its shape during the sputtering because of atomic anisotropy;
- it is less affected by aberration effects, in particular astigmatism.

The number of pixel lines along which the observations of the diameter's length can be averaged is of course a function of the particle's size; it can be assumed, for example, that the diameter is constant for 1/5 of the diameter. If C, in pixel/nm, is the pixel size in the image, the number of observations that can be used to average the measurement, and thus to reduce the error, is:

$$n = \lfloor 0.2D \cdot C \rfloor + 1 \tag{5.6}$$

Once the function $n = n\,(D)$ has been tabulated, it is finally possible to express the 'Information Uncertainty' *IU* for each point of the *BallSize-Time* curve:

$$\frac{IU}{2}\,(D) = \frac{\Delta D}{\sqrt{n}} = \frac{\sigma/|\tan\theta_L| + \sigma/|\tan\theta_R|}{\sqrt{2}\sqrt{\lfloor 0.2D \cdot C \rfloor + 1}}\ . \tag{5.7}$$

5.3 Numerical Simulation

While *IU*, as shown in eq. 5.7, depends on the quality of the image through the parameter σ, the sputtering effect on a feature hit by an ion beam, and its shrinking with the time/dose, can be simulated with a numerical approach. The starting point is the sputtering yield Y, defined as the number of target atoms sputtered away for each incident ion. This parameter is strongly dependent on the Surface Binding Energy of the target, SBE, whose value is sometimes difficult to estimate, and it is usually approximated with the Heat of Sublimation of the target. The calculation of the sputtering yield has been carried out with TRIM, a free code distributed by J. Ziegler [2], which implements a Monte Carlo method. The SBE also changes under bombardment due to surface roughness and damage, and, for

---

[2] SRIM/TRIM reference website: `http://www.srim.org/`.

compounds, also due to changes in the surface stoichiometry, which makes the calculation of Y accurate only to about 30%. Y has been simulated as a function of the incidence angle of the beam on the target surface, α. This dependence is fundamental in the case of a spherical geometry, where the incidence angle of the ion beam is constantly changing along the surface of the feature. For each value of α, between $0°$ and $89.9°$ with a step of $1°$, the impact of 1000 Ga^+, with an energy of 30 keV has been simulated in order to have a reasonable accurate estimate of Y. The result is shown in fig. 5.8.

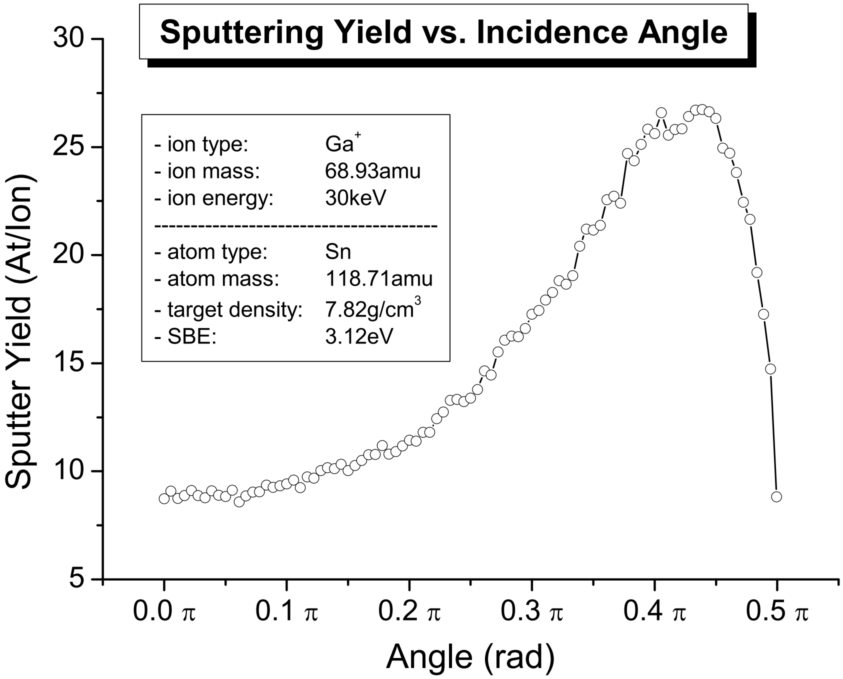

Figure 5.8: Sputtering Yield vs. Incidence Angle for 30 keV Ga$^+$ impacting on Sn, as obtained from Mont Carlo simulation using the TRIM code.

Once the Sputter Yield as a function of α is known, Y can be converted to a Sputter Rate (SpR), i.e. the pace at which a surface recedes under ion bombardment:

$$SpR(\alpha) = \frac{4AI}{\pi d^2 e \rho N_0} Y(\alpha) \ , \tag{5.8}$$

where e is the ions' charge, ρ and A are the target density and the target molecular weight, d is the beam diameter and I the beam current. If all the parameters are expressed in S.I. units, SpR will be expressed in m/s.

Indicating with $y_0(x)$ the feature profile before the ion bombardment starts, at each time-step Δt the profile of the particle that is being sputtered must be 'receded' with the amount $SpR \cdot \Delta t$; thus, the ball-profile at the time $n\Delta t$ is:

$$y_{n\Delta t}(x) = y_{(n-1)\Delta t}(x) - SpR(x) \cdot \Delta t \, . \tag{5.9}$$

In eq. 5.9 SpR has been written as a function of x because α is a function of x. The initial profile $y_0(x)$ can take any form; in the case of a spherical feature of radius r, $y_0(x) = \sqrt{r^2 - x^2}$ represents the upper-right quarter of the ball. Recursive application of eq. 5.9 gives the profile of the feature as it is changing because of the sputtering effect, as shown in fig. 5.9. At each time step, the size of the feature is given by the distance between the intersections of the curve $y_{n\Delta t}(\pm x)$ with the initial profile $-y_0(\pm x)$: the points of the curves $y_{n\Delta t}(\pm x)$ lying below the initial shape must not be considered.

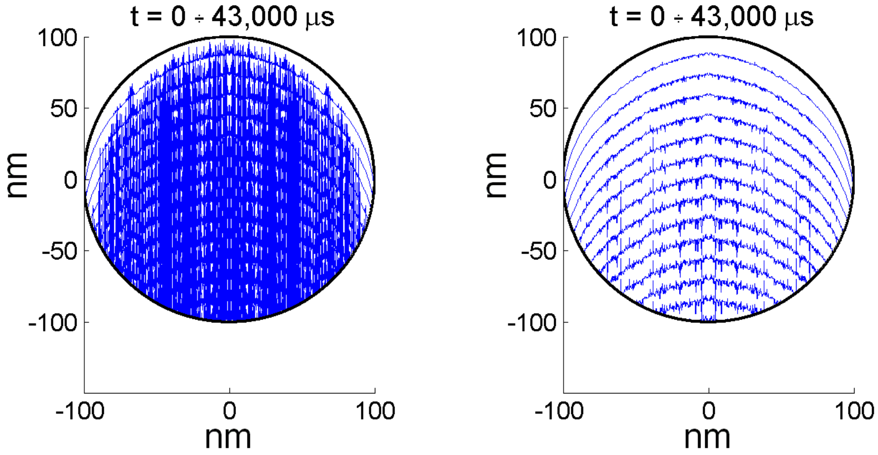

(a) (b)

Figure 5.9: The evolution, under ion bombardment, of the profile of a Sn-ball. In (a) the spikes are due to numerical errors and to the fact that $Y(\alpha(x))$ is not analytical; in (b) the curves have been smothered with a size 3 minimum filter, for an improved visualisation.

The *BallSize-Time* curve calculated in this way is merely numerical; still, it gives an idea of what should be expected in terms of size-shrinking of a feature hit by an ion beam. Moreover, the curve appears to be reasonably well fit by a second order polynomial (fig. 5.10).

As mentioned above, this numerical simulation is based on a 'continuum', isotropic approach. Therefore, it doesn't take into account the fact that the target's atoms are differently packed along different crystalline orientations, nor the 'channelling effect' (i.e. the ion range is higher for specific crystalline directions), that is intrinsically non-isotropic. The effect of redeposition, that can significantly change the shape assumed by the particles during the sputtering process, is also not considered.

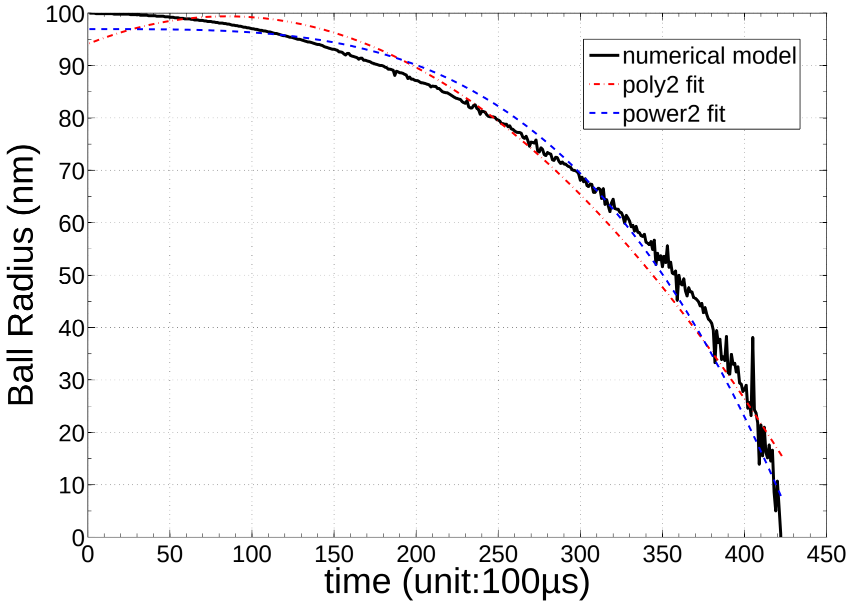

Figure 5.10: The *BallSize-Time* curve as obtained from fig. 5.9(b); fittings with a second order polynomial and with a power function are shown.

5.4 Application of the Model and Discussion

In the previous sections the expressions for both error contributions, the one related to the sputtering and the one related to the amount of collected information, have been shown; IU is given by eq. 5.7, while SU is the difference in size of the ball between two scans:

$$SU = \Delta y = \int_{t^*-\Delta t/2}^{t^*+\Delta t/2} \frac{dy}{dt}(t)\, dt \ , \tag{5.10}$$

where the function $y(t)$ is the fitting model chosen to describe the shrinking of the ball. At this point the model is complete, and can be applied to the sets of images summarised in table 5.1, in order to define the smallest detectable feature, as follows:

1. **image processing and analysis:** to determine the diameter and the slope of the edges, for each time frame; this should be done for each set for particles of similar initial size (sec. 5.2.1);
2. **fitting of the experimental data:** a second order polynomial is generally good, while in some cases a more complex one should be chosen (sec. 5.3);
3. **determination of *IU*:** for each point of the *BallSize-Time* curves this is accomplished using eq. 5.7;

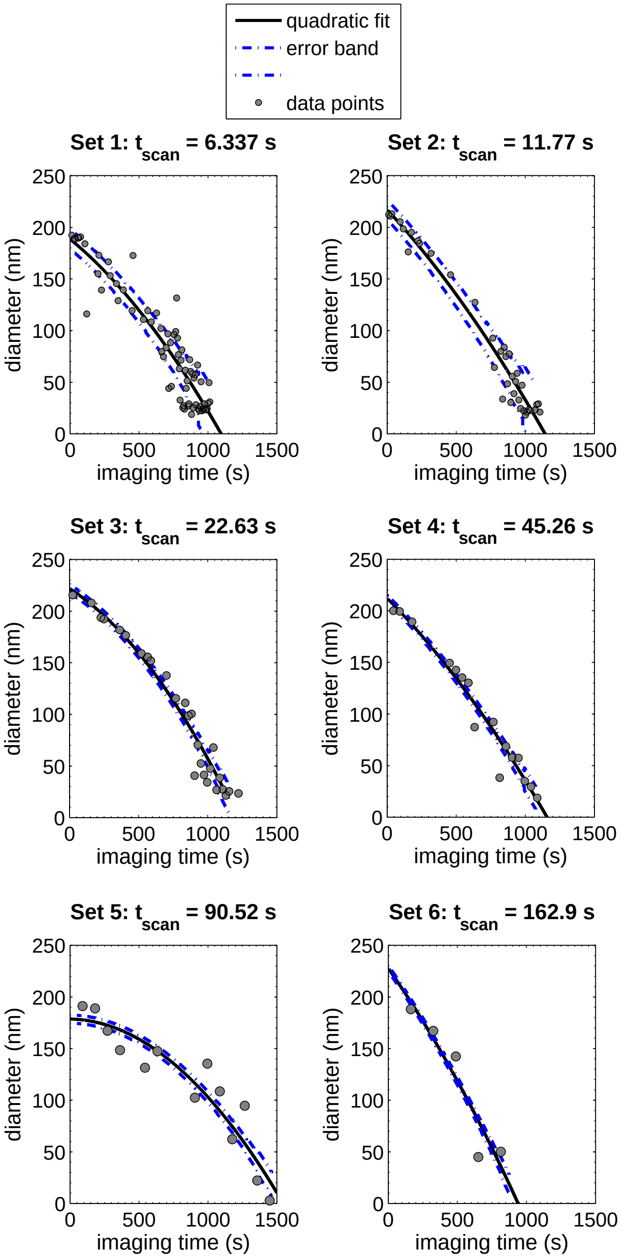

Figure 5.11: *BallSize-Time* curves for each of the six sets of images, for balls of approximately equal initial diameter (~ 200 nm); each diagram shows experimental data points, quadratic fit and error band connected to the noise.

4. **selection of IU and SU (in the limit of the smallest feature) for each set:** as already pointed out in sec. 5.2, none of these two quantities is constant along the curve. It is still possible, anyway, to define a single value of uncertainty for a given t_{scan}/dose, taking IU and SU at the time $\bar{t}$ for which $y\left(\bar{t}\right) = IU\left(\bar{t}\right)/2$; this is indeed the smallest diameter that can be measured, because for $y < y\left(\bar{t}\right)$ the lower limit of the error band would be negative;
5. **IU vs. t_{scan} and SU vs. t_{scan}:** a plot of these two curves on the same diagram gives immediate information about the highest accuracy that can be reached when measuring feature sizes with a FIB system.

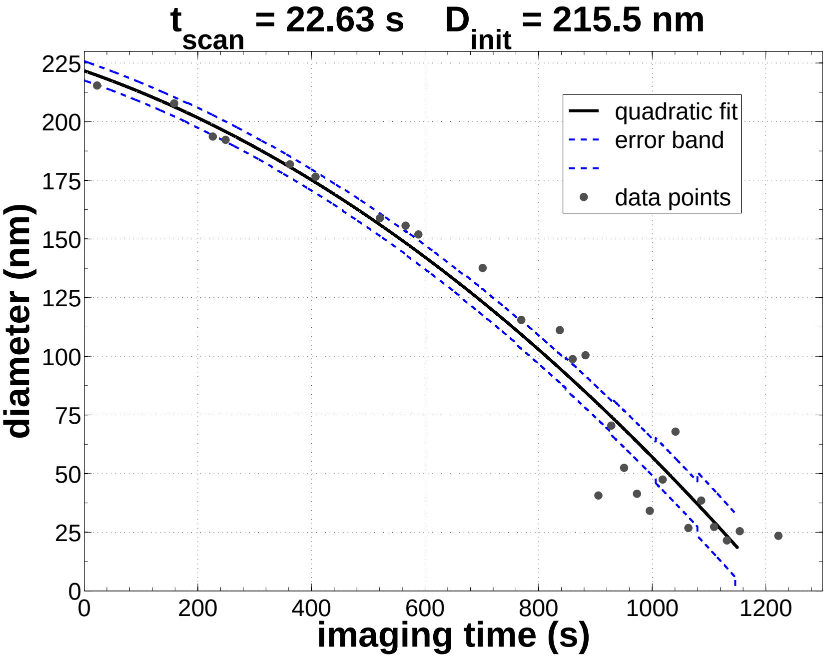

Figure 5.12: The third curve of fig. 5.11 for a better visualisation; the initial diameter of the ball is ~215.5 nm, and the feature totally disappears after ~1200 s of scanning with a current of 1 pA.

The procedure was implemented following, for each set of images, the evolution of balls of initial diameter of about 200 nm. Fig. 5.11 shows the *BallSize-Time* curves: experimental data points, quadratic fit and the error band connected to the shot noise. To speed up the calculation, a single value of θ_L and θ_R has been used for each set, which can be justified by the fact that the imaging conditions are exactly the same for all the frames of each set. Fig. 5.13 shows the plots, on the same diagram, of SU and IU as a function of the scanning time, evaluated for each curve of fig. 5.11 at the time $\bar{t}$ for which the lower limit of the error band becomes zero. The value of t_{scan} corresponding to the intersection of $IU(t_{scan})$ and $SU(t_{scan})$, $\bar{t}_{scan}$ is the scanning time for which both the Information Uncertainty and the Sputtering Uncertainty are minimised and represents, therefore,

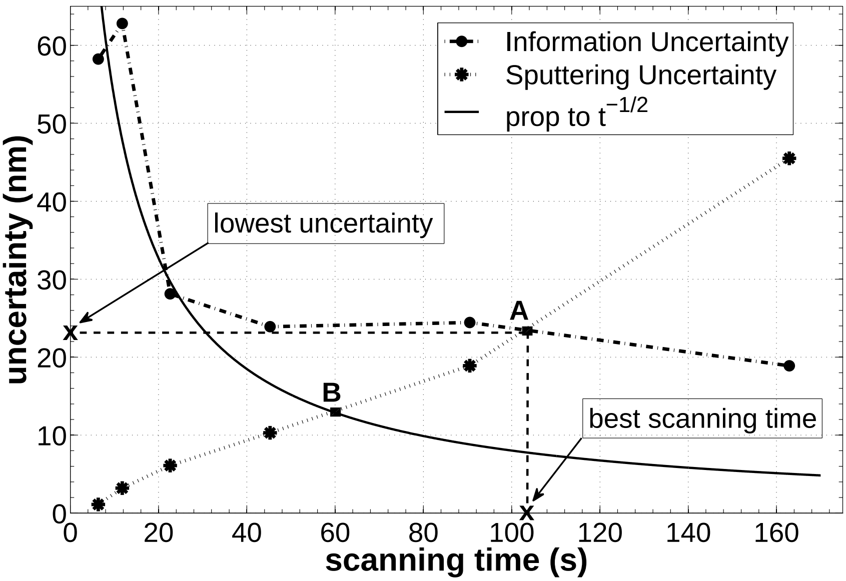

Figure 5.13: A plot of $SU(t_{scan})$ and $IU(t_{scan})$ on the same diagram gives an immediate evaluation of the best scanning time and the corresponding best accuracy that can be achieved in a measurement (for given imaging conditions) in a FIB imaging system. The solid line represents an 'ideal' IU curve, for which the uncertainty is pure shot noise.

the best operating condition. It must be pointed out that IU relates to the variance σ of the grey level distribution in a flat area (sec. 5.2.2), i.e. it relates to a given accuracy of the measurement. Assuming Gaussian-distributed gray levels (a good approximation for a high number of counts/pixels), the choice of 1σ returns a confidence level of 68.3%. This means that, if y^* is the best estimation for the particle's diameter at the time t^*, the probability for the particle's diameter to be in the range $[y^* - IU(t^*)/2, y^* + IU(t^*)/2]$ is 68.3%. Referring to fig. 5.3, the statement that $y(\bar{t})$ is the smallest measurable diameter implies the assumption that such minimum diameter is the one for which the probability to still observe 'something' is 84.15%. If 84.15% is found to be too low, or too high, the analysis may be implemented for a differnt confidence level.

From our experiments we found a best scanning time close to 100s, corresponding to $IU = SU = 23$nm. This means that using a FIB with those imaging conditions (focus, astigmatism, etc.) will give a precision in terms of measurement of features not higher than ±11.5 nm, a value that is achieved only using 100 s to take a single picture; scanning for less than 100 s will give higher uncertainty because of the insufficient collected information, while for scanning times $>$ 100 s the sputtering effect will be the limiting factor: the collected information is not exploited because the reduction of feature's size during the scan is higher than IU.

It is interesting to observe that, from eq. 5.3, a scanning time of 100s, assuming $\delta = 2$ and $\Omega = 0.5$, corresponds to a SNR $K \sim 26$, which in turn, using eq. 5.1 or eq. 5.4, or simply looking at the diagram in fig. 5.1, gives a minimum detectable feature size of $\sim$ 12nm (for a sputtering sensitivity of 2μm^2/nC). This is surprisingly close to the minimum uncertainty obtained with our analysis, considering that the two values have been obtained with two completely different methods, and the fact that the theory of Orloff doesn't take into account the redeposition (which is implicitly included in our experimental approach) nor the dependence of the sputtering sensitivity on the incidence angle of the beam.

Some considerations about $IU(t_{scan})$ and $SU(t_{scan})$ are needed. As it appears from eq. 5.10, *IU* depends on the shape of the feature being observed, ultimately because the sputtering is a strong function of the incidence angle. This means that the optimum scanning time $\bar{t}_{scan}$ will be different for different samples. Even when all features have the same initial shape, like in the case of the Sn-balls, care must be taken in defining the optimum operating conditions; balls of different initial diameter will have different *BallSize-Time* curves, and thus different *SU*, because the shape changes from a sphere to a disk (fig. 5.9): a feature of initial diameter, for example, of 100 nm, once reduced by the sputtering to a diameter of 50 nm, will be different from a feature whose initial diameter is 50 nm. About *IU*, it must not be forgotten that while the term σ is in principle only related to the scanning time, the slope of the feature's edge, θ, can be different for different imaging conditions, like focus and astigmatism. These parameters can also affect $\bar{t}_{scan}$.

Fig. 5.13 shows how the sputtering and the collection of information compete to determine the smallest observable feature. Assuming shot noise limited information collection, IU should follow the $1/\sqrt{t_{scan}}$ curve shown as a solid line. It is clear that due to some other factors there is a deviation, whose effect is to reduce the smallest observable feature dependence with the sputtering. We expect that under more favourable conditions the IU curve will follow for longer the shot noise limited curve, thus the intersection point moves from point A to point B, where the slope of the IU curve is greater, and so the dependence on the sputtering.

5.5 Conclusions

In this paper a procedure for finding the best scanning time and the corresponding minimum measurement error when imaging with a FIB system is proposed. The approach is experimental, and complements the theory of sputtering developed by J. Orloff et al. The procedure is based on following the shrinking of spherical features while imaging with the ion beam, and has been tested on six different sets of images, each one with a different scanning time. As a result we plotted the measurement error connected with the collection of signal (SE) and the error connected to the change in the feature's size due to the sputtering, both as a function of the scanning time. For the imaging condition under which our pictures were taken, we found a best scanning time of ~100s, and a minimum error of ~23nm, a value that is not far from the minimum detectable size obtained by Orloff for the same SNR. The minimum error and the best scanning time are both dependent on the imaging conditions: assuming that parameters like focus and astigmatism weren't optimised during our experiments, it is reasonable to assume that the curve $IU = IU\left(t_{scan}\right)$ can be moved towards smaller values, bringing the minimum error even closer to the theoretical sputter-limited resolution.

The analysis of the performances of a FIB system is interesting especially because of the fact that different new ion sources are now appearing or are being studied, for which the expectation, for the scientific community and for the industry, is very high.

Acknowledgments: *This work is part of the research programme "Microscopy and Modification of Nano-structures with focused electron and ion beams" (MMN) of the "Stichting voor Fundamenteel Onderzoek der Materie" (FOM), which is financially supported by the "Nederlandse Organisatie voor Wetenschappelijk Onderzoek" (NWO). The MMN programme is co-financed by FEI Company.*

6 CHAPTER

On the Influence of the Sputtering in Determining the Resolution of a Scanning Ion Microscope

V. Castaldo, C.W. Hagen, P. Kruit, E. van Veldhoven, and D. Maas.
Journal of Vacuum Science and Technology B, 27(6):3196–3202, 2009.

"The real voyage of discovery consists of not in seeking new landscapes but in having new eyes."
Marcel Proust

The determination of the quality of an imaging system is not an easy task, for in general at least three parameters, strictly interdependent, concur in defining it: resolution, contrast and Signal-to-Noise Ratio (SNR). The definition of resolution itself in Scanning Microscopy is elusive, and the case of Scanning Ion Microscopy (SIM) is complicated by the damage of the sample under the ion beam, which, especially for small features, can be the limiting factor. This is indeed the case for most Focused Ion Beam (FIB) systems, which exploit beams of Ga^+. The only way to overcome this limit is to exploit sources of low mass ions, such as H^+ and He^+. In this paper we analyse the way the sputtering may affect the resolution, defined as *smallest detectable feature* in an image, of a Scanning Ion Microscope, for heavy and light ions, in the case of spherical features. It appears that the fundamental limit to the resolution in Scanning Microscopy is not given by the spot size, but by the *dynamics* of the interaction of the beam with the sample and the consequent modification of the sample's geometry, even for beams of light ions. For example, in the case of Sn nano spheres under a He^+ beam, we found a minimum theoretical detectable particle size limit of $\sim$1 nm and an experimental limit of $\sim$5 nm.

6.1 Introduction: Meaning and Interpretation of Resolution

The notion of *resolution* is invoked whenever the quality of an imaging (or writing) tool has to be stated, or advertised [81]. To obtain Scanning Microscope images with a high resolution, the attributes of the sample are equally important as is the resolving power of the Scanning Microscope. Consequently, the ultimate *resolving power* of an instrument is not easily demonstrated, as the attributes of the average sample are often not fit for imaging at extreme magnification. In addition, the meaning of *resolution* is actually often unclear (and hence mis-interpreted), as many different definitions and criteria co-exist. Therefore it is difficult, if not impossible, to propose a single number that serves as ultimate judgment for tools that become everyday more complex and multi-functional. The main reason is that the ability of resolving small details in an image (what is commonly referred to as resolution) strongly depends on parameters that are not included in the traditional definitions: Signal-to-Noise Ratio (SNR), contrast, sample composition. [82, 54] Moreover, the case of resolution in SIM is complicated by yet another factor: the imaged sample undergoes more or less strong geometrical and compositional modifications due to the high momentum that is carried, and eventually transferred, by the impinging ions. In this case, not only the same machine can perform differently with different observed materials (which might happen also with Electron Microscopes because of different electron/atom interactions and more or less clean vacuum), but even the same material in a different geometrical structure can shift the balance between signal extraction and sample modification. A good review of this topic is contained in [73]. [1]

In the present paper some experimental results are presented and discussed, together with some preliminary simulation results, in order to make a further step towards a deeper understanding of the imaging performance of SIMs. The major conclusion is that for every specific sample a dose for optimal image acquisition exists. At that specific dose the Sample Modification Uncertainty (U_{SM}), which increases with longer exposures, is optimally balanced against the Information Uncertainty (U_I), which obviously decreases when recording longer. [2]

6.2 Sputtering and Imaging Performance

Most definitions of resolution in micro-beam machines refer to the beam size at the sample. This works reasonably well at intermediate resolution for SEMs. However, they systematically ignore the destructive effect that a beam of massive particles, like ions in SIMs or fast electrons in STEM, can have on the sample: details

---

[1] For a more complex definition of resolution, see Sato and Orloff in [74].

[2] These two different, and competing, 'uncertainties' were first introduced by the authors in [55], under the names of Sputtering Uncertainty and Information Uncertainty; here a broader concept is proposed, U_{SM}, that is more general than U_S for it refers to any kind of sample modification (sputtering, contamination, redeposition), and not only to the removal of sample material; U_S is used in this paper when referring to pure sputtering effect.

might have disappeared before they can be seen against the noise in the image. Orloff [83] and Orloff et al. [54] addressed the issue, proposing the following equation for the size of the *smallest detectable particle* (D_{min}) in a FIB:

$$D_{min} = \sqrt[3]{\frac{eSK^2(1+\delta)}{\Omega^2\delta}} \,, \tag{6.1}$$

where K is the SNR, δ (Secondary Electrons/Primary Ion) is the Secondary Electron (SE) yield, Ω (Scan Step Size/Beam Diameter) is a measure of the overlap and S (μm^3/nC) is the *Sputtering Sensitivity*, defined as:

$$S = \frac{YA}{\rho N_0 e} \,, \tag{6.2}$$

where ρ and A are, respectively, the target density and the atomic weight, N_0 is the Avogadro's number (6.02×10^{23} at/mol), and Y is the sputter yield (Sputtered Atoms/Primary Ion). It can be more practical to express D_{min} as a function of scanning-time t_{scan} instead of SNR [55]:

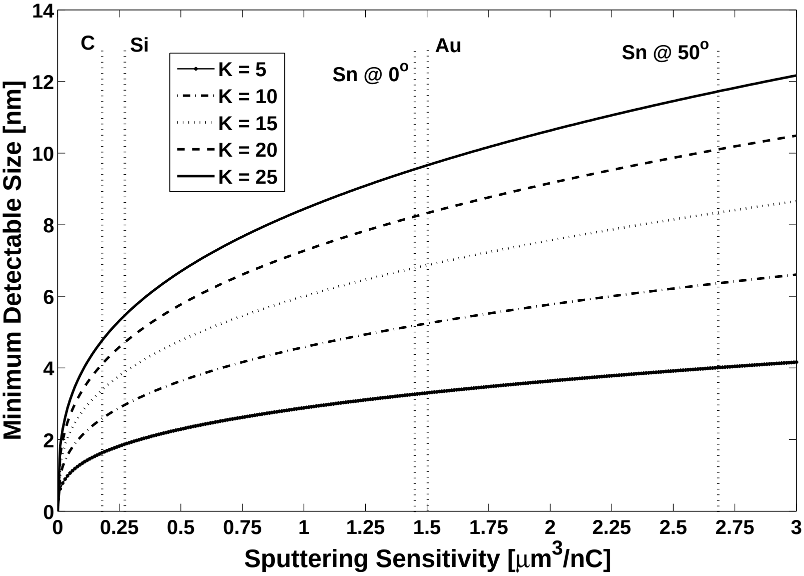

Figure 6.1: The minimum detectable feature size in a SIM from eq. 6.1, as a function of Sputtering Sensitivity S at different values of K, for $\delta = 2$ and $\Omega = 0.5$. In the graph the Sputtering Sensitivity of different target materials for 30 keV Ga$^+$ ions is highlighted.

$$D_{min} = \sqrt[3]{\frac{S}{\Omega^2}\,\frac{I_{beam}}{p_x}\,t_{scan}} \,, \tag{6.3}$$

where I_{beam} is the ion current, and p_x the total number of pixels in the image. Fig. 6.1 shows D_{min}, as a function of the sputtering sensitivity S for different levels of SNR in the image.

The conclusion is that, for features in the order of a few nm, the *resolution*, defined as the smallest observable particle, is actually determined by the competition between sputtering and SE production/collection, at least for heavy ions like Ga^+ (Atomic Weight: 69.723). Similarly to the limit posed by sputtering, other effects that damage the sample while imaging (e. g. contamination, heating, charging, to list some of the sample damaging factors that occur in both Electron and Ion Microscopy) also contribute to raising the lowest limit for detectable particles. Eq. 6.1 represents a fundamental limit to the imaging performance of a FIB. Even if the predicted resolution is hardly achieved in practice, as it has been stated under the assumptions of perfect collection of secondaries and Poisson-distributed primary beam and ejected SEs, it is important in the sense that it establishes a theoretical limit.

A semi-empirical method for evaluating the performance of a FIB imaging machine has been proposed by Castaldo et al. in [55]. The underlying idea is quite simple: a feature of a given size on the sample is imaged over and over till it fully disappears. The evolution of the feature size versus the scanning time (or ion dose, to normalise for different values of the ion current), as shown in fig. 6.2, together with the relative error connected to each measurement, contains actually a lot of information. There are two competing factors that determine the resolution: the removal of sample material (or, more in general, the modification of the sample), that gives rise to U_{SM}, and the collection of information from the sample, which leads to U_I. Clearly, by increasing the scanning time the collected information increases, but so does the sample modification by e.g. sputtering: U_{SM} and U_I move in opposite directions. In terms of ‘Size vs. Time’ curve, this means that increasing the scanning time the error band (U_I) at each point narrows, but the distance between two subsequent measuring points (connected to U_{SM}) increases. If these two quantities are plotted versus the scanning time, there will be a point in which the two curves intersect: for longer scanning time U_{SM} is the limiting factor, for shorter scanning times the resolution is limited by the noise in the image. This point represents in fact the optimum imaging condition for the machine and the specific sample: it represents the *optimal scanning time* (or *optimal imaging dose*), i. e. the scanning time for which the smallest detectable particles are visualised.

Despite its simplicity, the ‘Size vs. Time’ curve tells even more than that. Consider two different microscope users, one working in the IC industry, and one studying deposition mechanisms at the nanoscale. The first one will be interested in inspecting microchips and in precisely measuring the size of the features, while the second one will try to look at the smallest possible details. Both of them will look for high resolution, but in practice the two needs are *two different ones* This distinction is clearly visible on the ‘Size vs. Time’ curve. The smallest detail can be determined from the right side: when the semiamplitude of the error band comes to coincide with the size of the observed feature, the limit of the resolution is reached, for a smaller detail cannot be distinguished anymore from the background noise. But when it comes to the precision of the measurement, things are

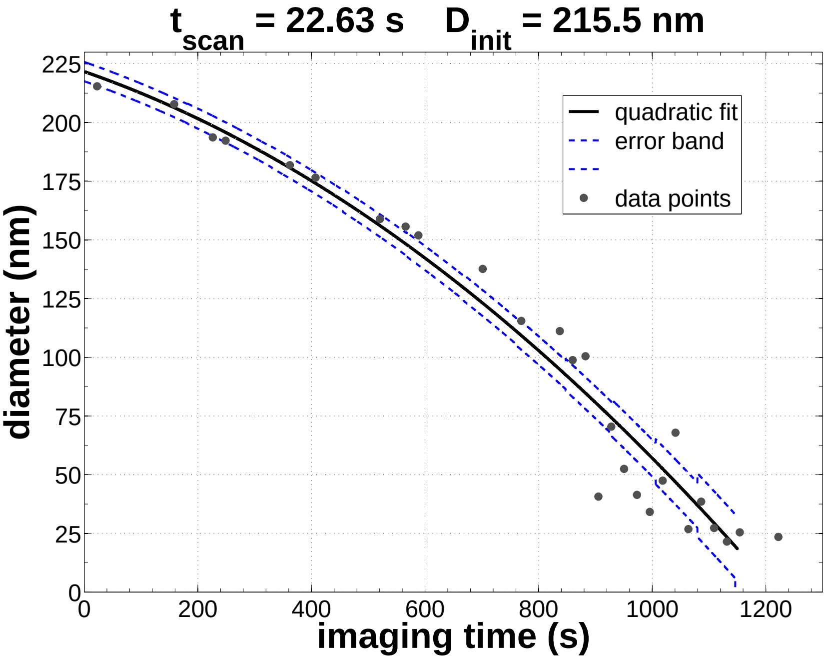

Figure 6.2: Size of a Sn-ball plotted versus the imaging time with Ga$^+$ ions at 30 keV.

different. Suppose we want to know the size of a line, we can image it with a FIB, many times, and build up a 'Size vs. Time' curve together with the error band. The curve can then be fitted, and the original size can be recovered tracing back to imaging time = 0. The error connected with this measurements is thus given by the amplitude of the band on the left side of the curve, and it is generally smaller. Of course, these two concepts coincide when the initial size of the feature is small enough to be already on (or below) the limit of detection, in which case there will be only one point in the curve. But in general these two concepts must be kept separated, and a curve like the one in fig. 6.2 is a good reminder of that.

6.3 Ga$^+$ vs. He$^+$: Simulations and First Results

The first step in an attempt to evaluate the possibilities of a FIB exploiting light ions, like He$^+$ (Atomic Weight: 4.003), is thus to calculate what the lowest theoretically achievable resolution is. This can be done easily, for example for Sn as target material, which has been used in the experiments discussed in this paper. Fig. 6.3 shows the sputter yields for Ga$^+$ and He$^+$ on Sn, at 30 keV, as obtained by Monte Carlo calculation with the popular code TRIM, freely distributed by J. Ziegler. [3] Equations 6.1 and 6.2 do not consider the dependence of Y on the incidence angle;

---

[3] SRIM/TRIM reference website: `http://www.srim.org/`.

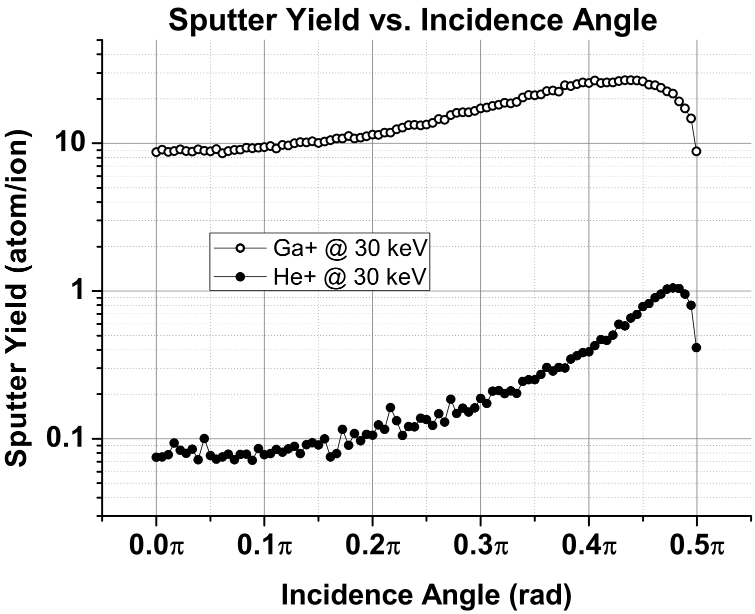

Figure 6.3: Sputter Yield versus Incidence Angle as obtained from TRIM simulation for Ga^+ and He^+ at 30 keV.

a mean value $\bar{Y}$ can thus be used. Tab. 6.1 shows the results obtained for $\delta = 2$ and $\Omega = 0.5$.

	$\bar{Y}\ \left[\frac{at}{ion}\right]$	$S\ \left[\frac{\mu m^3}{nC}\right]$	$D_{min}^{K=5}[nm]$	$D_{min}^{K=25}[nm]$
Ga^+	15.5	2.62	4.00	11.6
He^+	0.26	0.044	1.02	2.98

Table 6.1: Sputtering sensitivities and minimum detectable features as obtained from eq. 6.2 and eq. 6.1 for Sn target and beams of Ga^+ and He^+ at 30 keV.

This is an important result, showing that using He^+ ions the resolution in a FIB imaging system can never go below ∼1 nm, a value that is reached, in theory, only at the minimum acceptable level of the SNR. In any condition of noise, anyway, a He^+ beam allows for a resolution about 4 times higher than the one achievable using a Ga^+ beam in the same conditions.

At this point it is interesting to see what happens to a more realistic system under different sputtering conditions. Starting again from the simulated sputtering yields as a function of incidence angle, the shrinking of Sn-balls under irradiation with a Ga^+ beam and a He^+ beam at 30 keV have been simulated. The model is rather simple, based on a continuum approach and not taking into account the single ion/atom interactions (for the details of the simulation, see [55]). The result is shown in fig. 6.4: the two simulations have been carried out for a Sn-ball of initial diameter 130 nm, and the size is plotted against the ion dose, so that curves obtained for different ion currents, dwell times and magnifications can be directly compared. The scale on the x-axis is logarithmic, since the doses needed for an appreciable diameter reduction are rather different. What appears is that while the ratio between the average sputter yields is about 60 (from tab. 6.1, $\bar{Y}^{30keV}_{GaSn}/\bar{Y}^{30keV}_{HeSn} = 59.6$), the ratio of the dose required to totally destroy the ball is about 100, meaning that the different sputtering rates are somehow amplified when it comes to the modification of small features. [4] Fig. 6.5 shows the same curves, but this time based on experimental results: a standard Sn-balls sample for SEM calibration has been imaged with a Ga$^+$ FIB (Dual Beam Quanta 3d FEG from FEI) and with a He$^+$ FIB (ORION Plus from Zeiss SMT), and the evolution of two balls with similar initial diameter has been followed and plotted against the ion dose. [5] The imaging parameters for the two different experiments are listed in tab. 6.2. The graph also shows a linear fit, performed in order to estimate the rate

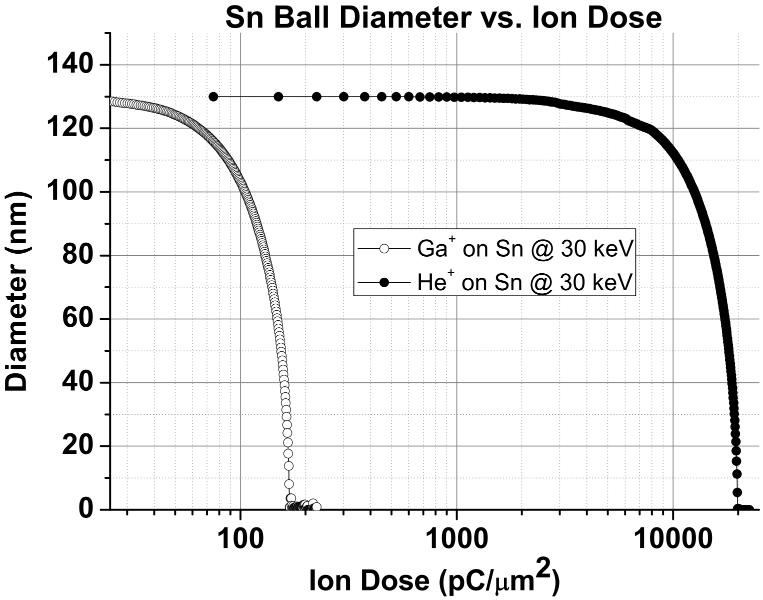

Figure 6.4: Simulation of the shrinking of a Sn-ball of initial diameter 130 nm under irradiation with Ga$^+$ and He$^+$ at 30 keV.

---

[4] Simply averaging the sputter rates is probably not the right metric for typical 3D objects like Sn-balls. A cleaner experiment would be studying sputtering damage to flat 2D objects, like lines.

[5] Since the Sputter Yield is a function of the incidence angle, a size effect is also present in the case of spherical features, because for smaller balls the relative weight of the edges, more sensitive to sputter than flat surfaces, is higher; this effect is more prominent in the case of He$^+$, for which the variation of the sputter yield for different angles of incidence is higher than for Ga$^+$, see fig. 6.3.

of shrinking [6]. First of all, it appears that the dose required to fully disintegrate a ball does not differ much from the dose as predicted by the simulation. This is encouraging, meaning that our simple model can already give a good account of reality. More interesting is the relative rate of shrinking. For the Ga^+, the features shrink with a rate of 1.3 nm/$\frac{pC}{\mu m^2}$, while for the He^+ the rate is 0.020 nm/$\frac{pC}{\mu m^2}$, leading to a ratio of ~65: the same feature under Ga^+ will disappear 65 times faster than under He^+ bombardment, a value that is in good agreement with the simulation.

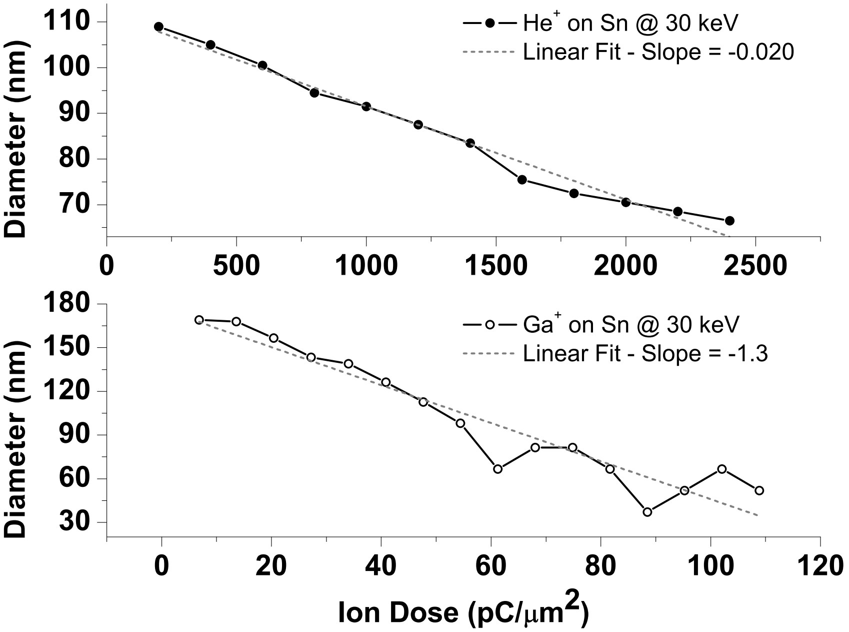

Figure 6.5: Measurement of the shrinking of two Sn-balls of similar initial diameter under irradiation with Ga^+ and He^+ at 30 keV.

	Dual Beam Quanta 3D	ORION
Calibration	0.274 pixels = 1 nm	2 pixels = 1 nm
Image Size	1024 × 1024 pixels	1024 × 1024 pixels
Field of View	3.65 μm	500 nm
Ion Current	1 pA	0.5 pA
Scanning Time	~90.5 s/frame	~100 s/frame

Table 6.2: Imaging parameters for the Sn-ball sample imaged with the Dual Beam Quanta 3D and with the ORION.

---

[6] From the simulation the shrinking appears to be quadratic rather than linear, but in this case the features are followed only in the initial phase of the shrinking, where a linear fit appears to be adequate.

6.4 On the Actual Resolution of the He$^+$ Microscope

In order to perform an analysis of the actual smallest detectable size of Sn-balls in the He-SIM, that takes into account also the effect of the beam on the sample, the procedure outlined in sec. 6.2, the details of which are explained in [55], has been used. We report here the formulas used to evaluate the U_I and the U_{SM}:

$$U_I = 2\frac{\sigma/|\tan\theta_L| + \sigma/|\tan\theta_R|}{\sqrt{2}\sqrt{\lfloor 0.2D \cdot C \rfloor + 1}} , \tag{6.4}$$

where σ is the standard deviation of the shot noise in the image corrected for the intensity level of the feature being observed, D is the ball's diameter, C the calibration factor in pixels/nm, and θ is the slope of the intensity profile evaluated at 50% of the step.

$$SU_{SM} = \int_{t^*-\Delta t/2}^{t^*+\Delta t/2} \frac{dy}{dt}(t)\, dt , \tag{6.5}$$

which is just a way to express the size change of the feature between two scans; here, $y(t)$ is the mathematical expression of the curve that fits the evolution of the ball's diameter in time.

Sets of images have been acquired for five different dwell times, ranging from 100 μs down to 5 μs, with imaging parameters (Image Size, Field of View, Ion Current, Ion Energy, Dwell Time) summarised in tab. 6.3. The number of frames acquired for each set and the total imaging time are shown in tab. 6.4. Fig. 6.6 shows the first image for each set, from the longest dwell time to the shortest one: the difference in the level of noise is evident. Six images from the set acquired at 20 μs of dwell time are shown in fig. 6.7, and it is immediately clear that, for these extremely small fields-of-view, the effect of the He$^+$ on the sample can not be neglected.

Imaging Parameter	**Value**
Image Size	1024×1024 pixels
Field of View	500 nm
Ion Current	0.3-0.5 pA
Ion Energy	~26 keV
Dwell Time	100μs, 50μs, 20μs, 10μs, 5μs

Table 6.3: Imaging parameters for the three different sets of scans analysed in the paper.

For each of the sets of images, the quantity U_I has been calculated according to eq. 6.4, for features of approximately 20nm in diameter. The calculation of U_{SM} has presented some difficulties, because it turned out that the features did not shrink continuously, but they tended to fade once a typical size of 20 nm in diameter had been reached. For this reason, the amount of sputtering between two subsequent frames at the point of disappearance of the feature has been approximated by dividing the smallest diameter reached by the number of further frames

Dwell Time	Scan Time	Number of Frames	Total Scan Time
100μs	~105 s	12	~1260 s
50μs	~52.5 s	30	~1575 s
20μs	~21 s	65	~1365 s
10μs	~10.5 s	135	~1417 s
5μs	~5 s	150	~750 s

Table 6.4: Number of acquired frames and total imaging time for each set of images.

that it took for the feature to disappear. The result of the analysis for the combination He$^+$-Sn is plotted in fig. 6.8, while fig. 6.9 shows the same curves for Ga$^+$ on Sn, for comparison. Both pictures also show the theoretical curves for U_S, as due to pure sputtering, which can be easily calculated multiplying the sputtering sensitivity S (μm^3/nC) for the dose rate d_r (nC/μm^{2}s) and then for the scanning time t_{scan} (s):

$$U_S = S d_r t_{scan} \; [=] \; \frac{\mu\mathrm{m}^3}{\mathrm{nC}} \frac{\mathrm{nC}}{\mu\mathrm{m}^2\mathrm{s}} \mathrm{s} = \mu\mathrm{m} \; , \tag{6.6}$$

with $d_r = I_{beam}/A$, where A is the area of the whole micrograph. Using for S the values in tab. 6.1 and referring to tab. 6.2 for the ion current and the field of view, the following is found:

$$U_S^{Ga-Sn}(t_{scan}) = 0.195 t_{scan} \; [=] \; \mathrm{nm} \tag{6.7}$$

and

$$U_S^{He-Sn}(t_{scan}) = 0.088 t_{scan} \; [=] \; \mathrm{nm} \tag{6.8}$$

Fig. 6.8 also shows the values of the smallest visible feature for each set. This curve is included as a double-check, as it takes into account both effects, uncertainty due to the collection of the secondaries and uncertainty due to the sputtering of target material. Here, the value of the smallest visible feature is rather arbitrary, for it depends on the threshold adopted in the definition of feature itself, but the fact that it shows a minimum for the same value of scan time for which the curves U_I and U_{SM} intersect is a good indication that the best value of scan time can be trusted.

Comparing fig. 6.8 and fig. 6.9, a few interesting observations can be made:

- the actual resolution for the Sn-balls sample found for the He-SIM is ~5nm, almost five times better than what found for the Ga-SIM (~23nm). In both cases the value is set by the beam/sample interaction. The observed limit of 5nm is of course linked to the sample used, both in terms of geometry and in terms of materials, and it could be lowered in special cases (flat geometries, samples with a lower sputter sensitivity);

- comparing the two curves of U_{SM} and U_S versus scan time, it appears that the two curves basically coincide in the case of the Ga$^+$ beam, while for the

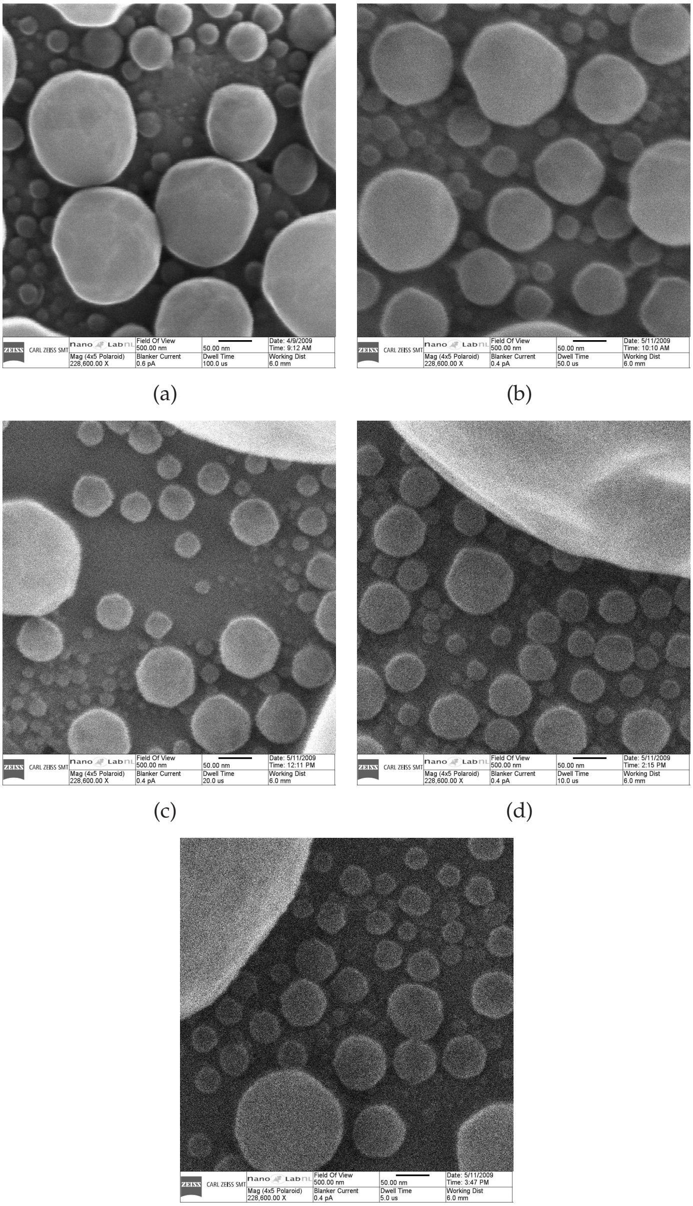

(a) (b)

(c) (d)

(e)

Figure 6.6: Images of the Sn-Balls sample acquired with different dwell times t_d, showing the increasing level of noise in the image; 6.6(a): t_d=100μs; 6.6(b): t_d=50μs; 6.6(c): t_d=20μs; 6.6(d): t_d=10μs; 6.6(e): t_d=5μs.

He$^+$ beam the observed U_{SM} is twice the calculated U_S; this translates in an experimental ratio of the sputtering rate between Ga$^+$ and He$^+$ of ~ 30,

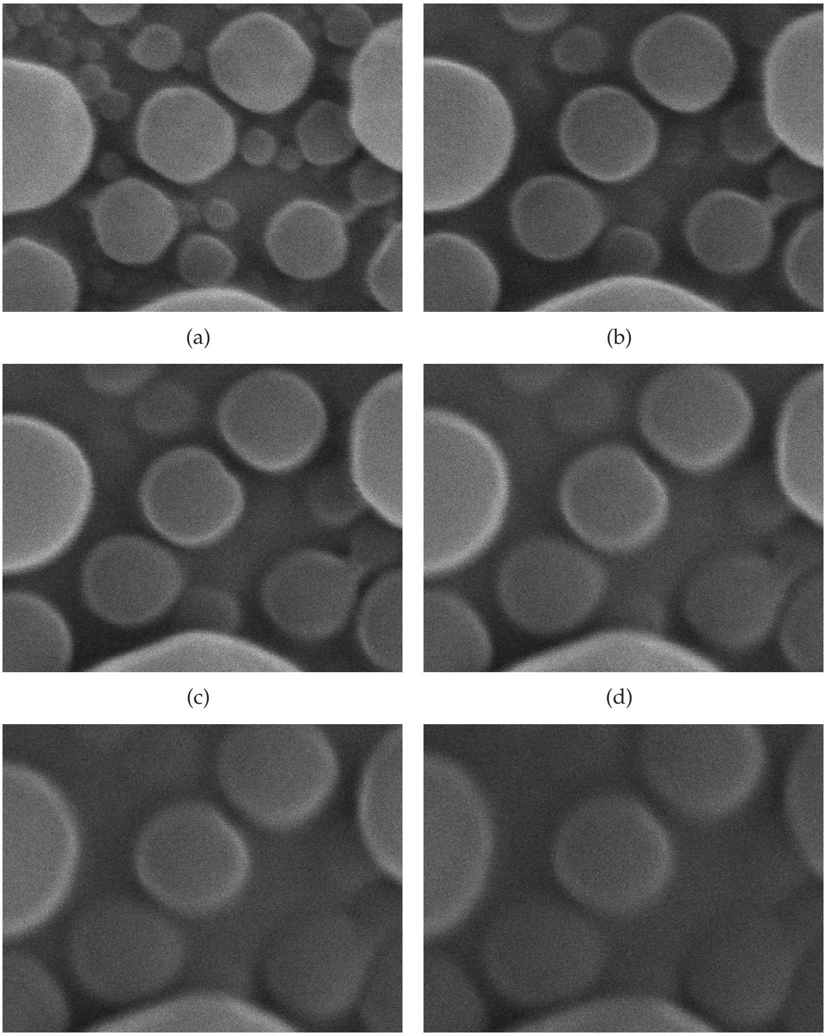
(a) (b) (c) (d) (e) (f)

Figure 6.7: Images from the series imaged with a dwell time of 50μs, showing the dramatic effect on the sample of the He^+ at high magnification; here the field of view is slightly less than 500nm because the images have been corrected for the shift; 6.7(a): after ∼52s of imaging at ∼0.3pA; 6.7(b): after ∼364s; 6.7(c): after ∼676s; 6.7(d): after ∼988s; 6.7(e): after ∼1300s; 6.7(f): after ∼1560s.

about half of the theoretical ratio;

- the lower sputtering is not the only advantage of the He-SIM, which exhibits very low values of the parameter U_I; recalling eq. 6.4, it can be seen that U_I takes into account three different effects: the shot noise in the image, that is

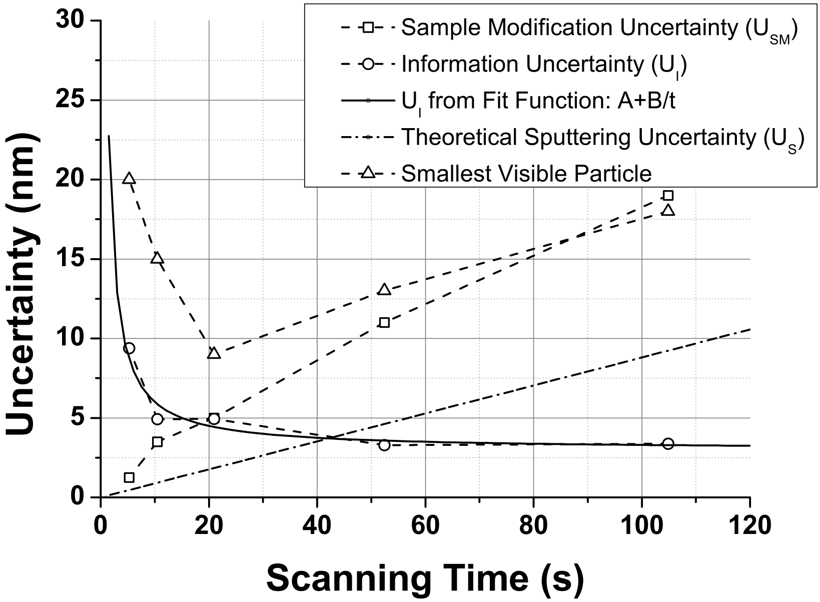

Figure 6.8: U_I, U_{SM} and U_S plotted for different values of scanning time for 0.4pA He$^+$ beam on Sn; a plot of the smallest visible particle for each different scan is also present, which confirms that the best resolution (~5nm) is achieved for a dwell time of 20μs (~20s of scanning time for a 1024×1024 micrograph). At this current and magnification, 100s of scanning time correspond to a dose of 160pC/μm^2.

connected with the detection of Secondary Electrons, the a priori knowledge on the sample, and the steepness of the edges in the intensity profile; the low values of U_I for the He-SIM have to be ascribed to the fact that the probe size is extremely small compared with the Ga-SIM (~0.3nm for the ORION, ~5nm for the Ga FIB);

- further investigation is required in order to understand and quantify the role of the local redeposition and the redeposition of atoms from different areas of the sample (contamination).

6.5 Conclusions

The main conclusions of this paper are here summarised:

- **Image Resolution in SIM is a *dynamic* concept:** at present the concept of resolution is presented as *static* in the sense that it is calculated based either on the optical system properties (probe size), or on the characteristics of a

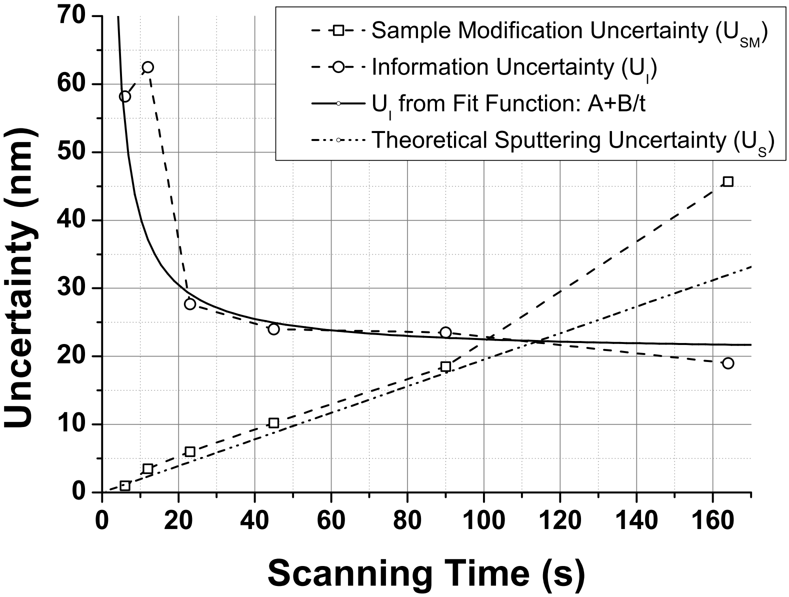

Figure 6.9: U_I, U_{SM} and U_S plotted for different values of scanning time for 1 pA Ga$^+$ beam on Sn, showing that the best resolution ($\sim$23 nm) is achieved for a scanning time of $\sim$100 s (corresponding to $\sim$100 μs dwell time for a 1024$\times$1024 micrograph). At this current and magnification, 100 s of scanning time correspond to a dose of 7.5 $\mathrm{pC}/\mu\mathrm{m}^2$.

single micrograph (edge resolution, gap resolution, inverse of the highest spatial frequency); this is not applicable when sample modification plays a role, in which case a *series* of images is required in order to quantify the effect of the beam on the target.

- **Image Resolution is *not* a property of the optical system *only*:** there is no case in which a single number can be assigned to a machine to characterise its performance, which is the result of the interaction between ions and sample; as a consequence, the system to be analysed is not only the microscope itself, but the combination of the microscope and the sample, both in terms of materials (different atom species are differently affected by the impinging ions) and geometry (even for the same material, features on the sample undergo different modification if, for example, they are flat or their size is different in different layers).

- ***Accuracy of Measurement* and *Smallest Detectable Feature* are two different concepts:** in particular the first one can be made independent of the sputtering effect, since this increases monotonically with the scanning time and can be modelled and quantified, while the second is intrinsically connected with the sample modification.

To support the concept of *dynamic resolution*, the procedure that has been proposed and defined in [55] has been applied to the combination He-SIM/Sn-balls-sample, which led to interesting results. In particular, it has been shown that, as expected, the performance (in terms of smallest detectable feature) of the He-SIM is better than the traditional Ga-SIM by a factor of, at least, 5.

Acknowledgments: *This work is part of the research programme "Microscopy and Modification of Nano-structures with focused electron and ion beams" (MMN) of the "Stichting voor Fundamenteel Onderzoek der Materie" (FOM), which is financially supported by the "Nederlandse Organisatie voor Wetenschappelijk Onderzoek" (NWO). The MMN programme is co-financed by FEI Company. In addition, support of the Bsik NanoNed programme of the Dutch Ministry of Economic Affairs is gratefully acknowledged.*

7 CHAPTER

Ion Microscopy Simulation

> *"What happens if a big asteroid hits Earth? Judging from realistic simulations involving a sledge hammer and a common laboratory frog, we can assume it will be pretty bad."*
> Dave Berry

Here is where most material, original and not, presented in the previous chapters is summarised and adapted to a full-scale analysis of the image formation in Scanning Ion Microscopes. The chapter is almost entirely made up of an article published this year (2011) in *Ultramicroscopy* on the simulation of ion imaging. At the end, an (unpublished) appendix illustrating in deeper detail the noise analysis that is performed and presented in the journal paper.

7.1 Simulation of Ion Imaging: Sputtering, Contrast, Noise

V. Castaldo, C.W. Hagen, and P. Kruit.

Ultramicroscopy, 2011; doi:10.1016/j.ultramic.2011.03.0191.

Abstract: *Scanning Ion Microscopy has received a boost in the last decade, thanks to the development of novel ion sources employing light ions, like He$^+$, or ions from inert gases, like Ne$^+$ and Ar$^+$. Scanning ion images, however, might not be as easy to interpret as SEM micrographs. The contrast mechanisms are different, and there is always a certain degree of sample sputtering. The latter effect, on the one hand, prevents assessing the resolution on the basis of a single image, and, on the other hand, limits the probing time and thus the Signal-to-Noise Ratio that can be obtained. In order to fully simulate what happens when energetic ions impact on a sample, a Monte Carlo approach is often used. In this paper, a different approach is proposed. The contrast is simulated using curves of Secondary Electron yields versus the incidence angle of the beam, while the surface modification prediction is based on similar curves for the Sputtering Yield. Finally, Poisson* *noise from primary ions and secondary electrons is added to the image. It is shown that the evaluation of an ion imaging tool can not be condensed in a single number, like the spot size or the edge steepness, but must be based on a more complex analysis taking into account at least three parameters: sputtering, contrast and Signal-to-Noise Ratio. It is also pointed out that noise contributions from the detector can not be neglected for they can actually be the limiting factor in imaging with Focused Ion Beams. While providing already good agreement with experimental data in some imaging aspects, the proposed approach is highly modular. Further effects, like edge enhancement and detection, can be added separately.*

7.1.1 Introduction

There are several reasons to choose ions instead of electrons in scanning microscopy, one of those being the smaller wavelength of ions when compared to electrons at the same energy, which results in a lower diffraction limit for the spot size of a focused beam. Other reasons include the possibility to use backscattered ions, with their enhanced sensitivity to crystallographic orientation (resulting in grain contrast), and the lower penetration power of ions, which relates the information in the image more directly to the surface of the sample [52, 84, 10, 11]. Ions, however, are heavier than electrons, and the momentum they carry is much higher when compared to electrons of the same energy; at 30keV, electrons carry a momentum of $\sim 9.5 \cdot 10^{-23}\ \mathrm{kg}\frac{\mathrm{m}}{\mathrm{s}}$, while for helium and gallium ions the momentum is, respectively, $\sim 8 \cdot 10^{-21}\ \mathrm{kg}\frac{\mathrm{m}}{\mathrm{s}}$ and $\sim 3.3 \cdot 10^{-20}\ \mathrm{kg}\frac{\mathrm{m}}{\mathrm{s}}$. It must also be pointed out that fixing the energy of the beam, the speed of the charged particles varies substantially: at 30keV, electrons travel at $\sim 10 \cdot 10^{7}\ \mathrm{m/s}$, helium ions at $\sim 12 \cdot 10^{5}\ \mathrm{m/s}$ and gallium ions at $\sim 3 \cdot 10^{5}\ \mathrm{m/s}$. That means that, at 30 keV, electrons are already in a relativistic regime, while ions are not. In order to slow electrons down to the speed of ions at 30keV, the beam energy should be no higher than a few units of eV.

In any case, when imaging with ions, particular attention must be devoted to the fact that the sample surface is sputtered away. This limits the dwell time used to acquire the image, and thus influences the obtainable resolution [55, 56]. It has been shown that the capability of resolving small details is ultimately limited by the sample modification [54]. In particular, two kinds of uncertainties must be taken into account; one due to the fact that the features are changing shape and size, the other connected with the noise in the image. Since the first quantity increases with the scanning time while the second one decreases, for each set of conditions (beam energy, magnification, atomic and ionic species) there is a value of ion dose for which the sputtering uncertainty and the noise uncertainty are exactly the same; increasing the ion dose will result in a sputtering-limited situation, while decreasing it will result in noise-limited conditions. One of the most interesting consequences of this scenario is that the concept of resolution itself ceases to be static, i.e. computable from a single picture. In fact, a sequence of micrographs is necessary in order to quantify the sample modification and to determine the limit it poses to the observation of small details. This concept of “dynamic resolution” makes the operation of determining the smallest measurable feature, for given imaging condition, a cumbersome one, for it requires a series of acquisitions and a differential analysis on the images. Therefore, it would be helpful to be able to simulate this competition of sputtering and information acquisition.

Codes are available to simulate the sputtering effect of an energetic ion beam on the sample surface, and they all employ either molecular dynamics [85] or Monte Carlo calculations [86, 87]. That means that each impinging ion must be followed from its impact point up to the point where either it finds its way out of the sample, or comes to rest inside the bulk, not having enough energy for further movements (thus creating defects in crystals, like interstitials and amorphisation). Considering that for each pixel in a typical scanning image there are tens, or more, of impinging ions, it is clear that building an image in such a way can not be fast. When wanting to assess the imaging qualities of an ion microscope, a simpler method is therefore preferred. In this article, a semi-analytical approach is proposed and implemented, that employs curves of sputter and Secondary Emission yields versus the incidence angle of the beam. The sputter yield γ is defined as the number of surface atoms sputtered away per incident ion, while the secondary electron yield δ_i is the number of emitted SEs per incident ion. Both γ and δ_i strongly depend on the angle α formed between the incident beam and the direction normal to the sample surface, and curves of γ and δ_i versus α can be simulated or experimentally obtained.

The main purpose of this article is to show that three elements in image formation, i.e. sputtering, contrast and Signal-to-Noise Ratio (SNR), are necessary and, often, also sufficient to quantitatively compare micrographs in terms of ultimate resolution,and to optimise the imaging conditions in terms of ion dose.

7.1.2 Simulation of Ion Imaging

In this section our procedure, used to obtain simulated ion images of first approximation, is explained in detail. Section 7.1.2.1 is dedicated to the definition of the sample, while the way the surface evolves under ion bombardment is the object of section 7.1.2.2; in section 7.1.2.3 the SE yield curves are applied in order to obtain the first-order contrast (as opposed to non-local effects due to the spreading of the beam under the surface, which are currently not taken into account). Section 7.1.2.4 is dedicated to the modelling of the noise from the beam and the SEs.

7.1.2.1 Definition of the Sample

The first step in simulating the behaviour of a Scanning Ion Microscope (SIM) is the definition of a suitable sample. The sample is here discretely defined as a $n \times m$ matrix $\mathbf{S}$, and the value of each point represents the height of the surface in the direction normal to the sample surface. In principle there is no connection between the size $n \times m = s$ of $\mathbf{S}$, the actual size of the sample, and the number of pixels p_x in the final image, as long as $s \geq p_x$, in order to avoid oversampling. In the following simulations, however, we assume that every point of $\mathbf{S}$ will be a pixel in the final image, and each pixel represents 1nm^2 on the sample. The surface of the sample is defined as a 2-variable discrete function:

$$\mathbf{S} = z = f\left(x, y\right) \ , \tag{7.1}$$

where x and y are the two Cartesian directions in the sample plane, and z is the normal direction. This poses some limitations, because for each point on the plane only one value of z is allowed, and complex three-dimensional topologies can not be represented in this way.

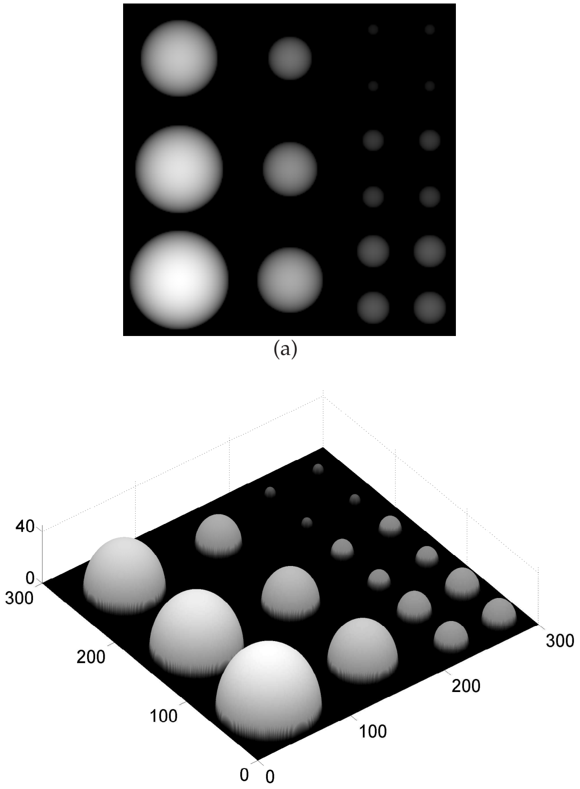

(a)

(b)

Figure 7.1: The sample defined for the simulations: a 300×300 matrix **S** with hemispherical features with radius in the range 5-45nm. It is shown as height map in fig. 7.1(b) and as 3D surface in fig. 7.1(a).

The sample used to experimentally validate the proposed model is a tin-balls specimen for medium resolution evaluation, from Agar[1]. It consists of a dispersion of tin spheres, with diameter range 10-100nm, on a carbon substrate. Since it appears from previous studies [55, 54] that the sputtering is scale-dependent (smaller features are sputtered away faster), a virtual sample has been defined

---

[1] Agar website: `http://www.agarscientific.com`.

	ρ (g/cm^3)	M (amu)	LBE	SBE	DE
C	2.253	12.01	3	7.41	28
Sn	7.282	118.71	3	3.12	25

Table 7.1: Target parameters used for obtaining the curves $\gamma = f(\alpha)$ via Monte Carlo calculation. M is the Molecular Mass, ρ is the density; LBE, SBE and DE are expressed in electronvolts.

with features in the same size range. This virtual sample is shown in fig. 7.1, as a height map (fig. 7.1(b)), and as a 3D surface (fig. 7.1(a)). It is a square of 300×300 points (thus nm), with hemispheres of different sizes on a flat surface ($z = 0$). In particular, there are six hemispheres of radius 45nm, 40nm, 35nm, 30nm, 25nm and 20nm respectively, plus three sets of four hemispheres of 15nm, 10nm and 5nm.

7.1.2.2 Sputtering from Ion Bombardment

The sputter yield γ ([=]atom/ion) expresses the number of atoms sputtered for each impinging ion, and it is a function of the incidence angle of the beam, for a given primary energy, and a given atom/ion pair. The reason for this dependence can be understood noticing that ions penetrating the sample at high angles travel closer to the surface, thus creating more havoc at the surface itself. Functions $\gamma = f(\alpha)$ have been obtained via Monte Carlo simulation with the software package TRIM [35], and are shown in fig. 7.2, for a 30keV Ga$^+$ beam on Sn and C (fig. 7.2(a)), and for a 25keV He$^+$ beam on Sn and C (fig. 7.2(b)). The energies chosen are the ones normally used in ion imaging).

It must be pointed out that the sputter yield is a strong function of target parameters like the Lattice Binding Energy (LBE), the Surface Binding Energy (SBE), and the Displacement Energy (DE); the values used to obtain the curves are summarised in table 7.1, together with other target parameters. In order to calculate how the sample surface changes during imaging, a more useful function, instead of the sputter yield γ, is the sputter rate γ_r, which expresses the speed of surface recession for a given ion current. γ_r can be calculated from γ, knowing the ion current and some target constants:

$$\gamma_r(\alpha) = \frac{\phi_b}{N}\gamma(\alpha) = \frac{I_b\,M}{e\,p_s^2\,N_o\,\rho}\gamma(\alpha)\ , \tag{7.2}$$

where ϕ_b is the ion flux (ion/nm^{2}s), N is the atomic density of the target material (atoms/nm^3), I_b is the beam current (A), M is the molecular mass (g/mol), ρ the target density (g/nm^3), N_o is Avogadro's constant ($6.02 \cdot 10^{23}$atoms/mol), e is the ion charge ($1.6 \cdot 10^{-19}$C/ion for single-charged ions) and p_s is the pixel size (in nm). To be able to compare different imaging conditions, it is convenient to express all the variable parameters as a function of the ion dose, i.e. the number of ions per unit area. Ion dose (D_i), dwell time (t_d) and scanning time (t_s) can be easily transformed into one another once the current has been assigned and the image size in pixels p_s and the imaged area A are known:

$$t_s = p_s \cdot t_d \ , \tag{7.3}$$

and

$$D_i = \frac{I_b p_s}{eA} \cdot t_d \ . \tag{7.4}$$

Since $\gamma_r = f(\alpha)$, the next step is to create a matrix $\mathbf{S}_\alpha$ whose points represent the

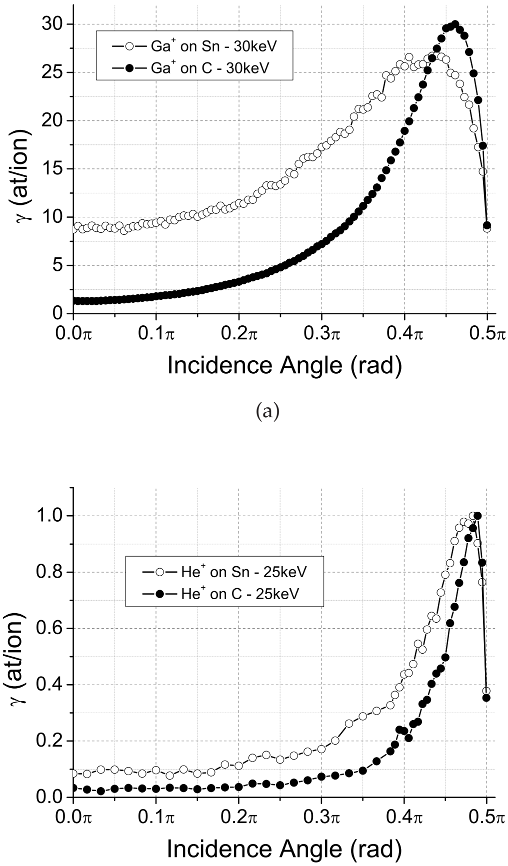

(a)

(b)

Figure 7.2: The dependency of the sputter yield γ on the incidence angle α as obtained from TRIM simulation, for 30keV Ga^+ beam on Sn and C (fig. 7.2(a)), and for 25keV He^+ beam on Sn and C (fig. 7.2(b)).

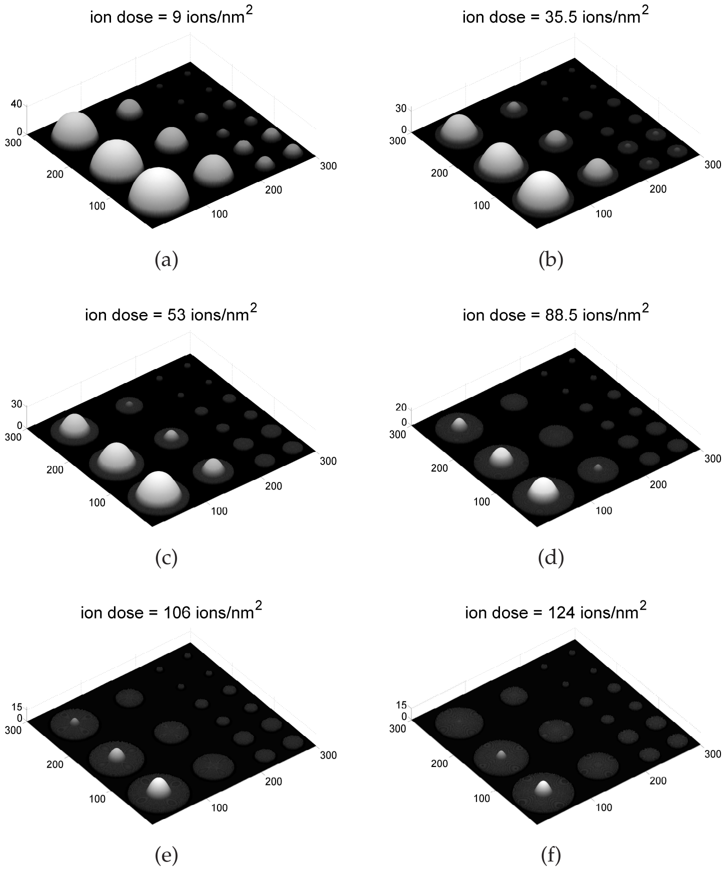

(a) (b)

(c) (d)

(e) (f)

Figure 7.3: The effect of sputtering; in this simulation, Ga^+ on the sample in fig. 7.1, with hemispheres of tin on an amorphous carbon substrate.

beam incidence angle for normal illumination:

$$\mathbf{S}_\alpha = \tan^{-1}\left[\left(\frac{\partial \mathbf{S}}{\partial x}\right)^2 + \left(\frac{\partial \mathbf{S}}{\partial y}\right)^2\right]^{1/2} \quad . \tag{7.5}$$

At this point, the formula 7.2 is applied to $\mathbf{S}_\alpha$ in order to calculate the amount of recession for a given scanning time; since the surface changes continuously, a time step Δt that is fine enough must be chosen, and eq. 7.2 applied iteratively:

$$\mathbf{S}^t = \mathbf{S}^{t-1} - \gamma_r\left(\mathbf{S}_\alpha^{\mathbf{t-1}}\right)\Delta t \;, \tag{7.6}$$

In order to avoid the propagation of numerical errors, a smoothing filter with unitary kernel (a bigger kernel would spread the features' material over the whole sample surface at every iteration) is applied to the sample surface at every iteration.

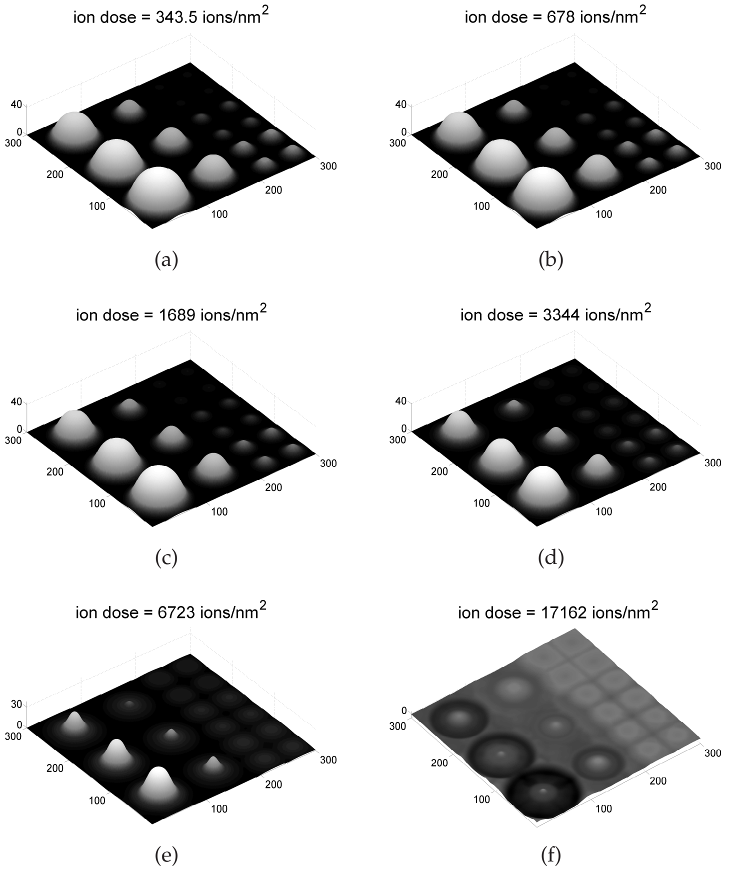

(a) (b) (c) (d) (e) (f)

Figure 7.4: The effect of sputtering; in this simulation, He$^+$ on the sample in fig. 7.1, with hemispheres of tin on an amorphous carbon substrate.

The function γ_r to apply depends on the target material; assuming that the sample is made of tin and carbon, eq. 7.6 can be rewritten using a different notation:

$$s_{ij}^{t} = s_{ij}^{t-1} - \gamma_r^{Sn,C}\left(s_{\alpha,ij}^{t-1}\right)\Delta t\ , \tag{7.7}$$

where s_{ij}^{t} and $s_{\alpha,ij}^{t}$ are the elements of $\mathbf{S}$ and $\mathbf{S}_\alpha$, respectively, at the time t; the choice of γ depends on the matrix element s_{ij}, and to what materials it belongs. In the present code, it has been assumed that a pixel belongs to the substrate if its z value is lower than or equal to 2nm.

Figures 7.3 and 7.4 show the result of the application of eq. 7.7 to the sample shown in fig. 7.1 (where the hemispheres are made of tin and the background is made of amorphous carbon), for Ga$^+$ at 30keV and for He$^+$ at 25keV respectively; the conversion between ion dose, dwell time and frame time is shown in tables 7.2 and 7.3, for a beam current of 1.5pA.

ion dose (ion/nm^2)	dwell time (μs)	frame time (s)
9	0.95	0.085
35.5	3.75	0.340
53	5.65	0.510
88.5	9.45	0.850
106	11.30	1.020
124	13.20	1.190

Table 7.2: Dwell time and frame time corresponding to the ion doses of fig. 7.3, assuming a Ga$^+$ current of 1.5pA.

ion dose (ion/nm^2)	dwell time (μs)	frame time (s)
343.5	36.5	3.30
678	72	6.51
1689	180	16.21
3344	357	32.10
6723	717	64.54
17162	1830.5	164.75

Table 7.3: Dwell time and frame time corresponding to the ion doses of fig. 7.4, assuming a He$^+$ current of 1.5pA.

7.1.2.3 Contrast from Secondary Electrons

Scanning microscopy images are built up simply counting the number of secondary species emitted at each pixel due to the momentum transfer from the impinging ions, and mapping them on a grey scale, in 8-bit (256 grey levels) or 16-bit (65,536 grey levels). Any secondary species can be used to create the map, each giving a different kind of contrast. In practice, the species that is most commonly used is the secondary electron, i.e. those electrons that receive enough momentum in the direction of the surface to travel to the surface itself, and then to escape through the surface energy barrier, which is of the order of a few units of eV.

The next step towards the final image **I** is therefore the sheer application of the function δ_i to the incidence angle matrix $\mathbf{S}_\alpha$. At this stage the effect of the finite size of the beam is not taken into account, and the image is still “noise-free”:

$$\mathbf{I}_\alpha(t) = \delta_i(\mathbf{S}_\alpha(t)) \; ; \tag{7.8}$$

just like γ_r in eq. 7.6, the function δ_i in eq. 7.8 is not unique for the whole sample, but must be specified for the specific material occupying a given position. The matrix $\mathbf{I}_\alpha$ contains at each point the value of δ_i corresponding to incidence angle given by the element with the same indices of the matrix $\mathbf{S}_\alpha$. In other words, $\mathbf{I}_\alpha$ contains the number of secondary electrons emitted at each position per incident ion. The functions δ_i can be obtained experimentally, or, in the case of He$^+$, they can be obtained via the simulation software IONiSE, developed by R. Ramachandra and D. Joy [45].

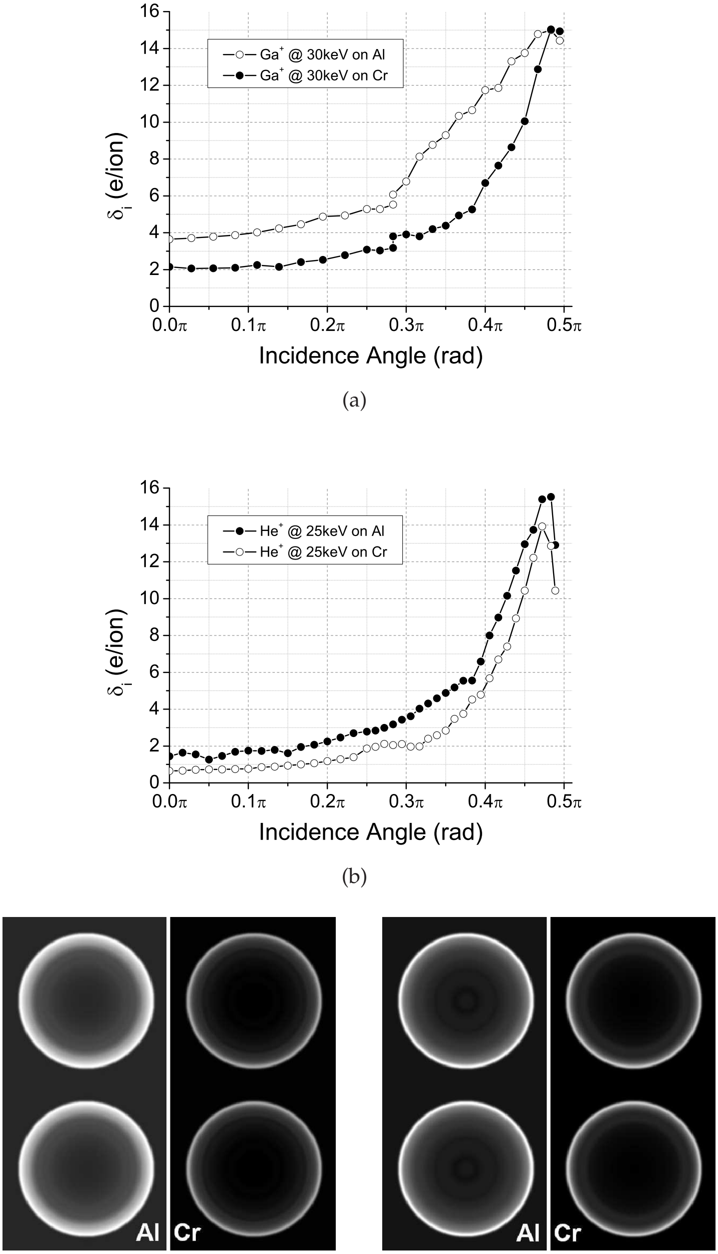

(a)

(b)

(c)

(d)

Figure 7.5: In figures 7.5(c) and 7.5(d), the SE contrast is shown on a sample made of Al and Cr, by applying eq. 7.8, with the experimentally obtained functions δ_i [88] plotted in figures 7.5(a) and 7.5(b), respectively.

In order to visualise the differences in contrast given by different atom/ion pairs, a sample with four hemispheres is defined, and then eq. 7.8 is applied, in the case of Ga^+ and He^+ beams, assuming that the two hemispheres on the left are made of Al, the two on the right of Cr. Experimentally obtained yield curves (subject of a previous study from the authors [88]) and the resulting images are shown in fig. 7.5. In fig. 7.5(c) the main contrast in Cr is at the edge, for in this case δ_i follows quite closely the secant law, while in Al the features are brighter also inside the edge, because δ_i is more linear and does not steep up only for very high angles. In fig. 7.5(d) the opposite happens, and the edges are in general more enhanced than in the case of Ga^+.

The effect of the finite size of the beam is taken into account convolving $\mathbf{I}_\alpha(t)$ with the beam; the shape of the beam can actually be rather exotic due to the aberrations inside the column [89]; a perfect spot can be represented as Gaussian of size d ($\mathbf{B}_\mathbf{d}$):

$$\mathbf{I}_\mathbf{d}\left(t\right) = \mathbf{I}_\alpha\left(t\right) \otimes \mathbf{B}_\mathbf{d} \; . \tag{7.9}$$

Application of eq. 7.9 simply blurs the image.

7.1.2.4 Signal-To-Noise Ratio

It has been shown [54, 50] that in the ideal case of perfect SE detection, and under the assumption that both the primary beam and the SEs are Poisson-distributed and all the other sources of noise in the system are negligible, the Signal-to-Noise-Ratio K can be expressed as:

$$k_{sn} = \sqrt{\frac{N_i\delta_i}{1+\delta_i}} \; . \tag{7.10}$$

where N_i is the number of impinging ions per pixel. Since the signal is the product $N_i\delta$, the amount of noise at each pixel is given by:

$$N = k_{sn}^{-1} N_i\delta_i = \sqrt{N_i\delta_i\left(1+\delta_i\right)} \; . \tag{7.11}$$

N is the standard deviation of the Poisson distribution at each pixel; assuming that the total process still follows a Poisson statistics, a "noise matrix" is generated as:

$$\mathbf{N} = \sqrt{N_i\mathbf{I}_\alpha\left(1+\mathbf{I}_\mathbf{d}\right)}\,\mathbf{R} \; , \tag{7.12}$$

where $\mathbf{R}$ is a matrix of size p_x containing pseudo-random values drawn from the Poisson distribution centred at $N_i\delta_i$. The final image is calculated as:

$$\mathbf{I} = N_i\mathbf{I}_\mathbf{d} + \mathbf{N} \; . \tag{7.13}$$

In eq. 7.13 the noise free image $\mathbf{I}_\mathbf{d}$ appears multiplied by the number of ions per each pixel, so that each point represents the actual number of emitted secondary electrons.

7.1.3 Comparison of simulation with real images

Putting together what has been discussed so far (sputtering, SE contrast, blurring effect from finite beam size, Poisson noise) simulated ion images can be produced, for various atom/ion pairs, various energies, primary current and spot sizes. Sets of simulated gallium images at 30keV (with a spot size of 3nm) and helium images at 25keV (with a spot size of 1.5nm) are shown in figures 7.6 and 7.7 respectively, together with real Ga-FIB and He-FIB images acquired with the same ion dose. The dose values are the same as in tables 7.2 and 7.3, excluding the highest values (124 ions/nm^2 and 17162 ions/nm^2 for Ga-FIB and He-FIB, respectively), at which all the features are sputtered away, and saturation phenomena are present both in the real and in the simulated images.[2]

In reality, the contrast from SEs is the result of the energy transfer in a finite volume around and beneath the impact point of the ion beam (interaction volume), and a 'local' approach like the one presented here gives only partial information on the real contrast. While the Ga images appear too noisy to make any kind of visual comparison, some observations can be done for the set of He micrographs. In particular, the edges in the real images are much thinner than the ones in the simulations; the reason for this is three-fold:

- the contrast is based on simulated δ_i curves, not experimental ones, and the accuracy of the simulations tends to decrease at high incident angles [88]
- the spot size in He microscopes seems to be subnanometric [4], while in the simulations a Gaussian of 1.5nm radius has been applied (given a sample definition of 1nm, it would have made little sense to apply a subnanometer spot);
- no effect of edge enhancing (i.e. lower SE emission from depressed points on the surface, higher SE emission from highly open points) is currently implemented in the code.

The real images also exhibit a shadow effect, due to the detection mechanism, that is also not implemented here. Nevertheless, just applying the function δ_i to $\mathbf{S}_\alpha$ is a very simple step, and one that already enables to compare the imaging capabilities of different tools. Effects like edge enhancing, transparencies and shadows can eventually be added to the code in a modular fashion: the "local contrast" presented here must thus be regarded as a first-order contribution to the total contrast. At present, thus, still many effects are left out, and the simulated images are not yet indistinguishable from real ones. For this reason, it seems more useful to use a modular approach also for the validation of the code.

An ideal evaluation of sputtering would involve the determination of the volume of the features for each micrograph. While this would be easy to do for simulated images, inferring accurate height information from a two-dimensional FIB

---

[2] The contrast appearing in the simulated Ga-FIB images of fig. 7.6 is actually based on SE yield curves for Ga$^+$ on Cr and Al (fig. 7.5(a)), instead of C and Sn, for the last curves are not available at the moment of writing; this does not affect the generality of the discussion.

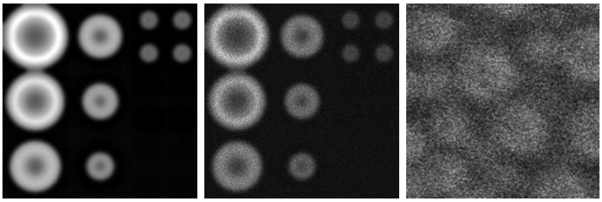

(a) 9 ions/nm^2 (b) 9 ions/nm^{2}05 (c) 9 ions/nm^{2}05

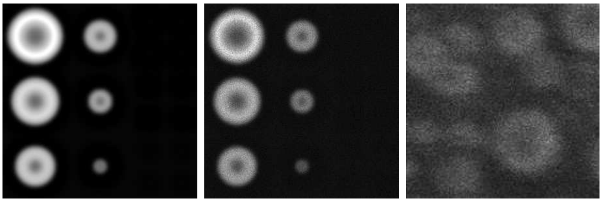

(d) 35.5 ions/nm^2 (e) 35.5 ions/nm^2 (f) 35.5 ions/nm^2

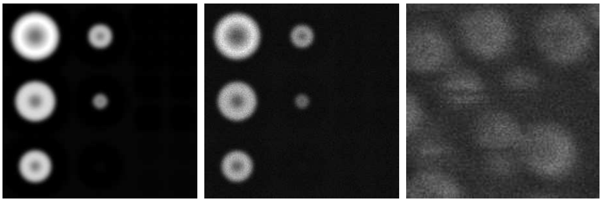

(g) 53 ions/nm^2 (h) 53 ions/nm^2 (i) 53 ions/nm^2

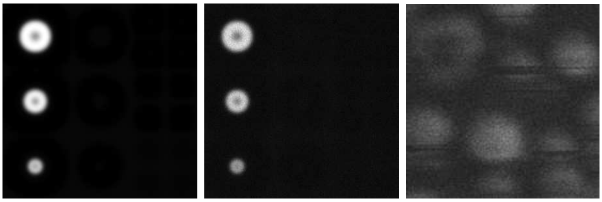

(j) 88.5 ions/nm^2 (k) 88.5 ions/nm^2 (l) 88.5 ions/nm^2

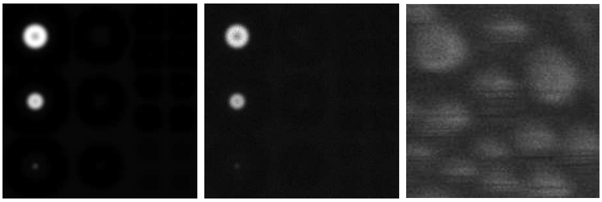

(m) 106 ions/nm^2 (n) 106 ions/nm^2 (o) 106 ions/nm^2

Figure 7.6: A set of simulated Ga-FIB images (noise free, in the left column, and with noise from eq. 7.13 in the central column) and a set of real images taken for the same values of ion dose (right column); the field of view is 300nm for all the images.

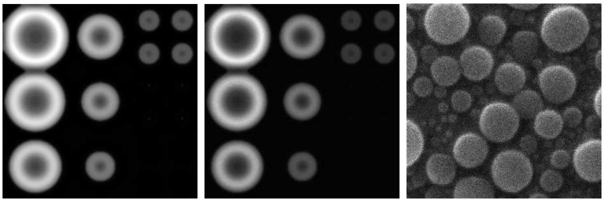

(a) 343.5 ions/nm^2 (b) 343.5 ions/nm^2 (c) 343.5 ions/nm^2

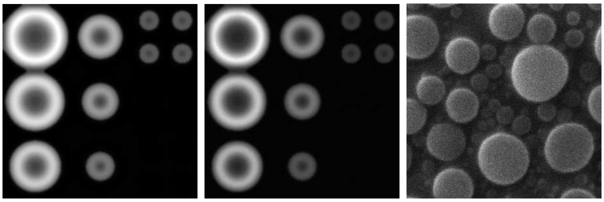

(d) 678 ions/nm^2 (e) 678 ions/nm^2 (f) 678 ions/nm^2

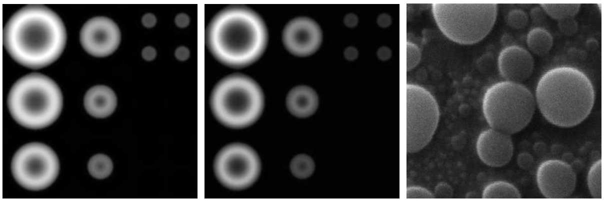

(g) 1689 ions/nm^2 (h) 1689 ions/nm^2 (i) 1689 ions/nm^2

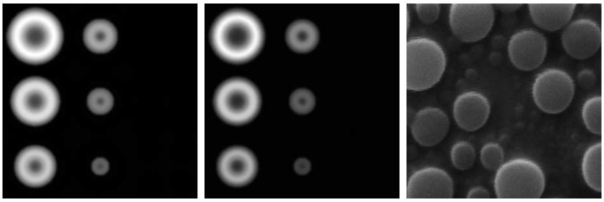

(j) 3344 ions/nm^2 (k) 3344 ions/nm^2 (l) 3344 ions/nm^2

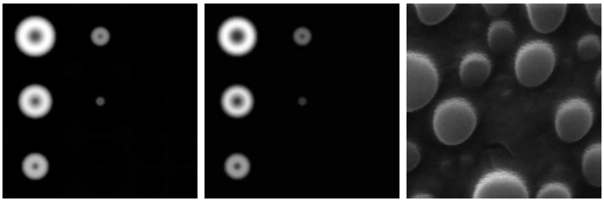

(m) 6723 ions/nm^2 (n) 6723 ions/nm^2 (o) 6723 ions/nm^2

Figure 7.7: A set of simulated He-FIB images (noise free, in the left column, and with noise from eq. 7.13 in the central column) and a set of real images taken for the same values of ion dose (right column); the field of view is 300nm for all the images.

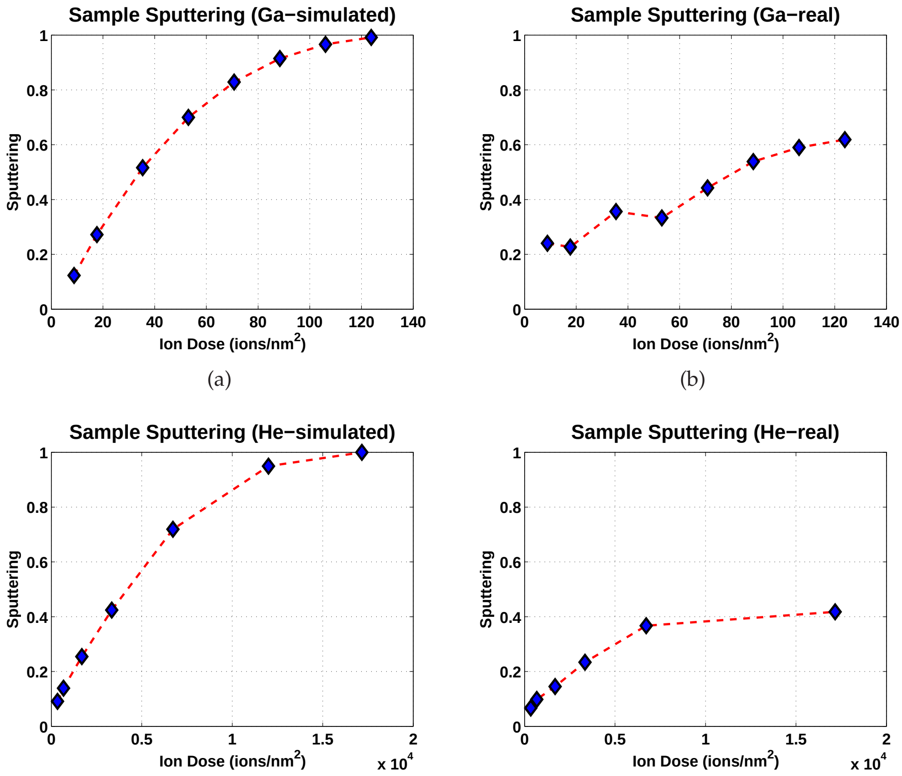

(a) (b)

(c) (d)

Figure 7.8: Sputtered fraction S versus ion dose for real and simulated sets of images; 30keV Ga$^+$ on Sn-balls (figures 7.8(a) and 7.8(b)); 25keV He$^+$ on Sn-balls (figures 7.8(c) and 7.8(d)).

picture is not possible; reason for which the sputtering has been evaluated in two dimensions, comparing the area, not the volume, occupied by the tin particles. The sputtering evaluation was thus performed with the following procedure:

- **thresholding:** each image of the set is 'binarised', assigning the value 0 to each background pixel, and the value 1 to each feature pixel; for the simulated set, the noise-free images have been used, to increase the accuracy of the thresholding operation; for the real images the operation has been performed on noisy images, with inevitable loss of accuracy:

$$\mathbf{I} \rightarrow \mathbf{I^b}; \tag{7.14}$$

- **pixel count:** once the image is binary, all the elements are just summed up, resulting in the total number of pixels (F) that belong to features:

$$F = \sum_{i,j} i^b_{i,j}; \tag{7.15}$$

- **comparison:** the amount of sputtering (S) in each image is defined as the fraction of feature pixels still present, compared with the same area of the sample before imaging:
$$S = \frac{F_{in} - F_{fin}}{F_{in}}. \tag{7.16}$$

For the real pictures, the fact that for each dose a different area on the sample is imaged does not affect the result, because the Sn balls distribution is assumed to be homogeneous. In order to compare the sample area after irradiation with the untouched status, however, before and after the exposure to the ion beam, images have been acquired with low doses, so that the sample could be assumed as unsputtered; the drawback is of course a loss of accuracy due to the high level of noise. The result of this operation is shown in fig. 7.8, for the sets in fig. 7.6 (figures 7.8(a) and 7.8(b)) and for the sets in fig. 7.7 (figures 7.8(c) and 7.8(d)). The curves must be compared bearing in mind that the real sample is made of spheres, while the simulation is based on hemispheres (thus, half of the material); with this caveat the rate of sputtering appears very similar in reality and simulation, in both cases. However, the real images show saturation before the sputtering is complete. In the view of the authors, this is due to the strong role of redeposition, that it is not taken into account in the present model. It must be added here that the thresholding operation is quite arbitrary regarding the choice of the threshold itself (the pixel value that discriminates between 'belong to the feature' and 'belong to the background'); the method chosen assigns a threshold value that makes the curves of sputtering versus doses extrapolate through the origin of the axes. Another important remark is that the difference in sputtering between Ga-FIB and He-FIB lies not only in the sheer amount of removed material, but also in a generally different shape evolution of the sample surface. Comparing fig. 7.3 and fig.7.4, it is evident that Ga$^+$ sputters in a more homogeneous way, in the sense that the original shape of the features is better preserved. This happens because the sputter yield is a stronger function of α for helium than for gallium (see fig. 7.2).

The next step is the noise comparison. The SNR is defined as the average pixel value divided by the standard deviation in a featureless portion of the image [90]:

$$k_{sn} = \frac{\mu(i) - \mu(j)}{\sigma(i)} \quad \forall i \in \mathbf{I_{fl}},\ \forall j \in \mathbf{I_{void}} \tag{7.17}$$

where $\mathbf{I_{fl}}$ is a 'flat' subset of $\mathbf{I}$, and $\mathbf{I_{void}}$ is a subset of $\mathbf{I}$ where no SE emission has occurred, i.e. $\mu(j)$ is the offset of the detector. There are two problems with the application of eq. 7.17. On the one hand, the offset $\mu(j)$ can not be determined from the image, but requires a calibration of the detector; on the other hand, k_{sn} is not unique for the whole image, but depends on the mean intensity level in the Region Of Interest (ROI). Thus, a more sophisticated analysis is required. Fig. 7.9 shows curves of variance versus mean intensity in featureless areas of the image, for the two sets of real images in figures 7.6 and 7.7, from the Ga-FIB (fig. 7.9(a)), and from the He-FIB (fig. 7.9(b)). Bearing in mind that each pixel in any of the pictures assumes a value in the range 0-255 (the 'intensity' that appears as unit in the plots), squaring eq. 7.11 shows that the variance of the intensity distribution, in each subset $\mathbf{I_{fl}}$, increases linearly with the intensity itself (given by the

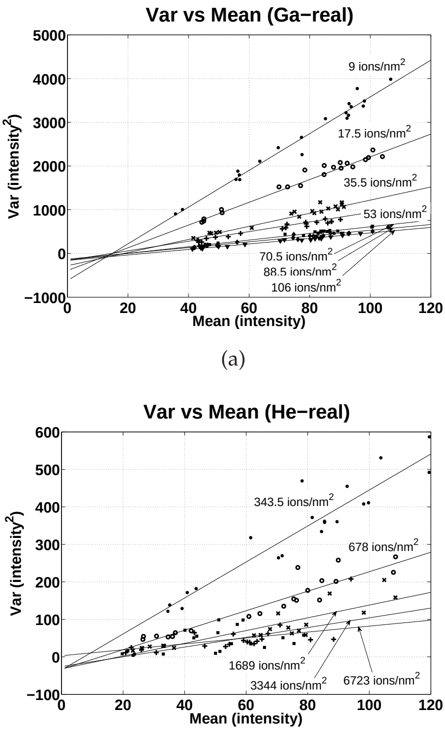

(a)

(b)

Figure 7.9: Curves showing the variance of the pixel values in flat ROIs, for the images in figures 7.6 and 7.7, as a function of mean intensity; as expected, the slope decreases for increasing ion dose.

product $N_i\delta_i$) when δ_i is not too big.[3] This kind of analysis solves both problems mentioned before. The intersection of the curves with the mean axis gives an estimate of the intensity level for which the noise is zero: the offset of the detection system; fig. 7.9 shows that for the Ga-FIB the images have been acquired with an offset of about 17 (on the 0-255 normalised intensity range), while in the He-FIB the offset was negligible. More importantly, the slope of the linear fit of each curve gives a measure of the noise in the corresponding micrograph that is not dependent on the mean intensity of the ROI, and is thus unique for the entire picture. A comparison of the noise level in the images, and of the way it varies with the ion dose used for the acquisition, can thus be performed comparing the slopes of the straight lines in fig. 7.9 as a function of the ion dose. Such curves are shown in fig. 7.10, for the Ga-FIB real and simulated images (figures 7.10(a) and 7.10(b), respectively), and for the He-FIB real and simulated images (figures 7.10(c) and 7.10(d)).

The He images are much less noisy than the Ga images, both for the simula-

---

[3] As it is shown in fig. 7.5, the value of δ_i is greater than 1, but not much greater; more importantly, δ_i is effectively lowered by the efficiency of the detector.

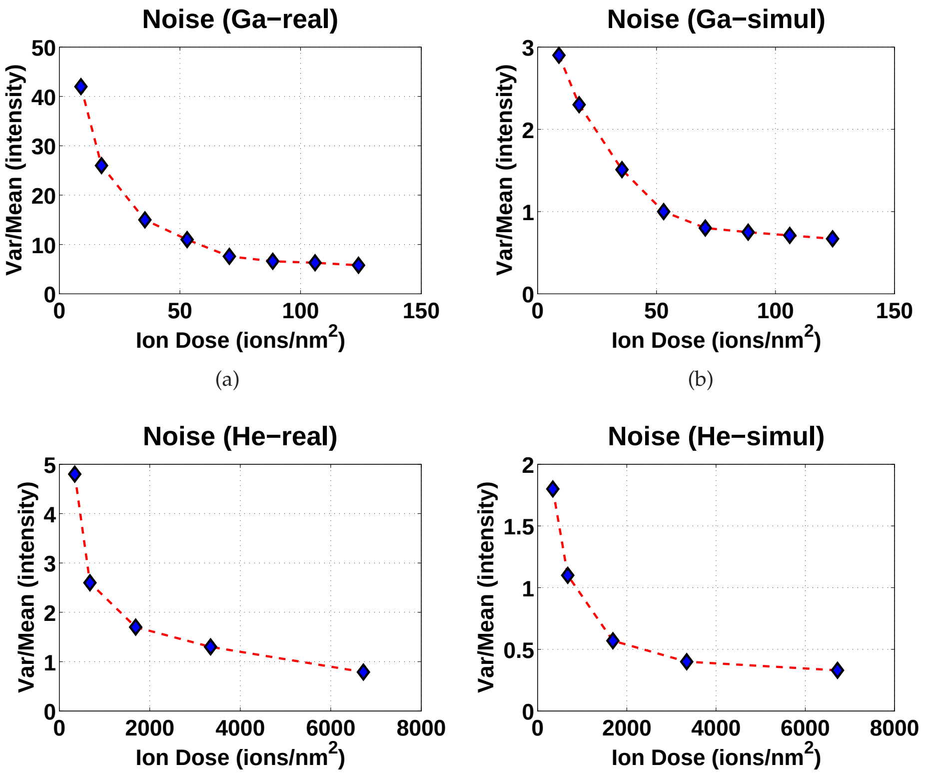

(a) (b)

(c) (d)

Figure 7.10: Noise comparison between real and simulated images; the plotted parameter is the slope of the variance curves, shown in fig. 7.9.

tions and for the real images; however, when comparing the two sets of images, produced/taken in the same conditions, the discrepancy is not-negligible, for the real images exhibit a much higher noise level than obtained from the model. The noise parameter plotted in fig. 7.10 differs with a factor of about 3 for the He-FIB, and up to an entire order of magnitude for the Ga-FIB. This means that the noise model presented in section 7.1.2.4, in which only the contributions from the primary ions and from the SEs are considered, is not sufficiently accurate. In particular, the appearance of the fit lines in fig. 7.9 suggests that the high level of noise in the real images is due to a low detector efficiency, because if the limiting factor were electronic noise they should exhibit a positive intensity-independent component; this is not the case, because all the lines intercept the vertical axis at values smaller or equal to zero. A quantitative discussion on the way the detector efficiency can be estimated from the variance curves is beyond the scope of the present study. It is noted, however, that a preliminary outcome of such an analysis suggests detector efficiencies of about 5% for the Ga-FIB and 3% (in the best case) for the He-FIB, including into this 'pseudo-efficiency' all what is missing between the model and the real pictures. These values are too low even when the Detec-

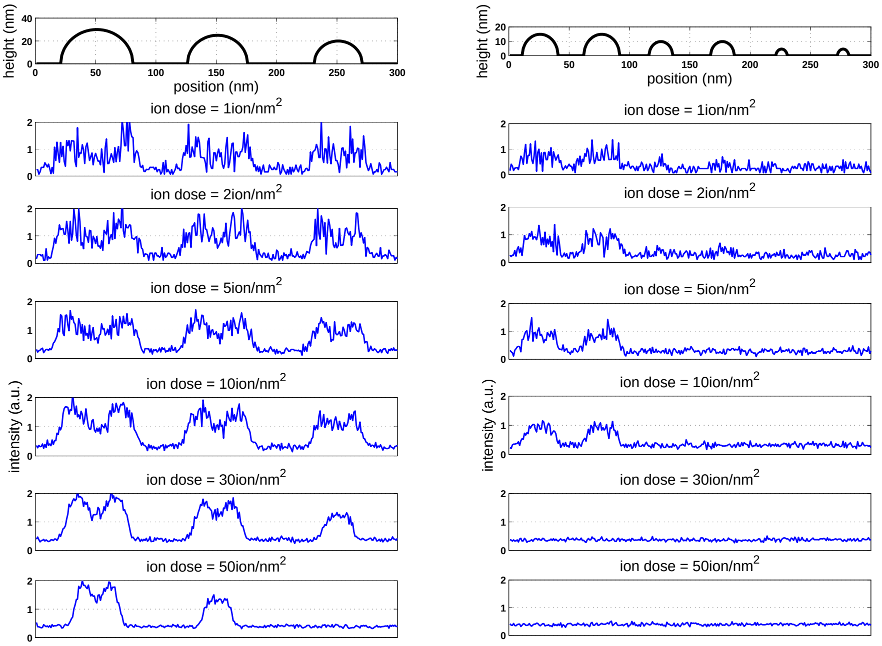

(a)

(b)

Figure 7.11: Diametrical line profiles for the simulated Ga images shown in fig. 7.6, across the hemispheres of 20nm, 25nm and 30nm radius (fig. 7.11(a)), and across the hemispheres of 5nm, 10nm and 15nm radius (fig. 7.11(b)).

tor Quantum Efficiency (DQE), typically of about 30%, is considered. One factor that could account for this gap is the fact that not all the SEs reach the detector grid, thus also the collection efficiency should be included. Another factor that might result in higher-than-expected levels of noise is the contrast with which the micrographs have been acquired; since the intensity in the simulated images is artificially normalised to the range 0-255, it spans the whole range; this is not necessarily true in raw (non-post-processed) images, which are directly acquired in 8-bits, with the consequence of possible signal loss. Finally, other external sources of noise, like environmental noise and instability of the ion beam, are also not implemented in the simulations. Such contributions are certainly present in practice, as it appears from the He images in fig. 7.7.

A useful application of the model under study is the ion dose optimisation for imaging small details, and the determination of the smallest detectable feature deriving from the competition of secondary information and secondary detection. Fig. 7.11 shows (normalised) diametrical line profiles of the hemispheres in the simulated Ga images. It appears that, due to the high sputtering, the 5nm and 10nm hemispheres can not be detected in any condition, and the smallest detectable feature is the one with 15nm radius. In this case, a dose of 10ions/nm^2

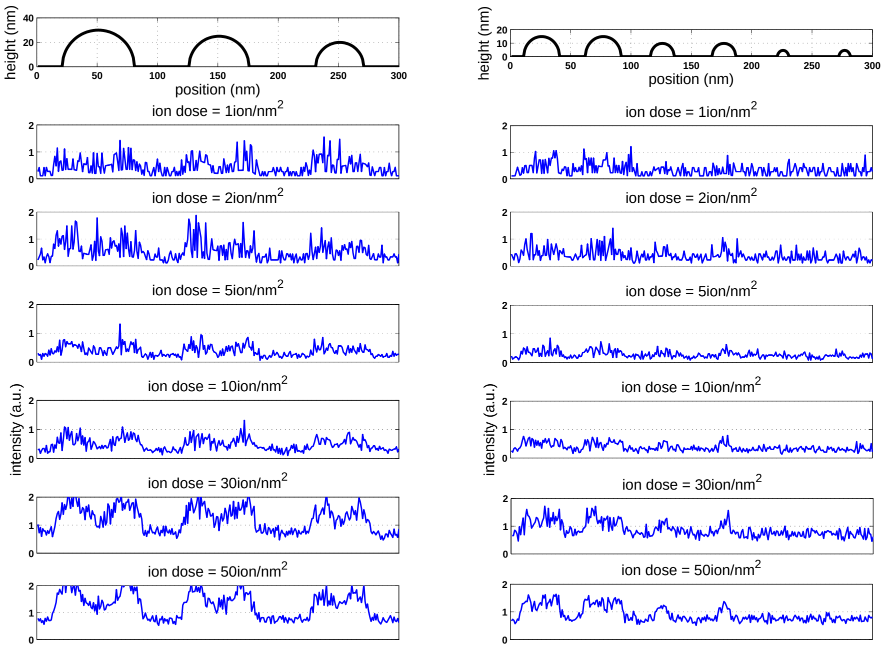

(a)

(b)

Figure 7.12: Diametrical line profiles for the simulated He images shown in fig. 7.7, across the hemispheres of 20nm, 25nm and 30nm radius (fig. 7.12(a)), and across the hemispheres of 5nm, 10nm and 15nm radius (fig. 7.12(b)).

seems the best choice, for the size is still reasonably preserved, and the SNR is obviously higher than the one obtained with a dose of 5ions/nm^2. On the other hand, for the hemispheres in the radius range of 20-30nm, the best choice is a dose of 5ions/nm^2, which is sufficient to give a decent contrast, and is less damaging than a dose of 10ions/nm^2. The same reasoning can be done for the profiles from the He images, shown in fig. 7.12. In this case imaging features of 10nm radius is already possible.

One last remark is that in some cases tricks can be used to improve the SNR without increasing the damage to the sample. Information can not be created from nowhere, but when a priori knowledge of the system is available, this knowledge can be converted into signal. Figures 7.13 and 7.14 show the same line profiles of figures 7.11 and 7.12, but this time three adjacent pixel lines are averaged. This operation is possible only when the shape of the features is known, thus to be sure to average quantities that represent (almost) the same real object. This works indeed; in the case of Ga imaging, it allows to detect the 10nm features, which in this case are visible with a dose of just 1 ion per nm^2.

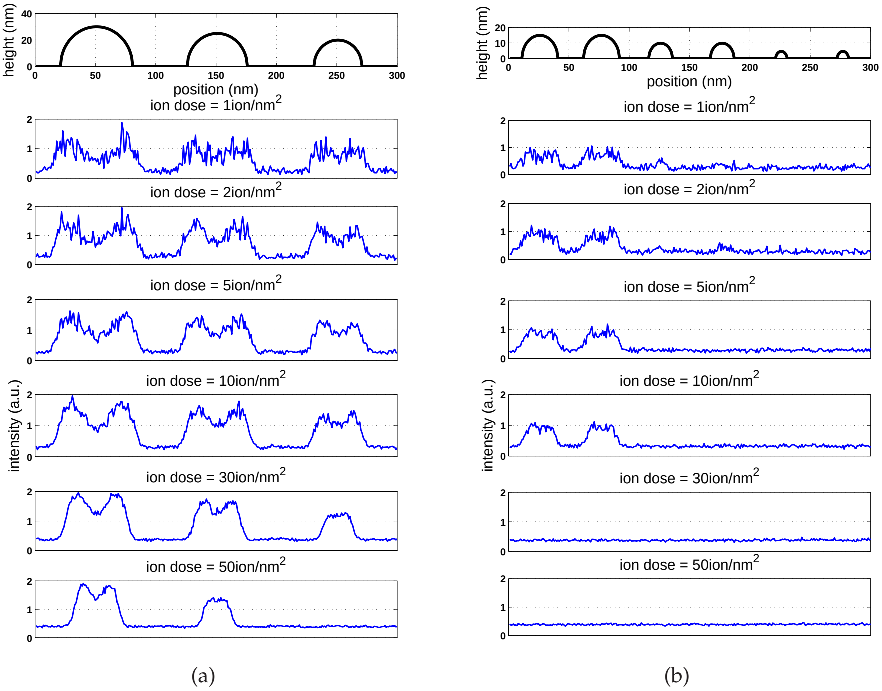

Figure 7.13: Same line profiles shown in fig. 7.11, but averaged on three adjacent pixel lines.

7.1.4 Conclusions

In this article, a step-by-step method to simulate SIM imaging, with the primary purpose of testing the building blocks of ion scanning imaging formation, is presented. Currently, only a limited number of aspects is taken into account, namely sputtering, local contrast and primary/secondary noise. These three key aspects must, in the view of the authors, be incorporated in any quantitative evaluation of the resolution in a scanning ion micrograph, as opposed to a simplistic definition of resolution based on the spot size of the microscope. The contrast mechanism implemented in the model does not yet incorporate non-local effects, leading, among other things, to edge enhancement and transparency, but is already able to explain some first-order differences between different microscopes, and in particular why SE contrast is higher in He-FIBs compared to Ga-FIBs. We have also shown that the noise contribution from the detector is non-negligible, and has to be taken into account. Furthermore, we have demonstrated that the algorithm is already suitable for the optimisation of the ion dose for imaging features of given size/material, and for the determination of the smallest observable feature in an ion microscope.

Looking forward, the first step will be to improve the algorithm by incorporating the redeposition of sputtered atoms. This could be done by adding to the sam-

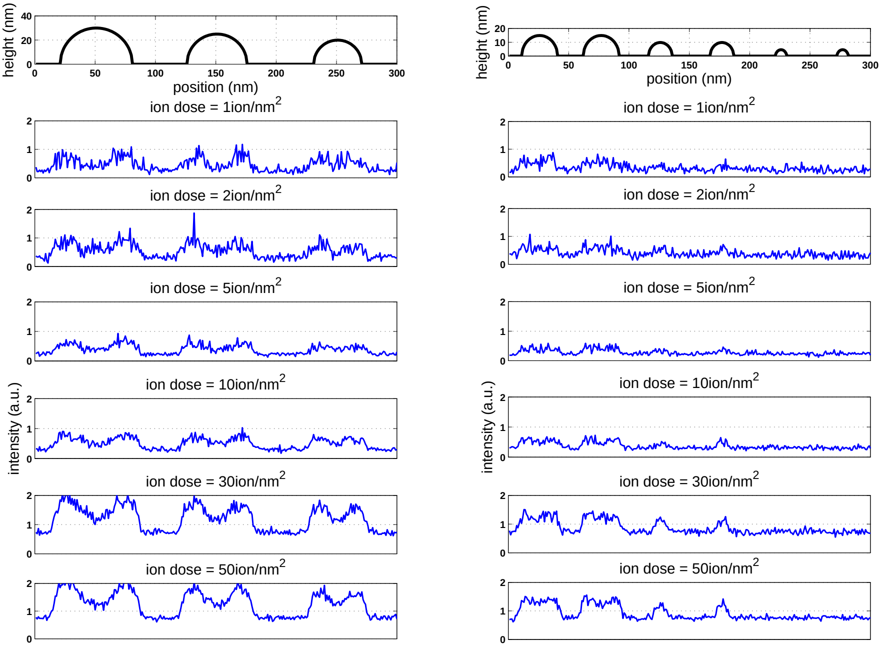

(a) (b)

Figure 7.14: Same line profiles shown in fig. 7.12, but averaged on three adjacent pixel lines.

ple surface **S** a thickness $\mathbf{S}_{red}$, obtained by convolving the recession $\gamma_r \left(\mathbf{S}_\alpha^{\mathbf{t-1}}\right) \Delta t$ with a redeposition function. The redeposition function should be proportional to the projection on the sample plane of the angular distribution of the sputtered atoms, usually assumed to be of the Sigmund-Thompson type [41]. Also, the model will have to be validated more extensively not only in terms of the amount of sputtered sample material, but also with respect to the topographic evolution of the probed surface. One more challenge will be to include the above mentioned non-local effects in a semi-analytical way, without any Monte Carlo calculation.

Acknowledgments: *This work is part of the research programme "Microscopy and Modification of Nano-structures with focused electron and ion beams" (MMN) of the "Stichting voor Fundamenteel Onderzoek der Materie" (FOM), which is financially supported by the "Nederlandse Organisatie voor Wetenschappelijk Onderzoek" (NWO). The MMN programme is co-financed by FEI Company. The authors wish to thank Diederik Maas and Emile van Veldhoven from TNO Delft, for providing imaging time and expertise on the He microscope.*

7.2 More on the Noise Analysis

In this section, the noise analysis presented in sec. 7.1 will be explained in more details and further developed. Fig. 7.9 shows plots of variance of the intensity distribution versus mean intensity. At each pixel, the intensity (i.e. the signal) is the total amount of emitted secondaries [4], $N_i\delta_i$, while the variance is obtained squaring eq. 7.11, which represents the standard deviation of the intensity distribution in a micrograph, under the assumptions of Poisson-distributed primary ions and secondary electrons, and perfect detection. Thus:

$$I = GN_i\delta_i \ , \tag{7.18a}$$

$$\sigma_I^2 = G^2N_i\delta_i\left(1+\delta_i\right) \ , \tag{7.18b}$$

G being a conversion factor that converts the particle counts to grey levels (on the scale 0-255 in an 8-bit picture) For ease of visualisation, the overlines that usually denote averaged quantities have here been omitted, but it must be kept in mind that all the variables addressed in the following discussion are stochastic in their nature. Based on eq. 7.18b, two different regimes can be recognised; one in which the limiting factor in the image formation chain is the number of produced SEs ($\delta_i >> 1$), and one in which the limiting factor is the number of primary ions hitting the sample ($\delta_i >> 1$):

$$\sigma_I^2 = \begin{cases} G^2N_i\delta_i & \text{for } \delta_i << 1 \\ G^2N_i\delta_i^2 & \text{for } \delta_i >> 1 \end{cases} . \tag{7.19}$$

In fig. 7.15, σ_I^2 from eq. 7.18b is plotted against I, together with the approximations 7.19, in the case of SE-limited regime (fig. 7.15(a)), and in the case of primary-limited regime (fig. 7.15(b)). The analysis of the previous section has been performed in the assumption of SE-limited signal; this could appear suspicious at the moment, for δ_i typically assumes values of a few units, but it will be better justified shortly. In this case, dividing eq. 7.18b by eq. 7.18a, the slope of the curves, which has been chosen as noise quantification, is written as:

$$\frac{\sigma_I^2}{I} = G \tag{7.20}$$

It is not immediately clear, then, from eq. 7.20, why the curves plotted in fig. 7.9 exhibit different slops. The reason is that each of those straight lines relates to a different image, acquired with a different ion dose; the conversion factor G maps these different signal values to the same grey level interval, meaning that both G and N_i have different values for different curves.

So far, so good, but there is more. It has been shown in the previous section that the assumption of perfect detection is not a realistic one. Without going too far in modelling detection noise, let's just assume that only a fraction of the SEs that are produced at the sample are actually counted. In this case, equations 7.18a

---

[4] In the assumption of perfect detection, the number of emitted secondaries is equal to the number of detected secondaries.

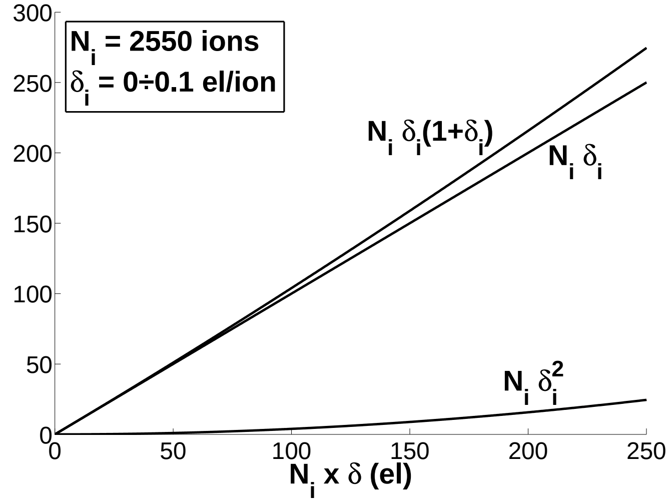

(a)

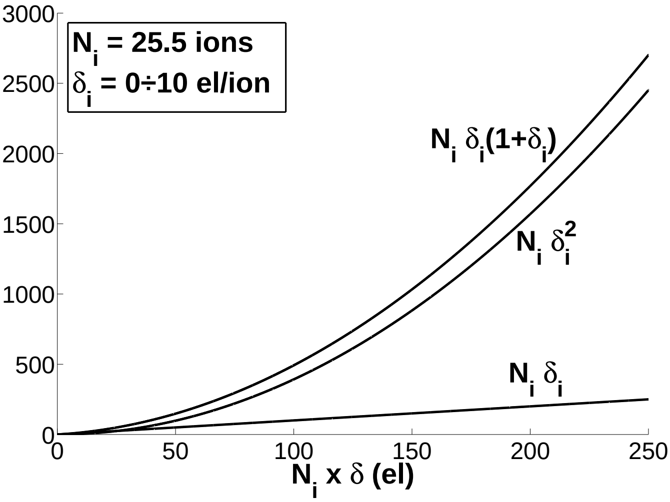

(b)

Figure 7.15: σ_I^2 from eq. 7.18b plotted against I, together with the approximations 7.19, in the case of SE-limited regime (fig. 7.15(a)), and in the case of primary-limited regime (fig. 7.15(b)); the conversion factor G is here assumed to be 1.

and 7.18b still hold, just substituting δ_i with the product $\eta\delta_i$, η being the efficiency of the detector:

$$I = GN_i\eta\delta_i \ . \tag{7.21a}$$

$$\sigma_I^2 = G^2 N_i\eta\delta_i\left(1+\eta\delta_i\right) \ , \tag{7.21b}$$

It would be very nice if something could be said about η. In fact, it can, once it is noted that:

$$\frac{I}{\sigma_I} = \frac{GN_i\eta\delta_i}{G\sqrt{N_i\eta\delta_i}} = \sqrt{N_i\eta\delta_i} \quad \Rightarrow \quad \eta = \frac{1}{N_i\delta_i}\frac{I^2}{\sigma_I^2} \ . \tag{7.22}$$

The terms I and σ_I^2 in eq. 7.22 are immediately obtained from the variance plot; N_i is known, because is user-defined; δ_i can be assigned an average value from the pertinent SE yields curves. Eq. 7.22, thus, allows an estimation of the detector efficiency η. In reference to figures 7.9(a) and 7.9(a), η can be estimated from any of the variance plots; of course, plots differing from each other only in the ion dose, but acquired with the same machine in the same configuration, should give the same value for η. The estimation of η from each of the variance curves for the Ga-FIB set of images is shown in tab. 7.4, while in tab. 7.4 the same calculations are performed for the He-FIB images set.

Ga$^+$ on Sn-C – $\langle\delta_i\rangle$ = 5			
N_i [ions/nm^2]	I	σ_I^2	η
9.0	120	4420	0.072
17.5	120	2730	0.060
35.5	120	1520	0.053
53.0	120	1160	0.047
70.5	120	762	0.054
88.5	120	662	0.049
106.0	120	596	0.046
124.0	120	546	0.043
averaged value for η: 5.30%			

Table 7.4: Estimation of the detector efficiency for for the Ga-FIB image set in the previous section.

He$^+$ on Sn-C – $\langle\delta_i\rangle$ = 2.5			
N_i [ions/nm^2]	I	σ_I^2	η
343.5	120	541	0.031
678.0	120	279	0.030
1689.0	120	172	0.020
3344.0	120	130	0.013
6723.0	120	97.7	0.009
averaged value for η: 2.05%			

Table 7.5: Estimation of the detector efficiency for for the He-FIB image set in the previous section.

In the case of the Ga-FIB, η seems not to vary with the ion dose, just as expected; for the He-FIB set, however, there appears to be a trend, with the detector efficiency slowly decreasing with the ion dose. The averaged values found for η, $\sim 5.5\%$ for the Ga-FIB and $\sim 2\%$ for the He-FIB, justify the initial assumption of SE-limited SNR, for the value of the product $N_i\eta\delta_i$ is in both cases much smaller than 1.

8 CHAPTER

Conclusions

"The trouble with our times is that the future is not what it used to be."
Paul Valéry

The most general and interesting conclusions that I was able to draw out of my thesis project are here summarised, as concisely and clearly as possible, followed by a short outlook on the field. Further personal impressions and a few pieces of advice for whoever comes and joins the world of Scanning Ion Microscopy are to be found in the Post Scriptum.

In chapter 3, a method to measure ion-induced SE yields has been proposed and curves of yields as function of the ion beam incident angle have been presented for different pairs ion/atom. Several factors have been analysed: modification of the sample surface under ion bombardment, effect of backscattered ions, production of SEs from places other than the sample. The influence of each of these factors has been discussed and, in the case of the backscattered ions, quantified. The curves have been compared either with the secant law or with simulations; in both cases the Cr appears to behave 'better' than than Al: the match is good up to 0.4π for Ga/Cr, and up to 0.48π for He/Cr; but only up to 0.25π for Ga/Al, and up to 0.4π for Ga/Cr. The maximum value of δ_i is very similar in all cases ($\sim 14 - 16$ el/ion), but the range for He is higher than for Ga, due to the lower SE emission at low angles. This translates in a better topographic contrast for the He microscope over a wider range of incidence angles.

When the sputtering is taken into account, the problem of evaluating the resolution becomes more subtle, because the uncertainty connected with the information gained from the sample ('Information Uncertainty'), which decreasing while increasing the scanning time, is coupled with a new kind of uncertainty, the 'Sputtering Uncertainty', which increases with the scanning time. The main consequences of this new scenario are the following.

- Imaging becomes a problem of optimisation. There is an optimum value of resolution for a given sample/microscope system, deriving from the competition between Information Uncertainty and Sputtering Uncertainty; this value is obtained with a precise amount of ion dose, or equivalently, a precise value of scanning/dwell time.

- The resolution is not a characteristic of the imaging system only. This is actually true for any kind of scanning microscopy, for the quality of an image depends on the contrast that is typical of the combination sample/machine. The role of the sample, however, both in terms of topology of the surface and of nature/structure of the materials, is much stronger in the case of ion microscopy, where a material, or a geometry, that is less sputter-sensitive than another, will generally provide, in the same conditions, a better resolution.
- The resolution becomes a dynamic concept, in the sense that it cannot be calculated on the basis of a single image, for the dynamics of the modification of the features on the sample surface must be taken into account; an image, thus, is not enough: a movie is needed.

In chapters 5 and 6, a procedure for finding the best scanning time and the corresponding minimum measurement error when imaging with a FIB system is proposed and applied to both the Ga-FIB and the He-Fib. The approach is experimental, and complements the theory of sputtering developed by J. Orloff et al. For the imaging condition under which the pictures were taken, and , a best scanning time of ∼100s and a minimum error of ∼23nm have been found for the system Ga/Sn, while for the system He/Sn the minimum error has been set at ∼5nm, for an optimum scanning time of ∼20s. Thus, the performances of the He-FIB, in terms of resolution, appear to be 4-5 times better than for the Ga-FIB, with a similar ratio in terms of acqusition time. Three main conclusions can be drawn from this study:

- **Atomic resolution appears to be unobtainable in FIB microscopy:** even with very light ions at very small doses, the sputtering of target atoms makes it impossible a real-time inmage of completely aperiodic and irregular structures at the atomic scale;
- **No definite resolution can be assigned to a FIB microscope:** since the level of detail that is visible in a micrographs strongly depends on the system ion/atom, the best parameter to describe the imaging capabilities of an ion microscope, is the spot size; it should, however, not be confused with the resolution.
- **Accuracy of Measurement and Smallest Detectable Feature are two different concepts:** in particular the first one can be made independent of the sputtering effect, for it can be modelled and quantified, while the second one is intrinsically connected with the sample modification.

In chapter 7, a method to simulate SIM imaging is presentedin its preliminary form. It is shown that there are three key aspects that must be incorporated in any quantitative evaluation of the resolution in a scanning ion micrograph: sputtering, local contrast and primary/secondary noise The contrast mechanism implemented in the model does not yet incorporate non-local effects, leading, among other things, to edge enhancement and transparency, but is able to explain first-order differences between different microscopes, and in particular why SE contrast is higher in He-FIBs compared to Ga-FIBs. Also, it is shown that the noise contribution from the detector is non-negligible, and has to be taken into account. It has been deomonstrated that the implemented algorithm is already suitable for the optimisation of the ion dose for imaging features of given size/material, and for the determination of the smallest observable feature. The code will have to be iproved by incorporating the redeposition of sputtered atoms and will have to be validated more extensively not only in terms of the amount of sputtered sample material, but also with respect to the topographic evolution of the probed surface. Last challenge will be to include the non-local effects in a semi-analytical way.

Talking about the future of any emerging technology is always, to say it midly, a gamble. I think, anyway, that it is quite clear that the FIB will never fully replace the SEM for imaging purposes, for the fundamental limit to its resolution. The hope for seeing atoms with a scanning machine seems to have been too optimistic. On the other hand, however, there are situations in which the sputtering effect can be overcome thanks to the periodicity of the sample structure. When this is the case, the higher depth of focus and the smaller spot size exhibited by the He-FIB could result in clearer and sharper images, especially where the height range of the sample surface is high. This can only be achieved in post-processing, while for real-time images the SEM remains, at the moment, in a superior position. There is, anyway, another key aspect that must be considered: FIB versatility. While there is only one kind of electrons, the possibilities with ions are as many as the species in the periodic table. Different kinds of ions sources are currently being developed and, while helium ions appear to be the best choice for general-case imaging, it is not hard to imagine that different ion species will perform differently in different beam/sample systems, making the problem of FIB design much more complex but also much more challenging and promising. The consequence of this scenario is that it will take probably many years before the real potential of ion microscopy is fully assessed. What is needed now, in my opinion, is a more systematic effort in order to build databases of SE and sputtering yields for all kind of pairs ion/atom and in order to tidy up all the data that can be found in literature. Finally, ions allow imaging in backscattered mode, a technique that produces a grain contrast that is not obtainable with SEMs. All this makes the FIB microscope a very 'charming' instrument capable of offering pieces of information that are complementary to the ones obtained with the standard electron microscope.

Bibliography

[1] R.L. Seliger, J.W. Ward, V. Wang, and R.L. Kubena. A high-intensity scanning ion probe with submicrometer spot size. *Appl. Phys. Lett.*, 34(5):310–312, 1979.

[2] J. Orloff. High-resolution focused ion beams. *Rev. Sci. Instrum.*, 64(5):1105–1130, 1993.

[3] J. Orloff, M. Utlaut, and L.W. Swanson. *High Resolution Focused Ion Beams, FIB and Its Applications*. Kluwer Academic/Plenum Publishers, 2003.

[4] B. Ward, J.A. Notte, and N.P. Economou. Helium ion microscope: A new tool for nanoscale microscopy and metrology. *J. Vac. Sci. Technol. B*, 24(6):2871–2874, 2006.

[5] R. Hill, J. Notte, and B. Ward. The ALIS He ion source and its application to High Resolution Microscopy. *Physics Procedia*, 1:135–141, 2008.

[6] P. Chen, H.W.M. Salemink, and P.F.A. Alkemade. Roles of secondary electrons and sputtered atoms in ion-beam-induced deposition. *J. Vac. Sci. Technol. B*, 6:2718–2721, 2009.

[7] P. Chen. PhD thesis. *TU Delft*, 2010.

[8] V.N. Tondare. Quest for high brightness, monochromatic noble gas ion sources. *J. Vac. Sci. Technol. A*, 23(6):1498–1508, 2005.

[9] T. Ishitani, Y. Madokoro, M. Nakagawa, and K. Ohya. Origins of material contrast in scanning ion microscope images. *J. Electron Microsc.*, 51(4):207–213, 2002.

[10] K. Ohya and T. Ishitani. Comparative study of depth and lateral distributions of electron excitation between scanning ion and scanning electron microscopes. *J. Electron Microsc.*, 52(3):291–298, 2003.

[11] T. Ishitani and K. Ohya. Comparison in spatial spreads of secondary electron information between scanning ion and scanning electron microscopy. *Scanning*, 25(4):201–209, 2003.

[12] K. Ohya and T. Ishitani. Monte Carlo simulation of topographic contrast in scanning ion microscope. *J. Electron Microsc.*, 53(3):229–235, 2004.

[13] K. Ohya and T. Ishitani. *Focused Ion Beams Systems, Basics and Applications - Chapter 4*. Ed. N. Yao, Cambridge University Press, 2007.

[14] T. Ishitani and H. Tsuboi. Objective comparison of Scanning Ion and Scanning Electron microscope images. *Scanning*, 19(7):489–497, 1997.

[15] CASINO - Monte Carlo Simulation of Electron Trajectory in Solids. `http://www.gel.usherbrooke.ca/casino/index.html`

[16] D.C. Joy *Monte Carlo Modeling for Electron Microscopy and Microanalysis*. In *Oxford Series in Optical and Imaging Science*, 9, Oxford University Press, 1995.

[17] M. Dapor. *Electron-Beam Interactions with Solids*. In *Springer Tracts in Modern Physics*, 186, Springer-Verlag Berlin Heidelberg, 2003.

[18] N. Bohr. The penetration of atomic particles through matter. *Mat. Fys. Medd. Dan Vid. Selsk.*, 18:8, 1948.

[19] O.B. Firsov. A qualitative interpretation of the mean electron excitation energy in atomic collisions. *Sov. Phys. JETP*, 36(9):1076–1080, 1959.

[20] J. Lindhard, V. Nielsen, and M. Scharff. Approximation method in classical scattering by screened Coulomb fields. *Mat. Fys. Medd. Dan Vid. Selsk.*, 36:10, 1968.

[21] J.F. Ziegler, J.P. Biersack, and U. Littmark. *The Stopping and Range of Ions in Solids*. Pergamon Press, New York, 2003.

[22] A. Sommerfeld. Asymptotische Integration der Differentialgleichung des Thomas-Fermischen Atoms *Z. Physik*, 78:283, 1932.

[23] G. Moliere. Theorie der Streuung schneller geladener Teilchen I. Einzelstreuung am abgeschirmten Coulomb-Feld. *Z. Naturforsch. A*, 2:133–145, 1947.

[24] W. Lenz. Über die Anwendbarkeit der statistischen Methode auf Ionengitter. *Z. Physik*, 77(11-12):713–721, 1932.

[25] H. Jensen. Die Ladungsverteilung in Ionen und die Gitterkonstante des Rubidiumbromids nach der statistischen Methode. *Z. Physik*, 77:722, 1932.

[26] W. Wilson, L. Haggmark, J.P. Biersack. Calculations of nuclear stopping, ranges, and straggling in the low-energy region. *Phys. Rev. B*, 15:2458–2468, 1977.

[27] D. O'Connor, J. Biersack. Comparison of theoretical and empirical interatomic potentials. *Nucl. Instrum. Meth. B*, 15:14–19, 1986.

[28] S. Nakagawa, Y. Yamamura. Interatomic potential in solids and its applications to range calculations. *Radiation Effects and Defects in Solids*, 105(3-4):239–256, 1988.

[29] W. Eckstein, S. Hackel, D. Heinemann, B. Fricke. Influence of the interaction potential on simulated sputtering and reflection data. *Z. Phys. D*, 24:171–176, 1992.

[30] R. Behrisch, W. Eckstein. *Sputtering by Particle Bombardment - Chapter 2*. In *Topics in Applied Physics*, 10, Springer-Verlag Berlin Heidelberg, 2007.

[31] M. Nastasi, J.W. Mayer, and J.K. Hirvonen. *Ion-Solid Interactions: Fundamentals and Applications*. Cambridge University Press, 1996.

[32] N. Imanishi. *Focused Ion Beams Systems, Basics and Applications - Chapter 2*. Ed. N. Yao, Cambridge University Press, 2007.

[33] K.B. Winterbon and P. Sigmund and J.B. Sanders. Spatial distribution of energy deposited by atomic particles in elastic collisions. *Mat. Fys. Medd. Dan Vid. Selsk.*, 37:14, 1970.

[34] J. Lindhard, M. Scharff, and H. Schiott. Range concepts and heavy ion rangesy. *K. Dan. Vidensk. Seslsk. Mat. Fys. Medd.*, 33(14):39–43, 1963.

[35] J. Ziegler. SRIM and TRIM. `http://www.srim.org/`

[36] R.A. Baragiola, E.V. Alonso, J. Ferron and A. Oliva-Florio. Ion-induced electron emission from clean metals. *Surf. Sci.*, 90(2):140–255, 1979.

[37] J. Lorincik, Z. Sroubek, H. Eder, F. Aumayr, and H. Winter. Kinetic electron emission from clean polycrystalline gold induced by impact of slow C^+, N^+, O^+, Ne^+, Xe^+, and Au^+ ions. *Phys. Rev. B*, 62(23):16116–16125, 2000.

[38] K. Ohya and T. Ishitani. Target material dependence of Secondary Electron images induced by Focused Ion Beams. *Surf. Coat. Tech.*, 158-159:8–13, 2002.

[39] L.A. Giannuzzi, B.I. Prenitzer, and B.W. Kempshall. *Introduction to Focused Ion Beams - Chapter 4*. Editors L.A. Giannuzzi and F.A. Stevie, 2005.

[40] M. Utlaut. *Handbook of Charged Particle Optics - 2^{nd} ed. - Chapter 11*. Ed. J. Orloff, CRC Press, 2009.

[41] P. Sigmund. Theory of sputtering I: sputtering yield of amorphous and polycrystalline targets. *Phys. Rev.*, 184(2):383–416, 1969.

[42] N. Matsunami. Energy dependence of the yields of ion-induced sputtering of monoatomic solids. *At. Dat. & Nuc. Dat. Tab.*, 31(1):1–80, 1984.

[43] Y. Yamamura. Energy dependence of the yields of ion-induced sputtering of monoatomic solids at normal incidence. *At. Dat. & Nuc. Dat. Tab.*, 62(2):149–253, 1996.

[44] H. Kahn. Random Sampling (Monte Carlo) Techniques in Neutron Attenuation Problems, I & II. *Nucleonics*, 6(5-6):27–33,60–65, 1950.

[45] R. Ramachandra, B. Griffin, and D. Joy. A model of secondary electron imaging in the helium ion scanning microscope. *Ultramicroscopy*, 109(6):748–757, 2009.

[46] H.A. Bethe. On the theory of secondary emission. *Phys. Rev.*, 59:940–941, 1941.

[47] H. Salow. Sekundarelektronen-emission. *Phys. Zeit.*, 41:434–436, 1940.

[48] R.C. Forbes and G.L.R. Mair. *Handbook of Charged Particle Optics - Chapter 2*. Ed. J. Orloff, CRC Press, 2009.

[49] W. Driesel, C. Dietzsch, and R. Muhle. In situ observation of the tip shape of AuGe liquid alloy ion sources using a high voltage transmission electron microscope. *J. Vac. Sci. Technol. B*, 14(5):3367–3380, 1996.

[50] O.C. Wells. *Scanning Electron Microscopy, pp. 20–36*. McGraw-Hill, New York, 1974.

[51] W. Shockley and J.R. Pierce. A Theory of Noise for Electron Multipliers *Proceedings of the Institute of Radio Engineers*, 26(3):321–332, 1938.

[52] D. Bell. Contrast Mechanisms and Image Formation in Helium Ion Microscopy *Microsc. Microanal.*, 15(2):147–153, 2009.

[53] S. Ogawa, W. Thompson, L. Stern, L. Scipioni, J. Notte, L. Farkas, and L. Barriss. Helium Ion Secondary Electron Mode Microscopy For Interconnect Material Imaging *Jpn. J. Appl. Phys.*, 49(4):04DB12 ,2010.

[54] J. Orloff, L.W. Swanson, and M. Utlaut. Fundamental limits to imaging resolution for focused ion beams. *J. Vac. Sci. Technol. B*, 14(6):3759–3763, 1996.

[55] V. Castaldo, C. W. Hagen, B. Rieger, and P. Kruit. Sputtering limits versus signal-to-noise limits in the observation of Sn-balls in a Ga^+ microscope. *J. Vac. Sci. Technol. B*, 26(6):2107–2115, 2008.

[56] V. Castaldo, C. W. Hagen, P. Kruit, E. van Veldhoven, and D. Maas. On the influence of the sputtering in determining the resolution of a scanning ion microscope. *J. Vac. Sci. Technol. B*, 27(6):3196–3202, 2009.

[57] H.D. Hagstrum. Auger ejection of electrons from tungsten by noble gas ions. *Phys. Rev.*, 96(2):325–335, 1954.

[58] H.D. Hagstrum. Theory of Auger ejection of electrons from metals by ions. *Phys. Rev.*, 96(2):336–365, 1954.

[59] L.A. Giannuzzi, M. Utlaut, and M. Scheinfein. Relative Contrast in Ion and Electron Induced Secondary Electron Images. *Microsc. Microanal.*, 14(suppl 2):1188–1189, 2008.

[60] B.J. Griffin, and D. Joy. Variation of Rutherford Backscattered Ion and Ion-induced Secondary Electron Yield with Atomic Number in the “Orion” Scanning Helium Ion Microscope. *Microsc. Microanal.*, 14(suppl 2):1190–1191, 2008.

[61] B. Svensson, Holmen, and A. A. Buren. Angular dependence of the ion-induced secondary-electron yield from solids. *Phys. Rev. B: Condens. Matter Mater. Phys.*, 24(7):3749–3755, 1981.

[62] J. Ferron, E. Alonso, R. Baragiola, A. Oliva-Florio. Dependence of ion-electron emission from clean metals on the incidence angle of the projectile. *Phys. Rev. B: Condens. Matter Mater. Phys.*, 24(8):4412–4419, 1981.

[63] E.J. Sternglass. Theory of Secondary Electron emission by high-speed ions. *Phys. Rev.*, 108(1):1–12, 1957.

[64] K. Ohya and J. Kawata. Monte Carlo study of incident-angle dependence of ion-induced kinetic electron emission from solids. *Nucl. Instrum. Meth. B*, 90(1-4):552–555, 1994.

[65] Y. Yamamura, C. Mossner, H. Oechsner. The bombarding-angle dependence of sputtering yields under various surface conditions. *Radiation Effects*, 103:25–43, 1987.

[66] H. Seiler. Secondary Electron emission in the Scanning Electron Microscope. *J. Appl. Phys.*, 54(11):R1–R18, 1983.

[67] B.W. Kempshall, S.M. Schwarz, B.I. Prenitzer, L.A. Giannuzzi, R.B. Irwin, and F.A. Stevie. Ion channeling effects on the focused ion beam milling of Cu. *J. Vac. Sci. Technol. B*, 19(3):749–754, 2001.

[68] Lord Rayleigh. Investigations in optics, with special reference to the spectroscope. *Philos. Mag.*, 8:261–274, 403–411, 477–486, 1879.

[69] G.B. Airy. On the diffraction of an object-glass with circular aperture. *Trans. Cambridge Philos. Soc.*, 5:283–291, 1835.

[70] J.E. Barth and P. Kruit. Addition of different contributions to the charged particle probe size. *Optik*, 101(3):101–109, 1996.

[71] P. Kruit, M. Bezuijen, and J. Barth. Source brightness and useful beam current of carbon nanotubes and other very small emitters. *J. Appl. Phys.*99(2):024315, 2006.

[72] A. van den Bos. Resolution in Model-Based Measurement. *IEEE T. Instrum. Meas.*, 51(5):1055–1060, 2002.

[73] M. Sato. *Handbook of Charged Particle Optics - Chapter 8*. Ed. J. Orloff, CRC Press, 2009.

[74] M. Sato and J. Orloff. A new concept of theoretical resolution of an optical system, comparison with experiment and optimum condition for a point source. *Ultramicroscopy*, 41(1-3):181–192, 1992.

[75] C.E. Shannon. A Mathematical Theory of Communication. *Bell Syst. Tech. J.*, 27:379–423, 1948.

[76] E.H. Linfoot. Information theory and optical images. *J. Opt. Soc. Am.*, 45:808–819, 1955.

[77] X.R. Jiang, J.E. Barth, and P. Kruit. Combined calculation of lens aberrations, space charge aberrations, and statistical coulomb effects in charged particle optical columns. *J. Vac. Sci. Technol. B*, 14(6):3747–3752, 1996.

[78] J.E. Barth and M.D. Nykerk. Dependence of the chromatic aberration spot size on the form of the energy distribution of the charged particles. *Nucl. Instrum. Methods Phys. Res., Sect. A*, 427(1-2):86–90, 1999.

[79] V.N. Tondare. *Towards a High Brightness, Monochromatic Electron Impact Gas Ion Source*. PhD thesis, Delft University of Technology, 2006.

[80] P.W. Verbeek and L.J. van Vliet. On the location error of curved edges in low-pass filtered 2-d and 3-d images. *IEEE Transactions on Pattern Analysis and Machine Intelligence*, 16(7):726–733, 1994.

[81] A. Vladár, M. Postek, and B. Ming. On the Sub-Nanometer Resolution of Scanning Electron and Helium Ion Microscopes *Microscopy Today*, 3:8-13, 2009.

[82] E. Kieft, E. Bosch. Refinement of Monte Carlo simulations of electron-specimen interaction in low-voltage SEM. *J. Phys. D: Appl. Phys.*, 41:215310 (10pp), 2008.

[83] J. Orloff. Limits on imaging resolution of focused ion beam system. *SPIE Proc. Ser.*, 2522:412–420, 1995.

[84] M. Postek and A. Vladár. Helium Ion Microscopy and its application to nanotechnology and nanometrology. *Scanning*, 30(6):457–462, 2008.

[85] T. Muramoto. MD study on temperature dependence of sputtering yield. *Nucl. Instrum. Meth. B*, 267(18):3232–3234, 2009.

[86] W. Boxleitner and G.J. Hobler. FIBSIM–dynamic Monte Carlo simulation of compositional and topography changes caused by focused ion beam milling. *Nucl. Instrum. Meth. B*, 180(1-4):125–129, 2001.

[87] H. Kim, G. Hobler, A. Steiger, A. Lugstein, and E. Bertagnolli. Full three-dimensional simulation of focused ion beam micro/nanofabrication. *Nanotechnology* 2007, 18(24):245303(8pp), 2007.

[88] V. Castaldo, J.M. Withagen, C.W. Hagen, E. van Veldhoven, and P. Kruit. Angular Dependence of the Ion-Induced Secondary Electron Emission for He^+ and Ga^+ Beams. *Microsc. Microanal.*, 17(4):xxxx–xxxx, 2011.

[89] J. Bi and P.W.H. de Jager and J.E. Barth, and P. Kruit. Influence of Coulomb interactions on current density distribution in a two-lens focused ion beam system. *Microelectron. Eng.*, 41-42:249–252, 1998.

[90] I.T. Young, J.J. Gerbrands, and L.J. van Vliet. Fundamentals of Image Processing. *Delft University of Technology*, version 2.3. `ftp://ftp.tudelft.nl/pub/DIPimage/docs/FIP2.3.pdf`

A

APPENDIX

Appendix A: List of Abbreviations

ADC	Analog-to-Digital Converter
BCA	Binary Collision Approximation
CM	Center of Mass
DQ	Detector Quantum Efficiency
FIB	Focused Ion Beam
FT	Fourier Transform
FW50	Full Width at 50%
FWHM	Full Width at Half Maximum
GFIS	Gas Field Ion Source
HV	High Vacuum
IBID	Ion Beam Induced Deposition
IC	Integrated Circuit
IPC	Information Passing Capacity
LBE	Lattice Binding Energy
LCC	Linear Collision Cascade
LAIS	Liquid Alloy Ion Source
LMIS	Liquid Metal Ions Source
MD	Molecular Dynamics
MFP	Mean Free Path
MTF	Modulation Transfer Function
OTF	Optical Transfer Function
PSF	Point Spread Function
PTF	Phase Transfer Function
RMS	Roat Mean Square

ROI	Region of Interest
SBE	Surface Binding Energy
SE	Secondary Elecron
SEM	Scanning Elecron Microscope
SM	Scanning Microscopy
SIM	Scanning Ion Microscope
SNR	Signal-to-Noise Ratio
STEM	Scanning Transmission Electron Microscope
TEM	Transmission Electron Microscope
UHV	Ulta High Vacuum

B APPENDIX

Appendix B: List of Symbols

SMALL GREEK

α	Beam Incidence Angle
α_i	Semi-aperture Angle at the Image Side
α_o	Semi-aperture Angle at the Object Side
β	Dimensionless Factor in the LCC Theory of Sputtering
γ	Sputter Yield
γ_{tot}	Total SPutter Yield
δ_e	Electron-Induced SE Yield
δ_i	Ion-Induced SE Yield
$\delta_{i,e}$	Fraction of δ_i produced by Secondary Electrons
$\delta_{i,i}$	Fraction of δ_i produced by Primary Ions
$\delta_{i,r}$	Fraction of δ_i produced by Recoils
ϵ	Reduced Energy (orBethe Parameter for iSE Emission)
η_e	SE Detector Quantum Efficiency
θ	Scattering Angle in the Laboratory System
θ_c	Scattering Angle in the Center of Mass System
λ	Wavelength (or Salow Parameter for iSE Emission)
ρ	Density
ρ_H	Density of Information Passing Capacity
σ	Cross-Section
τ	Optical Transfer Function
τ_{ar}	Acceptance Factor
τ_b	Spatial Frequency Response
τ_s	Fourier Transform of $J_s(r)$

ϕ	Work Function
φ	Recoil Angle in the Laboratory System
φ_c	Recoil Angle in the Center of Mass System
ψ	Ejection Angle from the Target Surface
ω	Relative Beam Overlap
$\bar{\omega}$	Complement to 1 of the Relative Beam Overlap

——————- BIG GREEK ——————-

Φ_L	Lindhard Screening Function
Φ_{LJ}	Lenz-Jensen Screening Function
Φ_M	Moliere Screening Function
Φ_S	Sommerfield Screening Function
Φ_{TF}	Thomas-Fermi Screening Function
Φ_U	Ziegler (Universal) Screening Function
Φ_{WHB}	Wilson-Haggmark-Biersack Screening Function
Ω	Solid Angle

——————- SMALL LATIN ——————-

a_0	Bohr Radius
a_B	Bohr Screening Length
a_F	Firsov Screening Length
a_L	Lindarhd Screening Length
a_U	Ziegler (Universal) Screening Length
d_a	Diffraction Contribution to the Probe Size
d_b	Probe Diameter
d_c	Chromatic Aberration Contribution to the Probe Diameter
d_g	Virtual Source Contribution to the Probe Diameter
d_s	Spherical Aberration Contribution to the Probe Diameter
d_v	Virtual Source Size
e	Electron Charge
k_{sn}	Signal-to-Noise Ratio

k_{sn}^{eff}	Effective Signal-to-Noise Ratio
l	Raster Size on the Sample
n	Density of Conduction Electrons
p	Impact Parameter
r_b	Probe Radius
s_e	Reduced Electronic Stopping Cross-Section
s_n	Reduced Nuclear Stopping Cross-Section
t	Depth of Sputtering Surface
t_d	Dwell Time
t_s	Scanning Time
v	Velocity (General)
v_c	Velocity of the Center of Mass System
v_B	Velocity of the Bohr Electron in the Hydrogen Atom
v_F	Fermi Velocity
$w_a(r)$	Point Spread Function

—————————- BIG LATIN —————————-

A_{px}	Pixel Area
C_c	Chromatic Aberration Coefficient
C_s	Spherical Aberration Coefficient
D_i	Ion Dose
E	Energy (General)
E_a	Energy of a Recoil
$E_b(E)$	Energy of the Primary Beam
E_F	Fermi Energy
E_g	Energy Gap in an Insulator
E_i	Ionisation Energy
E_{lat}	Lattice Binding Energy
E_{surf}	Surface Binding Energy
E_{th}	Ion Threshold Energy for Secondary Emission in Metals
F	Fourier Operator
H_A	Mean Information Content in a Micrograph

I_b	Beam Current
J_b	Current Density Distribution
$J_{b,p}$	Current Density Distribution from a Point Source
J_c	Angular Momentum in the Center of Mass System
J_n	Bessel Function of Order n
J_s	Current Density Distribution at the Image Plane
L	Raster Size on the Screen
M	Linear Magnification
M_M	Molecular Mass
M_{scr}	Screen Magnification
N_A	Avogadro's Number
N_a	Number of Atoms
N_e	Number of Electrons
N_g	Number of Gray Levels in a Micrograph
N_i	Number of Ions
N_l	Number of Pixels on a Scan Line
N_{px}	Total Number of Pixels
R_{es}	Resolution
$R_{es,RC}$	Rayleigh Resolution
S	Sputter Sensitivity
S_e	Electronic Stopping Cross-Section
S_n	Nuclear Stopping Cross-Section
T	Energy Lost by a Primary Ion in a Collision
U_I	Information Uncertainty
U_S	Sputtering Uncertainty
U_{SM}	Sample Modification Uncertainty
Z	Atomic Number
Z_{eff}	Effective Atomic Number

C APPENDIX

Appendix C: Curriculum Vitae

Vincenzo Castaldo was born on April 24th 1979 in Naples, Italy. After getting the diploma of High School for Classical Studies in 1998, he enrolled in the faculty of Material Engineering in the 'Università degli Studi di Napoli Federico II', Naples, Italy, where he received his MSc degree in February 2005, "magna cum laude". During the work for his master thesis, which was entitled: 'Experimental study of thermal fluctuations in Josephson devices employing NbN and superconducting oxides', he worked on the fabrication and carachterisation low-T_c and high-T_c Josephson Junctions. Just after graduating (ok, maybe after a couple of months of deserved holiday), he was employed by the Kuwait Petroleum Italia oil company as Capital Project Engineer, with the main task of coordinating the projects directed to rearrangement, innovation and optimization of the Q8 deposit in Naples (one of the largest in Europe). The projects were managed in all the steps, from budget assignment to realization.

The urge for something else, and somewhere else, had just been put on hold. In May 2006 he applied for a PhD position at the Charged Particle Optics Group at the Faculty of Applied Physics in TU Delft. The move was, to a certain extent, brave: he had never seen a microscope before, and he asked to be part of a group of microscope designers. Sometimes audacity is rewarded, and in September he was offered the job, to start his contract on November 1st 2006, under the supervision of prof. Pieter Kruit. The project had the broad title of: 'Ion/Matter Interaction', and was initially founded by the research group itself ('a bet', to quote prof. Kruit). After one year, the project found the sponsorisation of the FOM (Stichting voor Fundamenteel Onderzoek der Materie). During the 4-year PhD project in the Netherlands (to become four-and-a-half), new experiences, new challenges, new views and new people have been an invaluable treasure to never leave behind.

Publications

V. Castaldo, C. W. Hagen, B. Rieger, and P. Kruit.
Sputtering limits versus signal-to-noise limits in the observation of Sn-balls in a Ga^+ microscope.
Journal of Vacuum Science & Technology B, 26(6):2107–2115, 2008.

V. Castaldo, C. W. Hagen, P. Kruit, E. van Veldhoven, and D. Maas.
On the influence of the sputtering in determining the resolution of a scanning ion microscope.
Journal of Vacuum Science & Technology B, 27(6):3196–3202, 2009.

V. Castaldo, J.M. Withagen, C.W. Hagen, E. van Veldhoven, and P. Kruit.
Angular Dependence of the Ion-Induced Secondary Electron Emission for He^+ and Ga^+ Beams.
Microscopy & Microanalysis, 17(4):1–13, 2011.

V. Castaldo, C.W. Hagen, and P. Kruit.
Simulation of Ion Imaging: Sputtering, Contrast, Noise.
Ultramicroscopy, 2011; doi:10.1016/j.ultramic.2011.03.019

Post Scriptum

Like , I believe, most cases, my PhD project ended up being something somehow different, and certainly more definite, than it seemed it would be at the beginning, in the summer of 2006. It would be interesting to evaluate how much of a PhD project is shaped by its promotor, whose ideas are partially clear since the project is written down, and how much by the student that makes the project her/his own, who is surely much less aware of what the next four years are going to be. I think that anyone who has been into my position has wondered about the same. This flow of ideas, problems, solutions, dead-ends and little big hopes is generally concealed from the reader, who has in her/his hands something that appears to be pretty linear, from the introduction up to this conclusions chapter. In an effort to try and give the reader a taste of 'PhD evolution', i shall separately comment on each of the the four main challenges that I ended up facing during this four-and-a-half-years PhD project: *Resolution in Ion Scanning Microscopy*, *Helium Scanning Microscopy*, *Ion-Induced Secondary Electron Emission* and *Simulation of Ion Imaging*. The order in which these topics appear here is not the order in which they appear in the thesis, for the reasons mentioned above. I have, thus, chosen to sort these four themes according to the order in which they presented themselves to me.

Theme I: Resolution in Scanning Ion Microscopy

The topic of resolution in ion scanning microscopy fully occupied the first two of my 'Dutch years' (and partially all the remaining ones up to this very moment), and has been tackled in this thesis in chapters 4, 5 and 6. At the end of 2006, helium microscopy was not yet commercially available, and almost any FIB machine suitable for imaging was equipped with a Liquid Metal Ion Source, typically gallium. It was clear already for some time, however, that LIMS would not provide subatomic resolution (or, equivalently, better-than-SEM resolution), not only because not even the best sources/columns could focus enough current in a subnanometer spot, but also because of the sample damage. On the other hand, the microscopy community had already put much hope on novel Gas Field Ion Sources, and in particular in sources employing light ions, like helium, which promised to overcome the sputtering problem. We knew that the availability of such machines would only be a matter of time, and we did not want to be unprepared when the moment would arrive to assess their performances. It came as a surprise to me when i was told that no satisfactory 'definition' of resolution, leave alone evaluation method, existed for ion scanning microscopy. This became thus the first challenge, and the outcome was my first journal paper, here in chapter 5. In this paper we proposed a definition of resolution based on a compromise between 'noisy Rayleigh resolution', based on the quality of a single micrograph, and 'sputtering resolution', which is intrinsically dynamic for it takes into account the fact that each small feature on the sample plane is, partially or entirely, sputtered away during imaging. The first message, therefore, was that resolution in FIB microscopy had to cease to be 'static': a single microscope image can not reveal the amount of detail with which a sample surface can be magnified and reproduced on screen, because the surface modification taking place during imaging can not be quantified from an instantaneous picture. Resolution became thus 'dynamic', in the sense that it is defined not by a picture, but by a movie. Another fundamental consequence of the sample surface dynamics is that there is no way to quantify the resolution obtainable with a given machine with a single number. In other words, no FIB manufacturer should ever write things like: 'This machine provides 3nm resolution'. The reason is simple: since the ultimate capability of observing small details depends on the amount of sample sputtering, and since the sputter yields depends, among other things, on the pair ion/atom, then the smallest observable feature will be also a function of the sample material. There is one third consequence of the sputtering problem, one that is even more subtle than the previous two. It has been pointed out more than once that the definition of resolution itself is not unique, but it depends on what needs to be quantified. In the most general case, in my opinion, resolution should be intended 'á la Rayleigh', i.e. as the ability to distinguish small features on the image plane. In this case, I believe (of course) that the best method to quantify it is via the procedure explained in chapters 5 and 6. In this case the resolution is necessarily sputtered-limited, and the best sample to determine it would be one with features of the material of interest, with a nearly-continuous size range of the order of the expected resolution, on a sputter-insensitive substrate (thus, not much dissimilar to the tin-ball sample, apart for the substrate). However, there could be instances in which the purpose of imaging is not showing small details, but, for example, very sharp edges. In this case, the obtainable sharpness could be made (almost) completely independent on the sputtering. The trick would be to take a sample whose surface repeats itself in the beam direction (that is, the sputtering direction), so that its image remains approximately[1] the same also when subsequent layers are removed. The perfect sample would therefore be a perfect edge, or, in other words, two perfect hemiplanes at different positions in the beam direction. And the obtained sharpness would not be dependent on the sputtering (and thus on the sample material), but almost entirely on the spot size. Another case could be the one in which the important parameter is not the smallest detectable feature, but the accuracy of a measurement on the image plane. In chapter 4 it has been shown that these two concepts are very closely related, if not coincident, in absence of sputtering. When sputtering is taken into account, however, they diverge. In particular, 'the first one can be made independent of the sputtering

---

[1] The approximations here is due to the fact that sputtering is observed also on vertical walls, mainly due to the scattering of ions inside the sample.

effect, since this increases monotonically with the scanning time and can be modelled and quantified, while the second is intrinsically connected with the sample modification'[2]. One more aspect that i want to highlight here, and that has been suggested here and there in this thesis, is the importance of a priori knowledge on the system under study. If the knowledge of the pair ion beam/sample were deterministic and complete, than in theory infinite resolution could be obtained, simply deconvolving sample surface topography and ion current distribution. In practice, requiring complete knowledge of the sample would be non-sense, for such knowledge is the purpose of microscopy, while requiring complete knowledge of the current distribution would simply be naïve, for this knowledge is intrinsically impossible to gather. As a matter of fact, however, any little piece of a priori knowledge, either on the ion current or on the sample, could be converted in an additional amount of image resolvability, in the postprocessing phase. As an example, consider the problem of spot measurement on a sharp edge. As I have mentioned just before, even a perfect edge would degrade after some time of ion imaging, because of the sputtering of the vertical walls. But if the edge repeats itself along one pixel-line direction, then the noise affecting a pixel profile of the edge acquired with low ion dose could be reduced, in theory down to negligibility, simply averaging a great number of profiles from different pixel lines. I shall conclude this section with a suggestion: when describing a microscope no mention should be made of the word 'resolution', for the simple reason that it would tell nearly nothing to anybody describing, or considering to buy, the machine. The only parameter that can be rightly assigned to a FIB microscope is its spot size (which, however, plays a big role in determining the quality of an imaging tool), together with information relating to how the spot size has been obtained. Any further piece of information relating the actual current distribution in the beam would be highly valuable.

Theme II: Helium Microscopy

No doubt that there was much luck in the fact that after two years of working with traditional FIBs, a novel helium microscope became available for me to use (not without some diplomatic effort) in the building next to the one i am sitting in this moment. Much of what I know about helium microscopy has thus been gathered though hand on experience. About the resolving power, it is no surprise that the He-FIB performs way better than the Ga-FIB, and the reason is two-fold: a sub-nanometric spot size and a very light ion species. Therefore, it was a bit disappointing to discover that atomic resolution seems unreachable still because of the sputtering[3]. The helium microscope, however, remains a jewel of ion-optics technology, already capable, at a very early stage of commercial development, to impress any SEM enthusiast with its sharp edges, clear SE contrast, impressive depth of focus, and sheer beauty. It is true that a more stable current would be desirable, that much must be done in terms of environmental noise reduction,

---

[2] From sec. 6.5.

[3] In order to see single atoms, any sample would be sputter sensitive, because at the atomic level no layer is indistinguishable from the others.

overall resilience and ease of operation[4]. But when you consider that it is just a-few-years-old technology, that it offers and/or promises a lot in terms of source brightness (nobody had managed before to focus so many ions in such a small spot), adaptability (in theory the same technology would work in the same way with other gaseous ion species), material analysis (thanks to the backscattered ion imaging mode, not available in an SEM) and beauty of images (which is a quality not to underestimate: in the end we are talking about fancy photographic tools), then not loving this brilliant device becomes hard.

Theme III: Ion-Induced Secondary Electron Emission

This third challenge is an example of things that I had no idea I would have to tackle before the problem showed itself. When I started working on my ion simulation code, I realised that curves of ion-induced secondary emission versus incidence angle of the beam were hard to find and even harder to simulate with the available (to me) Monte Carlo software. The obvious solution was to measure the emission myself, and so I resolved to do. The fact that it would take much longer than forecast was clear since the beginning, just because that is always the case; the fact that a well reviewed lengthy paper would come out of it was unexpected and welcome. Seen from here, it has been a great opportunity for me to appreciate the complexity of physical system, the difficulty to model them properly for the purpose dismissing all what is not needed, and the fundamental role played by data processing and analysis in order to obtain interesting results. The procedure to obtain SE yield curves has been designed, tested, redesigned, and so on, till the results and their reliability were satisfactory. It became clear very soon that several factors were playing a role: modification of the sample surface under ion bombardment, backscattered ions, production of SEs from places other than the sample. The influence of each of these factors has been recognised and discussed in the paper, and, in the case of the backscattered ions, quantification has been attempted. The final curves have been compared either with simple theoretical models or with simulations, available for helium beams; in all cases the agreement was good up to certain incidence angles, and the deviation for higher angles has been explained in terms of surface roughness of the sample. The 'local' explanation for the high contrast observed in the helium microscope has been identified with the low He-induced SE emission at normal incidence. Complex effects have been observed but not quantified. In particular, it became evident that the sputtering strongly influences the dynamics of secondary emission, which quickly decreases after the ion beam is shined on a certain spot on the sample. Even more interestingly, the signal dynamics at each new spot appear to be highly repeatable for each incidence angle, showing that the electronic dynamics are uniquely correlated with the topology of the surface. A quantitative analysis of the SE current recordings could result in a better understanding of the sample modification under ion bombardment.

---

[4] To be honest, operating an ORION® PLUS is not that difficult; however, if you spend so much money for such a delicate machine, you are quite reluctant to let anybody on it.

Theme IV: Simulation of Ion Imaging

The idea of simulating ion contrast and sputtering was already there at the time of my first article (chapter 5), where a preliminary, bi-dimensional, sputtering simulation has been presented. The main motivation was the realisation that using a Monte Carlo approach for a full ion imaging simulation would not be computationally practical. We wanted a code that would allow a fast determination of the capabilities of a given pair microscope/sample. Choice was made to use a semi-analytical approach, whose core would be the simulation of 'local' SE contrast and 'local' sputtering, through the yield-versus-incidence angle curves, and of noise from primary ions and secondary electrons. The code had to be designed in such a way that any further complication, like redeposition from sputtered atoms, noise from other sources and real collection efficiency, could be added independently, in a modular fashion. In the form which has got the honor of publication, only the above-mentioned core aspects are taken into account. Even with a contrast mechanism that incorporated no non-local effects, however, the proposed algorithm is already able to explain some first order differences between different microscopes, and in particular why SE contrast is higher in He-FIBs compared to Ga-FIBs. Furthermore, the code is already suitable for the optimisation of the ion dose for imaging features of given size/material, and for the determination of the smallest observable feature in an ion microscope. Another thing that the simulation made very clear, is that the noise contribution from the detector is non negligible, and has to be taken into account. In order to make the simulations more and more realistic, the first step will have to be to implement a model for the redeposition of sputtered atoms. This will be challenging, for it will imply the loss of that locality which is a (limiting) feature of the present algorithm.

Vincenzo Castaldo
Delft, April 2011

Acknowledgments

> *"Every time I see an adult on a bicycle,*
> *I no longer despair for the future of the human race."*
> Herbert George Wells

There are several people I wish to thank. Some of them have contributed greatly to this thesis project, others gave no direct contribution but have represented the bulk of my universe in these four and a half years, and have participated in shaping my view on things.

First of all, the 'big men' of the Charged Particle Group in Delft: Pieter Kruit, my boss, promotor and main scientific advisor; Kees Hagen, for his endless patience and the enjoyable company, always; and the late Jim Barth, for his precious advices, that came all for free.
Immediately after, my colleagues of 'first level', the ones that belong to my PhD batch: Benjamin John Cook and Ali Mohammadi Gheidari, two of the most interesting persons I have ever met and my dearest friends; and David Jun, with whom, unfortunately, I have shared a bit less.
Colleagues of 'second level', the ones that were already here when I arrived: Anand Dokania, my favourite Indian ever, Aurélien Botman, a gentleman, Merijn Bronsgeest and Willem van Dorp.
Colleagues of 'third level', the ones, not necessarily PhD students, that joined the CPO group later than I did: Angela Carolina Narváez Gonzalez, Nalan Liv and Ivan Lazić, the three best ways to conclude a PhD, Christian Zonnevylle and Jacob Hoogenboom.
Only one person has had the luck to belong to the category 'my students': Jos Withagen, who is now a fantastic funny friend. The technicians of the CPO group: Vladimir Kutchoukov, Frans Berwald, Jan de Looff, Carel Heerkens and Jacques Nonhebel.
The secretaries that saved my day (and probably hated my laziness) in countless occasions: Margaret van Fessem, Elly van der Most and Anjella van Vliet. Some people have contributed, in different ways, from outside the CPO group: Sanneke Brinkers and Libertario Demi, who also happen to be my close friends, Bernd Rieger, Paul Alkemade, Emile van Veldhoven and Diederik Maas.
The three heroes that have been the victims of my software experimentations: Ronald Ligteringen, Wilfred van der Wees and Paul Keekstra.
A few people from FEI company; some entered the picture by default, for their

position in the chain of command: Greg Schwind, Frank de Jong and David Tuggle; some are here only due to their kindness: Alan Bahm, Sean Kellog and Hans Mulders.

Two ‘field experts’ that probably do not even remember my name, but whose answer to my question have always been swift, cooperative and polite: David Joy and James Ziegler.

The people that have not been directly involved in my research, but whose friendship made the TU world worthy to me (girls first): Lara Babich, Eleonora Congiu, Katerina Stanková and Valentina Koschatzky; Markus Haase, Paolo Massioni, Federico La Torre, Anton Schlesinger, Giannandrea Abbate, Alexander Kostenko and Caner Hamarat.

Of course the biggest thanks goes to my family; not only my sister, my mother, and my father, but also those very few persons that I feel as family, not by blood, but by acquisition. They know who they are.

I feel to owe a final, special thanks, to the Netherlands: a country not void of defects, but that approximates perfection better than any other I have ever lived. A country held by gentle, sometimes awkward people, that gave me the chance to become what I am, without ever making me feel out of place. I am proud to live and pay taxes here.

Vincenzo Castaldo
Delft, April 2011